Techniques to Improve the Efficiency of Data Transmission in Cable Networks

A Thesis Submitted
to the College of Graduate Studies and Research
in Partial Fulfillment of the Requirements
for the Degree of Doctor of Philosophy
in the Department of Electrical and Computer Engineering
University of Saskatchewan

by

Tung T. Nguyen

Saskatoon, Saskatchewan, Canada

Permission to Use

In presenting this thesis in partial fulfillment of the requirements for a Postgraduate degree from the University of Saskatchewan, it is agreed that the Libraries of this University may make it freely available for inspection. Permission for copying of this thesis in any manner, in whole or in part, for scholarly purposes may be granted by the professors who supervised this thesis work or, in their absence, by the Head of the Department of Electrical and Computer Engineering or the Dean of the College of Graduate Studies and Research at the University of Saskatchewan. Any copying, publication, or use of this thesis, or parts thereof, for financial gain without the written permission of the author is strictly prohibited. Proper recognition shall be given to the author and to the University of Saskatchewan in any scholarly use which may be made of any material in this thesis.

Request for permission to copy or to make any other use of material in this thesis in whole or in part should be addressed to:

Head of the Department of Electrical and Computer Engineering
57 Campus Drive
University of Saskatchewan
Saskatoon, Saskatchewan, Canada
S7N 5A9

Abstract

The cable television (CATV) networks, since their introduction in the late 1940s, have now become a crucial part of the broadcasting industry. To keep up with growing demands from the subscribers, cable networks nowadays not only provide television programs but also deliver two-way interactive services such as telephone, high-speed Internet and social TV features. A new standard for CATV networks is released every five to six years to satisfy the growing demands from the mass market. From this perspective, this thesis is concerned with three main aspects for the continuing development of cable networks: (i) efficient implementations of backward-compatibility functions from the old standard, (ii) addressing and providing solutions for technically-challenging issues in the current standard and, (iii) looking for prospective features that can be implemented in the future standard.

Since 1997, five different versions of the digital CATV standard had been released in North America. A new standard often contains major improvements over the previous one. The latest version of the standard, namely DOCSIS 3.1 (released in late 2013), is packed with state-of-the-art technologies and allows approximately ten times the amount of traffic as compared to the previous standard, DOCSIS 3.0 (released in 2008). Backward-compatibility is a must-have function for cable networks. In particular, to facilitate the system migration from older standards to a newer one, the backward compatible functions in the old standards must remain in the newer-standard products. More importantly, to keep the implementation cost low, the inherited backward compatible functions must be redesigned by taking advantage of the latest technology and algorithms.

To improve the backward-compatibility functions, the first contribution of the thesis focuses on redesigning the pulse shaping filter by exploiting infinite impulse response (IIR) filter structures as an alternative to the conventional finite impulse response (FIR) structures. Comprehensive comparisons show that more economical filters with better performance can be obtained by the proposed design algorithm, which considers a hybrid parameterization of the filter's transfer function in combination with a constraint on the pole radius to be less than 1.

The second contribution of the thesis is a new fractional timing estimation algorithm based on peak detection by log-domain interpolation. When compared with the commonly-used timing detection method, which is based on parabolic interpolation, the proposed algorithm yields more accurate estimation with a comparable implementation cost.

The third contribution of the thesis is a technique to estimate the multipath channel for DOCSIS 3.1 cable networks. DOCSIS 3.1 is markedly different from prior generations of CATV networks in that OFDM/OFDMA is employed to create a spectrally-efficient signal. In order to effectively demodulate such a signal, it is necessary to employ a demodulation circuit which involves estimation and tracking of the multipath channel. The estimation and tracking must be highly accurate because extremely dense constellations such as 4096-QAM and possibly 16384-QAM can be used in DOCSIS 3.1. The conventional OFDM channel estimators available in the literature either do not perform satisfactorily or are not suitable for the DOCSIS 3.1 channel. The novel channel estimation technique proposed in this thesis iteratively searches for parameters of the channel paths. The proposed technique not only substantially enhances the channel estimation accuracy, but also can, at no cost, accurately identify the delay of each echo in the system. The echo delay information is valuable for proactive maintenance of the network.

The fourth contribution of this thesis is a novel scheme that allows OFDM transmission without the use of a cyclic prefix (CP). The structure of OFDM in the current DOCSIS 3.1 does not achieve the maximum throughput if the channel has multipath components. The multipath channel causes inter-symbol-interference (ISI), which is commonly mitigated by employing CP. The CP acts as a guard interval that, while successfully protecting the signal from ISI, reduces the transmission throughput. The problem becomes more severe for downstream direction, where the throughput of the entire system is determined by the user with the worst channel. To solve the problem, this thesis proposes major alterations to the current DOCSIS 3.1 OFDM/OFDMA structure. The alterations involve using a pair of Nyquist filters at the transceivers and an efficient time-domain equalizer (TEQ) at the receiver to reduce ISI down to a negligible level without the need of CP. Simulation results demonstrate that, by incorporating the proposed alterations to the DOCSIS 3.1 down-link

channel, the system can achieve the maximum throughput over a wide range of multipath channel conditions.

Acknowledgments

I am very grateful for an opportunity of meeting many people during my studies who had helped me to make this dissertation possible. A few words mentioned here cannot adequately express my appreciation.

I would like to express my deepest gratitude to my academic supervisors, Prof. Ha Nguyen and Prof. Eric Salt, as well as my industrial supervisor, Dr. Brian Berscheid. Throughout my research program at the university, it is a great honor to receive Prof. Ha Nguyen's invaluable support and extremely helpful guidance, without which, this dissertation cannot be made possible. I am highly impressed by his professionalism in doing research, because of which, I feel thankful for the opportunity to work with him in the early stage of my career. Also, it is difficult to overstate my gratitude to my co-supervisor, Prof. Eric Salt, with whom I had a lot of joy in performing research. I appreciate his great effort on explaining things so simply and clearly. Especially, I find his criticism highly motivated as it always brings me ideas for new inventions. Lastly, it is truly my honor to have an opportunity to work with Dr. Berscheid, who provides me with a lot of encouragement and good company. His industrial oriented advices quite often steer me to the meaningful and practical research problems.

I would like to thank the other members of my committee, Profs. Jean-Yves Chouinard, Scott Noble, Rama Gokaraju, Francis Bui and Seok-Bum Ko for the assistance they provided at all levels of the research project.

I would also like to express my deepest gratitude and love to my family for their unconditional love, care and support for each and every endeavor in my life.

Finally, I gratefully acknowledge Vecima Networks Inc., Natural Sciences and Engineering Research Council of Canada (NSERC) and University of Saskatchewan for their financial support of my studies.

Table of Contents

List of Tables

List of Figures

List of Abbreviations

A/D	Analog to Digital
ADC	Analog-to-Digital Converter
AWGN	Additive White Gaussian Noise
BER	Bit Error Rate
BPSK	Binary Phase Shift Keying
CATV	Cable Television
CIR	Channel Impulse Response
CM	Cable Modem
CMTS	Cable Modem Termination System
CP	Cyclic Prefix
CSI	Channel State Information
D/A	Digital to Analog
DAC	Digital-to-Analog Converter
DFT	Discrete Fourier Transform
DOCSIS	Data Over Cable Service Interface Specification
DSL	Digital Subscriber Line
FD	Frequency Domain
FEQ	Frequency-Domain Equalizer
FIR	Finite Impulse Response
FPGA	Field-Programmable Gate Array
GN	Gauss-Newton
ICE	Iterative Channel Estimation
IDFT	Inverse Discrete Fourier Transform
IIR	Infinite Impulse Response
ISI	Inter-Symbol Interference
LDPC	Low Density Parity Check
LMMSE	Linear Minimum Mean-Square Error

LMS	Least Mean Squared
LPF	Low-Pass Filter
LS	Least Square
MMSE	Minimum Mean Square Error
MSE	Mean Squared Error
NCO	Numerically Controlled Oscillator
OFDM	Orthogonal Frequency-Division Multiplexing
OFDMA	Orthogonal Frequency-Division Multiple Access
P/S	Parallel-to-Serial
PR	Positive Realness
QAM	Quadrature Amplitude Modulation
QPSK	Quadrature Phase Shift Keying
RF	Radio Frequency
S/P	Serial-to-Parallel
SC-QAM	Single-Carrier Quadrature Amplitude Modulation
SIR	Signal-to-Interference Ratio
SM	Steigliz-McBride
SNR	Signal-to-Noise Ratio
SRRC	Square Root Raised Cosine
TD	Time Domain
TDR	Time Domain Reflectometry
TEQ	Time-Domain Equalizer
ZF	Zero Forcing

List of Symbols

$C[m]$	frequency-domain equalizer's coefficients
D	integer timing adjustment
$D(\omega)$	target frequency response
E_s	average energy per symbol
$F[k]$	multipath channel's frequency response over the entire channel bandwidth
F_s	sampling rate in Hz
$F_\Theta(z;\epsilon)$	transfer function of an order-Θ Thiran allpass filter with fractional delay ϵ
F_{sym}	symbol rate in Hz
$G[m]$	multipath channel's frequency response at sub-carrier $\mathcal{S}[m]$
$H[m]$	multipath channel's frequency response at sub-carrier $\mathcal{S}[m]$
$H_{\text{RC}}(f)$	frequency responses of a raised cosine filter
$H_{\text{RX}}(f)$	frequency responses of a matched filter
$H_{\text{TX}}(f)$	frequency responses of a pulse shaping filter
$I_0(\cdot)$	the zeroth-order modified Bessel function of the first kind
$J(\boldsymbol{X})$	the cost function for the given vector $\boldsymbol{X}$ of filter's parameters
K	sub-carrier skipping factor
L	definition for chapter 5: number of channel paths
L	definition for chapter 2,3&6: ratio of the sampling rate to the symbol rate
M	definition for chapter 2: length of preamble sequence
M	definition for chapter 3,5&6: number of active sub-carriers
N	total number of sub-carriers
N_0	one sided power spectral density
N_F	FIR filter length in samples
N_τ	length of the digital-equivalent multipath channel in samples
N_g	guard interval length in samples

N_p	number of paths in a multipath channel
N_{CP}	cyclic prefix length in samples
N_{skip}	sub-carrier skipping factor
P	number of real poles
$P_E^{\max}$	maximum Thiran interpolation error
P_M	BER for M-QAM constellation with Gray mapping
P_e	false alarm probability
P_{ISI}	normalized ISI power
Q	number of complex poles
R	number of real zeros
$R_{bb}[k]$	auto-correlation function of the preamble sequence
$R_{xy}[n]$	correlation between the transmitted and the received sequences
T_g	guard interval duration in seconds
T_{sym}	symbol period in seconds
U	resolution factor
$W[m]$	frequency-domain AWGN noise samples
W_i	the weight of frequency ω_i
$X[m]$	transmitted frequency-domain QAM symbols
$Y[m]$	received frequency-domain symbols before equalization
Z	number of complex zeros
Δt	timing offset in seconds
Ω	definition for chapter 6: FIR filter order
Θ	Thiran all-pass filter order
$\Theta_{\max}$	maximum order allowed for any Thiran interpolator in the TEQ
$\Upsilon(\cdot)$	channel path kernel function
α	definition for chapter 3: Kaiser window shape parameter
α_i	gain factor of a channel path

β	definition for chapter 5: slope of the linear approximation
β	roll-off factor of a raised cosine filter
$\boldsymbol{X}$	vector of filter's parameters
$\boldsymbol{\delta}$	vector of iterative update parameters
$\boldsymbol{\mathcal{S}}$	vector of data sub-carrier indexes
χ	scaling factor
δ	the Dirac delta function
ϵ	definition for chapter 6: fractional delay in samples
$\epsilon_{\max}$	multipath channel delay spread in samples
η	definition for chapter 3: SM method sharp peak damping factor
η	definition for chapter 6: integer delay in samples
γ_0	complement of the negative delay in seconds
$\hat{\varphi}$	FIR filter delay in samples
$\hat{v}[n]$	the sampler's complex output
$\hat{v}_{\mathrm{I}}[n]$	in-phase component of the sampler's output
$\hat{v}_{\mathrm{Q}}[n]$	quadrature component of the sampler's output
κ	definition for chapter 2: location of the main tap of $h_\tau[n]$
κ	definition for chapter 4: ratio of magnitude of the 2 samples in the vicinity of the peak
λ_T	threshold to differentiate channel paths from the noise
$\mathbf{g}$	vector of coefficients for the 24-tap equalizer
$\mathbf{g}^{\mathrm{opt}}$	vector of optimum equalizer coefficients
$\mathcal{F}$	Fourier/ inverse Fourier transformation
$\mathcal{H}$	complex transpose
$\mathcal{Q}(\cdot)$	the $\mathcal{Q}$-function
μ	update step size
μ_i	relative delay of the i^{th} path to the main path in seconds

$\nabla_x H$	the gradient vector of $H(e^{j\omega}; \boldsymbol{X})$ with respect to $\boldsymbol{X}$
ν	iteration number
ω	frequency in radian/sample
ω_p	pass band corner frequency
ω_s	stop band corner frequency
ρ	maximum pole radius
σ_w^2	AWGN noise variance
τ_i	delay of a channel path in samples
τ_{peak}	timing offset in seconds
MSE^{avg}	average mean squared error
MSE^{max}	maximum mean squared error
θ_i	distance from nearest sample point to the peak
φ	phase delay
$\widehat{X}[m]$	received frequency-domain symbols after equalization
a_i	denominator coefficients
$b[m]$	preamble symbols
b_i	numerator coefficients
d_0	integer delay in samples
f	frequency in Hz
f_c	carrier frequency
$g(t)$	definition for chapter 4: channel impulse response
$h_\tau(t)$	impulse response of an equivalent band-limited multipath channel
$h_c(t)$	impulse response of a multipath channel
$h_\Delta(t)$	raised cosine impulse response with timing offset
$h_{\text{RX}}(t)$	impulse response of a matched filter
$h_{\text{TR}}(t)$	cascading of the pulse shaping and matched filters
$h_{\text{TX}}(t)$	impulse response of a pulse shaping filter

m	definition for chapter 3: order of the numerator polynomial
n	definition for chapter 3: order of the denominator polynomial
n_{frac}	the fractional timing component
n_{peak}	the integer timing component
p_j	pole radius
$p_{\text{RC}}(t)$	raised cosine impulse response
q	number of input bits for a QAM mapper
r	definition for chapter 4: roll off factor
$r[n]$	definition for chapter 6: rectangular window function
s_i	complex symbol in a constellation
$u_{\text{I}}(t)$	in-phase component of the matched filter's output
$u_{\text{Q}}(t)$	quadrature component of the matched filter's output
$v[n]$	complex QAM symbol
$v_{\text{I}}[n]$	in-phase component of a symbol
$v_{\text{Q}}[n]$	quadrature component of a symbol
$w(t)$	AWGN process
$x_a(t)$	transmitted RF signal
$x_d[n]$	transmitted time-domain samples
$x_{\text{I}}(t)$	in-phase component of transmitted signals
$x_{\text{Q}}(t)$	quadrature component of transmitted signals
$y_a(t)$	received RF signal
$y_d[n]$	discrete-time samples of a received RF signal

1. Introduction

1.1 Motivation

The later part of the twentieth century observed a significant growth in communication technologies. Technological inventions in the telecommunication industry enable society to enter the era of telephony, Internet, and multimedia services. Broadband communications over cable networks was in the heart of this trend. In the early beginnings, from connecting cables between homes and providing one to two channels of early television, the cable industry has, in just over 50 years, moved into the 500-channel universe. Since then, cable operators have branched out to become television broadcasters, radio broadcasters, telephone and cell-phone service providers. They have expanded their business model to include the entertainment arenas and have purchased Internet networks, sports teams and major performance venues.

Cable television (CATV) networks are dominant by wired broadband technology in the United States and Canada. Earlier CATV networks carried analog television signals, but since 2000s all cable operators have switched to or are in process of switching to digital technology.

CATV networks provide high-speed interactive services, including Internet access and telephone service, that are delivered over the cable television infrastructure. The demand for data services has steadily increased to a point where there is tremendous pressure on data services providers to continually increase the data throughput of their networks.

Fig. 1.1 shows a simplified structure of a cable network. There are two main components in the network: a cable modem (CM), which is located at the customer premises, and a cable

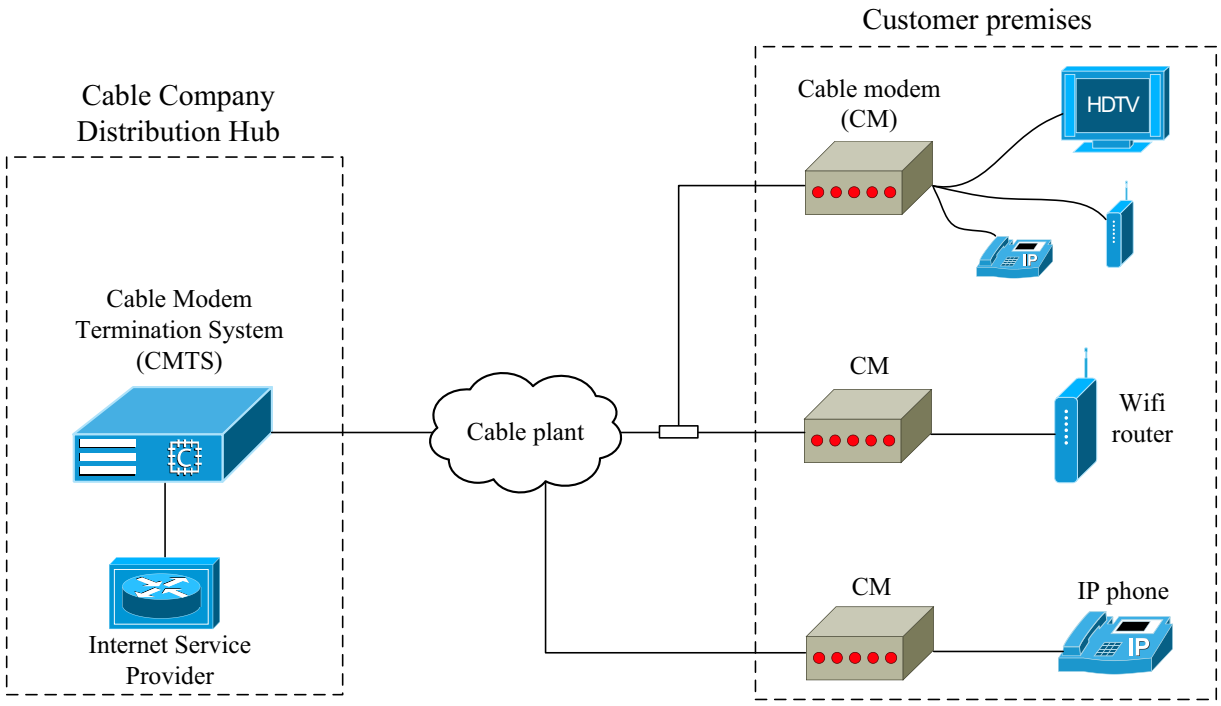

Figure 1.1 Cable modem network.

modem termination system (CMTS), located at the cable company's headend. The CMTS is responsible for managing a large number of cable modems residing in subscribers' homes. The CMTS allocates channel resources for each CM and schedules times for sending and receiving packets. Most CMTS have both Ethernet and Radio Frequency (RF) interfaces. In this way, the Internet traffic can be routed through the Ethernet interface, through the CMTS and then onto the RF ports that are connected to coaxial cable networks, eventually reaching the cable modem in the subscriber's home.

Version	Release date	Modulation scheme	Downstream throughput	Upstream throughput
1.0	03/1997	Single-carrier QAM	42.88 Mbits/s	10.24 Mbits/s
2.0	12/2001		42.88 Mbits/s	30.72 Mbits/s
3.0	08/2006		1372.16 Mbits/s	245.76 Mbits/s
3.1	10/2013	Multi-carrier (OFDM)	10 Gbits/s	1 Gbits/s

Table 1.1 DOCSIS versions.

CATV networks are governed by the Data Over Cable Service Interface Specification (DOCSIS) standards, which are developed by the not-for-profit organization CableLabs,

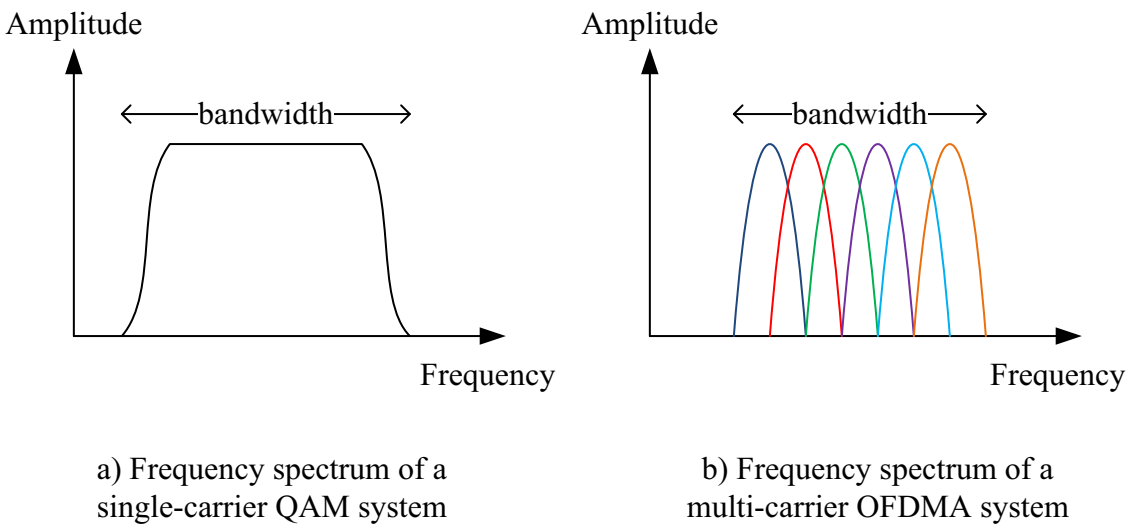

a) Frequency spectrum of a single-carrier QAM system

b) Frequency spectrum of a multi-carrier OFDMA system

Figure 1.2 Frequency domain spectra in single-carrier QAM and multi-carrier OFDMA systems.

which is funded by the cable operators and cable equipment manufacturers. Released in 1997, the first version of DOCSIS standard promotes multi-manufacturer interoperability and introduces a retail model for the consumer's direct purchase of a cable modem (CM) of choice. The original DOCSIS 1.0 standard supports a single channel with maximum throughputs of 42.88 Mbit/s for downstream and 10.24 Mbit/s upstream. Since then, substantial changes in the sub-sequence versions of DOCSIS standard, as highlighted in Table 1.1, facilitated higher system throughput. Released in 2001, DOCSIS 2.0 tripled the upstream throughput in responding to higher demand in upstream traffic. Five years later, the advances in fiber optics technology and pressure from digital subscriber line (DSL) competitors caused the birth of DOCSIS 3.0. DOCSIS 3.0 is able to simultaneously support multiple channels and bind them together to increase performance. A maximum of 32 downstream channels and 8 upstream channels can be bonded together to reach a throughput of 1372.16 Mbit/s downstream and 245.76 Mbit/s upstream.

The latest version of DOCSIS standard, DOCSIS 3.1, was released in 2013. DOCSIS 3.1 is markedly different from prior versions of the standard. State-of-the-art data coding employing Low Density Parity Check (LDPC) codes provides superior data protection against noisy channels. Additionally, while prior versions of DOCSIS employ single-carrier quadrature amplitude modulation (SC-QAM), DOCSIS 3.1 adopts orthogonal frequency division

modulation (OFDM) in the downstream direction and orthogonal frequency division multiple access (OFDMA) in the upstream direction in order to make more efficient use of CATV cable networks, especially those that have committed narrow bandwidths to other services.

The main difference between single-carrier and multi-carrier systems is in the way the available bandwidth is utilized as illustrated in Fig. 1.2. Basically OFDMA contains many closely-spaced narrow bandwidth SC-QAM signals. There is no real performance advantage to either system on an additive white Gaussian noise (AWGN) channel if they occupy the same bandwidth. However, if strong narrow bandwidth ingress interference is present, which usually occurs intermittently in CATV plants, it will severely impact the entire SC-QAM channel. In this scenario the OFDMA system loses only one narrow bandwidth SC-QAM signal, while the entire broadband SC-QAM signal is lost.

It is pointed out that DOCSIS devices need to be fully backward compatible. Therefore a newer cable modem must support all previous versions of DOCSIS. Moreover, considering that OFDM/OFDMA are very different from SC-QAM, the development of DOCSIS 3.1 CMs and CMTS's is challenging and much more complicated.

1.2 Research Objectives

There are three distinct objectives in this research and they are elaborated below.

i) **Redesign old backward compatible functions**: Each time a new communication standard with new features is implemented, the old backward compatible functions can be redesigned to take advantage of new technology and algorithms. Of interest here is the DOCSIS standards prior to Version 3.1 that employs SC-QAM (see Table 1.1). Therefore the main thrust of this research objective is to improve the implementation efficiency of the backward compatible functions for legacy SC-QAM channels in the implementation of DOCSIS 3.1 and beyond. Specifically, this part of the research focuses on two improvements that can be made for the backward compatible functions. The first improvement is made by redesigning the pulse shaping filters employed in the SC-QAM system. For DOCSIS systems prior to version 3.1, such pulse shaping filters are

commonly realized by the FIR structure. However, FIR filters require quite a large number of coefficients as compared to filters designed with the IIR structure and thus have higher computational complexity. An efficient algorithm shall be developed to minimize the number of coefficients of a standard Squared-Root Raised Cosine (SRRC) pulse-shaping filter without affecting its performance.

The second improvement is made on improving the timing offset estimation function, which determines the time of arrival of the transmitted data packet. Accurately determining such timing information helps to recover the desired signal with less distortion and higher signal-to-noise ratio (SNR). The cross-correlation technique is mainly used for timing offset estimation of SC-QAM signals, in which the timing information is taken by locating the true peak of the cross-correlation signal. However, locating the true peak of such a signal after it has been sampled is a challenging task for a wide range of applications. A peak locator algorithm shall be developed that has a better accuracy without increasing the hardware cost.

ii) **Channel estimation and fine timing detection in DOCSIS 3.1 standard**: While OFDMA systems have been extensively discussed in the literature in recent years, the DOCSIS 3.1 standard is unique in that it seeks to combine OFDMA with very high density modulation schemes (up to 16384-QAM). Furthermore, the impairments in cable plants differ from those of wireless systems, which are the focus of OFDMA studied in much of the literature. In order to effectively demodulate the spectrally-efficient OFDMA signal, it is necessary to employ coherent demodulation which involves estimation and tracking of the channel parameters.

The goal of this part of the research is to develop algorithms for OFDMA channel estimation, which are among the most technically-challenging issues in DOCSIS 3.1 standard. To this end, system performance under the condition of having imperfect timing synchronization and echoes in the channel will be investigated. This would involve developing a realistic channel model for OFDMA systems where the timing offsets and echo delays are not integer multiples of the system's sampling period. Such offsets/delays threaten sub-carrier orthogonality and lead to poor quality channel es-

timation, at least with the conventional estimators in the literature. Considering the realistic channel model, algorithms for finding timing offset will be explored as well as algorithms for performing channel estimation. In all cases, it will be necessary to verify, through theory and simulation, that the proposed algorithms are capable of operating successfully while subjected to the distortions typically present in a cable plant. Additionally, the algorithms must be optimized to minimize the logic resources required for implementation in an field-programmable gate array (FPGA).

iii) **Improvements for future standards**: Despite many advantages, an obvious drawback of OFDMA systems is the requirement to use a cyclic prefix (CP), which is inserted at the beginning of each transmitted OFDM symbol to mitigate inter-symbol interference (ISI). In general, not only the channel but also the digital filters built in the transceiver determine the length of the CP. The CP insertion reduces the overall transmission throughput, by up to 25% for DOCSIS 3.1 downstream transmission.

This part of the research will consider all aspects that affect the CP length. Then techniques to reduce the CP length will be investigated in order to increase the transmission throughput. Although shortening the CP has motivated many investigations reported in the literature, the existing techniques are complicated as they require either the calculation of eigenvalues and/or matrix inversion and/or division, etc. These techniques are not easily implemented in hardware. The goal of this research is to find a practical implementation that consumes a small amount of hardware resources. If the length of the CP can be reduced or even eliminated with a technique that is "hardware friendly", then it will be a promising candidate for inclusion in the next version of DOCSIS standard.

1.3 Organization of the Thesis

This thesis is organized in a manuscript-based style. The results obtained are included in the form of published or submitted manuscripts. In each chapter, a brief introduction precedes each manuscript in order to connect the manuscript to the main context of the thesis. The thesis is organized as follows.

There are seven chapters in total. The first chapter gives the motivation of the research

and states the research objectives.

Chapter 2 provides an in-depth look at the single-carrier QAM and multi-carrier OFDM/OFDMA systems. The fundamental difference between the two systems will be discussed. This chapter explains the advantages of switching from SC-QAM to OFDM/OFDMA, and points out difficult technical problems on deploying OFDMA on the DOCSIS 3.1 uplink channel.

In Chapter 3, the pulse shaping filter design problem is discussed and various conventional design techniques are reviewed. A novel design technique, which is the thesis' first main contribution, is presented. The proposed design is more economical than conventional designs, thus directly benefiting the backward-compatibility functions of newer cable network products.

Another backward-compatibility function that can be efficiently redesigned is peak detection. Chapter 4 is dedicated for an improved peak detection method, which can be used for a wide range of applications, including but not limited to, detection of the optimal sampling time for the SC-QAM systems and, multipath channel estimation for OFDM/OFDMA systems. This chapter proposes a technique for finding the approximate location of the peak in an analog signal after it has been sampled. Of particular interest is the output of the preamble correlator located inside an SC-QAM receiver. The technique involves transforming the sampled data into the logarithm domain and then fitting a parameterized function to the two points neighboring of its peak. The function is parameterized such that it has characteristics of the analog pulse shaping and matched filter in the system. Then the location of the peak is calculated from the parameters obtained in the fitting process. Simulation results show that the proposed estimator significantly outperforms the conventional estimators at a comparable or lower hardware cost.

The manuscript included in Chapter 5 proposes a novel channel estimation technique that can be applied for OFDMA signals in DOCSIS 3.1 cable networks. In this chapter, first the channel estimation problem inherent to OFDMA systems is studied. Then conventional techniques that can be used to estimate the multipath channel parameters are discussed.

Then an iterative channel estimation technique is proposed. The technique is developed to work well with the pilot sub-carrier schemes imposed by DOCSIS 3.1 standard. Furthermore, it is shown that the performance of the iterative technique can be improved without increasing its complexity by applying the log-domain peak detection algorithm developed in Chapter 4.

Chapter 6 includes a manuscript that proposes a scheme to transmit OFDM signals without CP. The manuscript first evaluates the performance degradation of conventional OFDM systems without CP or with insufficient CP. Then it will show that using Nyquist filters for the reconstruction/anti-aliasing filters and making them matched would eliminate the ISI caused by band-limiting and there would be no need to use CP. Lastly, a novel TEQ is introduced to efficiently inverse the multipath channel in the time-domain and significantly suppress ISI due to the multipath channel. By incorporating the proposed scheme, simulation results show that the DOCSIS 3.1 down-link transmission can obtain maximum throughput under certain multipath channel conditions.

Finally, Chapter 7 summarizes the contributions of this thesis and suggests potential research problems for future works.

2. Digital Communication Systems

This thesis is concerned with signal processing of cable network communications. To provide background knowledge and motivation for research problems addressed in this thesis, this chapter discusses the basics of digital communication systems using single-carrier QAM and multi-carrier OFDMA.

2.1 Single-Carrier Quadrature Amplitude Modulation (SC-QAM)

Figure 2.1 illustrates main signal processing components of the transmitter and receiver in a digital SC-QAM system. It should be noted that the illustration is simplified and synchronization modules, such as timing, frequency and phase recovery, are not shown.

At first, the data bits to be transmitted are packed into symbols using a QAM mapping module. With quadrature amplitude modulation (QAM), every q bits are mapped into a symbol represented by a complex value consisting of an in-phase (I) component, $v_{\mathrm{I}}[n]$, and a quadrature (Q) component, $v_{\mathrm{Q}}[n]$. For q input bits, there are 2^q possible symbols, denoted as $s_i,\ i = 0, 1, \ldots, 2^q - 1$, which can be visualized on a 2-dimensional complex plane. The resulting illustration is often referred to as a constellation diagram. Fig 2.2 shows examples of quadrature phase shift keying (QPSK, i.e., 4-QAM), 8-QAM, 16-QAM and 32-QAM constellations, which deliver $q = 2$, 3, 4 and 5 bits per symbol, respectively. Moreover, the average energy per symbol of the transmitted signal is proportional to the average energy of the constellation, which can be computed as the average of the squared distances, measured from the origin, of all symbols in the constellation plot. It is given as

$$E_s = \frac{1}{2^q} \sum_{i=0}^{2^q-1} |s_i|^2. \tag{2.1}$$

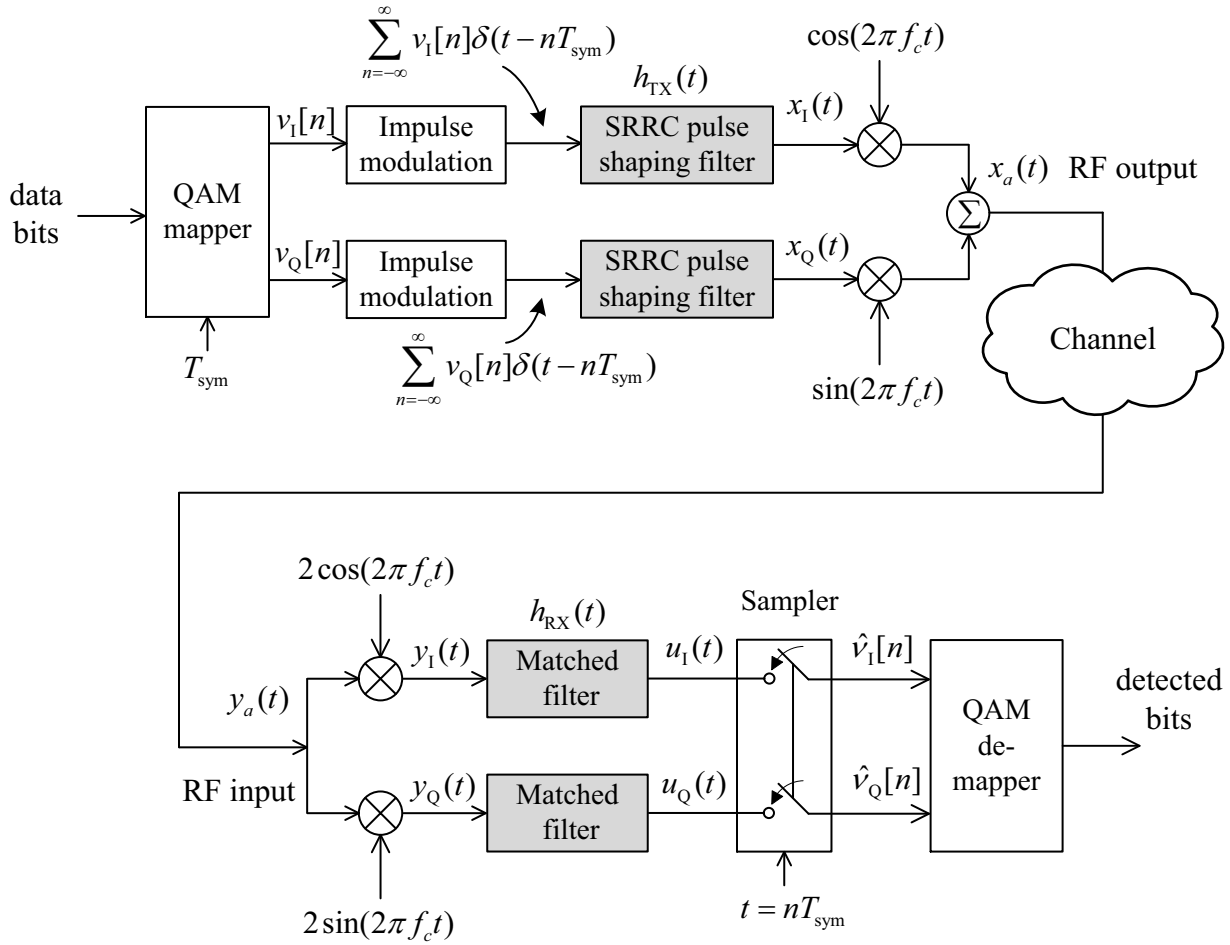

Figure 2.1 Simplified block diagram of a SC-QAM system.

The bandwidth efficiency of a communication link may be increased by using a denser constellation. However, since the average energy of the constellation is typically constrained to a fixed amount, the constellation points must be closer together and thus are more susceptible to noise and other impairments. This results in a higher bit error rate (BER). Thus, in general, for the same average constellation energy, a higher-order QAM can deliver more data than a lower-order QAM but less reliably. With the help of the impulse modulators, the in-phase and quadrature values at the output of the QAM mappers are represented as trains of impulses, $\sum_{n=-\infty}^{\infty} v_{\mathrm{I}}[n]\delta(t - nT_{\mathrm{sym}})$ and $\sum_{n=-\infty}^{\infty} v_{\mathrm{Q}}[n]\delta(t - nT_{\mathrm{sym}})$, where T_{sym} is the symbol period in seconds. These trains of impulses are passed through pulse shaping filters, which have impulse response $h_{\mathrm{TX}}(t)$ as indicated in Fig. 2.1. The pulse shaping filters are low-pass filters required to limit the bandwidth of transmitted signals to 6 MHz[1]. The

[1]As specified for North America DOCSIS channels [C2.1], or 8 MHz according to the Europe DOCSIS.

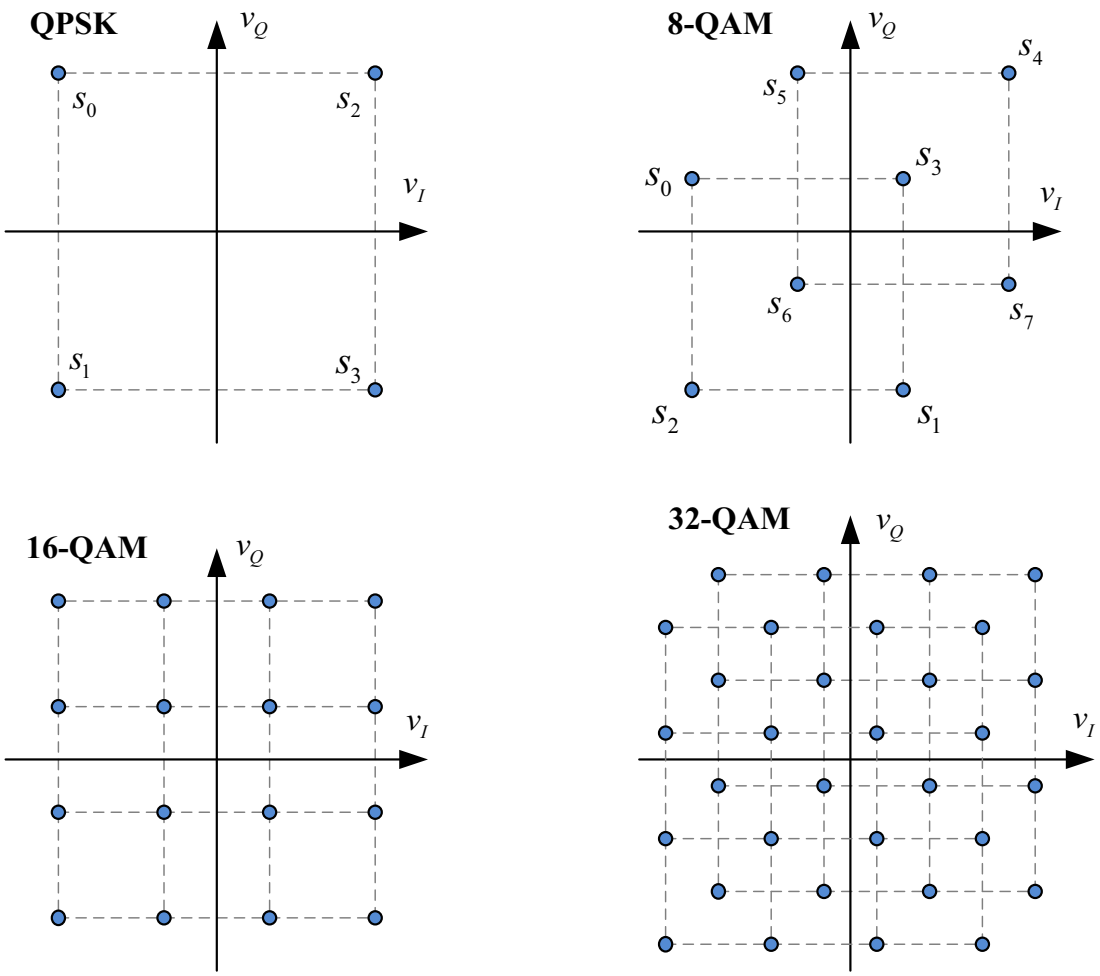

Figure 2.2 QAM symbol constellations.

outputs of the pulse shaping filters are continuous time-signals, one for the in-phase (I) and one for the quadrature (Q) channel. These signals can be expressed as

$$x_{\mathrm{I}}(t) = \sum_{n=-\infty}^{\infty} v_{\mathrm{I}}[n] h_{\mathrm{TX}}(t - nT_{\mathrm{sym}}) \tag{2.2}$$

$$x_{\mathrm{Q}}(t) = \sum_{n=-\infty}^{\infty} v_{\mathrm{Q}}[n] h_{\mathrm{TX}}(t - nT_{\mathrm{sym}}). \tag{2.3}$$

Then the outputs of the pulse shaping filters are multiplied (i.e., modulated) with a pair of sinusoidal carriers, which have frequency f_c and differ in phase by $\pi/2$ radians, i.e., sine and cosine signals. The two modulated carriers are then added together, generating a band-pass radio frequency (RF) signal $x_a(t)$. That is

$$x_a(t) = x_{\mathrm{I}}(t)\cos(2\pi f_c t) + x_{\mathrm{Q}}(t)\sin(2\pi f_c t). \tag{2.4}$$

The RF signal is sent across the cable channel. In case there is no channel impairment, i.e., $y_a(t) = x_a(t)$, the demodulation process at the receiver starts with down-converting the received RF signal to baseband. This is done by multiplying $y_a(t)$ with quadrature carriers. The resulting in-phase signal is

$$\begin{aligned} y_{\mathrm{I}}(t) &= y_a(t) 2\cos(2\pi f_c t) \\ &= x_{\mathrm{I}}(t)\cos(2\pi f_c t) 2\cos(2\pi f_c t) + x_{\mathrm{Q}}(t)\sin(2\pi f_c t) 2\cos(2\pi f_c t) \\ &= x_{\mathrm{I}}(t) + x_{\mathrm{I}}(t)\cos(4\pi f_c t) + x_{\mathrm{Q}}(t)\sin(4\pi f_c t), \end{aligned} \tag{2.5}$$

and the quadrature signal is

$$\begin{aligned} y_{\mathrm{Q}}(t) &= y_a(t) 2\sin(2\pi f_c t) \\ &= x_{\mathrm{I}}(t)\cos(2\pi f_c t) 2\sin(2\pi f_c t) + x_{\mathrm{Q}}(t)\sin(2\pi f_c t) 2\sin(2\pi f_c t) \\ &= x_{\mathrm{Q}}(t) - x_{\mathrm{Q}}(t)\cos(4\pi f_c t) + x_{\mathrm{I}}(t)\sin(4\pi f_c t). \end{aligned} \tag{2.6}$$

The first terms of (2.5) and (2.6) are the useful baseband components, whereas the second and third terms are high-frequency components centering at $2f_c$. In order to remove those high-frequency components, low-pass filters are applied. In practice, the low-pass filters are called matched filters, which are identical to the pulse-shaping filter if its impulse response is an even function, i.e. $h_{\mathrm{RX}}(t) = h_{\mathrm{TX}}(-t) = h_{\mathrm{TX}}(t)$. While the pulse shaping filter serves the purpose of keeping only a baseband signal, the matched filter is important to mitigate distortions that occur in the transmission/reception process, such as AWGN noise and inter-symbol-interference (ISI).

The signals at the outputs of the matched filters can be written as

$$\begin{aligned} u_{\mathrm{I}}(t) &= y_{\mathrm{I}}(t) * h_{\mathrm{RX}}(t) = x_{\mathrm{I}}(t) * h_{\mathrm{RX}}(t) \\ &= \sum_{k=-\infty}^{\infty} v_{\mathrm{I}}[k] h_{\mathrm{TX}}(t - kT_{\mathrm{sym}}) * h_{\mathrm{RX}}(t) \\ &= \sum_{k=-\infty}^{\infty} v_{\mathrm{I}}[k] h_{\mathrm{TR}}(t - kT_{\mathrm{sym}}), \end{aligned} \tag{2.7}$$

$$
\begin{aligned}
u_{\mathrm{Q}}(t) &= y_{\mathrm{Q}}(t) * h_{\mathrm{RX}}(t) = x_{\mathrm{Q}}(t) * h_{\mathrm{RX}}(t) \\
&= \sum_{k=-\infty}^{\infty} v_{\mathrm{Q}}[k] h_{\mathrm{TX}}(t - kT_{\mathrm{sym}}) * h_{\mathrm{RX}}(t)(t) \\
&= \sum_{k=-\infty}^{\infty} v_{\mathrm{Q}}[k] h_{\mathrm{TR}}(t - kT_{\mathrm{sym}}), \qquad (2.8)
\end{aligned}
$$

where $h_{\mathrm{TR}}(t) = h_{\mathrm{TX}}(t) * h_{\mathrm{RX}}(t)$ is the impulse response of the equivalent filter obtained by cascading the pulse shaping filter with the matched filter. At sampling time $t = nT_{\mathrm{sym}}$ the sampler's outputs are

$$
\hat{v}_{\mathrm{I}}[n] = u_{\mathrm{I}}(t)\big|_{t=nT_{\mathrm{sym}}} = v_{\mathrm{I}}[n] h_{\mathrm{TR}}(0) + \sum_{k=-\infty,\, k\neq n}^{\infty} v_{\mathrm{I}}[k] h_{\mathrm{TR}}\big((n-k)T_{\mathrm{sym}}\big), \qquad (2.9)
$$

$$
\hat{v}_{\mathrm{Q}}[n] = u_{\mathrm{Q}}(t)\big|_{t=nT_{\mathrm{sym}}} = v_{\mathrm{Q}}[n] h_{\mathrm{TR}}(0) + \sum_{k=-\infty,\, k\neq n}^{\infty} v_{\mathrm{Q}}[k] h_{\mathrm{TR}}\big((n-k)T_{\mathrm{sym}}\big). \qquad (2.10)
$$

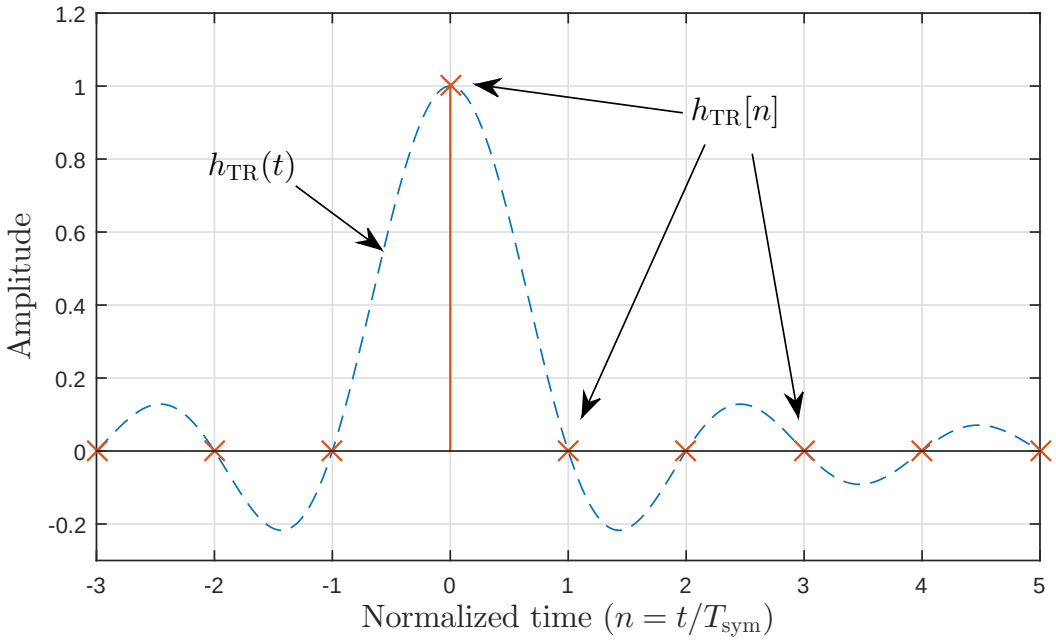

Figure 2.3 Zero-ISI condition on the samples of $h_{\mathrm{TR}}(t)$ at the sampling times.

The second terms in (2.9) and (2.10) represents ISI. In order to suppress the ISI, the cascade of the pulse shaping and matched filters must satisfy the Nyquist criterion [C2.2], which states that the samples of the pulse at interval T_{sym}, i.e. $h_{\mathrm{TR}}[n] = h_{\mathrm{TR}}(t)\big|_{t=nT_{\mathrm{sym}}}$, must

be 1 at $n = 0$ and zero at all other sampling times. This is illustrated in Fig. 2.3.

Let $H_{\mathrm{TX}}(f)$ and $H_{\mathrm{RX}}(f)$ be the frequency responses of the pulse shaping and matched filters, respectively, i.e.,

$$H_{\mathrm{TX}}(f) \quad \overset{\mathcal{F}}{\longleftrightarrow} \quad h_{\mathrm{TX}}(t), \tag{2.11}$$

$$H_{\mathrm{RX}}(f) \quad \overset{\mathcal{F}}{\longleftrightarrow} \quad h_{\mathrm{RX}}(t), \tag{2.12}$$

where $\mathcal{F}$ denotes Fourier transform pair and f is frequency in Hz. In many communication systems, including DOCSIS, the pulse-shaping and matched filters are typically selected so that

$$H_{\mathrm{TX}}(f)H_{\mathrm{RX}}(f) = H_{\mathrm{RC}}(f), \tag{2.13}$$

where $H_{\mathrm{RC}}(f)$ is a raised cosine filter. A raised cosine filter is a Nyquist filter and is defined in the frequency domain as follows:

$$H_{\mathrm{RC}}(f) = \begin{cases} 1, & \text{for } |f| \leq \frac{1-\beta}{2T_{\mathrm{sym}}} \\ \frac{1}{2}\left[1 + \cos\left(\frac{\pi T_{\mathrm{sym}}}{\beta}\left(|f| - \frac{1-\beta}{2T_{\mathrm{sym}}}\right)\right)\right], & \text{for } \frac{1-\beta}{2T_{\mathrm{sym}}} < |f| \leq \frac{1+\beta}{2T_{\mathrm{sym}}} \\ 0, & \text{otherwise,} \end{cases} \tag{2.14}$$

where β is the roll-off factor of the raised-cosine filter and T_{sym} is the symbol period. Fig. 2.4 and Fig. 2.5 show frequency and impulse responses of the raised-cosine filters with various roll-off factors, respectively. Observe that the raised-cosine filter has a limited bandwidth of $\frac{1+\beta}{2T_{\mathrm{sym}}}$ and its impulse response crosses zero at integer multiples of the sampling time.

In order to design $H_{\mathrm{TX}}(f)$ and $H_{\mathrm{RX}}(f)$ to satisfy the zero-ISI criterion, a natural approach is to attempt to maximize the signal-to-noise ratio [C2.2]. This can be accomplished by choosing $H_{\mathrm{TX}}(f)$ and $H_{\mathrm{RX}}(f)$ to be square-root raised-cosine (SRRC) filters, i.e.,

$$H_{\mathrm{TX}}(f) = H_{\mathrm{RX}}(f) = \sqrt{H_{\mathrm{RC}}(f)} \tag{2.15}$$

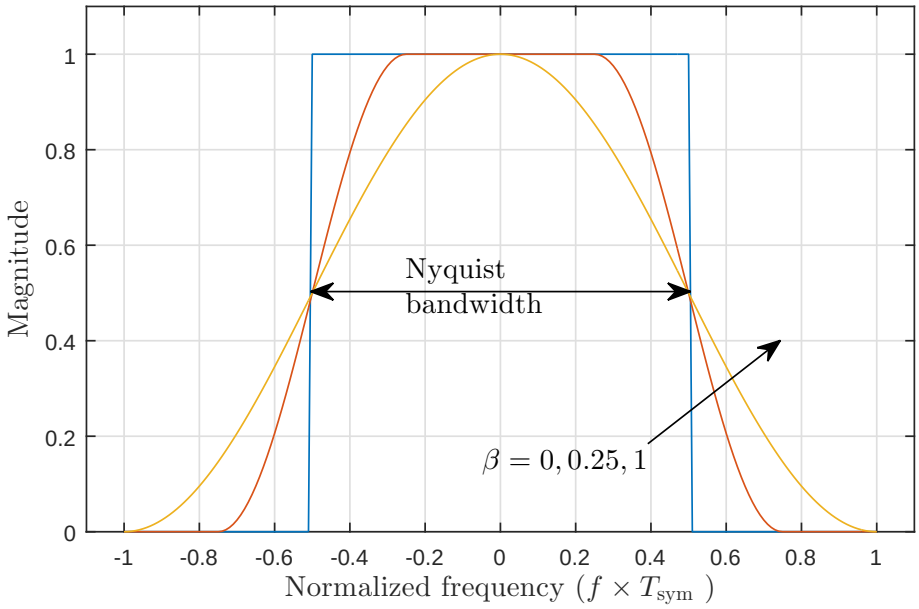

Figure 2.4 Frequency responses of raised-cosine filters with various roll-off factors.

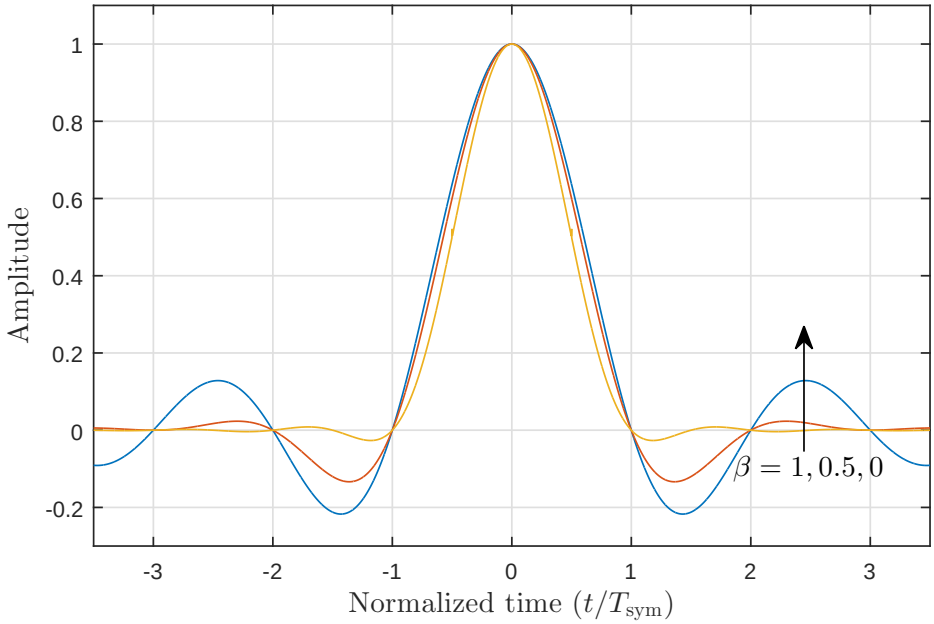

Figure 2.5 Impulse responses of raised-cosine filters with various roll-off factors.

It can be shown that the impulse response of a SRRC filter is given by [C2.2]

$$h_{\text{TX}}(t) = h_{\text{RX}}(t) = \frac{(4\beta t/T_{\text{sym}})\cos[\pi(1+\beta)t/T_{\text{sym}}] + \sin[\pi(1-\beta)t/T_{\text{sym}}]}{(\pi t/T_{\text{sym}})[1-(4\beta t/T_{\text{sym}})^2]} \tag{2.16}$$

The time waveform of the above impulse response is plotted in Fig. 2.6 for various roll-off factors. Note that for any $\beta \neq 0$, the SRRC waveform does not go to zero at nonzero integer multiples of T_{sym}.

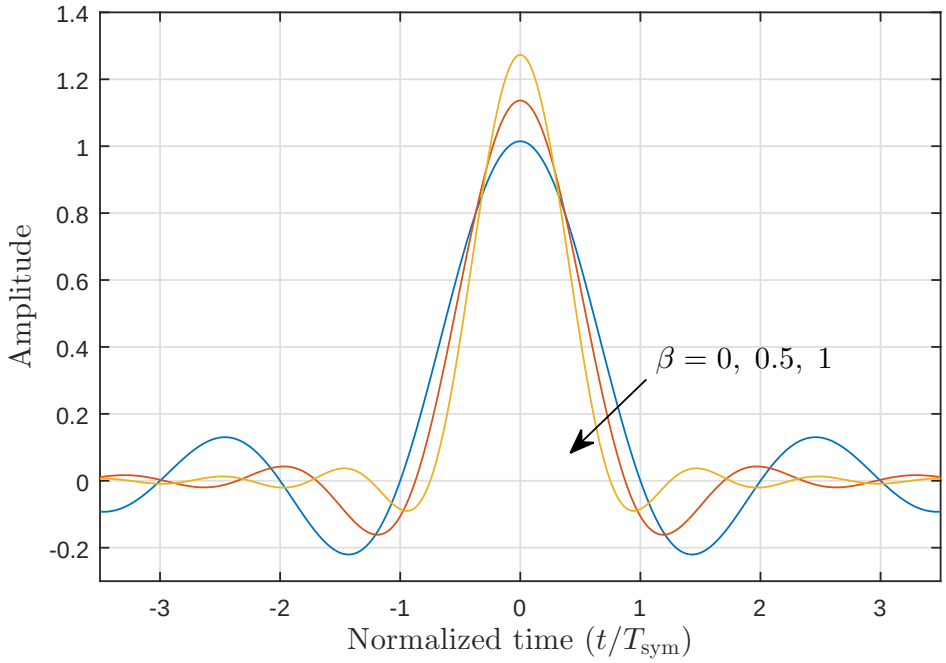

Figure 2.6 Impulse responses of SRRC filters with various roll-off factors.

To facilitate mathematical representation and analysis, the in-phase and quadrature signals can be combined into a complex signal, where the in-phase component corresponds to the real part and the quadrature component corresponds to the imaginary part of the complex signal. For instant, the QAM symbols can be expressed as $v[n] = v_{\text{I}}[n] + jv_{\text{Q}}[n]$, where $j = \sqrt{-1}$. Accordingly, the sampler's outputs in (2.9) and (2.10) can be collectively represented as

$$\hat{v}[n] = \hat{v}_{\text{I}}[n] + j\hat{v}_{\text{Q}}[n] = \sum_{k=-\infty}^{\infty} v[k]h_{\text{RC}}\big((n-k)T_{\text{sym}}\big). \tag{2.17}$$

An example of symbol recovery with the raised cosine pulse and when $v[n] = \pm 1$ (i.e., real BPSK constellation) is given in Fig. 2.7. It should be noted that the symbol recovery is perfect since no channel impairments are taken into account. The impact of channel impairments on symbol recovery performance will be discussed in the next sections.

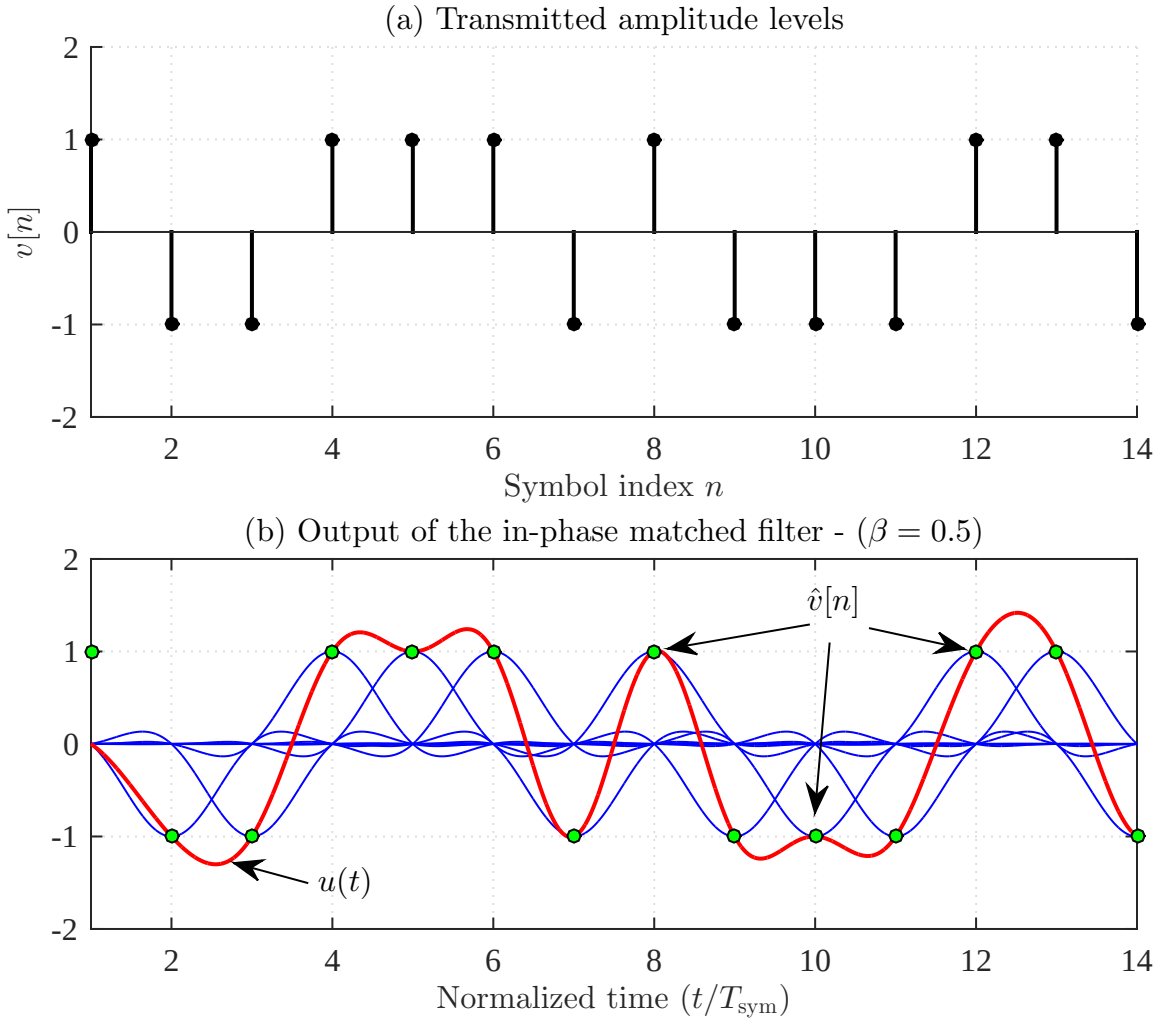

Figure 2.7 Illustration of symbol recovery with raised-cosine pulse.

2.1.1 Channel impairments

The cable network is not an ideal channel. Instead it contains various impairments that can be harmful for data transmission. The following sections discuss the main impairments, which must be taken into account in designing a communication system.

Additive White Gaussian Noise

Additive white gaussian noise (AWGN) is the most fundamental imperfection that any electronic communication system has to face with. The reason is that thermal noise is created by the virtue of the movement of the electrons in the electronic circuits used for processing the received signal. This thermal noise is random in nature. Another noise source is spurious transmission from adjacent channels. Although such noise is not totally random, it can't be determined at the receiver and is usually treated/approximated as AWGN.

Taking AWGN into account, the RF input signal can be written as

$$y_a(t) = x_a(t) + w(t). \tag{2.18}$$

The AWGN process $w(t)$ is modeled as having the amplitude following a Gaussian probability density function and a constant (white) power spectral density of $\frac{N_0}{2}$ Watts/Hz. Simple mathematical manipulations show that the sampler's output for the SC-QAM system under the presence of AWGN is

$$\hat{v}[n] = \sum_{k=-\infty}^{\infty} v[k] h_{\mathrm{RC}}\big((n-k)T_{\mathrm{sym}}\big) + w[n], \tag{2.19}$$

where $w[n]$ is an independent and identically distributed (i.i.d) *complex* Gaussian process with zero mean and variance N_0, i.e., $w[n] \sim \mathcal{CN}(0, N_0)$.

The impact of AWGN on a SC-QAM system has been studied thoroughly in the literature [C2.2, C2.3]. In fact, AWGN is the most fundamental limiting factor on the performance of a digital communication system, which is commonly measured in terms of the bit error rate (BER). The signal-to-noise ratio, commonly measured as SNR $= E_s/N_0$, is directly related

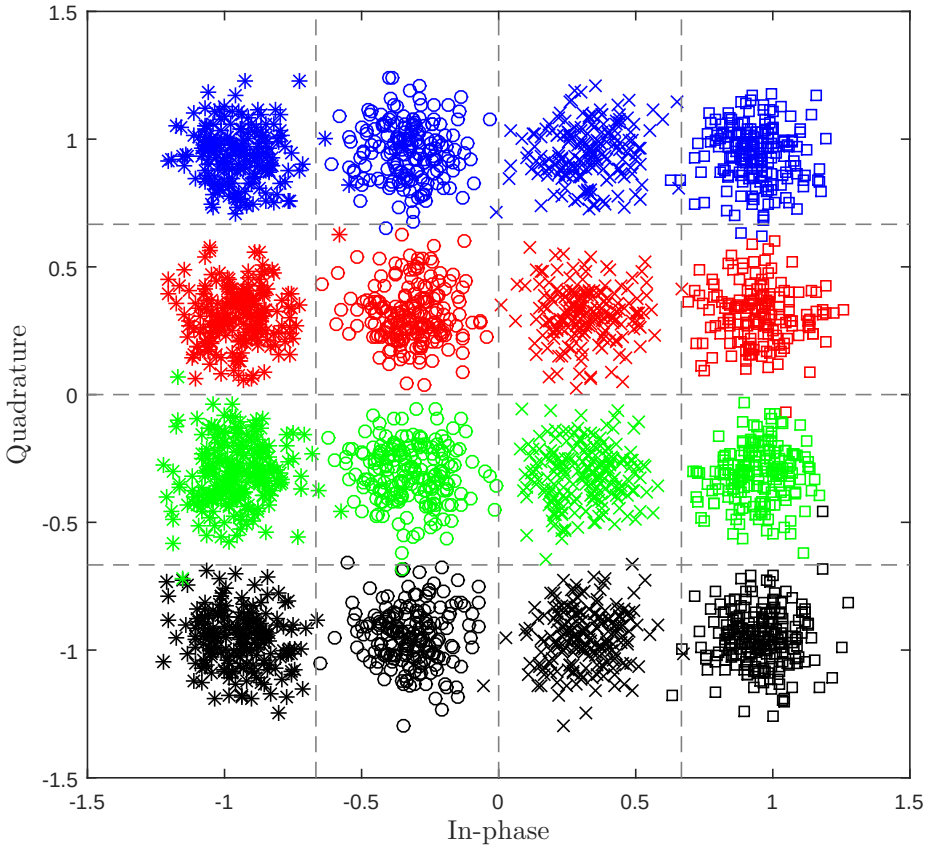

Figure 2.8 Scatter plot of 16-QAM signals with AWGN (SNR = 16 dB).

to the BER. For an M-QAM constellation with Gray mapping [C2.2], the BER of the system under an AWGN channel can be approximated as [C2.3, C2.2]

$$P_M \simeq 2\left(1-\frac{1}{\sqrt{M}}\right)\mathcal{Q}\left(\sqrt{\frac{3\,\mathrm{SNR}}{M-1}}\right), \tag{2.20}$$

where $\mathcal{Q}(\cdot)$ is the $\mathcal{Q}$-function, defined as the tail probability of the standard normal distribution:

$$\mathcal{Q}(\cdot) = \frac{1}{\sqrt{2\pi}}\int_x^\infty \exp(-t^2/2)\mathrm{d}t. \tag{2.21}$$

Fig. 2.8 shows the scatter plot of 16-QAM received symbols under the effect of AWGN when SNR = 16 dB. There are 3000 samples on the scatter plot, each of them is represented using its in-phase and quadrature values, i.e., $\hat{v}_\mathrm{I}[n]$ and $\hat{v}_\mathrm{Q}[n]$. To ease visualization, symbols

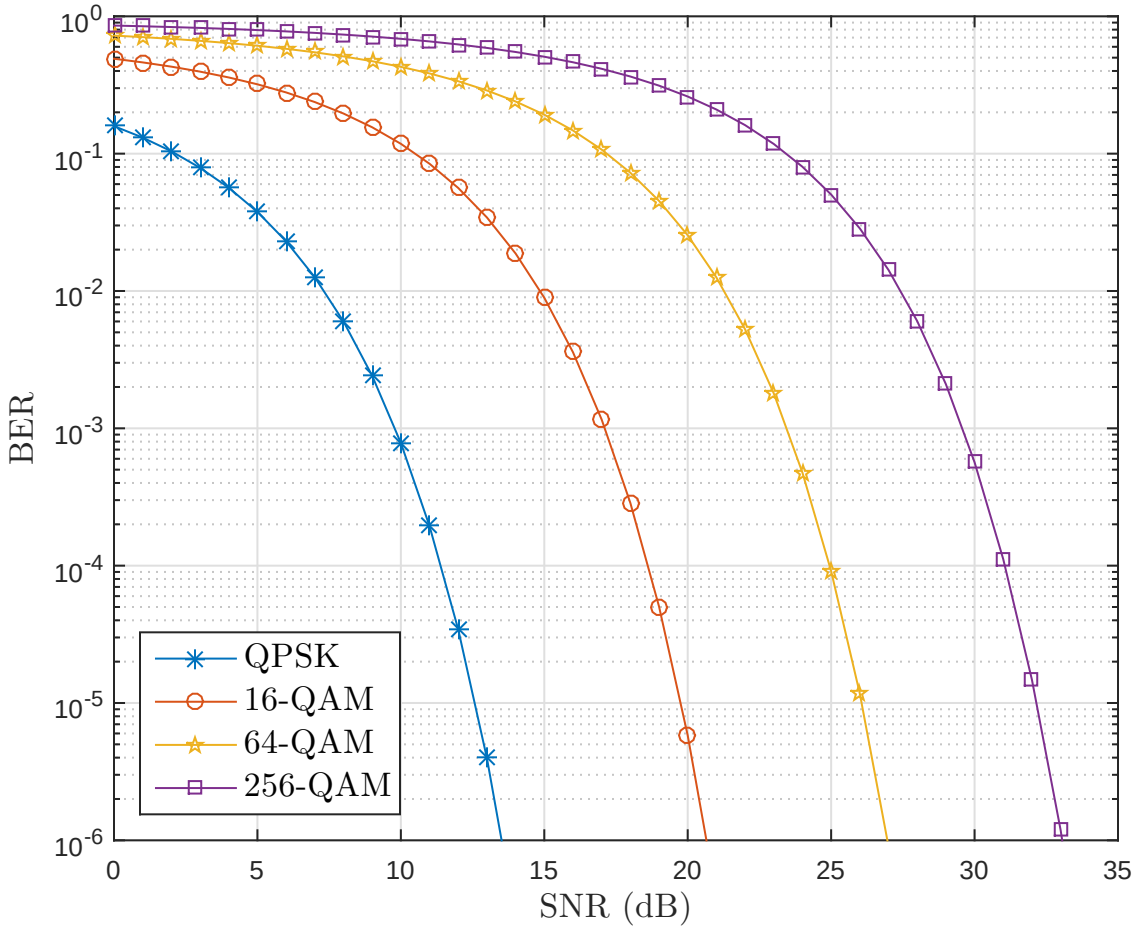

Figure 2.9 BER versus SNR for various QAM constellations.

that correspond to a constellation point are distinguished by a unique combination of color and marker shape. The dashed lines on the figure show the decision boundaries for 16-QAM. Note that the sample points in the scatter plot do not lie exactly on the transmitted constellation points as shown in Fig. 2.2 for 16-QAM. Instead there are 16 clusters of points centered around the ideal 16-QAM points because of AWGN. Note that there are few points that crossed decision boundaries, thus causing errors.

Fig. 2.9 plots the theoretical BER versus SNR for various QAM constellation: QPSK, 16-QAM, 64-QAM and 256-QAM. It can be seen that for a given BER level, say 10^{-5}, the additional SNR required to send two more bits per transmitted symbol approaches 6 dB.

Timing Offset

Timing offset refers to the error in the sampling moment at the digital receiver. As discussed and shown in Fig. 2.1, the sampler at the receiver must sample the filtered signal at precise time instants $t = nT_{\text{sym}}$ in order to recover the transmitted symbols without ISI. In a real-world system, there are many factors that contribute to sampling moment uncertainty. For instant, the travel time of an electrical signal from a transmitter to a receiver, which depends on the cable length and cable network setup, is generally unknown at the receiver. In addition, every analog and digital filter in the system adds some amount of delay to the signal. Therefore, the arrival time of the signal must be estimated every time the receiver is turned on. The difference between the actual and estimated times of arrival is generally referred to as timing offset or timing phase.

Taking into account the timing offset, the RF input signal can be written as

$$y_a(t) = x_a(t - \Delta t) + w(t), \tag{2.22}$$

where Δt is the timing offset in seconds. Then the input/output relationship of an SC-QAM system with timing offset and AWGN can be written as

$$\hat{v}[n] = \sum_{k=-\infty}^{\infty} v[k] h_{\Delta}\big((n-k)T_{\text{sym}}\big) + w[n], \tag{2.23}$$

where

$$h_{\Delta}(t) = h_{\text{RC}}(t - \Delta t), \tag{2.24}$$

which is the equivalent impulse response with timing offset. With a perfect channel, i.e., $\Delta t = 0$, $h_{\Delta}(t)$ would be that of a perfect Nyquist pulse shape with uniformly-spaced zero crossings, similar to that shown in Fig. 2.5. In that case, if the response is sampled at the optimum point (i.e., at the peak), the recovered symbols will not have interference from others.

However, if the sampling time has a small error, then the sampled value is affected by interference from other symbols, (i.e., ISI) as illustrated in Fig. 2.10. The figure shows the

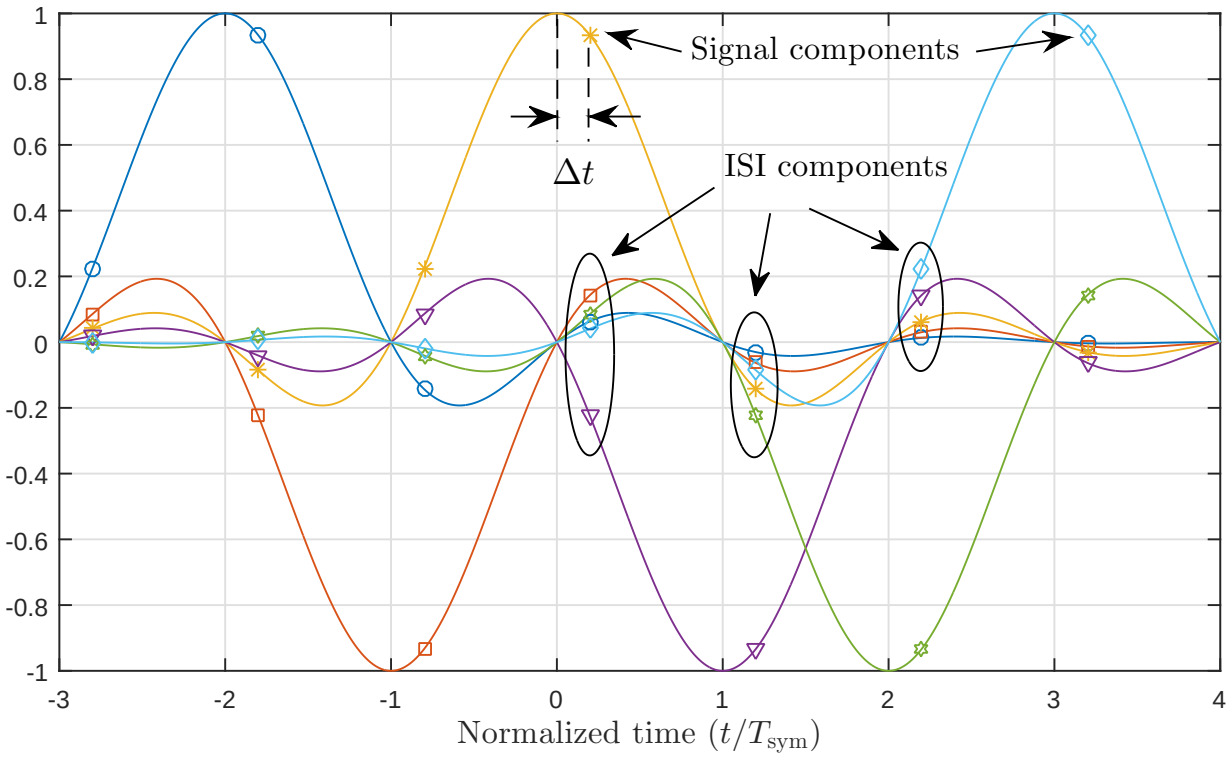

Figure 2.10 Illustration of signal samples containing ISI for timing offset $\Delta t = 0.2\,T_{\text{sym}}$.

transmission of 6 consecutive QAM symbols, shaped by the RC pulse with $\beta = 0.25$. The solid lines represent the analog pulses, where pulses modulated by different QAM symbols are marked with different colors. The markers denote discrete samples taken by the sampler. It can be seen that, if there is a non-zero timing offset, the signal sample contains not only the desired signal component, but also ISI components from adjacent transmitted symbols. The reason for the phenomenon is that bandwidth-efficient signaling pulses (such as the RC pulse shown in Fig. 2.5) extends over many symbol intervals (theoretically, infinite number of symbol intervals). Therefore, in the presence of a timing offset, the tails of pulses due to previous and future symbols corrupt the current decision variable.

Fig. 2.11 shows the scatter plot of 16-QAM received symbols with timing offset $\Delta t = 0.2T_{\text{sym}}$ and under zero AWGN condition. There are 1000 samples on the scatter plot. Observe that a large amount of samples cross the decision boundary, implying very poor detection performance.

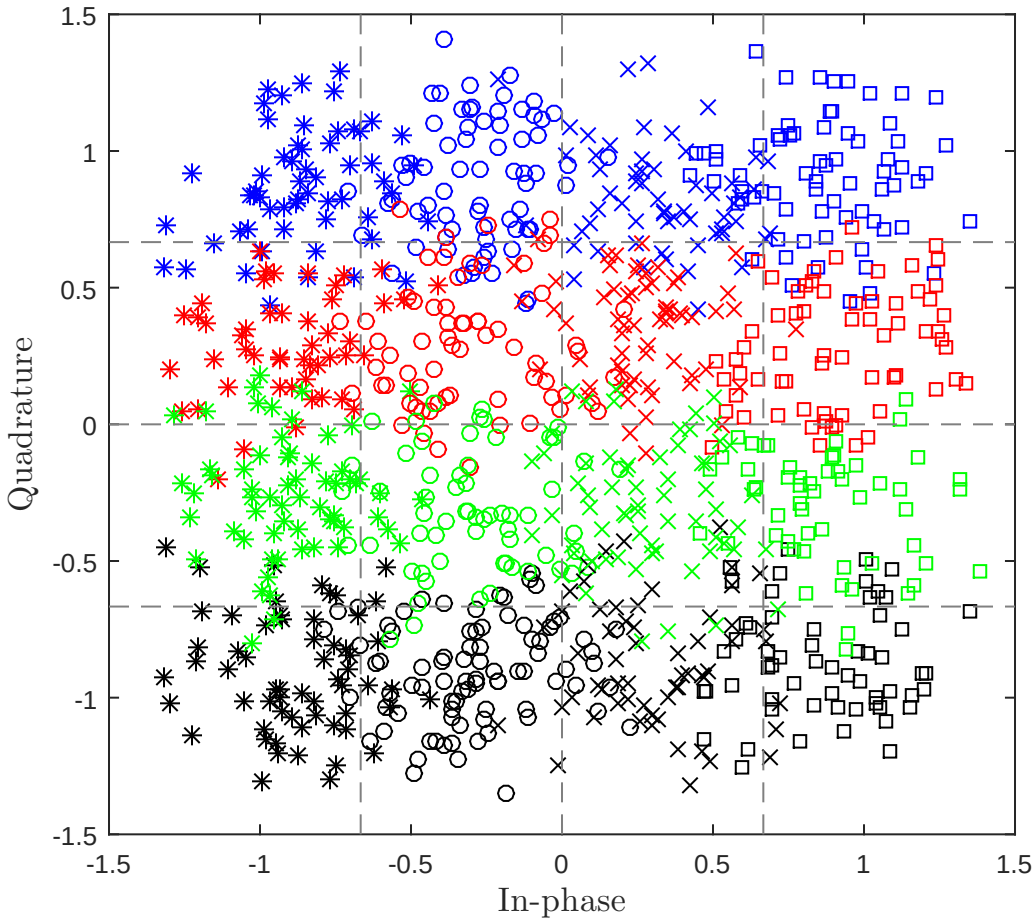

Figure 2.11 Scatter plot of 16-QAM signals with timing offset $\Delta t = 0.2T_{\text{sym}}$ and zero AWGN.

Fig. 2.12 plots the BER versus SNR performance for 16-QAM signal with various timing offsets. It can be seen that the detection performance of SC-QAM is very sensitive to timing offset. Specifically any timing error greater than $0.05T_{\text{sym}}$ would significantly increase the BER.

Multipath Channel

A multipath channel is a channel in which the signals from the transmitter reach the receiver by two or more paths, including a main/direct path and possibly several echo paths. This happens because imperfections in the coaxial cable network cause impedance mismatches and non-linear characteristics. Echo paths delay and attenuate the transmitted

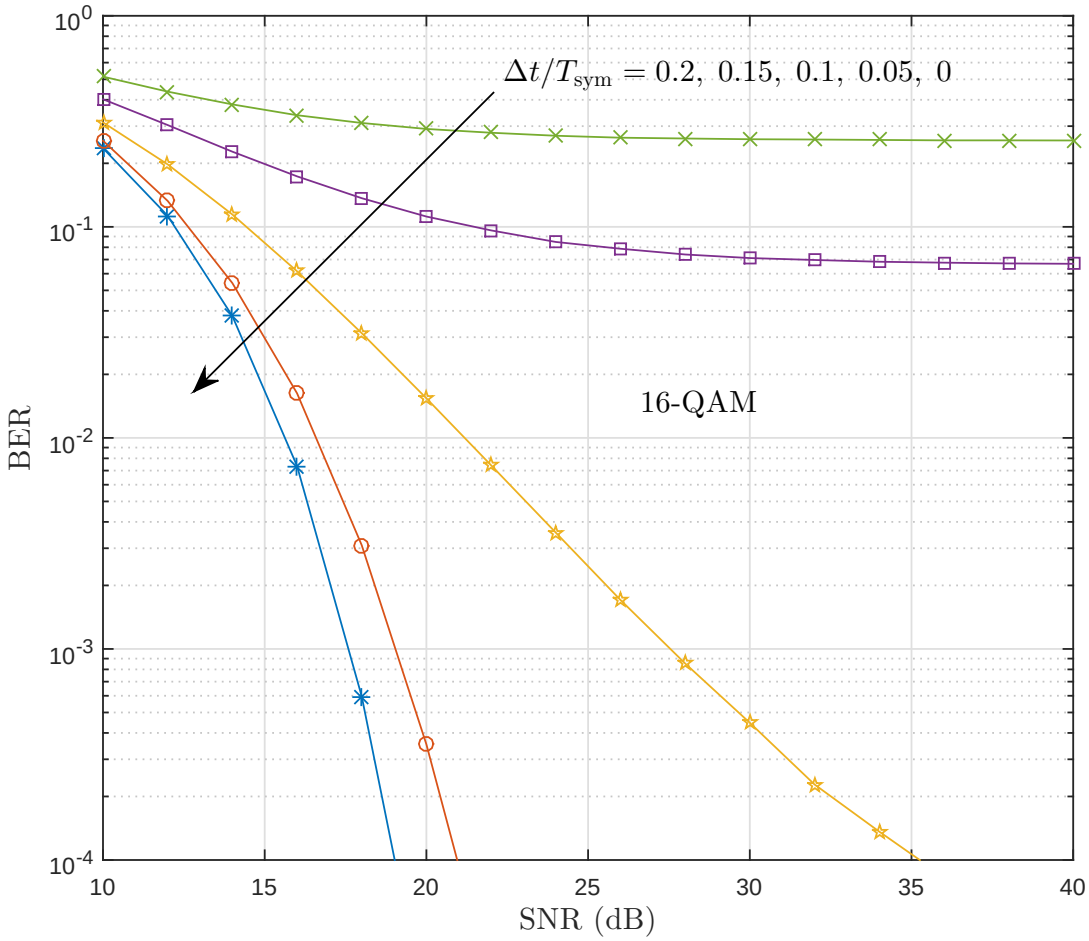

Figure 2.12 BER versus SNR for 16-QAM signal with various timing offset.

signal, creating replicas of the main signal at the receiver. Each path in the multipath channel is characterized by a gain factor α_i and an associated delay τ_i normalized to the symbol duration T_{sym}. The impulse response of the multipath channel is given by

$$h_c(t) = \sum_{i=0}^{N_p-1} \alpha_i \delta(t - \tau_i T_{\text{sym}}) \tag{2.25}$$

where $\delta(\cdot)$ is the Dirac delta function and N_p is the number of paths in the multipath channel.

It follows that the input/output relationship of an SC-QAM system under multipath

channel, timing offset and AWGN can be shown as

$$\hat{v}[n] = \sum_{k=-\infty}^{\infty} v[k] h_\tau\big((n-k)T_{\text{sym}} - \Delta t\big) + w[n], \tag{2.26}$$

where

$$h_\tau(t) = h_{\text{RC}}(t) * h_c(t) = \sum_{i=0}^{N_p-1} \alpha_i \, h_{\text{RC}}(t - \tau_i T_{\text{sym}}) \tag{2.27}$$

is the impulse response of the equivalent band-limited multipath channel.

Fig. 2.13 shows an example of $h_\tau(t)$ corresponding to a multipath channel with 2 paths: a main path and an echo path. The echo path has the gain factor of -10 dB relative to the main path and its delay is $1.8T_{\text{sym}}$ relative to the main path. It can be seen that the multipath effect distorts the RC pulse and thus the Nyquist zero-ISI criterion is not fulfilled.

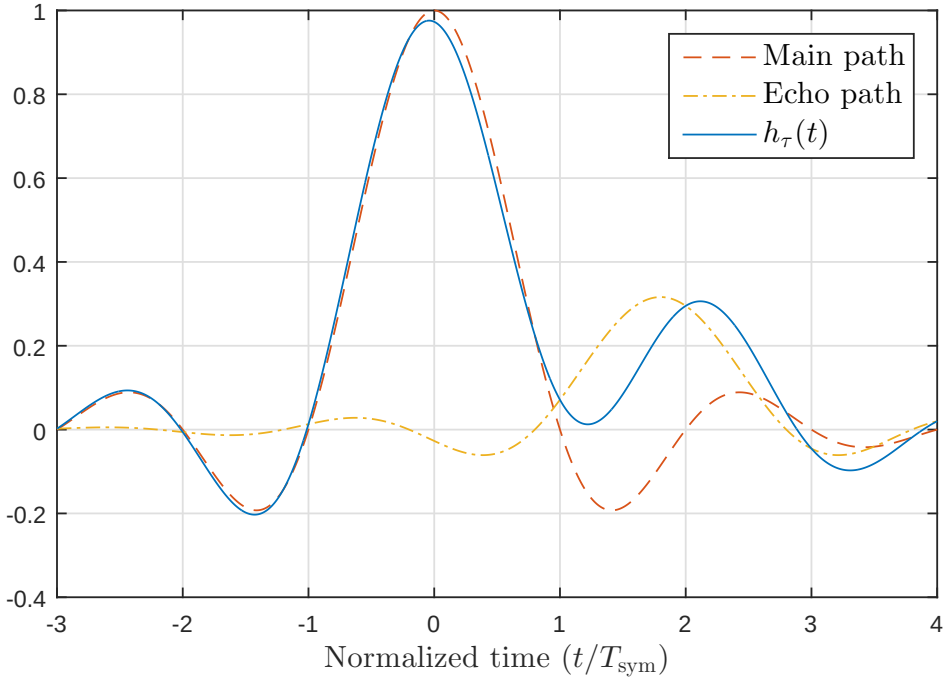

Figure 2.13 Impulse response of an equivalent single-echo multipath channel, $h_\tau(t) = h_{\text{RC}}(t) + \frac{1}{\sqrt{10}} h_{\text{RC}}(t - 1.8T_{\text{sym}})$.

Fig. 2.14 shows the ISI effect caused by the multipath channel, even when there is zero timing offset (i.e., perfect timing). As before, the figure shows the transmission of 6 consecutive QAM symbols, indicated by different colors. Since there is no timing offset, the output

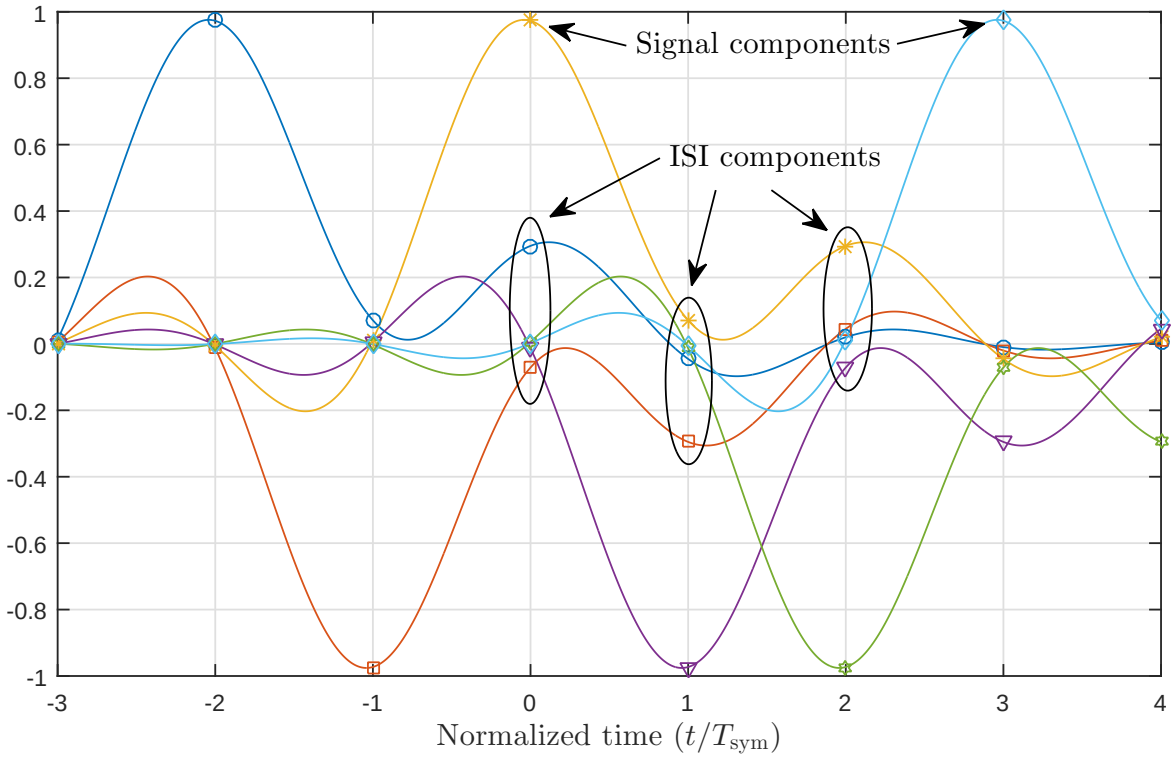

Figure 2.14 ISI caused by the multipath channel.

of the sampler is the sum of all values indicated by the markers located at time $t = nT_{\text{sym}}$. As can be seen, because of the multipath channel, the sampled signal contains interference from adjacent symbols.

Fig. 2.15 shows a scatter plot of 16-QAM signals under the single-echo channel described in Fig. 2.15. Even when the channel has no noise and timing error, the scatter plot shows many symbol errors. To further evaluate the impact of echo on the detection performance, Fig. 2.16 plots the BER versus SNR of 16-QAM for several single-echo channels. The echo delay is set at $1.8T_{\text{sym}}$ with respect to the main path, while the echo power is varied for -30, -20, -15 and -10 dB in relative to the power of the main path. It can be seen that, if the ISI is treated as noise, it will severely reduce the SNR of the system hence increasing the BER. Therefore, in order to recover the transmitted symbols properly, it is necessary to remove most of the ISI from the sampled signal. For this to be done, the characteristics of the multipath channel must be tracked and an equalizer must be employed to inverse the multipath channel effect. The principle of an equalizer will be discussed in the next section.

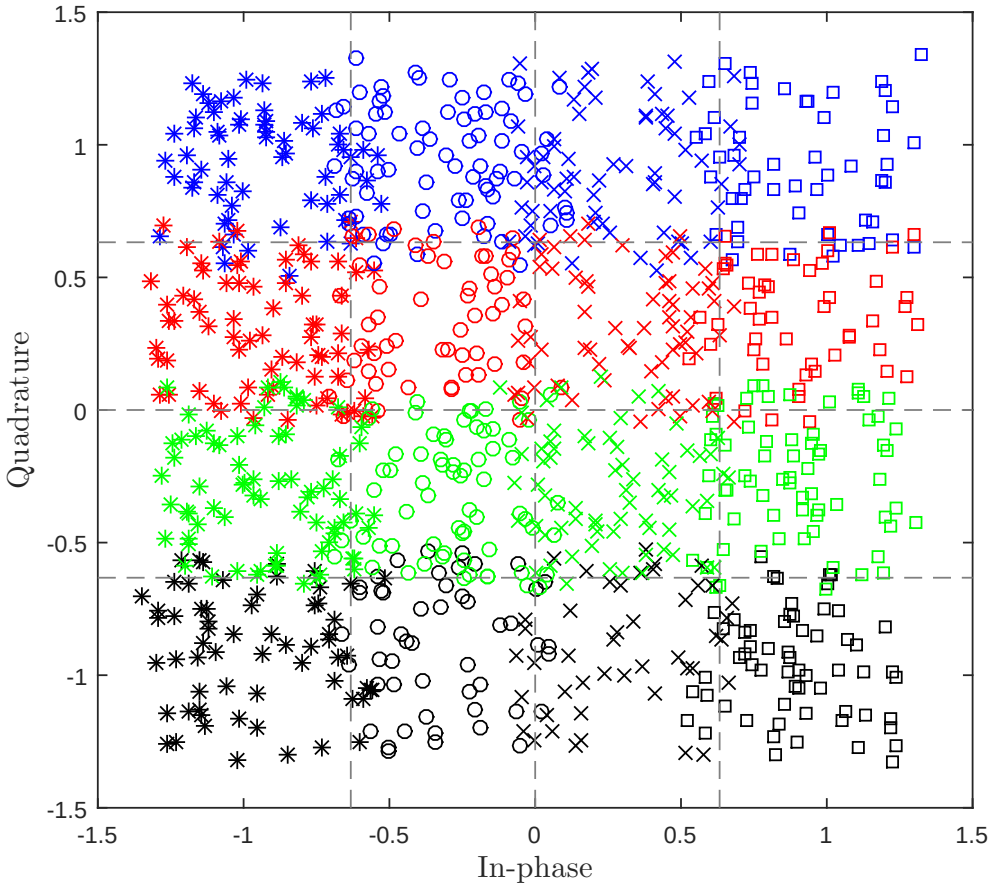

Figure 2.15 Scatter plot of 16-QAM signals under the multipath channel specified in Fig. 2.13.

2.1.2 Digital implementation of SC-QAM systems

Today almost all of the signal processing of analog signals is done in the digital domain. The first rule of system design seems to be "get the signal into the digital domain as soon as possible and do as much signal processing in the digital domain as is possible". Following this rule, Fig. 2.17 shows a practical implementation of a SC-QAM system.

Digital SRRC Filters

Perhaps the digital SRRC pulse shaping filter is the most important part of the digital SC-QAM transmitter. Digital implementation of the pulse shaping filter requires the filter to run at a rate higher than the symbol rate $F_{\text{sym}} = 1/T_{\text{sym}}$. It is because the roll-off factor

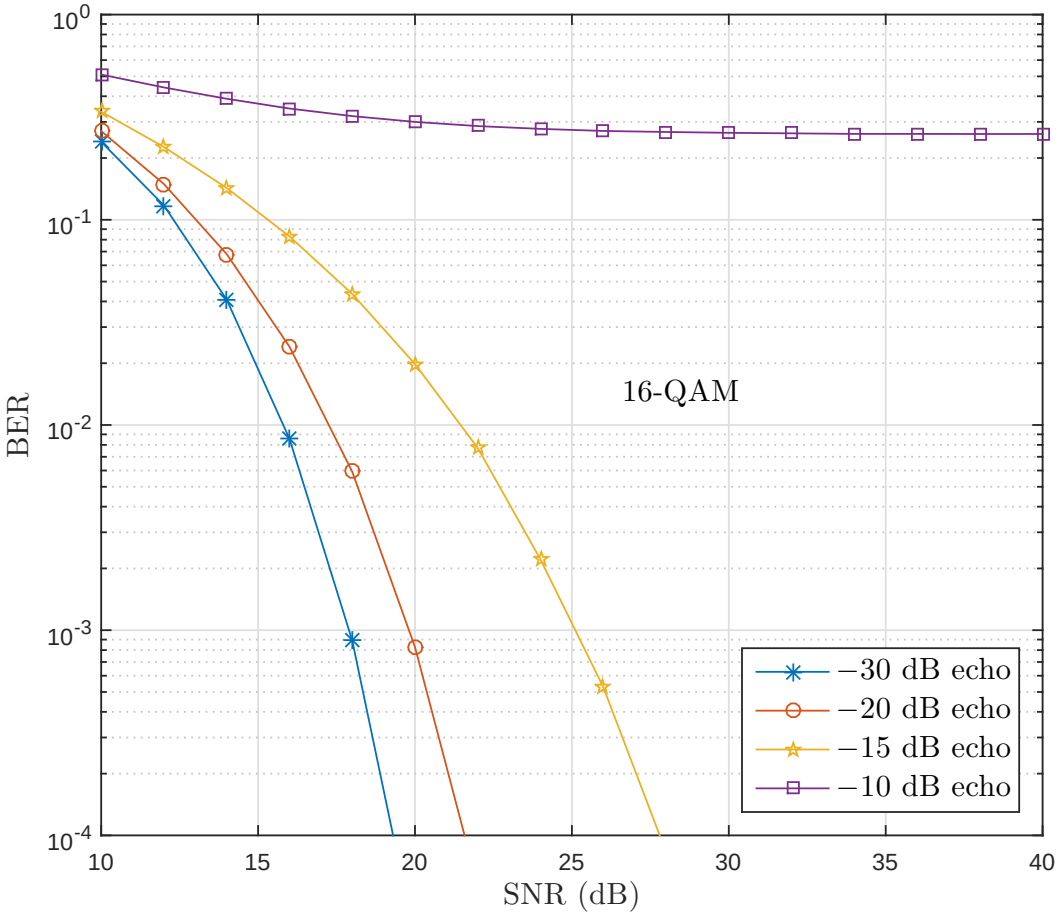

Figure 2.16 BER versus SNR for 16-QAM signal under a single-echo channel with various echo powers.

β causes an excess bandwidth in the amount of β/T_{sym} (see (2.14) and Fig. 2.4). In general, digital SRRC filters run at sampling rate $F_s = LF_{\text{sym}}$, which is an integer multiple of the symbol rate. In particular, the ideal digital pulse shaping filter is an infinite-length SRRC filter with the following frequency response

$$\begin{aligned} H_{\text{TX}}(\mathrm{e}^{j\omega}) &= H_{\text{SRRC}}(\mathrm{e}^{j\omega}) \\ &= \begin{cases} \mathrm{e}^{-j\varphi\omega}, & \text{for } |\omega| \le \frac{\pi(1-\beta)}{L} \\ \mathrm{e}^{-j\varphi\omega}\sqrt{\frac{1}{2}\left[1+\cos\left(\frac{\pi}{2\beta}\left(\frac{|\omega|L}{\pi}-1+\beta\right)\right)\right]}, & \text{for } \frac{\pi(1-\beta)}{L} < |\omega| \le \frac{\pi(1+\beta)}{L} \\ 0, & \text{otherwise,} \end{cases} \end{aligned} \tag{2.28}$$

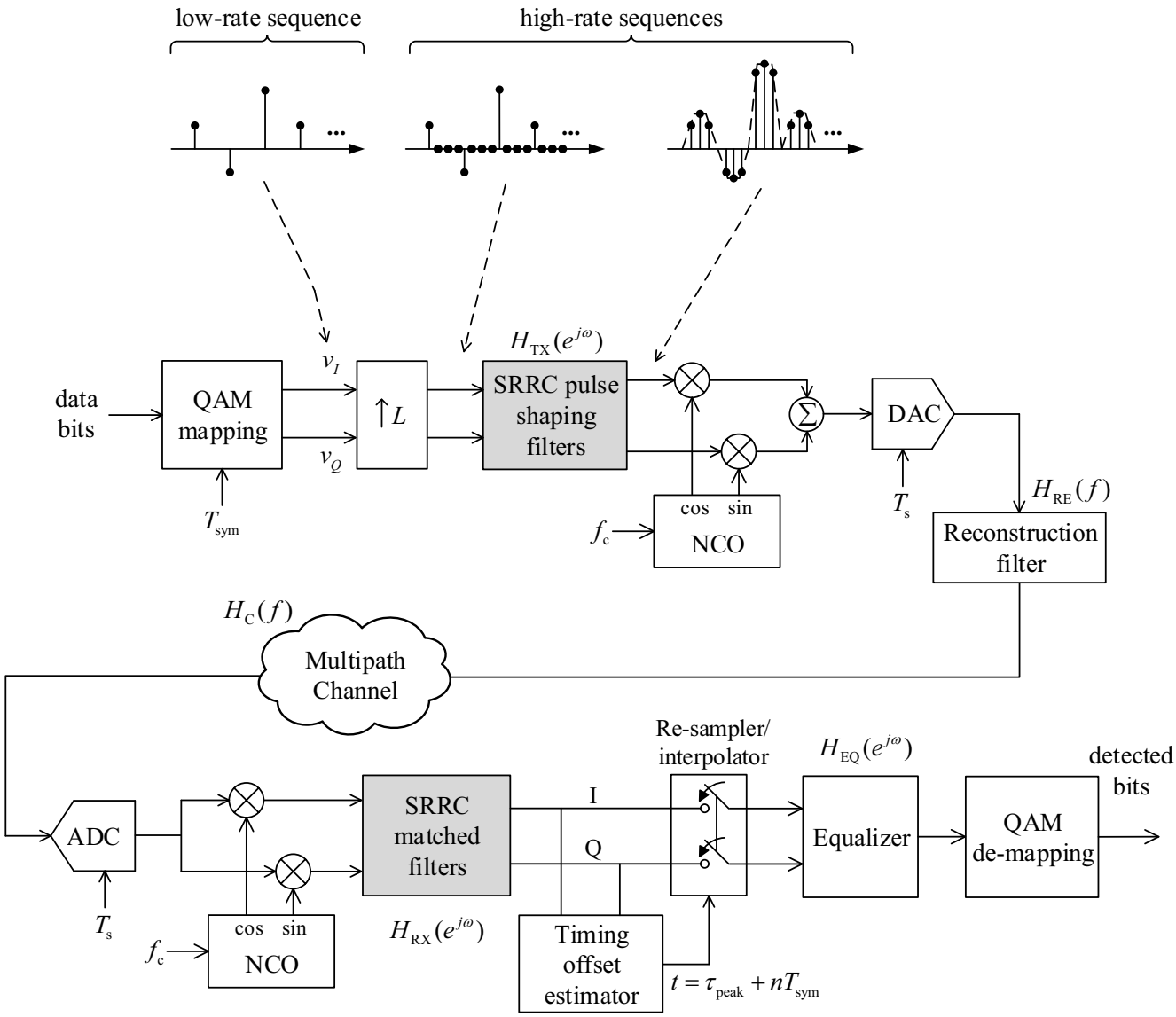

Figure 2.17 Block diagram of a digital SC-QAM system.

where ω is digital frequency in radians/sample, φ is phase delay and L is the ratio of the sampling rate to the symbol rate, i.e., $L = F_s/F_{\mathrm{sym}}$.

The simplest method to obtain the impulse response of an SRRC filter by taking the inverse discrete-time Fourier transform of (2.28). Such an impulse response has a "sinc-like" shape. Therefore, it cannot be implemented exactly in practice, unless the "sinc-like" function is truncated on both sides. As such, the coefficients for a causal FIR filter are obtained by taking the N_F values of the theoretical SRRC impulse response closest to $n = 0$.

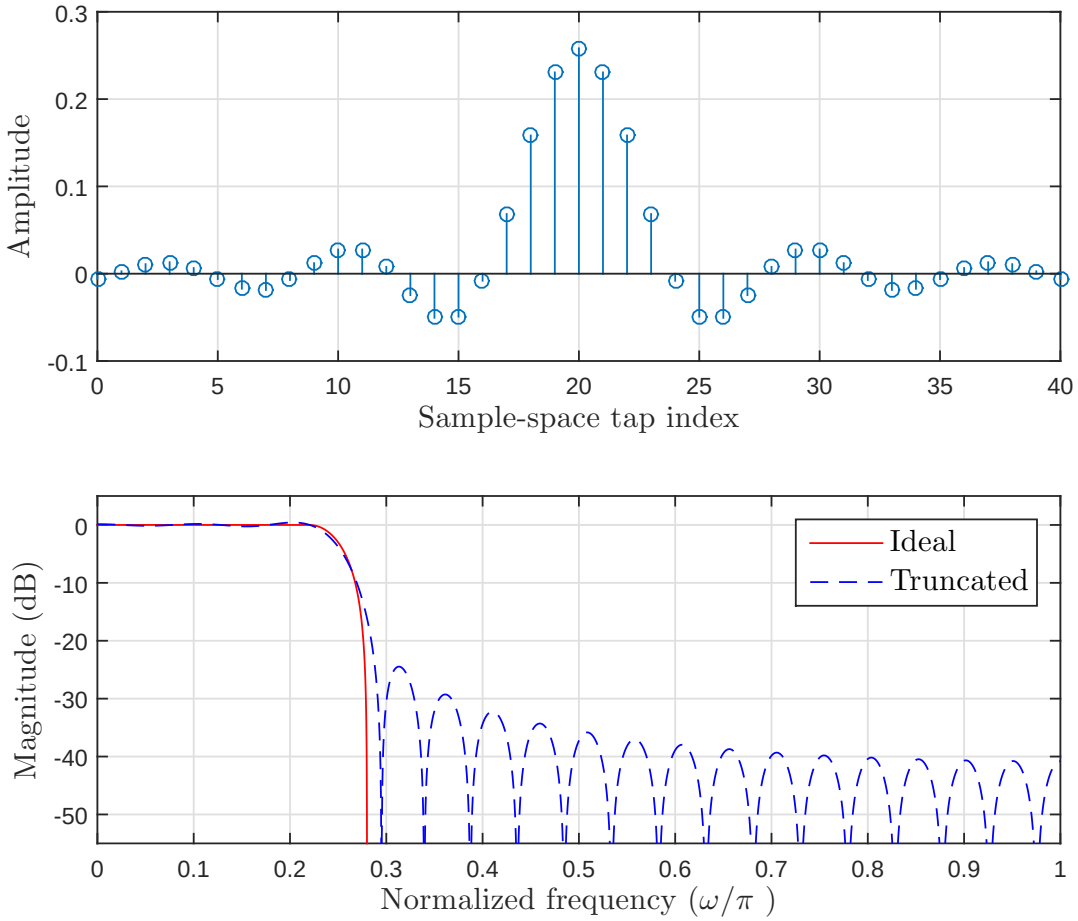

Figure 2.18 Impulse response and magnitude frequency response of a length-41 truncated SRRC filter.

The result is a sample-space truncated impulse response, given by

$$h_{\mathrm{TX}}[n] = \begin{cases} \frac{1}{L}\left(1-\beta+\frac{4\beta}{\pi}\right), & \text{for } n = \frac{N_F-1}{2} \\ \frac{\beta}{\sqrt{2}L}\left[\left(1+\frac{2}{\pi}\right)\sin\left(\frac{\pi}{4\beta}\right)+\left(1-\frac{2}{\pi}\cos\left(\frac{\pi}{4\beta}\right)\right)\right], & \text{for } n = \frac{N_F-1}{2} \pm \frac{L}{4\beta} \\ \dfrac{\sin\left(\frac{\pi(1-\beta)(n-\hat{\varphi})}{L}\right)+\frac{4\beta(n-\hat{\varphi})}{L}\cos\left(\frac{\pi(1+\beta)(n-\hat{\varphi})}{L}\right)}{\pi(n-\hat{\varphi})\left[1-\left(\frac{4\beta(n-\hat{\varphi})}{L}\right)^2\right]}, & \text{for } \begin{array}{l} 0 \le n \le N_F-1, \\ n \ne \frac{N_F-1}{2}, n \ne \frac{N_F-1}{2} \pm \frac{L}{4\beta} \end{array} \\ 0, & \text{otherwise.} \end{cases} \tag{2.29}$$

where $\hat{\varphi} = \frac{N_F-1}{2}$ is delay in samples of the truncated FIR filter.

Fig. 2.18 plots the impulse response of a truncated SRRC filter as well as the magnitude frequency responses of the ideal and truncated SRRC filters. The filter parameters are $\beta = 0.12$ and $L = 4$, and the length of the truncated filter is $N_F = 41$. Truncation of the ideal impulse response results in the presence of non-zero out-of-band power in the frequency domain, i.e., the pulse shaping filter's spectrum is no longer zero for $|f| > \frac{1+\beta}{2T_{\text{sym}}}$. Furthermore, truncation of the theoretical SRRC impulse response causes ISI because the pulse shaping and the corresponding matched filter are no longer perfectly matched. One objective of this research is to address these practical issues faced in the design of a SRRC pulse shaping filter. A solution for a cost-effective design of SRRC pulse shaping filters will be presented in Chapter 3.

As seen in Fig. 2.17, the pair of sinusoidal carriers, generated by a digital numerically controlled oscillator (NCO) [C2.4], is used to up-convert the outputs of the pulse shaping filters to pass-band. Then a digital-to-analog converter (DAC) is employed to convert the digital pass-band signal to an analog RF signal. The sample-and-hold at the output of a practical DAC causes aliasing, therefore a reconstruction filter $H_{\text{RE}}(f)$, which is typically an analog low-pass filter, is employed to smooth the sample-and-hold signals coming from the DAC.

Digital Timing Offset Estimator

In order to synchronize the receiver to the transmitter, an important step is to detect the timing offset. After the timing offset is estimated, the estimated timing information is passed to the sampler. The sampler is a filter that interpolates between the receiver's samples [C2.5, C2.6]. The purpose is to produce samples as close to the sampling moment established at the transmitter as possible.

There are two types of timing offset estimator, which use feedback or feed-forward structures to perform the timing estimation task. A timing estimator that uses a feedback loop is called a feedback timing detector. An alternative to the feedback structure is the feed-forward structure. The main difference is that the feed-forward timing offset estimator produces an estimate of the timing offset independently of the size of the offset, whereas

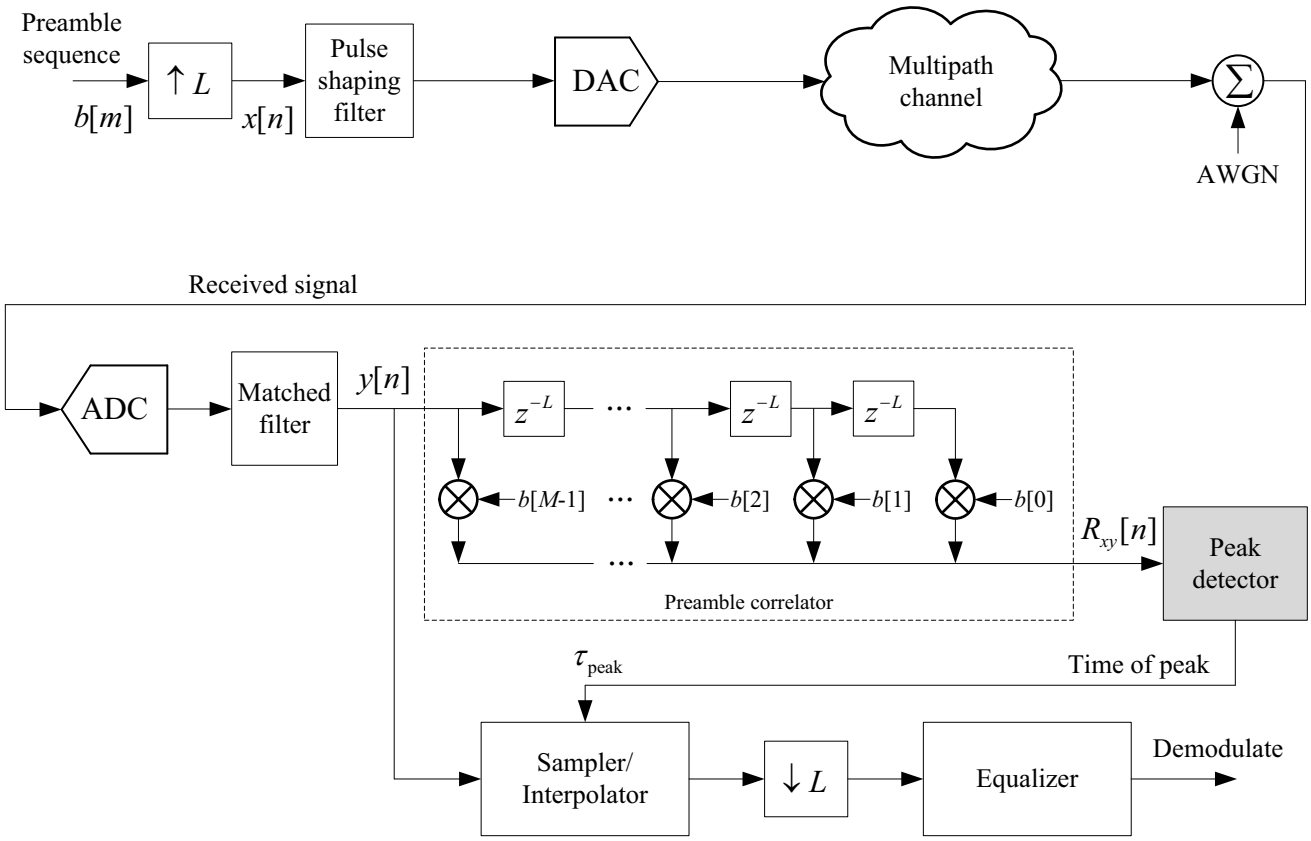

Figure 2.19 Typical structure of a feed-forward timing offset estimator circuit.

the feedback timing offset estimator produces an error signal, which can be of large variance when the offset is large. This error signal is used in a feedback loop to adjust the sampling and ultimately find the correct timing [C2.7]. It should be noted that, the feedback loop suffers the ills of stochastic descent algorithms, one of which is hangups [C2.8]. Hangups cause the estimation to dwell on incorrect sample points for short period of times, thereby lengthening estimation times [C2.7].

Feedback timing estimation techniques are not investigated within the scope of this thesis. Instead, the thesis focuses on a feed-forward timing estimation method, which is well-suited for burst-mode transmission in the DOCSIS upstream direction [C2.9]. A typical structure of a feed-forward timing offset estimator circuit is shown in Fig. 2.19. Since timing detection is independent of the carrier frequency, the NCOs and frequency up/down-convert blocks are omitted from the figure for simplicity.

Timing detection starts with sending a burst packet that contains preamble symbols,

$b[m]$, $m = 0, 1, \ldots, M-1$, to the receiver. At the receiver, timing estimation can be accomplished by locating the occurrence of the preamble packet. In general, packet detection method chooses a pseudo-random noise sequence as a preamble [C2.10], which has an auto-correlation function with low side-lobes. In particular, the auto-correlation function of the preamble sequence is defined as [C2.11]

$$R_{bb}[k] = \begin{cases} \sum_{m=0}^{M-k-1} b[m]b^*[m+k], & 0 \le k \le M-1 \\ R_{bb}^*[-k], & -M+1 \le k < 0 \\ 0, & \text{otherwise.} \end{cases} \tag{2.30}$$

Good sequences for timing offset estimation have impulse-like auto-correlation functions. In practice, the auto-correlation function has a main lobe that is tall and narrow but not an impulse, and has non-zero side lobes that are well below the peak of the main lobe. Preamble sequences with very good auto-correlation properties can be found in [C2.12] and its references. The ratio between the peak and side lobe powers, which is called the *merit factor*, is approximately proportional to the length of the preamble sequence. Because synchronization systems with larger merit factors are more immune to noise, longer preamble sequences are desirable.

In order to limit the bandwidth occupied by the preamble sequence, the preamble sequence $b[m],\ m = 0, 1, \ldots, M-1$, is up-sampled by a factor of L by zero-stuffing to obtain the sequence $x[n]$. Then $x[n],\ n = 0, 1, \ldots, ML-1$, is passed through the pulse shaping filter to become the transmitted signal. The signal propagates through the channel, eventually reaching the receiver. At the receiver, a matched filter is applied to the received signal in order to reject adjacent channel interference, limit noise power and most importantly, to reduce ISI.

Denote the output of the matched filter as $y[n],\ n = 0, 1, \ldots, ML-1$. Then the preamble packet detection is accomplished by employing a preamble correlator. Since the upsampled preamble pattern $x[n]$ is known *a priori*, it can be correlated with the output of the matched filter $y[n]$. The correlation between $x[n]$ and $y[n]$ is denoted as $R_{xy}[n]$, and indicated in

Fig. 2.19. It is well known that, for any two band-limited analog signals, they can be sampled then correlated, or correlated then sampled [C2.3], since both ways give the same result. Therefore, it can be shown that $R_{xy}[n]$ is the sampled version of an analog correlation signal, denoted as $R_{xy}(t)$, with sampling duration T_s, i.e., $R_{xy}[n] = R_{xy}(t)\big|_{t=nT_s}$.

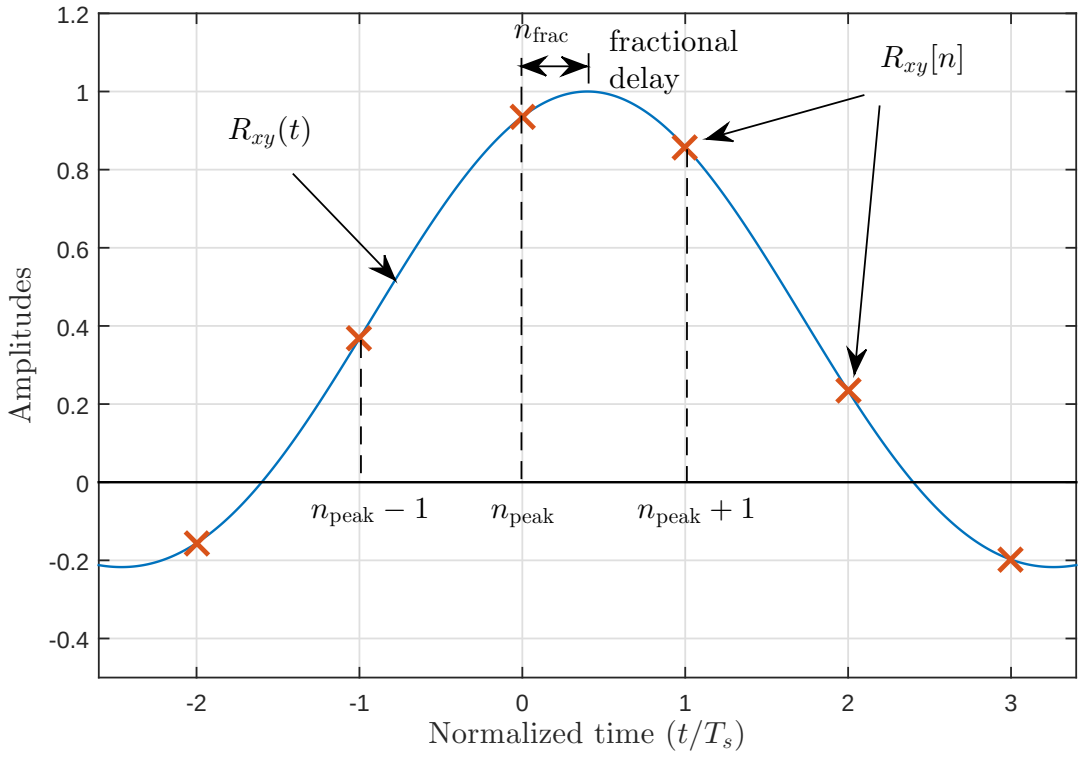

Figure 2.20 Signals generated by analog and digital correlators.

Fig. 2.20 shows the signals generated by analog and digital correlators. The timing offset can be estimated by locating the peak of the output of the analog correlator, as shown in the figure. The problem is the correlation is performed digitally to get $R_{xy}[n]$, as illustrated in Fig. 2.19, which provides samples of the analog correlation at times $t = nT_s$. In general, the timing offset contains an integer component and a fractional component, normalized to the sampling duration T_s. While the integer component can be easily detected by locating the peak of $R_{xy}[n]$, i.e., n_{peak}, estimating the fractional component is not as easy, because it is unlikely that a sample point will coincide with the peak of the analog correlator. Therefore the digital interpolating peak detector circuit, which is also shown in Fig. 2.19, is needed to estimate the fractional timing component, denoted as n_{frac} as shown in Fig. 2.20. Eventually

the estimated timing offset in seconds can be obtained as $\tau_{\text{peak}} = (n_{\text{peak}} + n_{\text{frac}})T_s$.

A simple, but inaccurate estimation for the location of the peak in the analog signal is the location of the largest sample. This method has a resolution of $\pm$ 1/2 the sampling interval. The brute force method of improving the accuracy is to first up-sample the signal and then locate the sample largest in magnitude. Clearly, the accuracy will be improved by the up-sampling factor. Up-sampling is a well-known process [C2.13, C2.14] whose implementation has been well explored [C2.15]. Even with efficient implementation, up-sampling is relatively expensive.

Another approach is to approximate the analog signal in the vicinity of its peak with a parameterized analog function. Any class of function can be used providing one of the parameters is the location of its peak. The parameter of interest, which is the location of the peak, is calculated using samples in the vicinity of the peak. One such function suggested in [C2.13] is a concave down parabola given by $f(t) = a + c(t - \tau_{\text{peak}})^2$, where τ_{peak} is the parameter of interest. Since the function has three parameters, three digital samples in the vicinity of the peak are required to calculate τ_{peak}. This particular function has been used for peak location in many different applications [C2.14, C2.15, C2.16, C2.17, C2.18].

Since the parabolic function is the second order Taylor series expansion about the peak of the analog signal, it will be very accurate providing the three digital samples used to compute τ_{peak} are in close proximity to the peak. The shape of the function approximating the analog signal would be more accurate if a third or fourth-order Taylor series expansion is used. However, four or five samples would be needed to calculate τ_{peak} and the additional samples used to find τ_{peak} would be located farther from τ_{peak}, perhaps outside the region where the 3$^{\text{rd}}$ or 4$^{\text{th}}$ order function is a good approximation.

Chapter 4 of this thesis investigates the quality of two-parameter functions for approximating the signal in the vicinity of its peak. For timing offset estimation and some other applications [C2.19], a two-parameter function can very accurately model the analog signal in the vicinity of its peak. It will be explained later that the complexity of the calculation of τ_{peak} is comparable to that of using a parabolic function, if the two-parameter function is

restricted to a class where its logarithm is nearly linear in the vicinity of the peak.

Equalizer

As previously discussed, there are factors/imperfections that give rise to ISI in a digital SC-QAM system:

1. Truncation of digital pulse shaping and matched filters.
2. Error in timing offset estimation.
3. Echoes in the multipath channel.

As such, the receivers in DOCSIS systems typically employ equalizers to suppress most of the ISI caused by the aforementioned imperfections, so that the received signal can be accurately demodulated and de-mapped into data bits.

The problem of ISI corrupting a received signal and causing degradation to the overall system performance is certainly not unique to the DOCSIS upstream channel. In fact, equalization techniques which are capable of mitigating the effects of ISI have been well-studied in open literature [C2.4, C2.20]. The DOCSIS system that employs SC-QAM modulation does not explicitly specify the type of equalizer, but rather constraints the structure of the equalizer to be a 24-tap symbol-spaced FIR filter that follows the matched filter [C2.1]. For the purpose of explaining the working principle of an equalizer and evaluate the system's performance, the method of least mean squared (LMS) equalization shall be given as an example.

Denote $h_\tau[n] = h_\tau(t)\big|_{t=nT_{\text{sym}}-\Delta t}$ as the symbol-spaced impulse response of the equivalent band-limited channel. Then (2.26) can be express as

$$\hat{v}[n] = v[n] * h_\tau[n] + w[n], \tag{2.31}$$

where $*$ denotes convolution operation. Let N_τ be the length of $h_\tau[n]$. Then $\boldsymbol{h}_\tau = \big[h_\tau[0], h_\tau[1], \ldots, h_\tau[N_\tau - 1]\big]^T$ contains samples taken from $h_\tau(t)$ at the symbol rate. Assume that $\boldsymbol{h}_\tau$

contains the decision point at element $h_\tau[\kappa]$, where $\kappa \in [0, N_\tau)$. The decision point is the location of the tap that is largest in magnitude (see Fig. 2.13). If the impulse response of the channel is infinite, the vector $\boldsymbol{h}_\tau$ is truncated to length N_τ, where N_τ is sufficiently large to include 99.9999% of the energy. That is N_τ is sufficiently large to satisfy

$$10\log_{10}\left(\frac{\sum_{i\geq N_\tau}^{\infty}\left|h_\tau[i]\right|^2}{\sum_{l=0}^{N_\tau-1}\left|h_\tau[l]\right|^2}\right) < -60 \text{ dB}. \tag{2.32}$$

Prior to equalizing, the normalized ISI power is calculated as follows

$$P_{\text{ISI}} = \frac{\sum_{i=0,i\neq\kappa}^{N_\tau-1}\left|h_\tau[i]\right|^2}{\left|h_\tau[\kappa]\right|^2} = \frac{\sum_{i=0}^{N_\tau-1}\left|h_\tau[i]\right|^2}{\left|h_\tau[\kappa]\right|^2} - 1 \tag{2.33}$$

Let $\mathbf{g} = [g(0), g(1), \ldots, g(23)]^T$ be the coefficients for the 24-tap equalizer. For the purposes of characterizing ISI with the symbol-spaced equalizer, the main tap of the equalizer is positioned at $g(8)$, as it is a common choice for reducing multi-path channel distortions in the DOCSIS systems. The coefficients in $\mathbf{g}$ are chosen to minimize the mean squared error $\|\mathbf{h}_\tau * \mathbf{g} - \boldsymbol{\Delta}_{\kappa+8}\|^2$, where $\boldsymbol{\Delta}_{\kappa+8}$ is a length-$(N_\tau + 23)$ column vector where all elements are zeros except for the $(\kappa+8)^{\text{th}}$ row , which has the value of 1. Therefore, the optimum equalizer coefficients, denoted as $\mathbf{g}^{\text{opt}}$, can be found by solving

$$\mathbf{g}^{\text{opt}} = \underset{\mathbf{g}}{\text{argmin}} \left\| \underbrace{\begin{bmatrix} h_\tau(0) & 0 & \cdots & 0 & 0 \\ h_\tau(1) & h_\tau(0) & \cdots & 0 & 0 \\ \vdots & \vdots & \ddots & \vdots & 0 \\ h_\tau(22) & h_\tau(21) & \ddots & h_\tau(0) & 0 \\ h_\tau(23) & h_\tau(22) & \ddots & h_\tau(1) & v(0) \\ \vdots & \vdots & \ddots & \vdots & \vdots \\ 0 & 0 & \ddots & h_\tau(N_\tau-1) & h_\tau(N_\tau-2) \\ 0 & 0 & \ddots & 0 & h_\tau(N_\tau-1) \end{bmatrix}}_{\mathbf{V}} \underbrace{\begin{bmatrix} g(0) \\ g(1) \\ g(2) \\ \vdots \\ g(8) \\ \vdots \\ g(22) \\ g(23) \end{bmatrix}}_{\mathbf{g}} - \underbrace{\begin{bmatrix} 0 \\ 0 \\ 0 \\ \vdots \\ 1 \\ \vdots \\ 0 \\ 0 \end{bmatrix}}_{\boldsymbol{\Delta}_{\kappa+8}} \right\|^2, \tag{2.34}$$

where $\mathbf{V}$ in (2.34) is a size $(N_\tau + 23) \times 24$ Toeplitz convolution matrix. It is obvious that (2.34) is a conventional least squares problem, which can be solved as

$$\mathbf{g}^{\text{opt}} = \mathbf{V}^{+}\boldsymbol{\Delta}_{\kappa+8}, \tag{2.35}$$

where $\mathbf{V}^{+}$ is Moore-Penrose pseudo-inverse matrix of $\mathbf{V}$[2]. The above means that the equalizer coefficients are the elements of the $(\kappa+8)^{\text{th}}$ row of $\mathbf{V}^{+}$. The ISI power after equalization can be approximated with high-precision by

$$P_{\text{ISI}}^{(\text{eq})} = \|\mathbf{V}\mathbf{g}^{\text{opt}} - \boldsymbol{\Delta}_{\kappa+8}\|^2 \tag{2.36}$$

To illustrate the effectiveness of LMS equalization, consider the multipath channel described in Fig. 2.13. The corresponding symbol-spaced discrete-time impulse response of the channel is $h_\tau[n] = h_\tau(t)\big|_{t=nT_{\text{sym}}}$ and it is plotted in Fig. 2.21-(a). Such discrete-time impulse response shows a main tap located at $\kappa = 10$ along with several non-zero taps, which are created by the echo in $h_\tau(t)$ that is $1.8T_{\text{sym}}$ away from the main path. The ISI power prior to the equalization is determined to be -10.3 dB, which is quite high and could significantly degrade the BER performance. Fig. 2.21-(b) plots 24 taps of the LMS equalizer $g[n]$, which is used to reverse the multipath channel effect. The impulse response of the cascade of the multipath channel and the equalizer, i.e., $h_\tau[n] * g[n]$, is shown in Fig. 2.21-(c), which appears almost like an impulse. Nevertheless, a close inspection of the samples of $h_\tau[n] * g[n]$ reveal that there are small but non-zero samples, which contribute to the residual ISI after equalization. The power of the residual ISI is determined to be -81.8 dB, which is much less than -10.3 dB before equalization. Thus, the LMS equalizer has successfully removed the majority of ISI power. The scatter plot of signal samples after applying the LMS equalizer is shown in Fig. 2.22 and one can see almost a perfect 16-QAM constellation, which gives another visual confirmation of the effectiveness of the LMS equalizer.

[2]This pseudo-inverse can be computed with Matlab function `pinv()`.

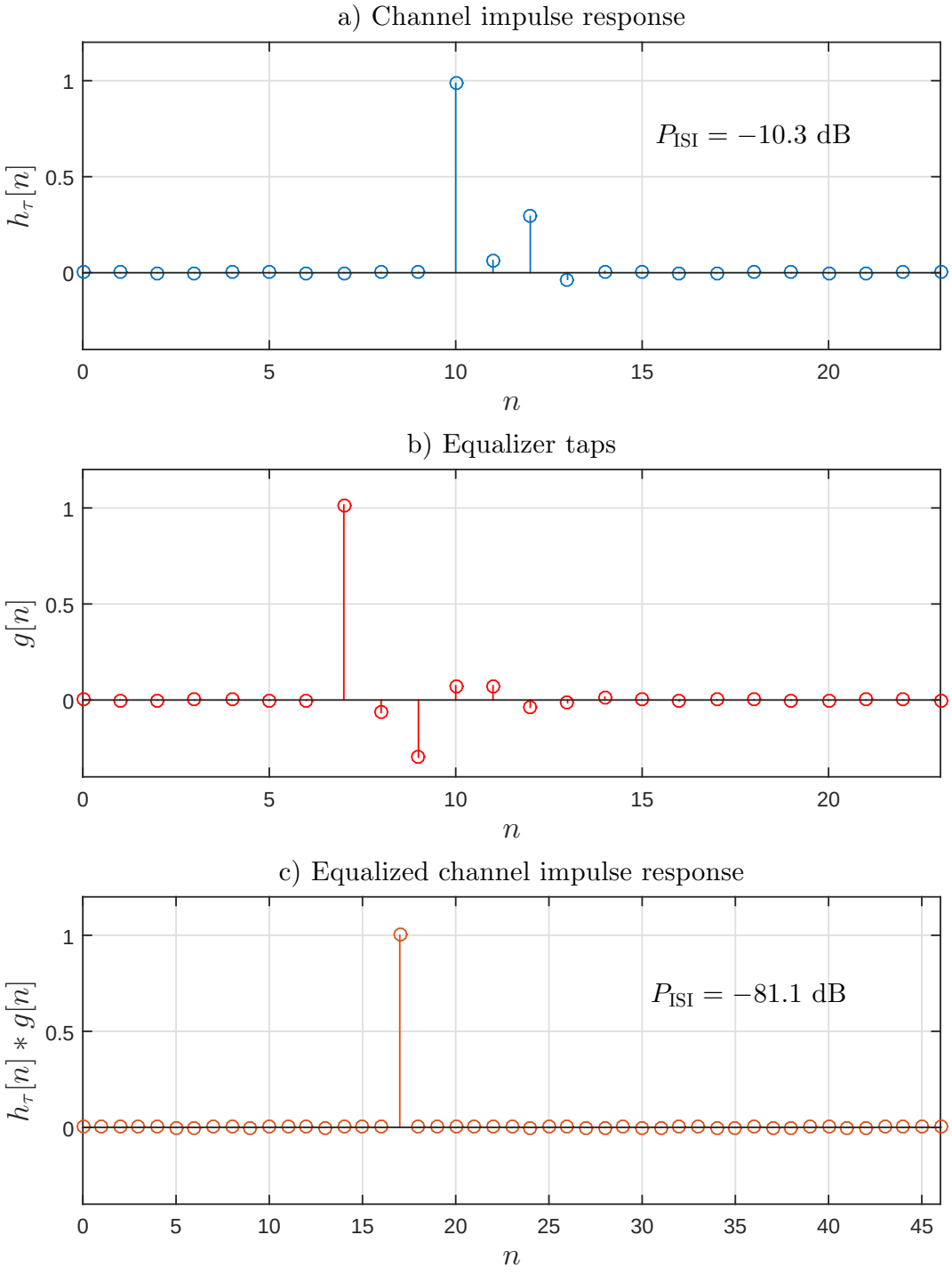

Figure 2.21 LMS equalization example for the multipath channel specified in Fig. 2.13.

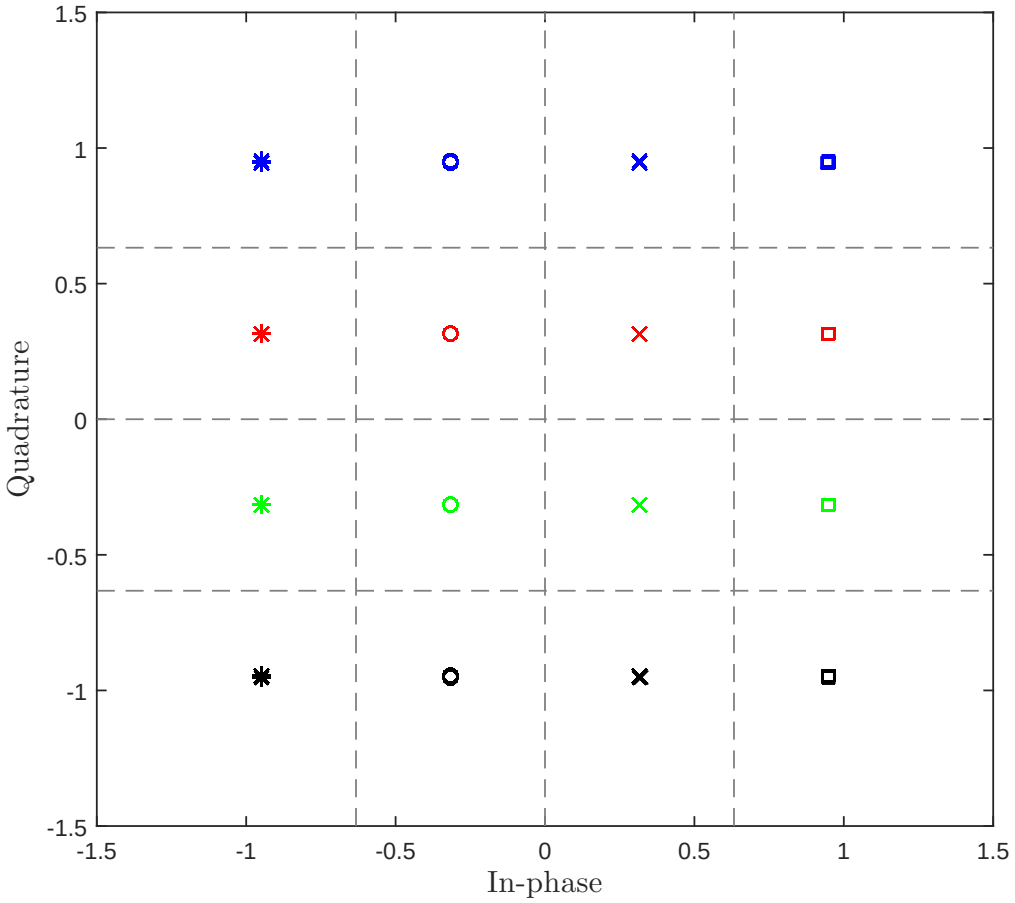

Figure 2.22 Scatter plot of 16-QAM signals after LMS equalization.

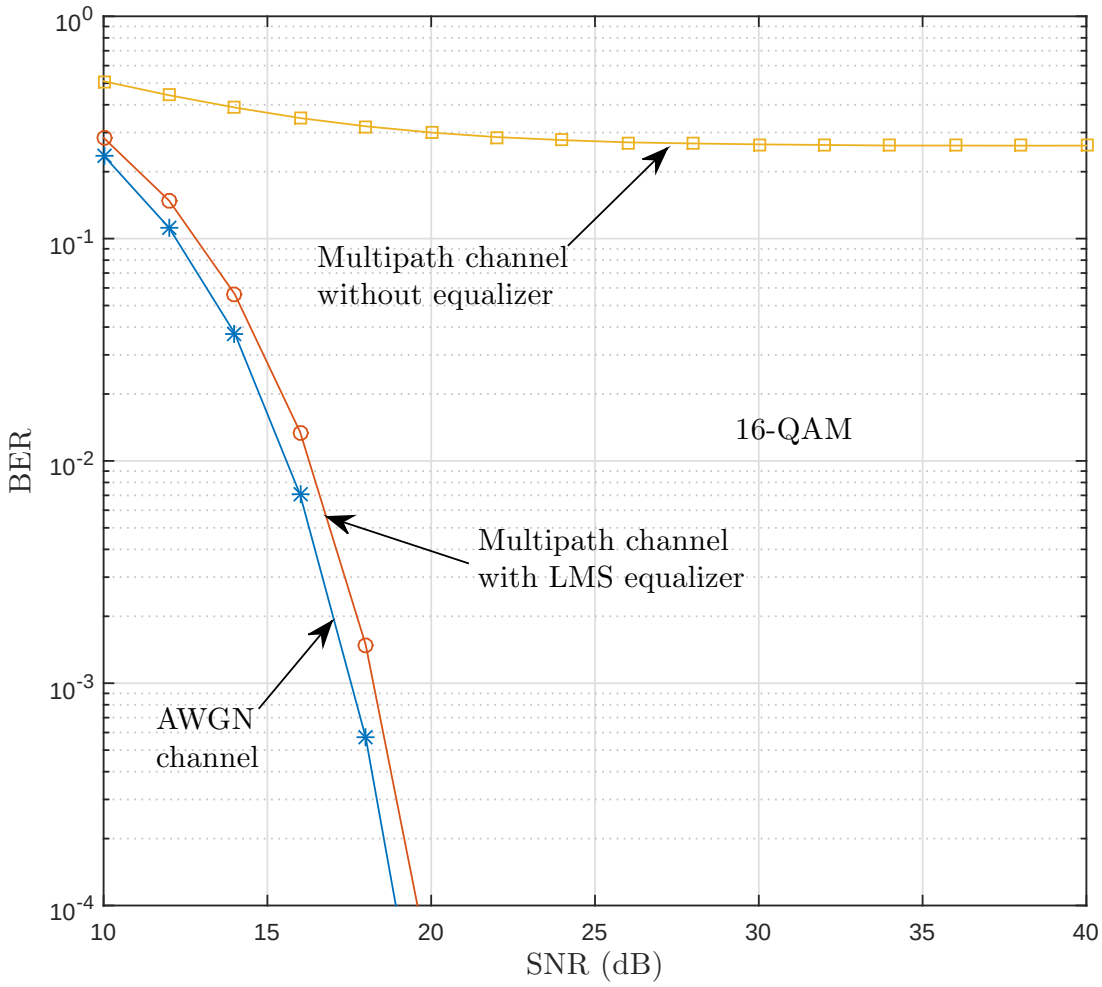

Figure 2.23 BER versus SNR for 16-QAM signal under AWGN channel and the multipath channel specified in Fig. 2.13 for the cases with and without equalization.

Fig. 2.23 plots the BER versus SNR for 16-QAM signal under an AWGN channel (i.e., without multipath components) and the multipath channel specified in Fig. 2.13 for the cases with and without equalization. It can be seen that the LMS equalizer almost perfectly removes the multipath channel effect as the BER performance under the multipath channel obtained with the help of the LMS equalizer is almost as good as the BER performance under an AWGN channel.

It should be pointed out that a longer equalizer can help suppress ISI better, thus enhance the detection performance at the cost of a more complex equalizer. In practice, the length of the equalizer must be at least equal to the channel's delay spread, which is the delay of the longest echo in relative to the main path. The 24-tap equalizer employed for DOCSIS system prior to version 3.1 is shown to be good enough for cable channels [C2.4] in the sense that the residual ISI power is considerably less than the AWGN power.

Complexity of the equalizer becomes more problematic when designers try to increase the data rate. For example, if one tries to send data twice as fast by doubling the symbol rate, then it would require reducing the symbol duration T_{sym} by half. This means that for the same physical channel with the same delay spread, the equalizer should have twice the number of taps as before, i.e., 48 taps. As a consequence, the complexity of the equalizer, which relies on matrix inversion operation (2.34), is at least quadruply increased.

Because of the equalizer's complexity issue for high-speed transmission, SC-QAM is not a good candidate for wide-band systems. For that reason, SC-QAM is being replaced by multi-carrier OFDM in the current and next versions of the DOCSIS standard. Details about OFDM/OFDMA are given in the next section.

2.2 Multi-Carrier OFDMA

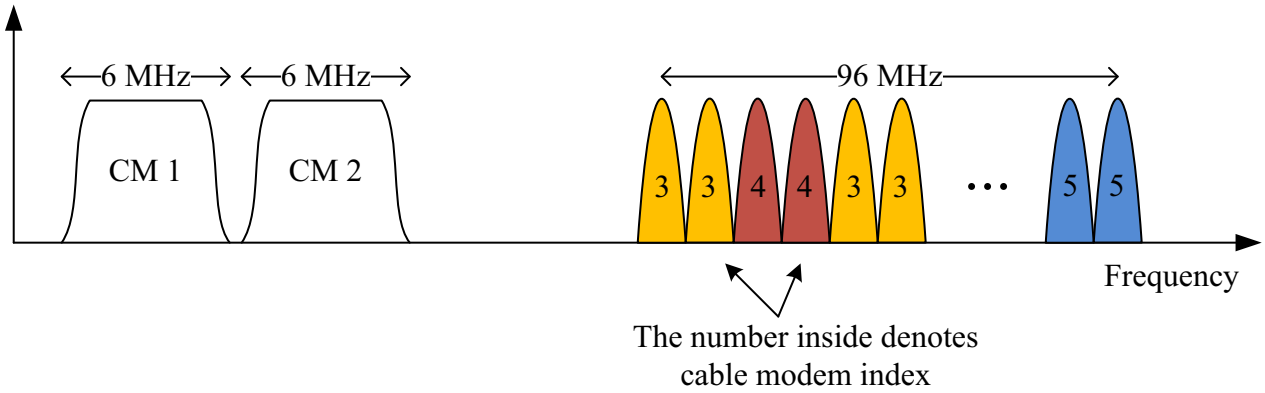

Figure 2.24 Example of SC-QAM (CMs 1 and 2) and OFDMA (CMs 3, 4 and 5)

Compared to prior versions of DOCSIS, the unique feature of DOCSIS 3.1 is that OFDM is used for downstream transmissions and OFDMA is used for upstream transmissions. Although OFDM and OFDMA both partition a wideband channel into a multiplicity of overlapping narrow subcarriers, they differ in how the subcarriers are allocated to transmitters. In OFDM, a single device transmits data on all of the subcarriers in the channel, which is well suited to the broadcast nature of downstream traffic, in which a single CMTS sends data to multiple CMs. In constrast, OFDMA allows multiple transmitters (CMs) to simultaneously transmit on disjoint sets of subcarriers.

OFDMA offers a significant complexity reduction and increased flexibility in supporting multiple users as compared to SC-QAM. As illustrated in Fig. 2.24, unlike SC-QAM systems where each CM occupies a bandwidth of 6 MHz, OFDMA allows all CMs to share a large bandwidth of 96 MHz. The large bandwidth consists of 1900 or 3800 very-narrow-bandwidth sub-carriers, with a sub-carrier spacing of either 50 kHz or 25 kHz, depending on the transmission mode. Each of these sub-carriers is used to transmit a small percentage of the total payload at a low data rate. This implementation allows different amounts of bandwidth to be given to different CMs based on their current demands.

Another advantage of OFDMA is the ability to adapt to the multipath channel and other severe channel conditions. By splitting the bandwidth into extremely-narrow-band sub-carriers, each sub-carrier typically experiences what is known as “flat fading”, making

the equalization process relatively simple. This is very different from a SC-QAM signal that occupies a wide bandwidth and is susceptible to distortion across the full bandwidth. Moreover, flexibility in channel resource allocation allows OFDMA to avoid bad parts of the spectrum by simply turning off sub-carriers at those locations.

While OFDMA systems have been studied for many years, the DOCSIS 3.1 standard is unique in that it combines OFDMA with very high-order modulation schemes (up to 16384-QAM). Furthermore, cable plants generate a number of channel impairments, some of which differ from impairments in wireless OFDMA systems which are typically discussed in the literature.

Consider the OFDMA system shown in Fig. 2.25, in which the frequency translating up/down-converters are omitted for simplification. This system is referred to as the baseband-equivalent system. The channel bandwidth is divided into N sub-carriers, M of which are used for data transmission and assigned QAM symbols $X[m]$, $m = 0, 1, \ldots, M-1$. As specified in DOCSIS 3.1 [C2.21], there are guard bands at both ends of the allocated spectrum that cannot be used for data transmission. This restricts the locations of the data sub-carriers, which are usually centered at the middle of the allocated spectrum.

For OFDMA systems, the two most popular sub-carrier allocation strategies are localized frequency-division multiple access (L-FDMA) and interleaved frequency-division multiple access (I-FDMA). Denote the vector of data sub-carrier indexes as $\boldsymbol{\mathcal{S}} = [\mathcal{S}(0), \mathcal{S}(1), \ldots, \mathcal{S}(M-1)]$, where the elements are related by

$$\mathcal{S}(m) = \mathcal{S}(0) + mK, \quad m = 0, 1, \ldots, M-1. \tag{2.37}$$

Here $\mathcal{S}(0)$ is the start sub-carrier and K is an integer number denoting the sub-carrier skipping factor. The case $K = 1$ corresponds to L-FDMA, whereas $K > 1$ means I-FDMA.

The OFDMA transmitter employs an inverse discrete Fourier transform (IDFT) module of size N for modulation. DOCSIS 3.1 applies modified IDFT/DFT operations, where sub-carrier indexing is shifted by $-N/2$ sub-carriers. Using DOCSIS 3.1 IDFT, the transmitted

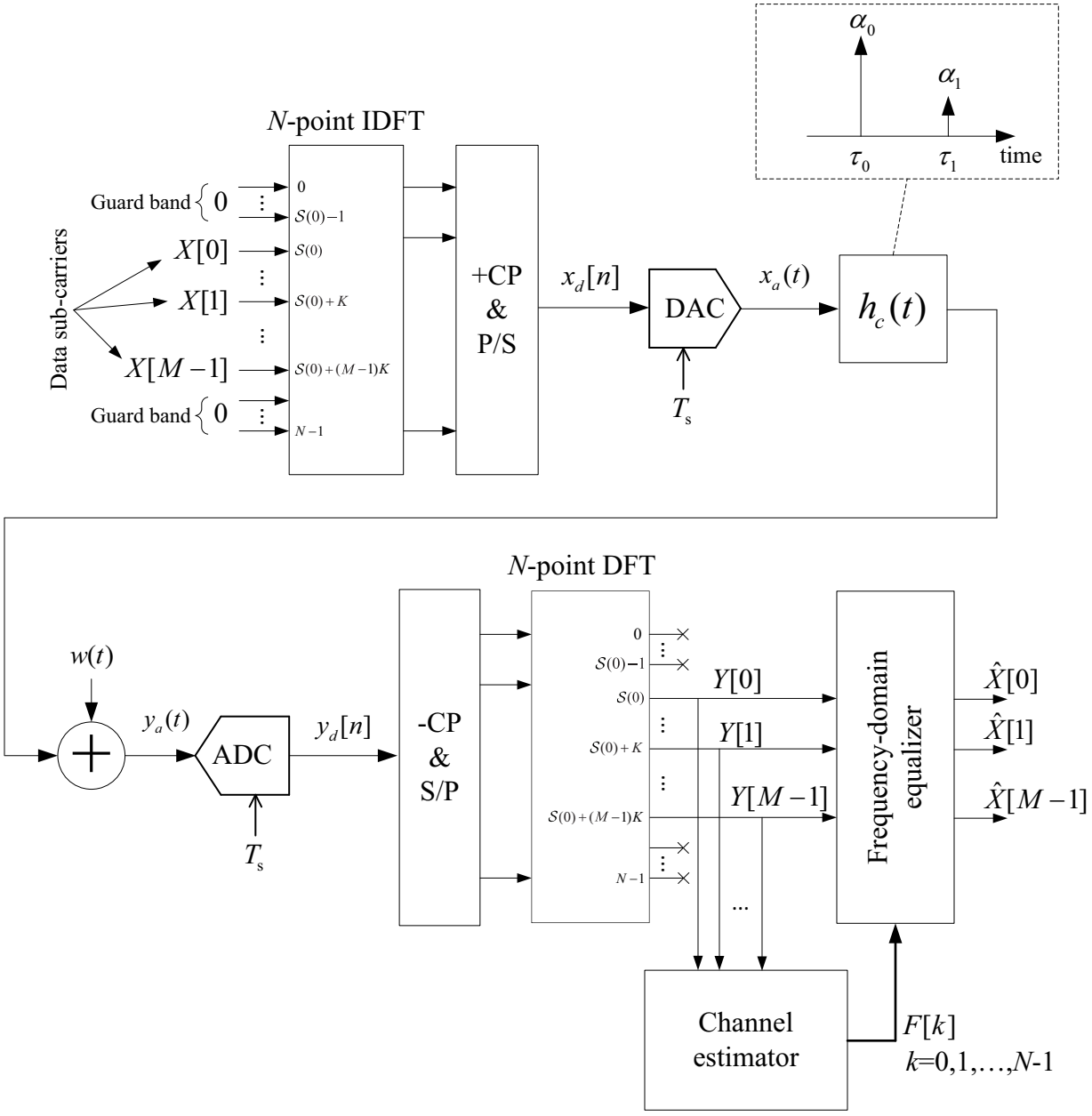

Figure 2.25 Baseband-equivalent OFDMA system model.

time-domain samples are written as

$$x_d[n] = \frac{1}{\sqrt{N}} \sum_{m=0}^{M-1} X[m] \exp\left(\frac{j2\pi(\mathcal{S}(m) - N/2)n}{N}\right), \tag{2.38}$$

where $n = 0, 1, \ldots, N-1$ is the sample index. One OFDMA symbol contains N samples, which are sent out to the channel at sampling rate F_s.

Although OFDMA does not suffer from ISI degradation due to imperfect matching between the pulse shaping and matched filters as in SC-QAM systems, the multipath channel can still cause ISI. To combat ISI in the receiver, a cyclic prefix consisting of N_{CP} samples from the end of the OFDMA symbol is added to the front of the symbol.

After performing parallel-to-serial (P/S) conversion, the time-domain samples are serially passed through a DAC clocked at sampling rate F_s and filtered with an image rejection filter to generate a continuous-time signal $x_a(t)$. Assuming ideal digital-to-analog conversion, the continuous-time signal $x_a(t)$ can be expressed as

$$x_a(t) = \frac{1}{\sqrt{N}} \sum_{m=0}^{M-1} X[m] \exp\left(\frac{j2\pi(\mathcal{S}(m) - N/2)(t - T_g)}{NT_s}\right), \quad 0 \le t \le NT_s + T_g, \tag{2.39}$$

where $T_s = 1/F_s$ is the sampling period and T_g is the guard interval (in seconds). Given that the number of CP samples is N_{CP}, the CP duration is simply $T_g = N_{\text{CP}}T_s$. It is clear that after the CP is inserted $x_a(t) = x_a(t + NT_s), \forall\, t \in [0, T_g]$. It is pointed out that, in practice, the validity of (2.39) depends on how well the up-conversion is performed.

As previously discussed, the impulse response of the multipath channel is

$$h_c(t) = \sum_{i=0}^{N_p-1} \alpha_i \delta(t - \tau_i T_s), \tag{2.40}$$

where N_p is the number of paths in the multipath channel. Then the continuous-time signal received at the receiver is the convolution of the transmitted signal and the impulse response

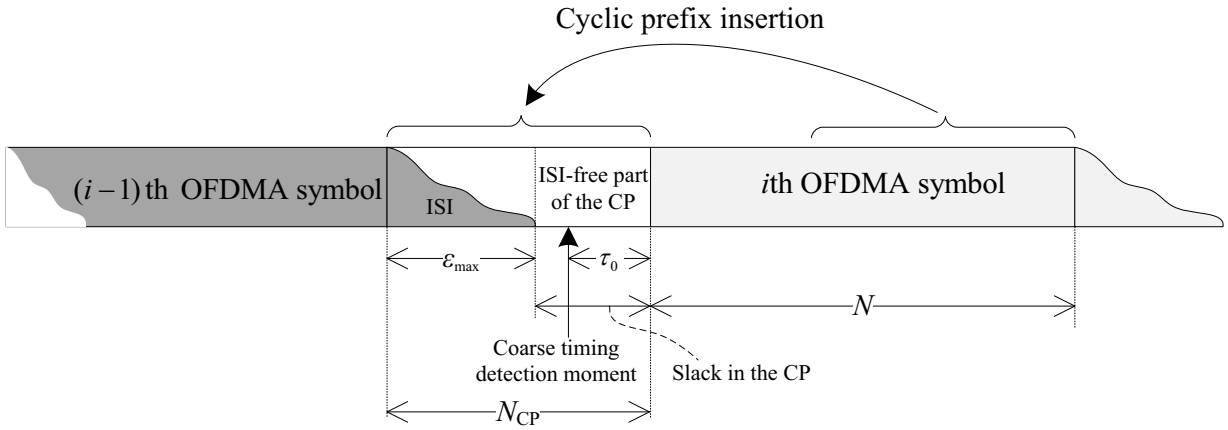

Figure 2.26 Illustration of ISI-free channel condition.

of the multipath channel, added by thermal noise. That is,

$$\begin{aligned} y_a(t) &= \int_0^{\infty} h_c(\lambda) x_a(t-\lambda) \mathrm{d}\lambda + w(t) \\ &= \sum_{i=0}^{N_p-1} \alpha_i x_a(t-\tau_i T_s) + w(t), \end{aligned} \tag{2.41}$$

where $w(t)$ is a zero-mean AWGN process. It should be noted that τ_0 is generally considered as the coarse timing offset (normalized to the sampling period T_s) introduced by error in detecting the start time of the received OFDMA symbol. There are many coarse timing estimation techniques, e.g. [C2.22, C2.23, C2.24, C2.25, C2.26], that can detect the start time of the received OFDMA symbol. After coarse timing recovery, the timing detection error can be a few samples.

One important factor to consider in a multipath channel is its delay spread. The channel's delay spread is defined as the delay of the longest multipath component relative to the shortest, denoted as $\epsilon_{\max} = \max_{i=1,\ldots,N_p-1} (\tau_i - \tau_0)$. For OFDM/OFDMA systems, delay spread has a significant impact on ISI, as longer delay spread leads to greater amount of ISI, as illustrated in Fig. 2.26.

Assume a well designed system where the length of the cyclic prefix is greater than the channel's delay spread, i.e., $T_g = N_{\mathrm{CP}} T_s > \epsilon_{\max} T_s$. This means that $N_{\mathrm{CP}} > \epsilon_{\max}$, as illustrated in Fig. 2.26. To ensure the DFT output is ISI-free, the error in the coarse timing

detection must not exceed the slack in the CP (see Fig. 2.26). This places the following constraint on the coarse timing error:

$$0 \leq \tau_0 \leq N_{\text{CP}} - \epsilon_{\max}. \tag{2.42}$$

The continuous-time signal is sampled at the receiver with sampling rate F_s. The ADC block shown in Fig. 2.25 is an ideal analog-to-digital converter (ADC), which contains a band-limiting filter (not shown in the figure) to prevent aliases caused by digital sampling. After coarse timing detection is performed, the cyclic prefix is removed. The discrete-time samples, after cyclic prefix removal, are given by

$$y_d[n] = y_a(t)\Big|_{t=nT_s+T_g} = \sum_{i=0}^{N_p-1} \alpha_i x_a(nT_s + T_g - \tau_i T_s) + w[n], \quad n = 0, 1, \ldots, N-1, \tag{2.43}$$

where $w[n]$ is $w(t)$ sampled at $t = nT_s + T_g$ and after it has been band-limited. It is a discrete-time complex white Gaussian noise process with zero mean and variance σ_w^2. To recover the QAM data, an N-point DFT block transforms the time-domain sequence back to the frequency-domain:

$$\begin{aligned} Y[m] &= \frac{1}{\sqrt{N}} \sum_{n=0}^{N-1} y_d[n] \exp\left(\frac{-j2\pi(\mathcal{S}(m) - N/2)n}{N}\right) \\ &= \frac{1}{N} \sum_{n=0}^{N-1} \sum_{i=0}^{N_p-1} \alpha_i \sum_{k=0}^{M-1} X[k] \exp\left(\frac{j2\pi(\mathcal{S}(k) - N/2)(nT_s - \tau_i T_s)}{NT_s}\right) \times \\ &\quad \exp\left(\frac{-j2\pi(\mathcal{S}(m) - N/2)n}{N}\right) + W[m], \quad m = 0, 1, \ldots, M-1, \end{aligned} \tag{2.44}$$

where

$$W[m] = \sum_{n=0}^{N-1} \frac{w[n]}{\sqrt{N}} \exp\left(\frac{-j2\pi(\mathcal{S}(m) - N/2)n}{N}\right), \tag{2.45}$$

is a complex Gaussian random variable with zero mean and variance σ_w^2. Then

$$\begin{aligned} Y[m] &= \frac{1}{N}\sum_{k=0}^{M-1} X[k] \sum_{i=0}^{N_p-1} \alpha_i \sum_{n=0}^{N-1} \exp\left(\frac{j2\pi(\mathcal{S}(k)-\mathcal{S}(m))n}{N}\right) \times \\ &\qquad \exp\left(\frac{-j2\pi(\mathcal{S}(m)-N/2)\tau_i}{N}\right) + W[m] \\ &= X[m]\sum_{i=0}^{N_p-1} \alpha_i \exp\left(\frac{-j2\pi(\mathcal{S}(m)-N/2)\tau_i}{N}\right) + W[m] \\ &= X[m]H[m] + W[m], \end{aligned} \tag{2.46}$$

where $H[m]$ is the multipath channel's frequency response at sub-carrier $\mathcal{S}(m)$, given as

$$H[m] = \sum_{i=0}^{N_p-1} \alpha_i \exp\left(\frac{-j2\pi(\mathcal{S}(m)-N/2)\tau_i}{N}\right). \tag{2.47}$$

With the input/output model of (2.46) and assuming the transmitted QAM symbols have unit average power, i.e., $\mathbb{E}\{|X[m]|^2\} = 1$, the signal-to-noise ratio (SNR) of the received signal is defined as

$$\text{SNR} = \frac{\mathbb{E}\{|X[m]H[m]|^2\}}{\mathbb{E}\{|W[m]|^2\}} = \frac{\sum_{i=0}^{N_p-1}|\alpha_i|^2}{\sigma_w^2}. \tag{2.48}$$

If the multipath channel's frequency response is perfectly known at the receiver, data recovery can be done with a simple single-tap equalizer, given as

$$\widehat{X}[m] = Y[m]C[m], \quad m = 0, 1, \ldots, M-1, \tag{2.49}$$

where $C[m]$ are complex coefficients that attempt to invert the channel response. The values for $C[m]$ can be obtained based on either the zero forcing (ZF) criterion or the minimum mean square error (MMSE) criterion [C2.27]. The ZF equalizer simply inverts the channel, making

$$C[m] = \frac{1}{H[m]}. \tag{2.50}$$

While simple, the ZF equalizer suffers from noise enhancement effect. As an alternative, the

MMSE equalizer is more robust in the presence of noise and is given as

$$C[m] = \frac{H^*[m]}{|H[m]|^2 + \mathrm{SNR}^{-1}}. \tag{2.51}$$

It should be noted that for either ZF or MMSE equalizer, the equalizer coefficient $C[m]$ at the m^{th} data sub-carrier only depends on the channel frequency response $H[m]$ at that frequency alone. This characteristic differs from a time-domain equalizer, in which each tap coefficient is a function of the entire channel impulse response. Therefore, OFDMA has a significant advantage over SC-QAM in terms of equalization complexity, provided that the channel frequency response is known or can be estimated. Furthermore, since the channel resources given to each CM can be dynamically allocated in DOCSIS 3.1, a channel estimator is required to obtain the frequency response over the *entire* channel bandwidth, which is ideally given as

$$F[k] = \sum_{i=0}^{N_p-1} \alpha_i \exp\left(\frac{-j2\pi(k - N/2)\tau_i}{N}\right), \quad k = 0, 1, \ldots, N-1. \tag{2.52}$$

In general, for an OFDMA system, the channel estimator needs to estimate $F[k]$, $k = 0, 1, \ldots, N-1$ based on the known values of $X[m]$, i.e., pilot sub-carriers, and the observed values of $Y[m]$. Since $F[k]$ is a function of $2N_p$ unknown parameters $\left\{\alpha_i, \tau_i\right\}_{i=0}^{N_p-1}$, an estimate of $F[k]$ is obtained from estimates of these $2N_p$ unknown parameters. Conventional methods estimate M values of $H[m]$ and then interpolate between them to get the entire frequency response, $F[k]$ [C2.28]. A contribution of this thesis, which is presented in Chapter 5, is a novel method to obtain $2N_p$ values of $\left\{\alpha_i, \tau_i\right\}_{i=0}^{N_p-1}$. It is demonstrated that, as long as $2N_p \ll M$, estimating $\left\{\alpha_i, \tau_i\right\}_{i=0}^{N_p-1}$ directly provides a better estimate of $F[k]$, which is required to perform frequency-domain equalization. Furthermore, it is pointed out that, the time-domain channel parameters $\left\{\alpha_i, \tau_i\right\}_{i=0}^{N_p-1}$ are required for the Zero-CP OFDM scheme developed in Chapter 6.

2.3 Summary and Outlook

In this chapter, two digital communication systems used in cable networks, which are SC-QAM and OFDM/OFDMA, were discussed. Aside from explaining the key theoretical concepts of each system, the imperfection factors that cause signal distortions were discussed in detail. Furthermore, the fundamental difference between the two systems was explained. In particular, different approaches that SC-QAM and OFDM/OFDMA systems have taken to mitigate the distortions and provide multiple access were carefully explained.

Since upgraded cable systems must maintain the backward-compatibility functions, Chapter 3 investigates an efficient design for pulse shaping filters, which is a crucial part in a SC-QAM transceiver. In Chapter 4, an algorithm to estimate the timing offset in a SC-QAM receiver is proposed. This algorithm is also used as an important signal processing part of the OFDM/OFDMA channel estimator introduced in Chapter 5. Furthermore, the estimated channel parameters, which are obtained by using the algorithm introduced in Chapter 5, can be used to mitigate ISI in OFDM systems that do not employ CP (i.e., Zero-CP). The proposed Zero-CP OFDM system is investigated in detail in Chapter 6.

References

[C2.1] Cable Television Laboratories, Inc., "Downstream RF Interface Specification," Nov. 2011.

[C2.2] H. H. Nguyen and E. Shwedyk, *A First Course in Digital Communications*. Cambridge University Press, 2009.

[C2.3] J. Proakis, *Digital Communications*. McGraw-Hill, 4 ed., 2001.

[C2.4] B. Berscheid, *FPGA-Based DOCSIS Upstream Demodulation*. PhD thesis, University of Saskatchewan, 2011.

[C2.5] F. M. Gardner, "Interpolation in digital modems. I. Fundamentals," *IEEE Trans. Commun.*, vol. 41, pp. 501–507, Mar. 1993.

[C2.6] L. Erup, F. M. Gardner, and R. A. Harris, "Interpolation in digital modems. II. Implementation and performance," *IEEE Trans. Commun.*, vol. 41, pp. 998–1008, June 1993.

[C2.7] E. R. Pelet, *Synchronization In All-Digital QAM Receivers*. PhD thesis, University of Saskatchewan, 2009.

[C2.8] F. Gardner, "Hangup in phase-lock loops," *IEEE Trans. Commun.*, vol. 25, pp. 1210–1214, Oct. 1977.

[C2.9] J. Wang and J. Speidel, "Packet acquisition in upstream transmission of the DOCSIS standard," *IEEE Trans. on Broadcasting.*, vol. 49, pp. 26–31, Mar. 2003.

[C2.10] E. Brigant and A. Mammela, "Adaptive threshold control scheme for packet acquisition," *IEEE Trans. Commun.*, vol. 46, pp. 1580–1582, Dec. 1998.

[C2.11] P. Stoica and R. Moses, *Spectral Analysis of Signals*. Pearson Prentice Hall, 2005.

[C2.12] M. Soltanalian and P. Stoica, "Computational design of sequences with good correlation properties," *IEEE Trans. Signal Process.*, vol. 60, pp. 2180–2193, May 2012.

[C2.13] R. Boucher and J. C. Hassab, "Analysis of discrete implementation of generalized cross correlator," *IEEE Trans. Acoustics, Speech and Signal Proc.*, vol. 29, pp. 609–611, June 1981.

[C2.14] K. Fyhn, M. Duarte, and S. Jensen, "Compressive parameter estimation for sparse translation-invariant signals using polar interpolation," *IEEE Trans. Signal Process.*, vol. 63, pp. 870–881, Feb. 2015.

[C2.15] V. Nguyen, "A low complexity parameter estimation technique for LFMCW signals," *IEEE Trans. Aerospace and Electronic Systems*, vol. 50, pp. 2554–2563, Oct. 2014.

[C2.16] A. Grennberg and M. Sandell, "Estimation of subsample time delay differences in narrowband ultrasonic echoes using the Hilbert transform correlation," *IEEE Trans. Ultrasonics, Ferroelectrics, and Frequency Control*, vol. 41, pp. 588–595, Sept. 1994.

[C2.17] Y. X. Yuan and J. Salt, "Range and depth estimation using a vertical array in a correlated multipath environment," *IEEE J. Oceanic Engineering*, vol. 18, pp. 500 – 507, Oct. 1993.

[C2.18] M. Simaan, "A frequency-domain method for time-shift estimation and alignment of seismic signals," *IEEE Trans. Geoscience and Remote Sensing*, vol. GE-23, pp. 132 – 138, Mar. 1985.

[C2.19] T. T. Nguyen, E. Salt, B. Berscheid, and H. H. Nguyen, "Digital interpolating peak locator," in *Proc. IEEE Int. Symp. Industrial Electronics.*, June 2016.

[C2.20] B. Farhang-Boroujeny, *Adaptive Filters: Theory and Applications*. Wiley, 2013.

[C2.21] Cable Television Laboratories, Inc., "DOCSIS 3.1 physical layer specification," Oct. 2013.

[C2.22] A. Nasir, S. Durrani, and R. Kennedy, "Performance of coarse and fine timing synchronization in OFDM receivers," in *IEEE Int. Conf. on Future Computer and Commun.*, vol. 2, pp. 412–416, May 2010.

[C2.23] T. Schmidl and D. Cox, "Robust frequency and timing synchronization for OFDM," *IEEE Trans. Commun.*, vol. 45, pp. 1613–1621, Dec. 1997.

[C2.24] M. Morelli, "Timing and frequency synchronization for the uplink of an OFDMA system," *IEEE Trans. Commun.*, vol. 52, pp. 166–166, Mar. 2004.

[C2.25] H. Minn, V. Bhargava, and K. Letaief, "A robust timing and frequency synchronization for OFDM systems," *IEEE Trans. on Wireless Commun.*, vol. 2, pp. 822–839, July 2003.

[C2.26] K. Shi and E. Serpedin, "Coarse frame and carrier synchronization of OFDM systems: a new metric and comparison," *IEEE Trans. on Wireless Commun.*, vol. 3, pp. 1271–1284, July 2004.

[C2.27] H. Sari, G. Karam, and I. Jeanclaud, "Frequency-domain equalization of mobile radio and terrestrial broadcast channels," in *Proc. IEEE Global Telecommun. Conf.*, pp. 1–5, Nov. 1994.

[C2.28] A. Khan, V. Jeoti, and M. Zakariya, "Improved pilot-based LS and MMSE channel estimation using DFT for DVB-T OFDM systems," in *IEEE Symp. on Wireless Tech. and Applications*, pp. 120–124, Sept. 2013.

3. Designing Pulse Shaping Filters for DOCSIS Systems

Published as:

Tung T. Nguyen, J. Eric Salt, Ha H. Nguyen and Brian Berscheid, "Optimizing pulse shaping filter for DOCSIS systems," *IEEE Transactions on Broadcasting*, vol. 62, pp. 470-481, Jun. 2016.

As discussed in the previous chapter, it is impossible in practice to implement a filter that has a frequency response exactly as shown in Fig. 2.4. Practical filters are obtained by truncating the ideal impulse response to yield a finite number of filter coefficients. Designers typically attempt to minimize the number of filter coefficients in order to reduce the implementation cost. Due to the restriction on the filter order and the limitations of finite-precision arithmetics, digital filters in practice have imperfections in the pass-band, transition-band and portions of the stop-band. Imperfections in the pass-band and transition-band generate ISI, which can be mitigated by an equalizer in the receiver. However, a non-zero stop-band results in out-of-band power, causing interference to adjacent channels.

The manuscript in this chapter first studies different approaches to design a practical pulse shaping filter. Then a novel design is proposed, which performs optimization on a hybrid parameterization of the IIR filter's transfer function. The design yields a low-cost pulse shaping filter that meets the DOCSIS 3.0 out-of-band requirement while introducing a minimal amount of ISI.

The main contribution to this manuscript comes from the student (first author), while the three co-supervisors provide equal supervision effort.

Optimizing Pulse Shaping Filter for DOCSIS Systems

Tung T. Nguyen, *Student Member, IEEE*, Eric Salt, *Member, IEEE*,
Ha H. Nguyen, *Senior Member, IEEE* and Brian Berscheid, *Member, IEEE*

Abstract

This paper proposes a cost efficient nearly linear phase approximation to a SRRC pulse shaping filter that satisfies the out-of-band spectral constraints of DOCSIS down-stream channels. A nearly linear phase filter structure is converted to a SRRC filter using a weighted and sampled least-squares criterion to fit the magnitude and phase responses. To ensure stability, the search for optimum coefficients is constrained using the Steigliz-McBride (SM) and Gauss-Newton (GN) methods, which unfortunately also eliminates sets of stable coefficients, one of which could be and probably is the optimum. To expand the sets of coefficients that produce stable filters in the SM and GN methods, the transfer function is parameterized in a special way. The effectiveness of the proposed filter is verified and compared with other approaches.

Index terms

Pulse shaping filter, square-root raised cosine filter, DOCSIS, inter-symbol interference, windowing.

3.1 Introduction

When a new communication standard is implemented, the inherited backward compatible functions can be redesigned to take advantage of the latest technology and algorithms. Of interest here is the pulse shaping filter, which is the Nyquist filter located in the transmitter,

used in DOCSIS single carrier QAM. Improving the performance of Nyquist filters in terms of reducing ISI is still an active research area [C3.1, C3.2, C3.3, C3.4]. However, DOCSIS pulse shaping filters must not only have low ISI, they must also stringently suppress out-of-band emission to avoid adjacent channel interference. Since the DOCSIS standards dictate Square Root Raised Cosine (SRRC) Nyquist filters, of interest here are SRRC pulse shaping filters with low ISI and low out-of-band emissions. The ideal pulse shaping filter is an infinite-length Square-Root Raised Cosine (SRRC) filter with complex frequency-domain response described by:

$$D(\omega) = \begin{cases} \mathrm{e}^{-j\varphi\omega}, & \text{for } |\omega| \leq \frac{\pi(1-\beta)}{L} \\ \mathrm{e}^{-j\varphi\omega}\sqrt{\frac{1}{2}\left[1+\cos\left(\frac{\pi}{2\beta}\left(\frac{|\omega|L}{\pi}-1+\beta\right)\right)\right]}, & \text{for } \frac{\pi(1-\beta)}{L} < |\omega| \leq \frac{\pi(1+\beta)}{L} \\ 0, & \text{otherwise,} \end{cases} \tag{3.1}$$

where ω is the frequency in radians/sample and β, L, φ are the filter's roll-off factor, ratio of sampling rate to symbol rate and phase delay, respectively.

The SRRC filter can be approximated by either a finite impulse response (FIR) or an infinite impulse response (IIR) filter. While FIR approximations have been widely used, they require large hardware resources (in terms of arithmetic circuits) to meet the out-of-channel portion of the DOCSIS spectral mask requirements. The alternative is a recursive IIR structure.

The main thrust of the paper is to improve the implementation efficiency of the SRRC pulse shaping filter for legacy single carrier down-stream QAM channels in the implementation of DOCSIS 3.1 and beyond. The specific objective is to provide a trade-off between ISI reduction and filter cost under the constraint the filter meets the DOCSIS 3.1 out-of-channel spectral mask. The filter derived from the approach proposed in this paper will be discussed and compared with filters designed with other techniques.

3.2 Review of Relevant Filter Design Techniques

3.2.1 FIR approach

Windowing technique

The simplest method is to obtain the impulse response of the SRRC filter by taking the inverse discrete-time Fourier transform of (3.1). The impulse response has a "sinc-like" shape, therefore it clearly cannot be implemented in practice, unless the "sinc-like" function is truncated on both sides. As such, the coefficients for a causal FIR filter are obtained by taking the N_F values closest to $n = 0$. The result is the sample-space impulse response given by

$$h(n) = \begin{cases} \frac{1}{L}\left(1-\beta+\frac{4\beta}{\pi}\right), & \text{for } n = \frac{N_F-1}{2} \\ \frac{\beta}{\sqrt{2}L}\left[\left(1+\frac{2}{\pi}\right)\sin\left(\frac{\pi}{4\beta}\right)+\left(1-\frac{2}{\pi}\cos\left(\frac{\pi}{4\beta}\right)\right)\right], & \text{for } n = \frac{N_F-1}{2} \pm \frac{L}{4\beta} \\ \dfrac{\sin\left(\frac{\pi(1-\beta)(n-\hat{\varphi})}{L}\right)+\frac{4\beta(n-\hat{\varphi})}{L}\cos\left(\frac{\pi(1+\beta)(n-\hat{\varphi})}{L}\right)}{\pi(n-\hat{\varphi})\left[1-\left(\frac{4\beta(n-\hat{\varphi})}{L}\right)^2\right]}, & \text{for } \begin{array}{l} 0 \le n \le N_F-1, \\ n \neq \frac{N_F-1}{2}, n \neq \frac{N_F-1}{2} \pm \frac{L}{4\beta} \end{array} \\ 0, & \text{otherwise.} \end{cases} \tag{3.2}$$

where $\hat{\varphi} = \frac{N_F-1}{2}$ is delay in samples of the truncated FIR filter.

Fig. 3.1 presents the impulse response of a truncated SRRC filter as well as the magnitude responses of ideal and truncated SRRC filters. The filter parameters are $\beta = 0.12$ and $L = 4$, with the length of the truncated filter being $N_F = 41$.

As can be seen in Fig. 3.1, truncating the impulse response introduces ripple in both the pass band and stop band of the magnitude response. To suppress the stop band ripple, the truncated "sinc-like" function must be tapered to force its extremity to approach zero. This can be done by multiplying the truncated impulse response by a window function to get the windowed impulse response:

$$h_w(n) = h(n)w(n), \quad n = 0, 1, \ldots, N_F - 1, \tag{3.3}$$

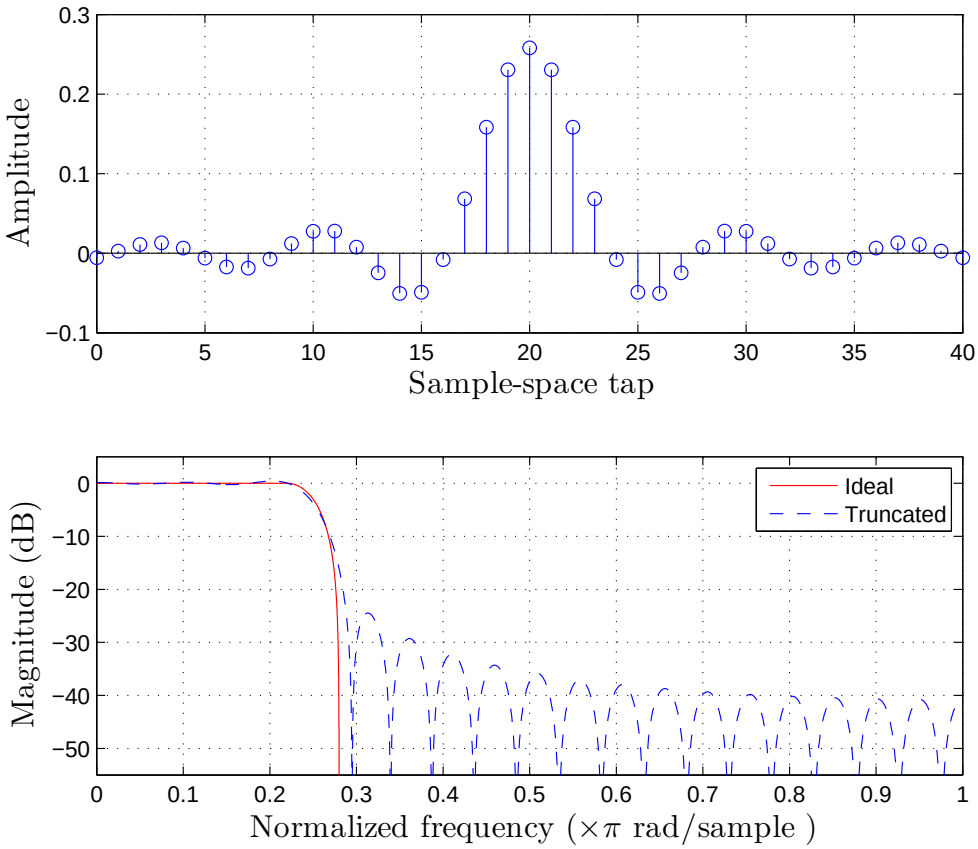

Figure 3.1 Impulse response and magnitude response of a length 41 truncated SRRC filter.

where $w(n)$ is the window function. The main source of signal distortion created by windowing is the widening of the transition band. The widening can be reduced by increasing the length of the filter or by pre-compensating by using a lower roll-off factor. There are many well-known window functions, such as Blackman, Hamming, Kaiser, Gaussian, Tukey, etc., each with its own stop band ripple rejection and transition band distortion characteristics. For an extensive comparison among various window functions, the interested reader is referred to [C3.5]. An appealing window is the Kaiser window, whose stop band ripple and transition band distortion characteristics are controlled by a single parameter. The Kaiser window function is given by

$$w(n) = \frac{I_0\left(\pi\alpha\sqrt{1-\left(\frac{2n}{N}-1\right)^2}\right)}{I_0(\pi\alpha)}, \quad n = 0, 1, \ldots, N_F - 1, \tag{3.4}$$

where $I_0(\cdot)$ is the zeroth-order modified Bessel function of the first kind, and α is the parameter that determines the shape of the window and balances the transition band distortion and stop band ripple suppression trade off. The Kaiser window method that minimizes the ISI for a filter of length N_F that satisfies the out-of-band portion of the DOCSIS specified spectral mask works as follows:

1. Choose the filter length N_F.
2. Set the roll off factor β to its nominal value as specified in the DOCSIS standard (0.18 for 64-QAM channels, or 0.12 for 256-QAM channels).
3. Decrease β by a small amount.
4. Set the Kaiser window parameter, α, to 0 and steadily increase it until the stop band response satisfies the out-of-channel portion of the spectral mask specified in DOCSIS.
5. Measure and record the values of α, β and ISI.
6. Reduce β and repeat steps 3 to 5 to minimize the ISI.
7. Choose the set α, β that produces minimum ISI.

fred harris' technique

harris approximates the SRRC filter with a linear phase 3-band minimax filter [C3.6]. In addition to specifying the pass band and stop band, a very narrow third band is specified in transition region at the 3dB-down frequency. harris designs the filter with the Parks McClellan algorithm using the following parameter vectors

$$\begin{array}{lllllll} \text{Frequency (radians/sample):} & \left[0 \right. & \omega_p/L & \pi/L & \pi/L & \omega_s/L & \left. \pi \right] \\ \text{Gain:} & [1 & 1 & \sqrt{2}/2 & \sqrt{2}/2 & 0 & 0] \\ \text{Weight:} & [2.4535 & & 1 & & 1 &]. \end{array}$$

where ω_p and ω_s are the pass band and stop band corner frequencies, given by

$$\omega_p = \pi(1-\beta), \quad \text{and} \quad \omega_s = \pi(1+\beta). \tag{3.5}$$

The first coefficient in the weight vector is manually adjusted to minimize the ISI level when the matched filter is the ideal SRRC filter truncated to the same length.

The filter created in this way has an unwanted spectral bump at the edge of the pass band, which is believed to be a major contributor to the ISI. To suppress this bump, harris suggests adjusting the coefficients in the frequency vector from ω_p to $\epsilon_1\omega_p$, and also fine tuning the stop band edge from ω_s to $\epsilon_2\omega_s$, where the values of ϵ_1 and ϵ_2 are slightly more than 1. The new target frequency vector is then given as

$$\text{Frequency (radians/sample):} \quad \left[0 \quad \epsilon_1\omega_p/L \quad \pi/L \quad \pi/L \quad \epsilon_2\omega_s/L \quad \pi \right].$$

The procedure is performed by first finding parameter ϵ_1 that minimize the ISI and then proceeding to find ϵ_2 with the same goal.

The problem with harris' approach is that it does not consider the out-of-channel emission and therefore harris' filter will not meet the out-of-channel portion of the spectral mask unless a relatively large filter order is chosen.

3.2.2 Nearly linear-phase IIR filter approximation

The design task is to find a stable IIR filter that has a system function of the form:

$$H(z) = \frac{b_0 + b_1 z^{-1} + \ldots + b_m z^{-m}}{1 + a_1 z^{-1} + \ldots + a_n z^{-n}}. \tag{3.6}$$

where b_i and a_i are real coefficients and m is the order of the numerator polynomial and n is the order of the denominator polynomial. The corresponding filter's frequency response is

$$H(\mathrm{e}^{j\omega}) = \frac{b(\omega)}{a(\omega)} = \frac{\mathbf{b}^T \mathbf{e}_{0m}(\omega)}{1 + \mathbf{a}^T \mathbf{e}_{1n}(\omega)}, \tag{3.7}$$

where $b(\omega)$ and $a(\omega)$ are the frequency responses on the numerator and denominator polynomials in (3.6) and the superscript T indicates the transpose of a vector or matrix. The numerator and denominator coefficients are represented by vectors $\mathbf{b} = [b_0, b_1, \ldots, b_m]^T$ and $\mathbf{a} = [a_1, \ldots, a_n]^T$ respectively. In addition, $\{\mathbf{e}_{lk}(\omega), \text{ for } l < k\}$, is defined as

$$\mathbf{e}_{lk}(\omega) = [\mathrm{e}^{-j\omega l}, \mathrm{e}^{-j\omega(l+1)}, \ldots, \mathrm{e}^{-j\omega k}]^T. \tag{3.8}$$

It is convenient to define the frequency response $H(\mathrm{e}^{j\omega})$ as a complex function of real parameters $\boldsymbol{X} = \begin{bmatrix} \mathbf{a} \\ \mathbf{b} \end{bmatrix}$ and refer to the frequency response as $H(e^{j\omega}; \boldsymbol{X})$. Furthermore, it can be seen that $H(e^{j\omega}; \boldsymbol{X})$ is a non-linear function of ω and has a non-linear dependency on parameters $\boldsymbol{X} = [a_1, \ldots, a_n, b_0, b_1, \ldots, b_m]^T$. When $H(e^{j\omega}; \boldsymbol{X})$ is designed to approximate the ideal frequency response $D(\omega)$ in (3.1), a weighted squared error is given by $J_i(\boldsymbol{X}) = W_i \left| D(\omega_i) - H(e^{j\omega_i}; \boldsymbol{X}) \right|^2$, where W_i is a non-negative weighting coefficient associated with frequency $\omega_i \in [0, \pi]$.

The goal is to find the parameter vector $\boldsymbol{X}$ that minimizes the sum of the weighted least square errors at frequencies $\omega_1, \omega_2, \ldots, \omega_M$ under the constraint the parameter $\boldsymbol{X}$ yields a stable filter. Since the total squared error is given by

$$J(\boldsymbol{X}) = \sum_{i=1}^{M} J_i(\boldsymbol{X}) = \sum_{i=1}^{M} W_i \left| D(\omega_i) - H(e^{j\omega_i}; \boldsymbol{X}) \right|^2, \tag{3.9}$$

finding the value $\boldsymbol{X} = \boldsymbol{X}_{\min}$ that minimizes $J(\boldsymbol{X})$ is difficult due to the non-linear nature of $J(\boldsymbol{X})$. However, the Steiglitz-McBride and Gauss-Newton non-linear iterative optimization approaches can be used to find $\boldsymbol{X}$.

Steiglitz-McBride (SM) technique

Theoretically, it is possible for the SM method [C3.7, C3.8, C3.9] to find the vector $\boldsymbol{X}$ that minimizes the objective function defined in (3.9). Practically, it finds a good estimate of that vector.

The SM method finds a sequence of vectors that minimize a carefully designed sequence of objective functions. The objective functions are denoted $J_{SM\_1}(\boldsymbol{X}), J_{SM\_2}(\boldsymbol{X}), \ldots$ and $\boldsymbol{X}_{SM\_min\_1}, \boldsymbol{X}_{SM\_min\_2}, \ldots$ are the vectors that minimize them. The SM sequence of objective functions are such that

$$\lim_{k\to\infty} \boldsymbol{X}_{SM\_min\_k} = \boldsymbol{X}_{\min}, \tag{3.10}$$

where $\boldsymbol{X}_{\min}$ is the vector that minimizes $J(\boldsymbol{X})$.

The SM objective functions are obtained by reformatting and rearranging the expression for $J(\boldsymbol{X})$ given by (3.9). The reformatting is done by substituting $\frac{b(\omega_i,\boldsymbol{X})}{a(\omega_i,\boldsymbol{X})}$ for $H(e^{j\omega_i};\boldsymbol{X})$ into (3.9). The rearranging is factoring $a(\omega_i,\boldsymbol{X})$ outside the absolute value operator. The reformatted, rearranged expression for $J(\boldsymbol{X})$ is:

$$J(\boldsymbol{X}) = \sum_{i=1}^{M} \frac{W_i}{|a(\omega_i;\boldsymbol{X})|^2} \left|D(\omega_i)a(\omega_i;\boldsymbol{X}) - b(\omega_i;\boldsymbol{X})\right|^2. \tag{3.11}$$

The sequence of SM objective functions are successively approximating $|a(\omega_i;\boldsymbol{X})|^2$ with a set of $M+1$ constants that converge to the true values. The constants used for the first objective function is obtained by guessing vector $\boldsymbol{X}_{\min}$ to be $\boldsymbol{X}_0$ and substituting it into $|a(\omega_i;\boldsymbol{X})|^2$. This produces

$$J_{SM\_1}(\boldsymbol{X}) = \sum_{i=1}^{M} \frac{W_i}{|a(\omega_i;\boldsymbol{X}_0)|^2} \left|D(\omega_i)a(\omega_i;\boldsymbol{X}) - b(\omega_i;\boldsymbol{X})\right|^2, \tag{3.12}$$

where $|a(\omega_i; \boldsymbol{X}_0)|^2, i = 0, 1, \ldots, M$ are the constants for iteration 1 and $\boldsymbol{X}_0$ is the initial guess for $\boldsymbol{X}_{\min}$. Unlike $J(\boldsymbol{X})$, $J_{SM\_1}(\boldsymbol{X})$ is quadratic in $\boldsymbol{X}$, which means $\boldsymbol{X}_{SM\_min\_1}$ can be found by a standard quadratic search algorithm.

In general, the $(k+1)^{\text{th}}$ SM objective function is the quadratic function of $\boldsymbol{X}$, given by

$$J_{SM\_k+1}(\boldsymbol{X}) = \sum_{i=1}^{M} \frac{W_i}{|a(\omega_i; \boldsymbol{X}_k)|^2} |D(\omega_i)a(\omega_i; \boldsymbol{X}) - b(\omega_i; \boldsymbol{X})|^2 \tag{3.13}$$

where $\boldsymbol{X}_k,\ k > 0$ is the k^{th} estimate of $\boldsymbol{X}_{\min}$, given by

$$\boldsymbol{X}_k = \mu \boldsymbol{X}_{SM\_min\_k} + (1 - \mu)\boldsymbol{X}_{k-1}, \tag{3.14}$$

where μ is a real number less than 1 used to damp the sequences $\boldsymbol{X}_k$.

The number of SM objective functions that need to be solved to get a good estimate of $\boldsymbol{X}_{\min}$ depends on the order of the filter $H(e^{j\omega}; \boldsymbol{X})$ and the step size μ. Making μ small ensures convergence to $\boldsymbol{X}_{\min}$, but increases the number of objective functions that must be solved. Typically μ is 0.2 or less.

In most cases $\boldsymbol{X}_{\min}$ produces an unstable filter making the algorithm useless. To ensure a useful result from the SM algorithm the searches for $\boldsymbol{X}_{SM\_min\_k},\ k = 1, 2, \ldots,$ must be constrained to the set $\mathcal{S}_{ST}$ which contains all values of $\boldsymbol{X}$ that produce a stable filter. Constraining the poles to be inside the unit circle, which is the ideal constraint, cannot be incorporated in the search algorithm. A constraint that can be incorporated into the search is Positive Realness (PR) [C3.8, C3.10], which limits $\boldsymbol{X}$ to the set $\mathcal{S}_{PR} = \{\boldsymbol{X} :\ \Re\{a(\omega; \boldsymbol{X})\} > 0, \forall \omega \in [0, \pi]\}$.

The set $\mathcal{S}_{PR}$ is a subset of the set that generates a stable filter, i.e. $\mathcal{S}_{PR} \subset \mathcal{S}_{ST}$. Therefore, the value of $\boldsymbol{X}_{SM\_min\_k}$ obtained using the PR constraint may be sub-optimum.

Another implementable constraint that can be placed on the search for the minimum is based on Rouche's theorem [C3.11]. This constraint limits the solution to set $\mathcal{S}_{RT}$ which ensures a stable filter, but $\mathcal{S}_{RT}$ is smaller in size than $\mathcal{S}_{PR}$. Furthermore, it was shown in

[C3.8] that filters obtained with the PR constraint have less mean squared error than those obtained with Rouche's method. Therefore the PR constraint is used with the SM method in this paper.

The issue with using the PR constraint is that solution can have sharp peaks in magnitude response creating pockets of large mean square error that is not accounted for in the sampling points used in $J(\boldsymbol{X})$. The optimization process places poles near the unit circle between two sampling points, e.g. ω_k and ω_{k+1}. Solutions without these sharp peaks in the magnitude response are obtained by modifying the PR constraint to limit the largest radius of a pole to less than $1-\eta$ in magnitude. This is done using the inequality $\{\Re\{a(\omega;\boldsymbol{X})\} > \eta,\ \forall\omega \in [0,\pi]\}$, where a good value for η is in the range of 0.01 to 0.05.

Gauss-Newton (GN) method

The GN algorithm [C3.11, C3.8, C3.12] is an iterative method based on the first-order Taylor approximation:

$$H(e^{j\omega};\boldsymbol{X}_k) \approx H(e^{j\omega};\boldsymbol{X}_{k-1}) + \nabla_x H(e^{j\omega};\boldsymbol{X}_{k-1})\cdot\boldsymbol{\delta}, \quad k = 1,2,\ldots, \tag{3.15}$$

where $\boldsymbol{X}_0$ is the initial guess, $\boldsymbol{\delta} = \boldsymbol{X}_k - \boldsymbol{X}_{k-1}$ and $\nabla_x H$ is the gradient vector of $H(e^{j\omega};\boldsymbol{X})$ with respect to $\boldsymbol{X}$. The vector $\boldsymbol{X}_{k-1}$ contains the coefficients of a stable filter obtained from the $(k-1)^{\text{th}}$ iteration, where the k^{th} iteration finds $\boldsymbol{\delta}$ by solving

$$\underset{\boldsymbol{\delta}}{\text{Minimize}} \quad J_{GN\_k}(\boldsymbol{\delta}) = \sum_{i=1}^{M} W_i \left| D(\omega) - H(e^{j\omega};\boldsymbol{X}_{k-1}) - \nabla_x H(e^{j\omega};\boldsymbol{X}_{k-1})\cdot\boldsymbol{\delta} \right|^2 \tag{3.16}$$

$$\text{Subject to} \qquad \boldsymbol{\delta} + \boldsymbol{X}_{k-1} \in \mathcal{S}_{ST}. \tag{3.17}$$

The k^{th} iteration coefficients are given by $\boldsymbol{X}_k = \boldsymbol{X}_{k-1} + \boldsymbol{\delta}$.

Unfortunately, practical methods of constraining $\boldsymbol{X}_{k-1} + \boldsymbol{\delta}$ restricts the solution space to a subset of $\mathcal{S}_{ST}$. Whether or not this subset contains the optimum solution or a near-optimum solution depends not only on the method of constraint but also on the way the filter's system function is parameterized.

- *Parameterizing the filter's transfer function in radii and angles form*:
  Similar to the approach introduced in [C3.12], one can represent the transfer function in the form

$$H(z) = \chi \frac{\prod_{j=1}^{R}(1 - r_j z^{-1}) \prod_{i=R+1}^{R+Z}(1 - 2r_i \cos(\theta_i) z^{-1} + r_i^2 z^{-2})}{\prod_{j=1}^{P}(1 - p_j z^{-1}) \prod_{i=P+1}^{P+Q}(1 - 2p_i \cos(\phi_i) z^{-1} + p_i^2 z^{-2})}, \tag{3.18}$$

  where χ is the scaling factor. The scalars R,Z,P,Q are the numbers of real zeros, complex zeros, real poles and complex poles, respectively. With the form of (3.18), a stable filter is ensured by constraining the pole radius, i.e., forcing $p_j, p_i \leq \rho$ where ρ is a real positive number less than 1.

- *Paramterizing the filter's transfer function in polynomial form*:

$$H(z) = \frac{b_0 + b_1 z^{-1} + \ldots + b_m z^{-m}}{1 + a_1 z^{-1} + \ldots + a_n z^{-n}} \tag{3.19}$$

  With this representation, one can use the PR condition to force a stable solution. The PR constraint at the k^{th} iteration limits $\boldsymbol{\delta}$ to the set $\{\boldsymbol{\delta} : \Re\{a(\omega; \boldsymbol{X}_{k-1} + \boldsymbol{\delta})\} > 0,\ \forall \omega \in [0, \pi]\}$.

  Another approach to constrain the pole radii is to exploit Rouche's theorem [C3.13], which states: if $f(z)$ and $g(z)$ are analytic inside and on a closed contour C, and $|g(z)| < |f(z)|$ on C, then $f(z) + g(z)$ has the same number of zeros inside C. Let the contour C be a circle with radius ρ centered at the origin of the complex plane. Then the denominator polynomial on the contour C can be expressed as

$$A(z) = 1 + a_1 z^{-1} + a_2 z^{-2} + \ldots + a_n z^{-n}\Big|_{z=\rho e^{j\omega}}, \quad \omega \in [0, \pi]. \tag{3.20}$$

  According to the Rouche's theorem, if the initial denominator polynomial $A_{k-1}(z) = 1 + a_{k-1,1} z^{-1} + a_{k-1,2} z^{-2} + \ldots + a_{k-1,n} z^{-n}$ has all of its zeros inside C, then the updated denominator polynomial, given as

$$A_k(z) = A_{k-1}(z) + \mu \Delta(z) \tag{3.21}$$

where $\Delta(z)$ is the function defined on domain C as

$$\Delta(z) = \delta_1 z^{-1} + \delta_2 z^{-2} + \ldots + \delta_n z^{-n}\Big|_{z=\rho e^{j\omega}}, \quad \omega \in [0, \pi] \tag{3.22}$$

with $\delta_i, i = 1, 2, \ldots, n$ are elements to update the denominator coefficients $a_i, i = 1, 2, \ldots, n$. The filter is stable if the update function (3.21) satisfies $|\Delta(z)| \leq |A_{k-1}(z)|, \forall z \in C$. Thus the optimization problem becomes:

$$\underset{\boldsymbol{\delta}}{\text{Minimize}} \qquad J_{GN\_k}(\boldsymbol{\delta}) \tag{3.23}$$

$$\text{Subject to} \quad |\Delta(\rho e^{j\hat{\omega}})| \leq \left|A_{k-1}(\rho e^{j\hat{\omega}})\right|, \quad \forall \hat{\omega} \in [0, \pi] \tag{3.24}$$

which is solvable by the *multiple exchange algorithm* proposed in [C3.11].

While the PR and the RT conditions are more conservative than having a direct constraint on the poles' radius, the polynomial representation of the transfer function $H(z)$ has a better convergence characteristic. In general, there is clearly a tradeoff between parameterizations in radii-angles form and polynomial form.

3.3 New Approach For Designing a Stable SRRC Filter

3.3.1 Hybrid parametrization and the stability constraint

Conventionally the transfer functions of IIR filters are parameterized in either radii-and-angles form or polynomial form. In this section, the transfer function is expressed as a hybrid with the numerator in polynomial form and the denominator in radii-and-angles form. The hybrid form is given by

$$H(z) = \frac{\sum_{i=0}^{m} b_i z^{-i}}{\prod_{j=1}^{P}(1 - p_j z^{-1}) \prod_{i=P+1}^{P+Q}(1 - 2p_i \cos(\phi_i) z^{-1} + p_i^2 z^{-2})}. \tag{3.25}$$

The parameters of this transfer function are organized within the parameter vector $\boldsymbol{X}$ as

$$\boldsymbol{X} = [p_1, p_2, \ldots, p_{P+Q}, \phi_{P+1}, \phi_{P+2}, \ldots, \phi_{P+Q}, b_0, b_1, \ldots, b_m]^T. \tag{3.26}$$

The form in (3.25) allows the poles to be constrained which is a necessary and sufficient condition for the GN method to produce a stable filter. The k^{th} iterative step still involves finding the $\boldsymbol{\delta}$ that minimizes $J_{GN\_k}(\boldsymbol{\delta})$, given by (3.16), but in this case subject to the constraint $p_i < \rho,\ 1 \leq i \leq P+Q$.

3.3.2 Putting the algorithm in quadratic form

Putting the algorithm in quadratic form begins by defining notation that simplifies the mathematical expressions involved. The gradient vector in the first-order Taylor approximation (3.15) is defined as

$$\nabla_x H(e^{j\omega}; \boldsymbol{X}_{k-1}) = \left[\frac{\partial H(e^{j\omega}; \boldsymbol{X}_{k-1})}{\partial p_1}, \ldots, \quad \frac{\partial H(e^{j\omega}; \boldsymbol{X}_{k-1})}{\partial p_{_{P+Q}}}, \quad \frac{\partial H(e^{j\omega}; \boldsymbol{X}_{k-1})}{\partial \phi_{_{P+1}}}, \ldots, \right. \\ \left. \frac{\partial H(e^{j\omega}; \boldsymbol{X}_{k-1})}{\partial \phi_{_{P+Q}}}, \quad \frac{\partial H(e^{j\omega}; \boldsymbol{X}_{k-1})}{\partial b_0}, \ldots, \quad \frac{\partial H(e^{j\omega}; \boldsymbol{X}_{k-1})}{\partial b_m} \right]. \tag{3.27}$$

The complex error term $D(\omega_i) - H(e^{j\omega_i}; \boldsymbol{X}_{k-1})$ in (3.16) is defined by $E_{k-1,i}$. This allows

$J_{GN\_k}(\boldsymbol{\delta})$ to be expressed as

$$\begin{aligned}
J_{GN_k}(\boldsymbol{\delta}) &= \sum_{i=1}^{M} W_i \left| E_{k-1,i} - \nabla_x H(e^{j\omega_i}; \boldsymbol{X}_{k-1}) \cdot \boldsymbol{\delta} \right|^2 \\
&= \sum_{i=1}^{M} W_i \left(E_{k-1,i} - \nabla_x H(e^{j\omega_i}; \boldsymbol{X}_{k-1}) \cdot \boldsymbol{\delta} \right)^* \left(E_{k-1,i} - \nabla_x H(e^{j\omega_i}; \boldsymbol{X}_{k-1}) \cdot \boldsymbol{\delta} \right) \\
&= \sum_{i=1}^{M} W_i \left(E^*_{k-1,i} - \boldsymbol{\delta}^T \cdot \nabla_x H(e^{j\omega_i}; \boldsymbol{X}_{k-1})^{\mathcal{H}} \right) \left(E_{k-1,i} - \nabla_x H(e^{j\omega_i}; \boldsymbol{X}_{k-1}) \cdot \boldsymbol{\delta} \right) \\
&= \sum_{i=1}^{M} W_i \Big[|E_{k-1,i}|^2 - E_{k-1,i} \boldsymbol{\delta}^T \cdot \nabla_x H(e^{j\omega_i}; \boldsymbol{X}_{k-1})^{\mathcal{H}} - E^*_{k-1,i} \nabla_x H(e^{j\omega_i}; \boldsymbol{X}_{k-1}) \cdot \boldsymbol{\delta} \\
&\qquad + \boldsymbol{\delta}^T \cdot \nabla_x H(e^{j\omega_i}; \boldsymbol{X}_{k-1})^{\mathcal{H}} \nabla_x H(e^{j\omega_i}; \boldsymbol{X}_{k-1}) \cdot \boldsymbol{\delta} \Big] \\
&= \sum_{i=1}^{M} W_i |E_{k-1,i}|^2 - \sum_{i=1}^{M} 2\Re \left\{ W_i E^*_{k-1,i} \nabla_x H(e^{j\omega_i}; \boldsymbol{X}_{k-1}) \right\} \cdot \boldsymbol{\delta} \\
&\qquad + \boldsymbol{\delta}^T \cdot \sum_{i=1}^{M} \left[\nabla_x H(e^{j\omega_i}; \boldsymbol{X}_{k-1})^{\mathcal{H}} W_i \nabla_x H(e^{j\omega_i}; \boldsymbol{X}_{k-1}) \right] \cdot \boldsymbol{\delta},
\end{aligned} \tag{3.28}$$

where the supercript $\mathcal{H}$ denotes the complex transpose. To further simplify the expression, define $\boldsymbol{\Lambda}_{k-1}$, $\mathbf{f}_{k-1}$ and c as follows

$$\begin{aligned}
\boldsymbol{\Lambda}_{k-1} &= \sum_{i=1}^{M} \left[\nabla_x H(e^{j\omega_i}; \boldsymbol{X}_{k-1})^{\mathcal{H}} W_i \nabla_x H(e^{j\omega_i}; \boldsymbol{X}_{k-1}) \right] \\
\mathbf{f}_{k-1} &= \sum_{i=1}^{M} \Re \left\{ W_i E^*_{k-1,i} \nabla_x H(e^{j\omega_i}; \boldsymbol{X}_{k-1}) \right\} \\
c &= \sum_{i=1}^{M} W_i |E_{k-1,i}|^2 .
\end{aligned} \tag{3.29}$$

It should be noted that $\boldsymbol{\Lambda}_k$ is a Hermitian matrix, i.e. $\boldsymbol{\Lambda}_{k-1} = \boldsymbol{\Lambda}^{\mathcal{H}}_{k-1}$, therefore $\boldsymbol{\delta}^T \boldsymbol{\Lambda}_{k-1} \boldsymbol{\delta} = \boldsymbol{\delta}^T \mathbf{A}_{k-1} \boldsymbol{\delta}$, where $\mathbf{A}_{k-1} = \Re \{ \boldsymbol{\Lambda}_{k-1} \}$. Then substituting $\mathbf{A}_{k-1}, \mathbf{f}_{k-1}$ and c into (3.28) produces

$$J_{GN\_k}(\boldsymbol{\delta}) = \boldsymbol{\delta}^T \mathbf{A}_{k-1} \boldsymbol{\delta} + 2\mathbf{f}_{k-1} \boldsymbol{\delta} + c. \tag{3.30}$$

Finding the $\boldsymbol{\delta}$ that minimizes $J_{GN\_k}(\boldsymbol{\delta})$ is now a typical quadratic optimization problem that

can be solved by a typical quadratic programming solver, like the solver in Matlab®. Note that c is a constant and does not affect the result.

3.3.3 Improving the convergence characteristic

Upon obtaining $\boldsymbol{\delta}$, the new set of coefficients can be found as $\boldsymbol{X}_k = \boldsymbol{X}_{k-1} + \boldsymbol{\delta}$. If $\boldsymbol{\delta}$ is anything but infinitesimal, $\boldsymbol{X}_k$ will likely be in error since a linearized model was used for the calculation. To ensure stability, the update equation is modified to be $\boldsymbol{X}_k = \boldsymbol{X}_{k-1} + \mu\boldsymbol{\delta}$, where μ is a positive constant that is less than 1. Convergence is declared and the iteration process stopped as soon as $\boldsymbol{\delta}$ is very small and there is no significant change from one iteration to the next.

However, since (3.30) needs to be optimized, it is convenient to directly limit the value of each element in $\boldsymbol{\delta}$ at each step, i.e., incorporating a new constraint $|\delta_i| < \kappa, ; \forall i = 1, 2, \ldots, N$. Incorporating such a constraint eliminates overshoot if $\kappa < 1$ and also narrows the search domain of $\boldsymbol{\delta}$, speeding up the search. Overall, the k^{th} iteration of the optimization problem can be formulated as

$$\underset{\boldsymbol{\delta}}{\text{Minimize}} \qquad \boldsymbol{\delta}^T \mathbf{A}_{k-1} \boldsymbol{\delta} + 2\mathbf{f}_{k-1}\boldsymbol{\delta} \tag{3.31}$$

$$\text{Subject to} \quad |\delta_i| \leq \min(\rho - X_{k-1,i},\ \kappa), \quad 1 \leq i \leq P+Q \tag{3.32}$$

$$|\delta_j| \leq \kappa, \quad P+Q+1 \leq j \leq N \tag{3.33}$$

where $X_{k-1,i}$ is the i^{th} element of the vector $\boldsymbol{X}_{k-1}$.

3.3.4 Target frequencies

The DOCSIS downstream specification in [C3.14] places limits on the out-of-band power in three different bands, which have bandwidths 750 kHz, 5.25 MHz and 6 MHz labeled as OB1, OB2 and OB3 in Fig. 3.2. The power in each of the two 750 kHz bands, which are part of the 6 MHz adjacent channels, must be at least 58 dB below the edge-to-edge power in the 6 MHz channel. The power in OB2, which is the remaining 5.25 MHz of the adjacent channels, must be at least 60 dB below the edge-to-edge power in the 6 MHz channel. The

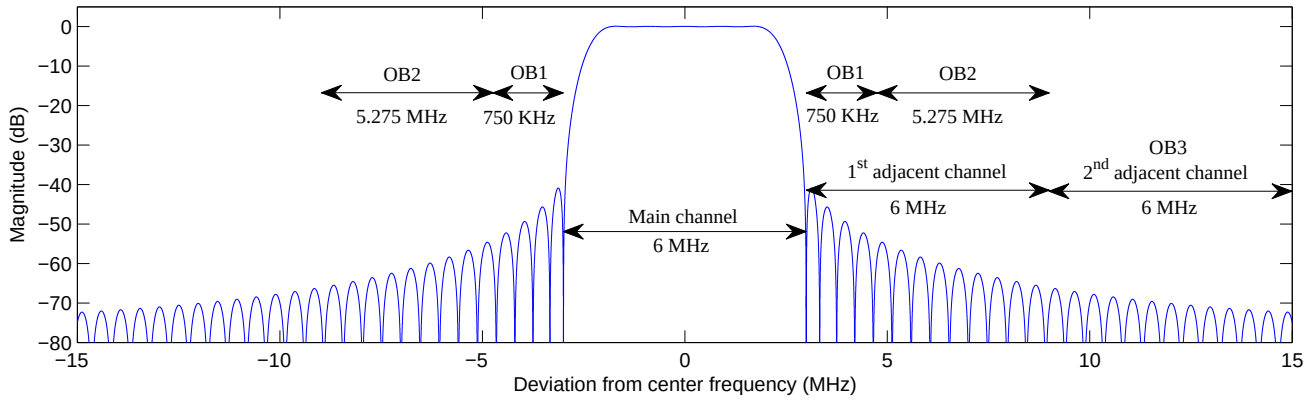

Figure 3.2 Adjacent channel specifications.

power in the second adjacent channel, which is the 6 MHz band labeled OB3 in Fig. 3.2, must be at least 63 dB below the power in the channel.

The out-of-band emissions for bands OB1 and OB2 in the first adjacent channel are the most difficult to meet. A filter that satisfies the out-of-band emission for OB1 and OB2 is likely to meet the out-of-band emission for the second adjacent channel. Moreover, the pulse shaping filter is often followed by a few other filters in the system, such as digital interpolation filters or analog band pass filters, which inherently help to mitigate the out-of-band emission to the second and subsequent adjacent channels. With this in mind the out-of-band emission restriction for the 2nd adjacent channel is largely ignored to reduce the complexity of the search for filter coefficients.

The optimization process that finds coefficients does not use the integrated power, but rather the power spectral density. Further to that, it weights the selected points to assign relative importance. A weighting factor of W_{OB1} is used for all selected frequencies in band OB1. Similarly, a weighting factor of W_{OB2} is used for the frequencies selected in band OB2 and a portion of band OB3. Weighting factors W_P and W_T are used for frequencies in the pass band and transition band of the channel, respectively. The number of points selected in the pass band, transition band, OB1 and OB2 together with some of OB3 are denoted M_P, M_T, M_{OB1} and M_{OB2}, respectively. The points are uniformly placed across the respective bands. In terms of normalized frequency in units of radians/sample, the distribution of points has M_P points between 0 and $(1-\beta)\pi/L$, M_T points between $(1-\beta)\pi/L$ and $(1+\beta)\pi/L$, M_{OB1} points between $(1+\beta)\pi/L$ and $5(1+\beta)\pi/(4L)$ and M_{OB2} points between $5(1+\beta)\pi/(4L)$

and π. Some of the M_{OB2} points are in the OB3 band as the band from $3\pi/L$ to π is in OB3. The parameter L is the ratio of sampling rate to symbol rate. A value of $L = 4$ samples/symbol is used in the analysis.

3.4 Simulation Results

3.4.1 Comparison of FIR designs

First an FIR square-root raised cosine filter that meets the out-of-band emission requirements for a DOCSIS CMTS transmitter is designed. The specific pulse shaping filter is for 256-QAM at a symbol rate of 5.36 Msym/sec, which requires a rolloff factor of 0.12. The most basic approach, which is a rectangular window applied to (3.2), requires a filter of order of 230 to meet the out-of-band emission requirement. Tapering the impulse response with a window function increases the stop band attenuation, which reduces the out-of-band emission, but increases the ISI. The ISI is compensated by windowing the ideal impulse response generated by (3.2), but with a reduced rolloff factor.

A design with a Kaiser window is examined by creating a filter with a rolloff factor equal to 0.05 and then applying a Kaiser window with shape factor $\alpha = 3.5$ to increase the stop-band attenuation and satisfy the emission requirement. The best combination of rolloff factor and shape factor was found by experiment to be 0.05 and 3.5, respectively. This produces a filter of order 90 that has integrated powers of -58.122 dB and -62.435 dB in band OB1 and OB2, respectively.

A filter designed with harris' technique requires an order of 104 in order to meet the DOCSIS out-of-band emission requirements. Although this filter has a higher implementation cost than a Kaiser windowed filter, it provides significantly better ISI performance, as will be shown later.

Table 3.1 shows details of implementation cost among the three aforementioned windowed filters. The columns P_{OB1} and P_{OB2} present integrated powers in bands OB1 and OB2, respectively. Fig. 3.3 shows the pass-band and stop-band detail of the three filters. Thanks to the roll-off in its stop-band, the rectangular windowed filter has much less power in band

OB2.

Table 3.1 Complexity, design parameters and performance of three FIR designs

FIR Design	Multiplies/sample	Design parameters	P_{OB1}	P_{OB2}
Rectangular windowed	116	$\beta = 0.12$	-58.5dB	-74.2dB
Kaiser windowed	46	$\beta = 0.05, \alpha = 3.5$	-58.1dB	-62.4dB
harris	53	$\beta = 0.12$, $\epsilon_1 = 1.02,\ \epsilon_2 = 1.015$	-58.2dB	-60.1dB

Table 3.2 in section B shows the ISI performance for many different combinations of pulse shaping and matched filters. In each case, the filter length used is the shortest which meets the DOCSIS spectral mask. Rectangular windowed, Kaiser windowed and harris' are among the filters compared. The convolution of a rectangular windowed impulse response with itself shows the least ISI, which is expected as its transition band is nearly ideal. In contrast, Kaiser's and harris' filters sacrifice ISI in exchange for lower implementation costs. While harris' approach requires slightly more coefficients than the Kaiser window approach, the ISI power is significantly lower.

Measuring the ISI at the output of the matched filter is not necessarily a true indication of system performance since the demodulators in DOCSIS cable modems typically employ equalizers that will suppress some of the ISI caused by the imperfect pulse shaping and matched filters [C3.15, C3.16]. To provide some insight into the actual performance, the ISI power is also calculated at the output of a 24-tap symbol-spaced LMS equalizer that follows the matched filter. Such an equalizer may or may not be the type and size used in cable modems. It is used in this analysis to produce an indication of the improvement obtained by equalization.

For the purpose of evaluating the ISI contributed by the pulse shaping and matched filters, the channel is assumed to be free of distortion and noise and the matched filter is followed by a symbol-spaced LMS equalizer. Let $\mathbf{v}$ be the vector of symbol spaced points obtained by down-sampling the impulse response of pulse shaping filter in cascade with the matched filter. Denote N_v as the length of $\mathbf{v}$, then $\mathbf{v} = [v(0), v(1), \ldots, v(N_v - 1)]^T$ contains samples taken at symbol rate. Perfect timing synchronization is assumed so that $\mathbf{v}$ contains the decision point in element $v(K)$, where $K \in [0, N_v)$. The decision point is the tap in

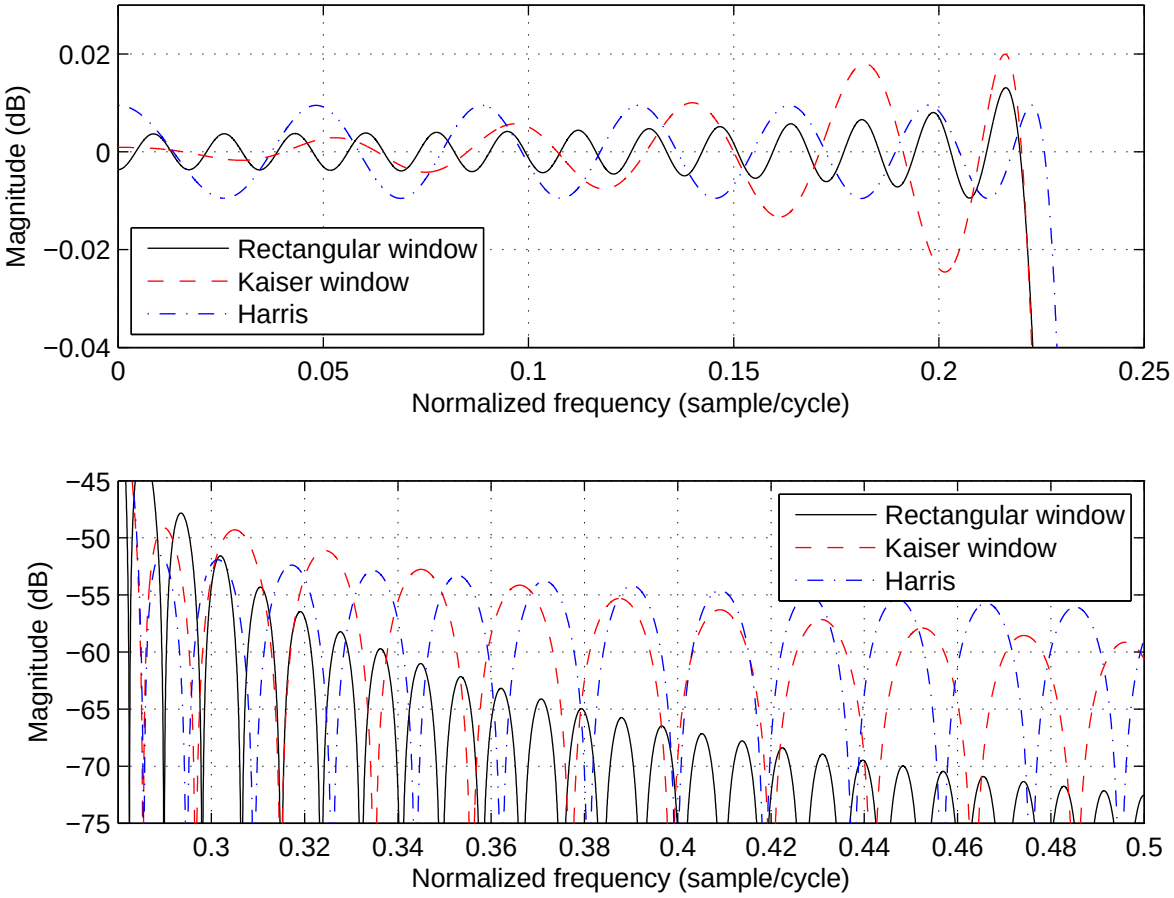

Figure 3.3 Pass-band and stop-band details of truncated, Kaiser windowed and harris' FIR filters.

the impulse response of the cascade of the pulse shaping and matched filters that is largest in magnitude. If the impulse response of the filters is infinite, the vector $\mathbf{v}$ is truncated to length N_v, where N_v is sufficiently large to include 99.9999% of the energy. That is N_v is sufficiently large to satisfy

$$10\log_{10}\left(\frac{\sum_{i>N_v}^{\infty}|v(i)|^2}{\sum_{i=0}^{\infty}|v(i)|^2}\right) < -60 \text{ dB}. \tag{3.34}$$

Prior to equalizing, the normalized ISI power is

$$P_{\text{ISI}} = \frac{\sum_{i=0,i\neq K}^{N_v-1}|v(i)|^2}{|v(K)|^2} = \frac{\sum_{i=0}^{N_v-1}|v(i)|^2}{|v(K)|^2} - 1 \tag{3.35}$$

Let $\mathbf{g} = [g(0), g(1), \ldots, g(23)]^T$ be the coefficients for the 24-tap equalizer. For the purposes of characterizing ISI with the symbol-spaced equalizer, the main tap is positioned at $g(8)$. While position $g(12)$ would yield lower ISI, $g(8)$ is a better choice for reducing multi-path channel distortions, which are common in DOCSIS systems. The coefficients in $\mathbf{g}$ are chosen to minimizes the mean squared error $\|\mathbf{v}*\mathbf{g}-\mathbf{\Delta}_{K+8}\|^2$, where $*$ denotes convolution operation and $\mathbf{\Delta}_{K+8}$ is a length (N_v+23) column vector where all elements are zeros except for the $(K+8)^{th}$ row , which has the value of 1. The optimum equalizer coefficients, denoted as $\mathbf{g}^{\text{opt}}$, therefore can be found by solving

$$\mathbf{g}^{\text{opt}} = \underset{\mathbf{g}}{\text{argmin}} \left\| \underbrace{\begin{bmatrix} v(0) & 0 & \cdots & 0 & 0 \\ v(1) & v(0) & \cdots & 0 & 0 \\ \vdots & \vdots & \ddots & \vdots & 0 \\ v(22) & v(21) & \ddots & v(0) & 0 \\ v(23) & v(22) & \ddots & v(1) & v(0) \\ \vdots & \vdots & \ddots & \vdots & \vdots \\ 0 & 0 & \ddots & v(N_v-1) & v(N_v-2) \\ 0 & 0 & \ddots & 0 & v(N_v-1) \end{bmatrix}}_{\mathbf{V}} \underbrace{\begin{bmatrix} g(0) \\ g(1) \\ g(2) \\ \vdots \\ g(8) \\ \vdots \\ g(22) \\ g(23) \end{bmatrix}}_{\mathbf{g}} - \underbrace{\begin{bmatrix} 0 \\ 0 \\ 0 \\ \vdots \\ 1 \\ \vdots \\ 0 \\ 0 \end{bmatrix}}_{\mathbf{\Delta}_{K+8}} \right\|^2, \tag{3.36}$$

Table 3.2 ISI powers for different combinations of pulse shaping filter and matched filter.

Window type (number of multiplies per sample)		Rectangular (116)	Kaiser (46)	harris (53)	SMP (61)	GNP (51)	GNR (41)	GNH (34)	GNH2 (41)
ISI before equalization (P_{ISI}(dB))	Rectangular	-55.9							
	Kaiser	-29.5	-24.4						
	harris	-55.3	-29.8	-52.8					
	SMP	-28.7	-25.2	-28.8	-22.8				
	GNP	-24.3	-22.0	-24.4	-21.7	-18.5			
	GNR	-25.2	-22.8	-25.3	-22.5	-18.9	-19.3		
	GNH	-35.4	-28.6	-35.3	-27.2	-24.1	-24.9	-29.4	
	GNH2	-43.4	-29.4	-44.7	-28.5	-24.2	-25.1	-35.5	-37.9
ISI after 24-taps equalization $\left(P_{\text{ISI}}^{(\text{eq})}(\text{dB})\right)$	Rectangular	-55.9							
	Kaiser	-42.2	-35.3						
	Harris	-59.5	-41.2	-56.1					
	SMP	-39.7	-34.3	-39.1	-33.3				
	GNP	-39.5	-34.0	-39.2	-33.1	-31.9			
	GNR	-40.1	-34.7	-40.3	-34.0	-32.7	-33.0		
	GNH	-35.8	-32.7	-35.7	-31.8	-32.1	-32.4	-29.8	
	GNH2	-47.7	-41.0	-48.3	-39.0	-38.8	-39.3	-36.0	-41.9

where $\mathbf{V}$ in (3.36) is a size $(N_v + 23) \times 24$ Toeplitz convolution matrix. It is obvious that (3.36) is a conventional least squares problem that can be solved as

$$\mathbf{g}^{\text{opt}} = \mathbf{V}^{+}\boldsymbol{\Delta}_{K+8}, \tag{3.37}$$

where $\mathbf{V}^{+}$ is Moore-Penrose pseudo-inverse matrix of $\mathbf{V}$ (which can be computed with Matlab function `pinv()`). It turns out the equalizer coefficients are the $(K+8)^{\text{th}}$ row of $\mathbf{V}^{+}$. The ISI power after equalization can be approximated with high-precision by

$$P_{\text{ISI}}^{(\text{eq})} = \|\mathbf{V}\mathbf{g}^{\text{opt}} - \boldsymbol{\Delta}_{K+8}\|^2 \tag{3.38}$$

The lower part of Table 3.2 shows the ratio of ISI power to signal power with the 24-tap symbol-spaced LMS equalizer in place for the three filters of discussion as well as others yet to be discussed.

3.4.2 IIR designs

First, a filter is obtained with the Steiglitz-McBride (SM) method, in which the objective function is minimized under the constraint of positive realness. This method can be applied to finding the coefficients for a filter that minimize the stop-band attenuation while main-

Table 3.3 Implementation cost, design parameters and performance of the IIR designs

IIR Design	Multiplies	Design parameters	P_{OB1}	P_{OB2}
SM method with PR condition (SMP)	61	$\varphi = 34, m = 50, n = 10,$ $\eta = 0.05, \mu = 0.2,$ $W_{OB1} = 400, W_{OB2} = 800$	−58.6dB	−61.4dB
GN method with polynomial parameterization and the PR constraint (GNP)	51	$\varphi = 26, m = 40, n = 10,$ $\eta = 0.05, \kappa = 1, \mu = 0.05,$ $W_{OB1} = 500, W_{OB2} = 800,$ $N = 200$	−58.1dB	−62.7dB
GN method with polynomial parameterization and the RT constraint (GNR)	41	$\varphi = 26, m = 30, n = 10,$ $\rho = 0.985, \kappa = 1, \mu = 0.05,$ $W_{OB1} = 200, W_{OB2} = 400,$ $N = 1024$	−58.2dB	−61.4dB
Proposed GN method with hybrid parameterization (GNH)	34	$\varphi = 37, m = 16, P = 1, Q = 16,$ $\rho = 0.985, \kappa = 0.2, \mu = 0.05,$ $W_{OB1} = 150, W_{OB2} = 200$	−58.1 dB	−62.9dB
2^{nd} GNH design (GNH2)	41	$\varphi = 46, m = 24, P = 0, Q = 16,$ $\rho = 0.985, \kappa = 0.2, \mu = 0.05,$ $W_P = 6, W_{OB1} = 250, W_{OB2} = 400$	−58.4 dB	−60.9dB

taining the desired pass-band response. To find the lowest order filter requires a cut-and-try approach using different filter structures and parameters. The set of parameters that yielded a filter with the lowest multiplies to sample ratio is given in Table 3.3, where the parameter φ defines the phase delay of the target SRRC frequency response, $D(\omega)$, as in (3.1). The result was a filter with 50 zeros and 10 poles requiring 61 multiplies. The integrated powers in bands OB1 and OB2 are -58.6 dB and -61.4 dB, respectively. The frequency and phase characteristics of the filter is shown in Fig. 3.4.

Next, consider the GN method with radii-angle parameterization. This method does not converge well when the numerator's order exceeds 12, and the method does not work at all with an order greater than 17. It is concluded that it is not possible to get a reasonable DOCSIS's shaping filter with this method.

Then, the GN method with polynomial parameterization under the PR constraint is used to obtain a filter referred to as a GNP filter. The design parameters are specified in Table 3.3. Fig. 3.5 provides results obtained from the proposed method. The algorithm takes 115 iterations to converge.

Finally, the GN method with polynomial parameterization and the RT constraint is used to obtain a filter referred to as a GNR filter. Its frequency domain characteristics are presented in Fig. 3.6. The constraint (3.24) is enforced with $N = 1024$ equally-spaced

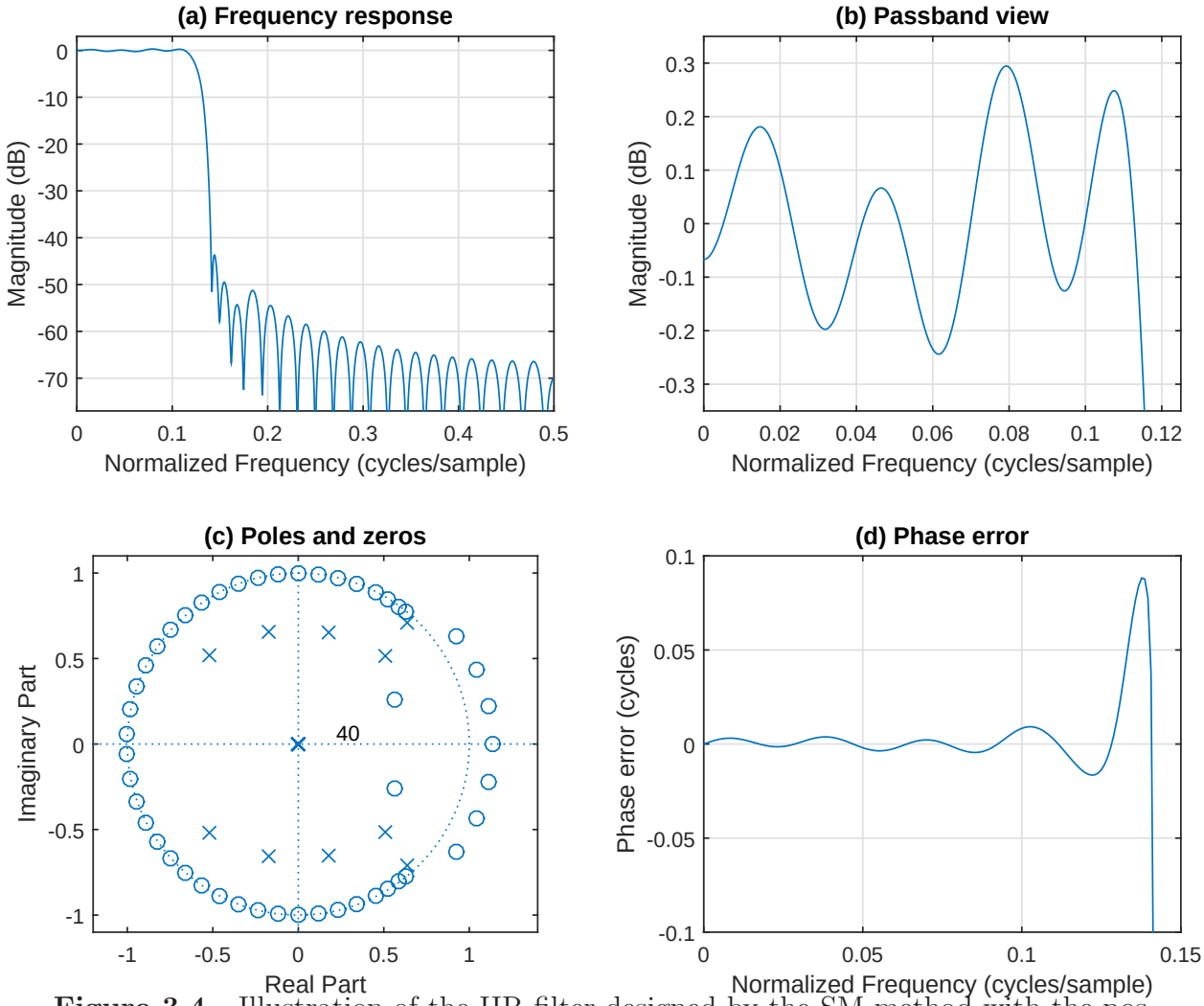

Figure 3.4 Illustration of the IIR filter designed by the SM method with the positive realness condition.

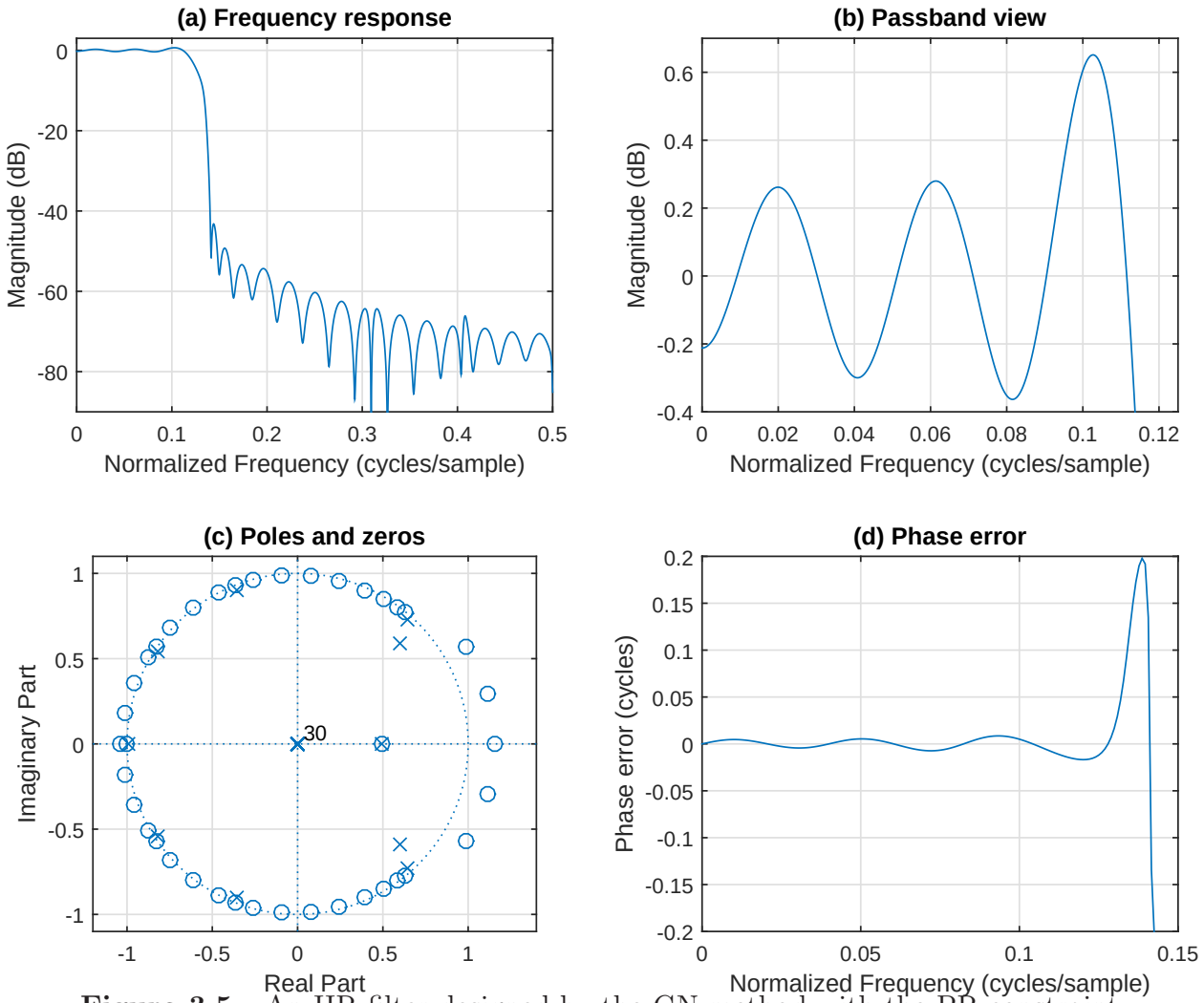

Figure 3.5 An IIR filter designed by the GN method with the PR constraint.

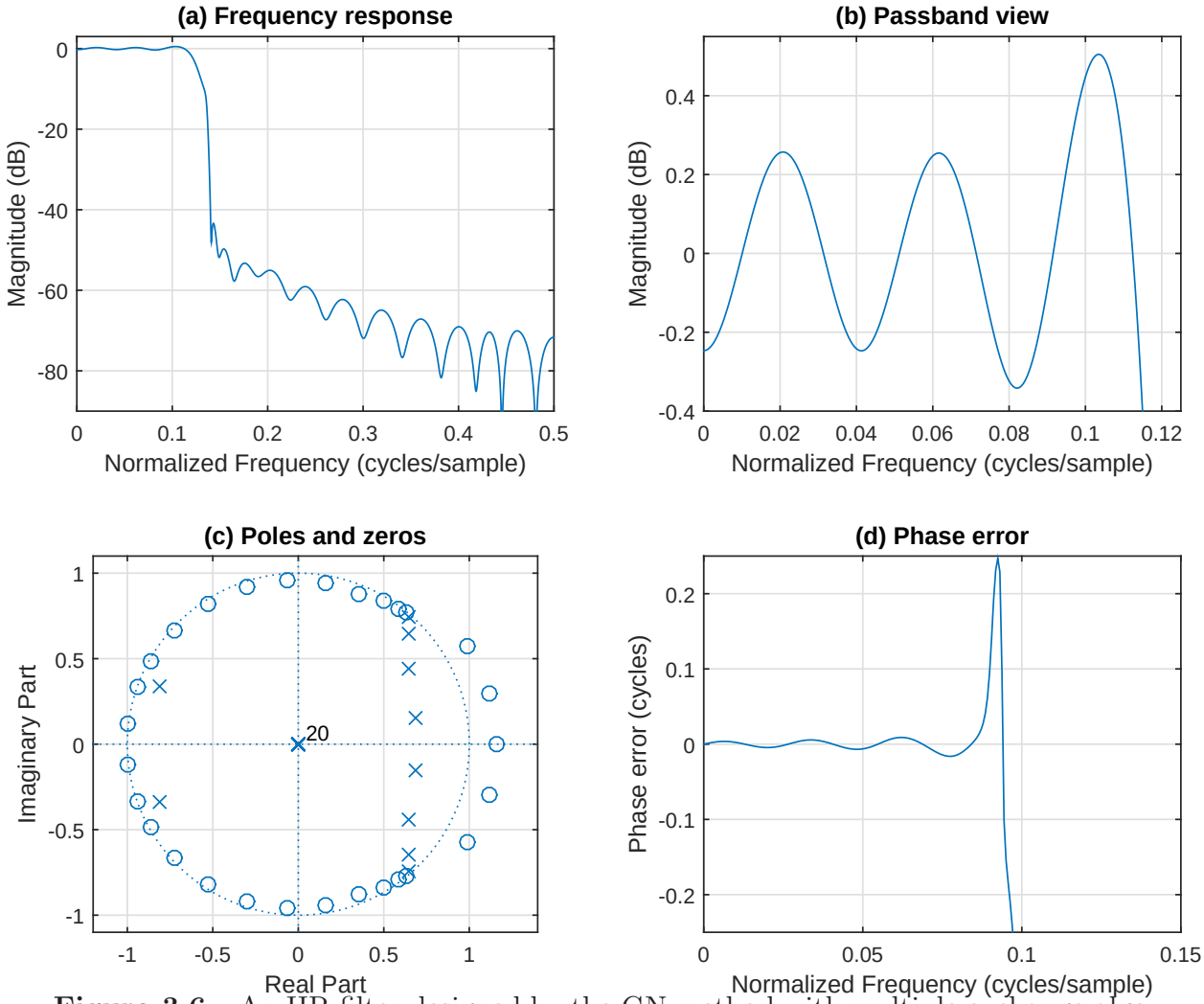

Figure 3.6 An IIR filter designed by the GN method with multiple exchange algorithm (GNR).

frequency points over $[0, \pi]$. Formulated with the multiple exchange algorithm, the GN method generates a very efficient filter requiring only 41 multiplies per sample. This is significantly less than any of the FIR filters. However, due to a conservative constraint, it does not yield a good result if the order of the denominator is increased further. The order is limited to $n = 10$ for both the GNP and GNR designs.

3.4.3 Improved design with hybrid parameterization

The frequency response characteristics of a filter obtained using the proposed method are shown in Fig. 3.7. The numerator polynomial is order-16 and is initiated with the

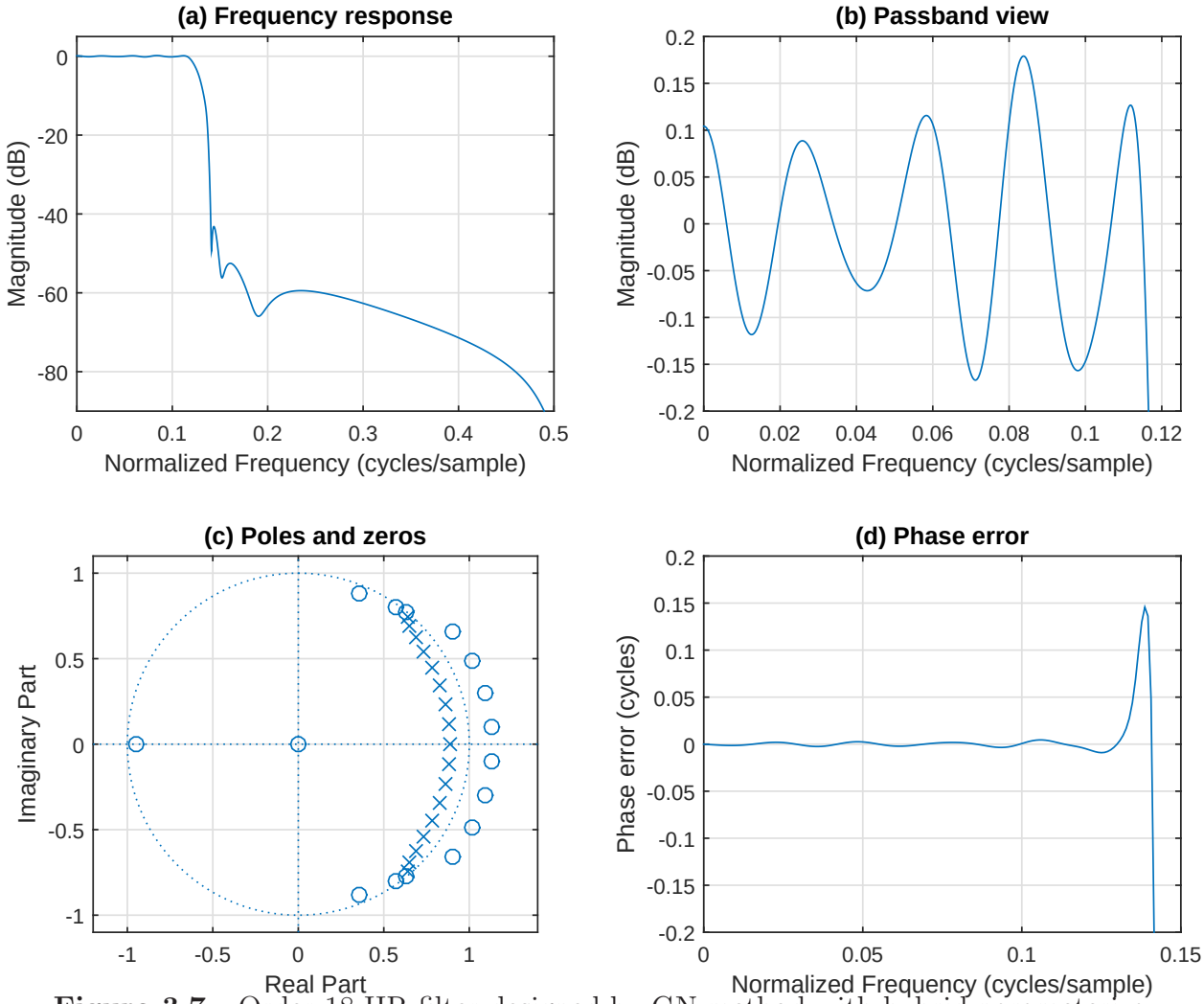

Figure 3.7 Order-18 IIR filter designed by GN method with hybrid parameterization.

coefficients of a truncated ideal FIR filter. The denominator contains 17 poles. Initially, all poles are set to have $\{p_i = 0,\ \forall i\}$, whereas all angles, $\{\phi_i,\ \forall i\}$, are equally distribute over the range $[-\pi, \pi]$. It appears that the algorithm cannot converge if all the angles are initially created equal. It is noticeable in Fig. 3.7 that the stop band of the proposed design has rolloff within it. This is a significant advantage for a shaping filter. Also, the least pass band ripple is smallest among the IIR designs. The zeros and poles of the filter are given by $-9.7121, -0.9483, 0.3561 \pm 0.8812i, 0.5706 \pm 0.8010i, 0.6306 \pm 0.7722i, 0.9027 \pm 0.6585i, 1.0172 \pm 0.4873i, 1.1312 \pm 0.1005i, 1.0930 \pm 0.2989i$ and $0.8879, 0.6404 \pm 0.7443i, 0.6495 \pm 0.6914i, 0.6885 \pm 0.6251i, 0.7326 \pm 0.5409i, 0.7829 \pm 0.4471i, 0.8272 \pm 0.3436i, 0.8611 \pm 0.2328i, 0.8817 \pm$

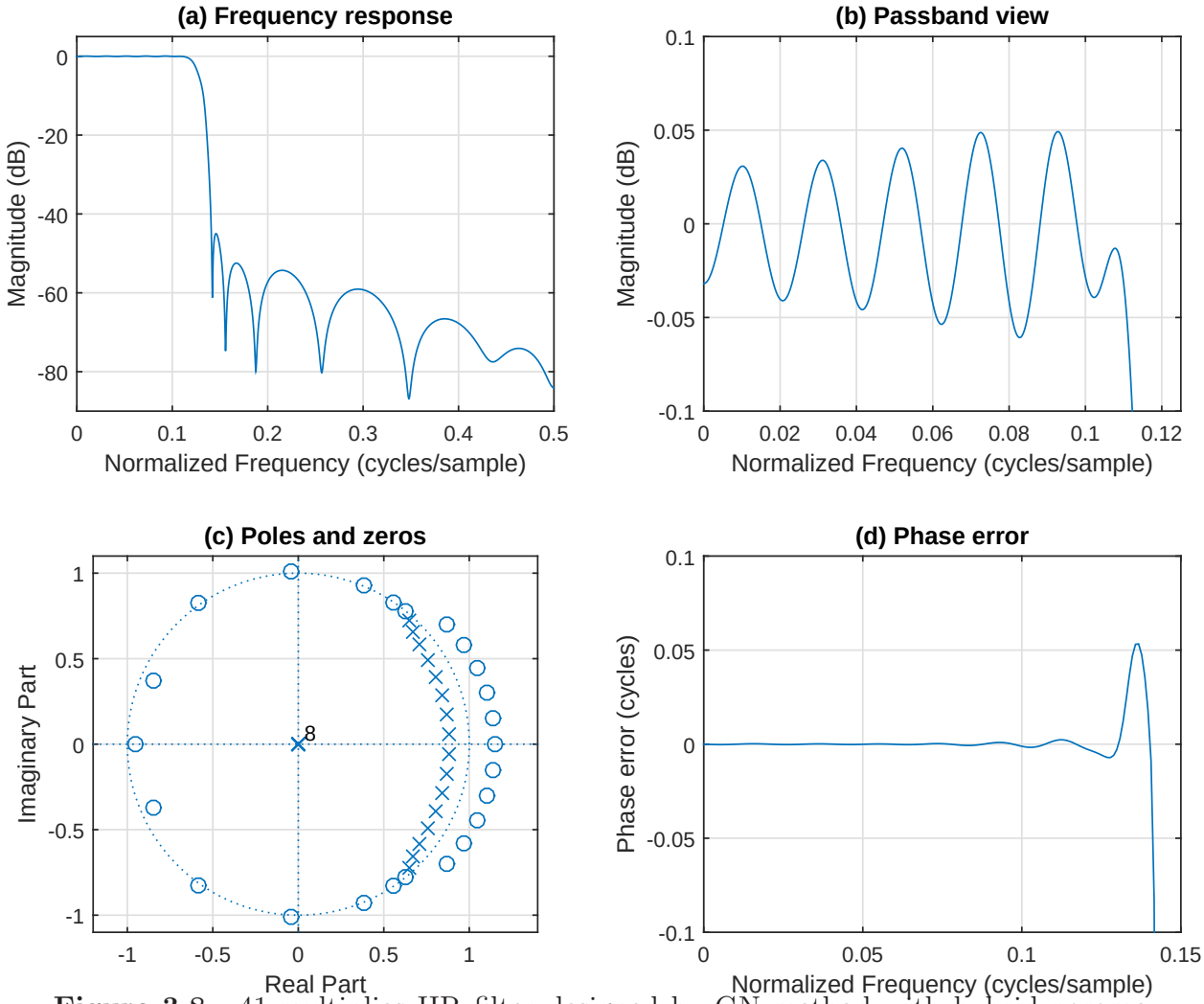

Figure 3.8 41-multiplies IIR filter designed by GN method with hybrid parameterization.

$0.1170i$, respectively.

Another example, which uses more multiplies/sample to achieve less ISI, is presented in Fig. 3.8. The filter is referred to as GNH2. Zeros of the filter are given by $-0.9526, -0.8470 \pm 0.3714i, -0.5844 \pm 0.8261i, -0.0421 \pm 1.0101i, 0.3838 \pm 0.9284i, 0.5563 \pm 0.8282i, 0.6268 \pm 0.7774i, 0.8687 \pm 0.7000i, 0.9683 \pm 0.5800i, 1.0466 \pm 0.4452i, 1.1506 \pm 0.0000i, 1.1385 \pm 0.1517i, 1.1036 \pm 0.3013i$ and the poles are $0.6492 \pm 0.7233i, 0.6705 \pm 0.6564i, 0.7083 \pm 0.5834i, 0.7578 \pm 0.4918i, 0.8037 \pm 0.3925i, 0.8416 \pm 0.2859i, 0.8817 \pm 0.0581i, 0.8682 \pm 0.1737i$.

Table 3.2 presents the ISI levels obtained when the pulse shaping and matched filters are

any combination of (1) rectangular windowed FIR, (2) Kaiser windowed FIR, (3) harris FIR, (4) SM IIR found with PR condition, (5) GN IIR found with PR constraint, (6) GN IIR found with RT constraint, (7) GN IIR found using hybrid parametrization with 34 coefficients and (8) GN IIR found using hybrid parametrization with 41 coefficients. It can be seen that the GNH design outperforms the Kaiser windowed design in terms of both performance (when cascading with rectangular window filter) and cost (34 versus 46 multiplies).

3.5 Conclusions

A properly designed IIR pulse shaping filter can satisfy the downstream DOCSIS 3.0's out-of-band emission requirements, and yield sufficiently low ISI with better efficiency, i.e., fewer multiplies/sample, than linear-phase FIR filters, windowed or otherwise. It was demonstrated that IIR filters have a cost versus ISI trade off. The least expensive IIR filter is obtained by the proposed design algorithm, which considers a hybrid parameterization of the filter's transfer function in combination with a constraint on maximum pole radius.

References

[C3.1] A. L. Balan and N. D. Alexandru, "Two improved Nyquist filters with piece-wise rectangular-polynomial frequency characteristics," *Int. Journal on Electron. and Commun.*, vol. 66, pp. 880–883, Nov. 2012.

[C3.2] S. D. Assimonis, M. Matthaiou, and G. K. Karagiannidis, "Two-parameter Nyquist pulses with better performance," *IEEE Commun. Letters*, vol. 12, pp. 807–809, Nov. 2008.

[C3.3] N. D. Alexandru and A. B. Onofrei, "Improved Nyquist Filters with Piece-Wise Parabolic Frequency Characteristics," *IEEE Commun. Letters*, vol. 15, pp. 473–475, May 2011.

[C3.4] A. L. Balan and N. D. Alexandru, "Improved Nyquist Filters with piecewise rectangular-sine frequency characteristics," *IEEE Trans. Commun.*, pp. 67–70, June 2012.

[C3.5] T. Roy and M. Morshed, "Performance analysis of low pass FIR filters design using Kaiser, Gaussian and Tukey window function methods," in *Int. Conf. on Advances in Electrical Engineering*, pp. 1–6, Dec 2013.

[C3.6] fred harris, C. Dick, S. Seshagiri, and K. Moerder, "An Improved Square-Root Nyquist Shaping Filter," in *Proc. IEEE Tech. Conf. and Product Exposition*, 2005.

[C3.7] W.-S. Lu, S.-c. Pei, and C.-C. Tseng, "A weighted least-squares method for the design of stable 1-D and 2-D IIR digital filters," *IEEE Trans. Signal Process.*, vol. 46, no. 1, pp. 1–10, 1998.

[C3.8] B. Dumitrescu and R. Niemisto, "Multistage IIR filter design using convex stability domains defined by positive realness," *IEEE Trans. Signal Process.*, vol. 52, no. 4, pp. 962–974, 2004.

[C3.9] W.-S. Lu and T. Hinamoto, "New algorithm for minimax design of sparse IIR filters," in *IEEE Trans. Circuits and Systems*, pp. 2920–2923, 2013.

[C3.10] A. Chottera and G. Jullien, "A linear programming approach to recursive digital filter design with linear phase," *IEEE Trans. Circuits and Systems*, vol. 29, no. 3, pp. 139–149, 1982.

[C3.11] M. Lang, "Least-squares design of IIR filters with prescribed magnitude and phase responses and a pole radius constraint," *IEEE Trans. Signal Process.*, vol. 48, no. 11, pp. 3109–3121, 2000.

[C3.12] M. Quelhas, A. Petraglia, and M. Petraglia, "Linear Programming for the design of IIR filters," in *IEEE Trans. Circuits and Systems*, pp. 1–4, Feb 2012.

[C3.13] E. Titchmarsh, *The theory of functions. 2nd ed.* London: Oxford University Press., 1975.

[C3.14] Cable Television Laboratories, Inc., "Downstream RF Interface Specification," Nov 2011.

[C3.15] Z. Andalibi, B. Berscheid, E. Salt, and H. Nguyen, "A Fast-Converging Equalizer for Upstream DOCSIS Channels," *IEEE Trans. on Broadcasting*, vol. 56, pp. 311–320, Sept. 2010.

[C3.16] H. M. Kim, S. I. Park, J. H. Seo, H. Eum, Y.-T. Lee, S. I. Lee, and H. Lee, "Modulation and Pre-Equalization Method to Minimize Time Delay in Equalization Digital On-Channel Repeater," *IEEE Trans. on Broadcasting*, vol. 54, pp. 249–256, June 2008.

4. Digital Peak Locator by Log-Domain Interpolation

Published as:

Tung T. Nguyen, J. Eric Salt, Brian Berscheid and Ha H. Nguyen "Digital peak locator by log-domain interpolation," *Submitted to IEEE Signal Processing Letters*, Jun. 2016.

In the previous chapter, efficient IIR filter designs that satisfy the out-of-band spectral constraints of DOCSIS 3.0 down-stream channels were proposed. The designs aim at lowering the ISI resulting from cascading the practical pulse shaping filter and matched filter. It was explained in Chapter 2 that, even when ideal pulse shaping and matched filters are used, in order for the receiver to recover the transmitted symbols without ISI, the down-converter, which is located at the receiver after the matched filter, must sample the filtered signal at precise moment of $t = nT_{\text{sym}}$ (see Fig.2.1). If the receiver instead samples the signal at incorrect time moments, ISI results, which, in turn, increases the probability of symbol errors. Therefore, to obtain accurate estimates of the transmitted symbols, the timing offset, which is also known as the error in the sampling time, must be detected.

The manuscript included in this chapter proposes an efficient method to estimate the location of the peak in an analog signal after it has been sampled. The proposed technique has a wide range of applications, such as time-domain reflectometry and timing offset estimation in a SC-QAM system. Moreover, it will be shown in the Chapter 5 that the technique can also be used in an important signal processing part of the OFDMA channel estimator. A shorter version of this manuscript is published as [C4.1].

The main contribution to this manuscript comes from the student (first author), while the three co-supervisors provide equal supervision effort.

Digital Peak Locator by Log-Domain Interpolation

Tung T. Nguyen, *Member, IEEE*, Eric Salt, *Member, IEEE*,
Brian Berscheid, *Member, IEEE* and Ha H. Nguyen, *Senior Member, IEEE*

Abstract

In applications such as radar, digital communication and time domain reflectometry, a digital circuit is required to estimate the time of occurrence of the peak in the analog equivalent of a sampled signal or in an analog signal after it has been sampled. This paper proposes a technique that is more accurate than the commonly used parabolic fit providing the distortion introduced by the channel is not too large. The technique approximates the analog signal in the vicinity of its peak with a two parameter function, the logarithm of which is approximated with a straight line. One of the parameters is the location and the other is the amplitude of the peak. Two samples, one on each side of the peak, are used to estimate the two parameters. Simulation results show that the circuit for the proposed estimator is comparable in cost to that of the parabolic fit, but is significantly more accurate when the distortion introduced by the channel is modest.

Index terms

Peak detection, reflectometry, timing detection.

4.1 Introduction

On occasion a signal processing function that finds the peak in an analog signal is needed. A peak-finding function estimates the location of the peak in an analog signal after it has been sampled or, equivalently, it estimates the location of the peak in the analog equivalent

of a sampled signal. Such functions are used in the areas of time-domain reflectometry, symbol timing recovery in QAM modems, pulsed radar, active and passive underwater sonar (e.g., fish/submarine) location, channel sounding as well as many other areas.

The least expensive and easiest function simply finds the sample with largest value and uses its location as the location of the peak in the analog signal. The estimation error for this method is uniformly distributed between $\pm$ 1/2 sampling interval, which is too large for many applications. Of course the accuracy can be improved by reducing the sampling interval, which amounts to up-sampling the sampled signal. Clearly, the accuracy will be improved by the up-sampling factor. Up-sampling is a well-known process [C4.2, C4.3] whose implementation has been well explored [C4.4]. Even with the most efficient implementation, up-sampling is relatively expensive.

Another approach, which is commonly used, approximates the analog signal in the vicinity of its peak with a parameterized analog function whose parameters are algebraically related to the location of the peak. The parameters of the function are calculated using samples in the vicinity of the peak. One such function suggested in [C4.2] is a concave down parabola given by $f(t) = a + c(t - \tau_{\text{peak}})^2$, where parameter τ_{peak} is the quantity of interest. Since the function has three parameters, three digital samples in the vicinity of the peak are required to calculate τ_{peak}. This particular function has been used for peak location in many different applications [C4.3, C4.4, C4.5, C4.6, C4.7].

Since the parabolic function is the second order Taylor series expansion about the peak of the analog signal, it will be very accurate providing the three digital samples used to compute τ_{peak} are in close proximity to the peak. The shape of the function approximating the analog signal would be more accurate if a third or fourth order Taylor series expansion is used. However, four or five samples would be needed to calculate τ_{peak} and the additional samples would be located farther from τ_{peak}, perhaps outside the region where the 3^{rd} or 4^{th} order function is a good approximation.

The authors of this paper investigate the quality of two-parameter functions for approximating the signal in the vicinity of its peak. For certain applications [C4.1], a two-parameter

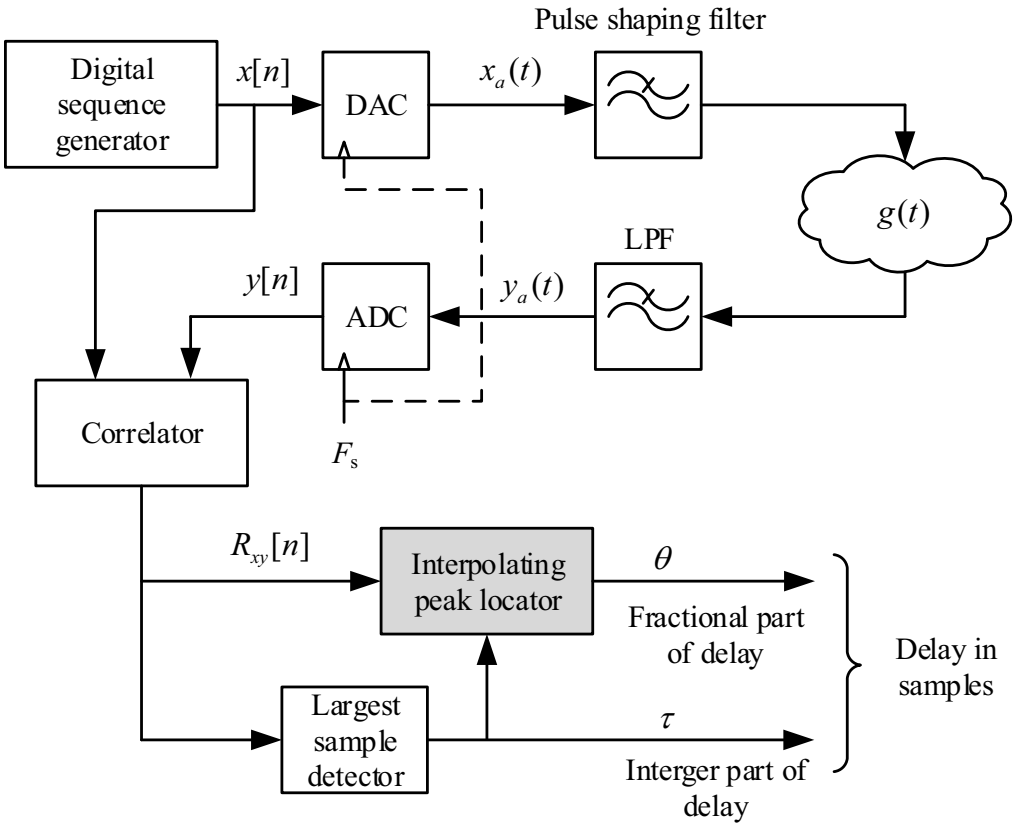

Figure 4.1 Generic model for digital time delay estimator.

function can very accurately model the analog signal in the vicinity of its peak. It will be explained later that the complexity of the calculation of τ_{peak} is comparable to that of a parabolic function, if the two-parameter function is restricted to a class where their logarithm is nearly linear in the vicinity of the peak.

4.2 Application to Timing Detection

A generic time delay estimator circuit is shown in Fig. 4.1. The transmission originates with the digital sequence, $x[n]$, which is known for $n = 0, 1, \ldots, N-1$ and equal to zero for $n \geq N$ and $n < 0$. The transmitted digital sequence has an auto-correlation function given by [C4.8]

$$R_{xx}[k] = \begin{cases} \sum_{n=0}^{N-k-1} x[n]x^*[n+k], & 0 \leq k \leq N-1 \\ R_{xx}^*[-k], & -N+1 \leq k < 0 \\ 0, & \text{otherwise.} \end{cases} \tag{4.1}$$

Good digital transmission sequences for time delay estimation have impulse-like auto-correlation functions. In practice, the auto-correlation function has a main lobe that is tall and narrow but not an impulse, and has non-zero side lobes that are well below the peak of the main lobe. Good sequences for $x[n]$ have been the topic of many papers and a collection of references can be found in [C4.8, C4.9].

In the model of Fig. 4.1, the digital sequence is converted to an analog waveform by the tandem combination of a digital to analog converter and a low-pass pulse shaping filter, which is the analog equivalent of a digital pulse shaping filter. The filter output, $x_a(t)$ in Fig. 4.1, propagates through the channel to reach the receiver. The channel may delay and distort the signal. At the receiver, the signal is band-limited to limit noise and prevent aliasing through the use of another low-pass filter (LPF) to produce the low-pass signal $y_a(t)$ shown in Fig. 4.1.

Passing an impulse response through the system in the absence of a channel (i.e. the case where $g(t) = \delta(t)$) produces a pulse that determines the performance of the time-delay estimation. Many pulse shapes have been studied in the literature, the most well known of which is perhaps the Raised Cosine[1] (RC) pulse which is given by [C4.10]

$$p_{\mathrm{RC}}(t) = \frac{\sin\left(\pi t/(LT_s)\right)}{\pi t/(LT_s)} \frac{\cos(\pi r t/(LT_s))}{1-(2rt/(LT_s))^2}, \tag{4.2}$$

where r is the roll-off factor, L is the ratio of sampling rate to the 6 dB bandwidth of the pulse and $T_s = 1/F_s$ is the sampling period. Of course, the presence of a real channel will change the shape of the pulse.

The objective of the system is to estimate the delay introduced by a channel with impulse response $g(t)$. This estimate is the location of the peak in the analog correlation of $x_a(t)$ and $y_a(t)$. The problem is the correlation is performed digitally, to get $R_{xy}[n]$ in Fig. 4.1, which provides samples of the analog correlation at times nT_s. It is unlikely a sample point will coincide with the peak of the analog correlator, therefore the digital interpolating peak locator circuit, which is also shown in Fig. 4.1, is needed to estimate the location of the peak

[1]Here, the term "raised cosine" describes the shape of the pulse in the frequency domain.

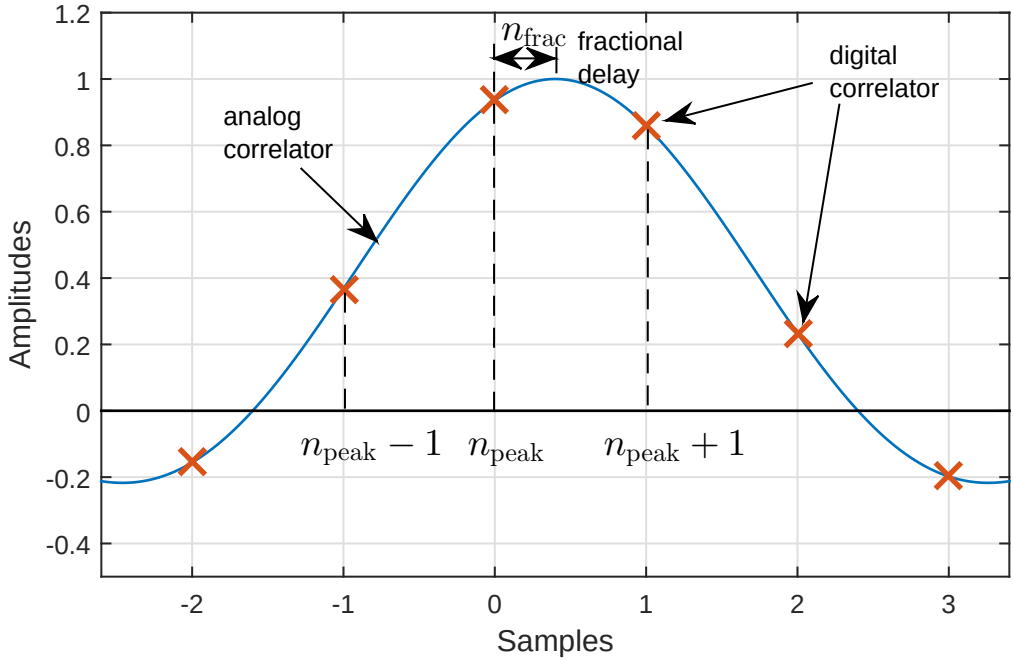

Figure 4.2 Signal generated by analog and digital correlator.

in the analog correlator. The quantity to be estimated from $R_{xy}[n]$ is illustrated in Fig. 4.2.

4.3 Digital Interpolating Peak Locator

4.3.1 Three-sample parabolic interpolation

Parabolic interpolation uses the 3 samples closest to the location of the peak in the analog correlation to find the parameter of interest, τ_{peak}, in the parabolic approximation $f(t) = a + c(t - \tau_{\text{peak}})^2$. The location of these 3 samples are $n_{\text{peak}} - 1$, n_{peak} and $n_{peak} + 1$, where n_{peak} is the value of n where $\left|R_{xy}[n]\right|$ is largest.

Mathematical manipulation shows that location of the analog peak with respect to $n_{\text{peak}}T_s$ is approximated by $\tau_{\text{peak}} \approx n_{\text{frac}}T_s$, where n_{frac} is a fractional delay between $-1/2$ and $1/2$ in samples and is given by

$$n_{\text{frac}} = \frac{|R_{xy}(n_{\text{peak}} - 1)| - |R_{xy}(n_{\text{peak}} + 1)|}{2|R_{xy}(n_{\text{peak}} - 1)| + 2|R_{xy}(n_{\text{peak}} + 1)| - 4|R_{xy}(n_{\text{peak}})|}. \tag{4.3}$$

If n_{frac} is positive then the peak in the analog correlation is to the right of n_{peak} as shown in

Fig. 4.2.

4.3.2 Two-sample log-domain interpolation

The two samples used to find α and τ_{peak} are the ones on either side of the analog peak, which are $\left|R_{xy}[n_{\text{peak}}]\right|$ and the larger of $\left|R_{xy}[n_{\text{peak}}-1]\right|$ and $\left|R_{xy}[n_{\text{peak}}+1]\right|$. Without loss of generality, assuming $\left|R_{xy}[n_{\text{peak}}+1]\right| > \left|R_{xy}[n_{\text{peak}}-1]\right|$, so that the fractional delay n_{frac} is between 0 and 0.5 and the location of the analog peak is approximated by $\tau_{\text{peak}} \approx (n_{\text{peak}} + n_{\text{frac}})T_s$.

Unlike parabolic interpolation, two sample interpolation relies on knowledge of the shape of the pulse at the receiver. The pulse whose peak is to be located is the output of analog correlator, $R_{xy}(t)$. It can be shown that $R_{xy}(t)$ is given by [C4.11]

$$R_{xy}(t) = (h * g)(t) + w(t) \tag{4.4}$$

where $*$ denotes convolution, $w(t)$ is noise, $g(t)$ is the impulse response of the channel and $h(t)$ is defined as

$$h(t) = \sum_{n=0}^{N-1} R_{xx}[n]\; p_{\text{RC}}(t - nT_s), \tag{4.5}$$

where $p_{\text{RC}}(t)$ is the system impulse response given in (4.2).

The shapes of $h(t)$ and $p_{\text{RC}}(t)$ in the vicinity of their peak will be similar if $R_{xx}[n]$ is an impulse-like function. To ensure this is so, the sequence $x[n]$ is selected to have such an auto correlation property [C4.9].

With two sample interpolation, the two unknown parameters are the amplitude and location of the peak of the pulse. While the method is somewhat tolerant of channel dispersion, the analysis assumes the channel is a scaled delay (i.e. $g(t) = \alpha\delta(t - \tau_{\text{peak}})$, where α is an unknown constant), so that the output of the digital correlator in Fig. 4.1 can be approximated as

$$R_{xy}[n] = R_{xy}(t)\big|_{t=nT_s} \approx \alpha h(t)\big|_{t=(n-n_{\text{peak}}-n_{\text{frac}})T_s}, \tag{4.6}$$

then the solution for n_{frac} can be found by simultaneously solving the two equations

$$\alpha h(-n_{\text{frac}}T_s) = \big|R_{xy}[n_{\text{peak}}]\big|, \tag{4.7}$$

$$\text{and} \quad \alpha h\big((1-n_{\text{frac}})T_s\big) = \big|R_{xy}[n_{\text{peak}}+1]\big|, \tag{4.8}$$

for $0 \le n_{\text{frac}} \le 0.5$. The system of two equations with two unknowns is reduced to a single equation with one unknown, which is n_{frac}, by dividing (4.7) by (4.8). This has

$$\frac{h(-n_{\text{frac}}T_s)}{h(1-n_{\text{frac}}T_s)} = \frac{\big|R_{xy}[n_{\text{peak}}]\big|}{\big|R_{xy}[n_{\text{peak}}+1]\big|} \tag{4.9}$$

Denoting $\kappa = \frac{\left|R_{xy}[n_{\text{peak}}]\right|}{\left|R_{xy}[n_{\text{peak}}+1]\right|}$ then substituting (4.2) and (4.5) into (4.9) yields

$$\frac{\sum_{n=0}^{N-1} R_{xx}[n]\ \frac{\sin(-\pi n_{\text{frac}}/L))}{(-\pi n_{\text{frac}}/L)}\frac{\cos(\pi r n_{\text{frac}}/L)}{1-(2rn_{\text{frac}}/L)^2}}{\sum_{n=0}^{N-1} R_{xx}[n]\ \frac{\sin(\pi(1-n_{\text{frac}})/L))}{\pi(1-n_{\text{frac}})/L}\frac{\cos(\pi r(1-n_{\text{frac}})/L)}{1-(2r(1-n_{\text{frac}})/L)^2}} = \kappa \tag{4.10}$$

Solving (4.10) for n_{frac} in the linear domain is far from straight forward and probably requires an iterative search, but in the log domain, a good approximation to the solution can be obtained quite easily. The key to the log domain solution is recognizing that n_{frac} found from (4.10) is a nearly linear function of $\ln(\kappa)$ in the range of $0 \le n_{\text{frac}} \le 0.5$. The degree of linearity depends on the pulse parameters L and r as illustrated in Fig.4.3.

The approximation for n_{frac} can be improved by segmenting the curves in Fig. 4.3 by a few straight lines. In particular, a curve can be sampled at M points with equally spaced ordinates and approximated by straight lines between the sample points. If the solution for n_{frac} is between points m and $m+1$, then the segmented approximation yields

$$n_{\text{frac}} \approx \frac{0.5/(M-1)}{\ln(\kappa_{m+1}) - \ln(\kappa_m)}\big(\ln(\kappa) - \ln(\kappa_m)\big) + \frac{0.5\ m}{M-1}, \tag{4.11}$$

where κ_m , $0 \le m \le M-1$ is the value of κ computed apriori from (4.10) using $n_{\text{frac}} = 0.5m/(M-1)$. The solution is between points m and $m+1$ if and only if $\kappa_m \le \kappa \le \kappa_{m+1}$. The single segment approximation (i.e. $M = 2$) is the easiest to implement and therefore of

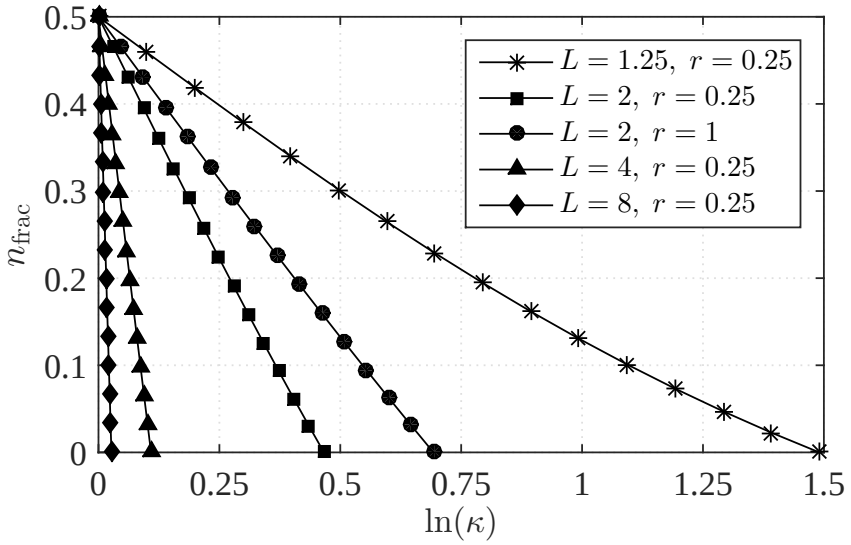

Figure 4.3 Fractional delay as a function of $\ln(\kappa)$, for various pulse shaping parameters.

most importance.

The cost of implementing (4.11) is reduced by expanding κ into its definition, which is $\kappa = \frac{\left|R_{xy}[n_{\text{peak}}]\right|}{\left|R_{xy}[n_{\text{peak}}+1]\right|}$, since the log of a ratio becomes a difference in logs. In doing this (4.11) becomes

$$n_{\text{frac}} = \frac{0.5/(M-1)}{\ln(\kappa_{m+1}) - \ln(\kappa_m)} \left(\ln\left(\left|R_{xy}[n_{\text{peak}}]\right|\right) - \ln\left(\left|R_{xy}[n_{\text{peak}}+1]\right|\right) - \ln(\kappa_m)\right) + \frac{0.5\ m}{M-1}. \tag{4.12}$$

Since the slope $\frac{0.5/(M-1)}{\ln(\kappa_{m+1})-\ln(\kappa_m)}$ and the constants $\ln(\kappa_m)$ and $\frac{0.5\ m}{M-1}$ can be pre-computed and stored in a ROM, the resources required to implement the interpolator are 1 multiplier, 1 log function and 3 adders. Should the interpolator be implemented in an FPGA, it is possible to incorporate the multiplier into the log function [C4.12], thereby eliminating the need for dedicated multiplier hardware. Thus the circuit complexity would be similar to the 3-sample parabolic interpolator.

4.4 Simulation Results

First the performance of the proposed peak locator is evaluated for a non-dispersive channel with impulse response $g(t) = \alpha\delta(t - \tau_{\text{peak}})$. This would be the case for time domain

reflectometry (TDR) applications [C4.13, C4.1], where the spectrum of the pulse is inside the bandwidth of the channel. The evaluation is done for a raised cosine pulse for roll-off factors of $r = 0.1$, $r = 0.25$, $r = 0.5$ and $r = 1$ and for sampling rates of 1.25, 2, 4 and 8 times the 6 dB bandwidth of the pulse. One million simulation runs were performed, with the fractional delay, n_{frac}, for each run selected from a uniform distribution between -0.5 and 0.5 samples. In order to solely validate the performance of the approximations, no noise is added to the system.

Table 4.1 shows the Mean Squared Error (MSE) of the estimate of τ_{peak}, normalized to the sampling period T_s. Three detection approaches were considered: parabolic interpolation and log-domain interpolation with 1 and 7 line segments, i.e., with $M = 2$ and 8.

Table 4.1 Mean squared error in decibel normalized to sampling duration T_s

Peak location method	L	Rolloff factor r			
		0.1	0.25	0.5	1
Parabolic interpolation	1.25	−25.9	−25.4		
	2	−34.8	−34.3	−32.6	−28.5
	4	−47.1	−46.6	−45	−40.9
	8	−59.3	−58.8	−57	−53
Log-domain interpolation with $M = 2$	1.25	−30.9	−31		
	2	−43.1	−43.4	−44	−45.4
	4	−56.6	−56.8	−57.6	−58.8
	8	−68.9	−69.2	−70	−71.1
Log-domain interpolation with $M = 8$	1.25	−53.2	−53.3		
	2	−64.3	−64.5	−65.2	−66.4
	4	−77.4	−77.6	−78.3	−79.5
	8	−89.7	−89.8	−90.6	−91.8

It can be seen from the table that the log-domain approach, even with just 1 segment, i.e. $M = 2$, is significantly better than the 3-sample parabolic approach in all cases. For example, for parameter L greater than or equal to 2, the proposed technique outperforms the parabolic approach by at least 10 dB. Moreover, the parabolic approach is more sensitive to the roll-off factor, as the MSE difference deteriorates by as much as 7 dB as the parameter changes from $r = 0.1$ to $r = 1$. The deterioration is much less in the log domain approach. Furthermore, if a higher precision result is required and additional computational complexity can be tolerated, increasing the number of linear segments from 1 to 7 (M=2 to M=8) yields

at least a 20 dB reduction in MSE.

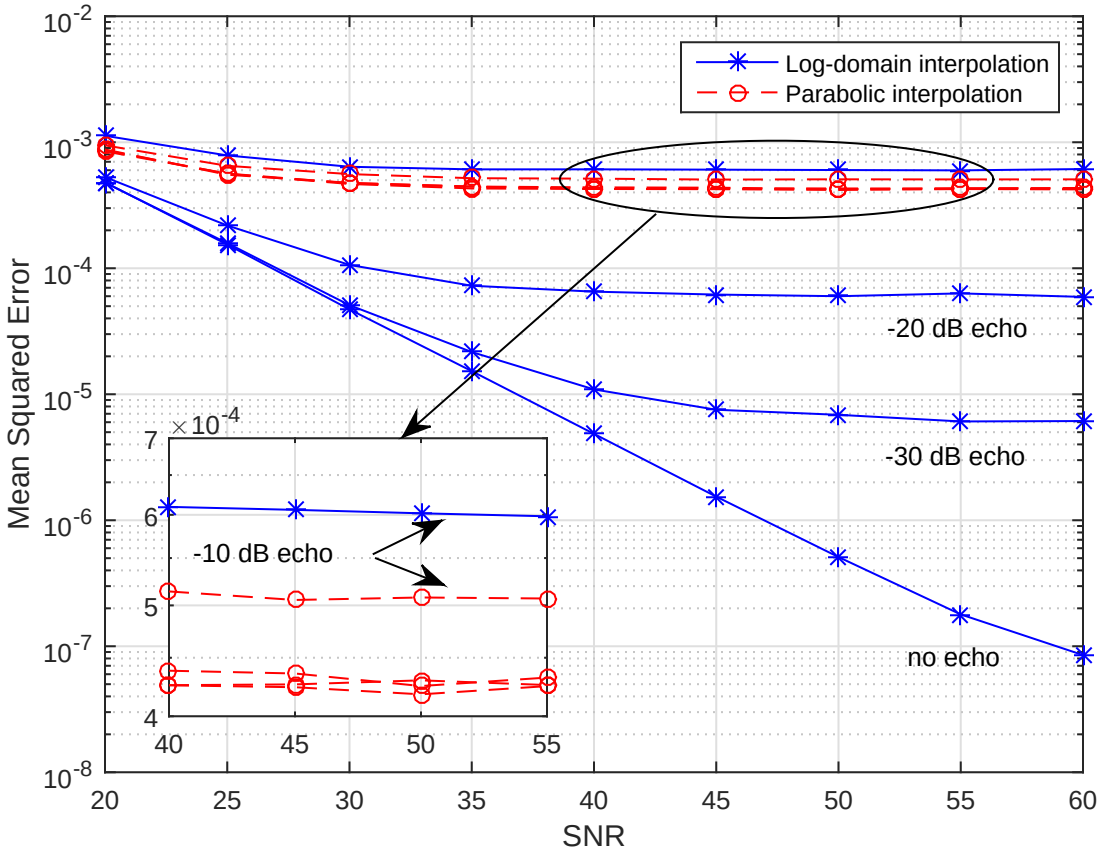

Figure 4.4 Detection accuracy versus SNR for various echo power.

Next, accuracy is measured when noise and distortion are added to the channel. The example used for the analysis is drawn from a DOCSIS 3.0 single carrier QAM receiver. The best sampling moment at the receiver is the peak of the timing recovery pulse [C4.14, C4.15]. DOCSIS 3.0 receivers are designed for a channel having a main path and possibly 3 echoes, but the strength of one will dominate the other two. The power in the dominant echo will be at most -10 dB with respect to the power of the main path. The delay of the dominant echo with respect to the main path is uniformly distributed between 0 and 3 samples. The timing recovery pulse is the output of a correlator. The digital sequence used for timing estimation is a Barker sequence [C4.9] with a length of 13 samples. The tandem of the pulse shaping and matched filter produces a raised cosine pulse with $L = 2$ and $r = 0.25$.

Fig. 4.4 shows the MSE on the estimation of τ_{peak} of the timing recovery pulse. Results

are shown for channels with echos of strength $-\infty$ dB, -30 dB, -20 dB and -10 dB. The delays for all echoes were uniformly distributed between 0 and 3 samples. It can be seen in Fig. 4.4 that without echo distortion the log-domain approach significantly outperformed the parabolic approach. Furthermore, timing MSE of the log-domain approach scales well with signal to noise ratio (SNR) while the timing MSE of the parabolic method reaches an apparent error floor around 4×10^{-4}. For the case of the strong -10 dB echo, the timing recovery pulse is sufficiently distorted to affect the log-domain approach, dropping its performance beneath that of the parabolic approach.

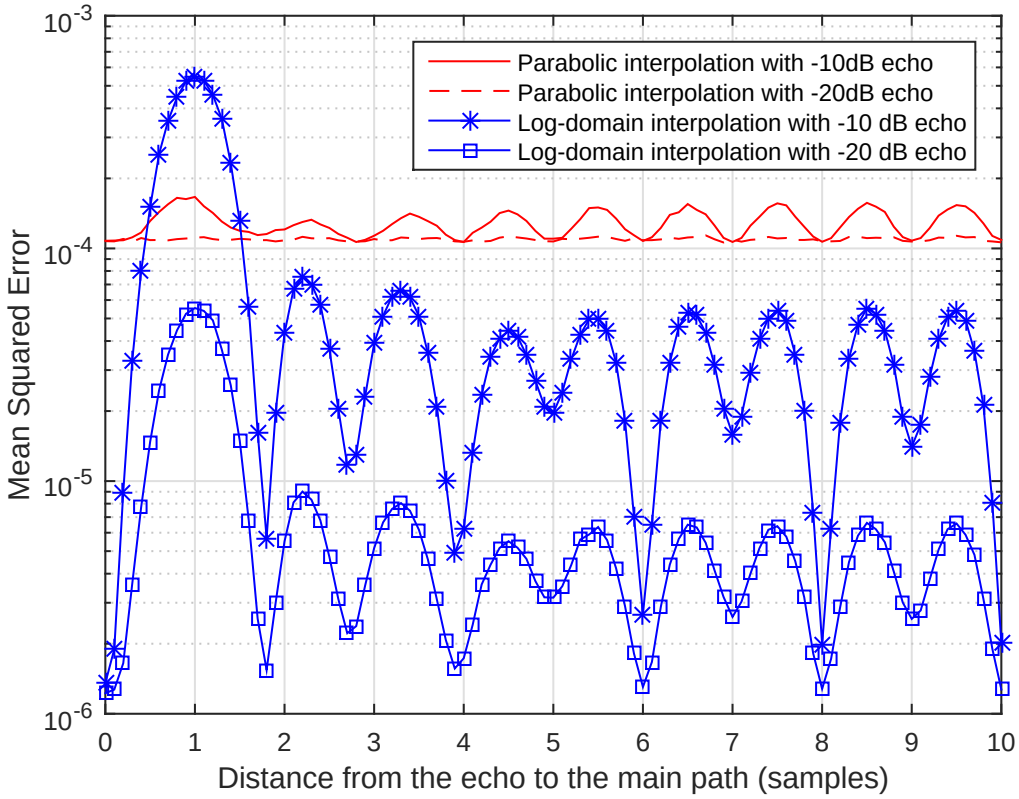

Figure 4.5 Comparing mean squared error versus echo delay for SNR = 40 dB.

To further analyze the influence of echo distortion on peak detection, Fig. 4.5 shows the MSE versus echo delay for a single echo with a power of -10 dB and -20 dB with respect to the main path and an SNR of 40 dB. As can be seen on the figure, for the case of -10 dB echo, the log-domain approach performs worse than the parabolic approach for echo delays that are about a sample away from the main path. However, for the case of -20 dB echo,

the log-domain approach is always better than the parabolic approach. It is obvious that the log-domain approach is sensitive to short echo delays which are in the range from 0.5 to 1.5 samples with respect to the main path.

4.5 Conclusions

This paper proposes a technique for accurately locating the peak of an analog signal after it has been sampled. The technique fits two samples in the vicinity of the peak to a parameterized pulse in log domain. The technique outperforms the well-known three sample parabolic interpolation in applications where the channel has either no echoes or weak echoes or echoes with long delays. Aside from the main advantage of being more accurate, a secondary advantage of the proposed technique is its economy.

References

[C4.1] T. T. Nguyen, E. Salt, B. Berscheid, and H. H. Nguyen, "Digital Interpolating Peak Locator," in *Proc. IEEE Int. Symp. Industrial Electronics.*, June 2016.

[C4.2] R. Boucher and J. C. Hassab, "Analysis of discrete implementation of generalized cross correlator," *IEEE Trans. Acoustics, Speech and Signal Proc.*, vol. 29, pp. 609–611, June 1981.

[C4.3] K. Fyhn, M. Duarte, and S. Jensen, "Compressive Parameter Estimation for Sparse Translation-Invariant Signals Using Polar Interpolation," *IEEE Trans. Signal Process.*, vol. 63, pp. 870–881, Feb. 2015.

[C4.4] V. Nguyen, "A low complexity parameter estimation technique for LFMCW signals," *IEEE Trans. Aerospace and Electronic Systems*, vol. 50, pp. 2554–2563, Oct. 2014.

[C4.5] A. Grennberg and M. Sandell, "Estimation of subsample time delay differences in narrowband ultrasonic echoes using the Hilbert transform correlation," *IEEE Trans. Ultrasonics, Ferroelectrics, and Frequency Control*, vol. 41, pp. 588–595, Sept. 1994.

[C4.6] Y. X. Yuan and J. Salt, "Range and depth estimation using a vertical array in a correlated multipath environment," *IEEE J. Oceanic Engineering*, vol. 18, pp. 500 – 507, Oct. 1993.

[C4.7] M. Simaan, "A Frequency-Domain Method for Time-Shift Estimation and Alignment of Seismic Signals," *IEEE Trans. Geoscience and Remote Sensing*, vol. GE-23, pp. 132 – 138, Mar. 1985.

[C4.8] P. Stoica and R. Moses, *Spectral Analysis of Signals*. Pearson Prentice Hall, 2005.

[C4.9] M. Soltanalian and P. Stoica, "Computational Design of Sequences With Good Correlation Properties," *IEEE Trans. Signal Process.*, vol. 60, pp. 2180–2193, May 2012.

[C4.10] J. G. Proakis, *Digital Communications*. McGraw Hill, 2001.

[C4.11] A. Papoulis and S. U. Pillai, *Probability, Random Variables, and Stochastic Processes*. McGraw-Hill Higher Education, 4 ed., 2002.

[C4.12] J. S. Walther, "A Unified Algorithm for Elementary Functions," in *Proc. Spring Joint Computer Conf.*, (New York, NY, USA), pp. 379–385, 1971.

[C4.13] P. Smith, C. Furse, and J. Gunther, "Analysis of spread spectrum time domain reflectometry for wire fault location," *IEEE Sensors J.*, vol. 5, Dec 2005.

[C4.14] Cable Television Laboratories, Inc., "Downstream RF Interface Specification," Nov 2011.

[C4.15] M. R. Choudhury and D. E. Dodds, "Effect of timing error on equalizer performance," in *IEEE Conf. on Electrical and Computer Engineering*, pp. 1–5, May 2013.

5. Channel Estimation Techniques for DOCSIS 3.1 Upstream Channels

Published as:

Tung T. Nguyen, Brian Berscheid, Ha H. Nguyen and J. Eric Salt,"A novel iterative OFDM channel estimation technique for DOCSIS 3.1 uplink channels," Submitted to *IEEE Transactions on Broadcasting*, Jul. 2016. [1] [2]

As explained in Chapter 2, the conventional time-domain equalizer is not suitable for wide-band systems due to the complexity issue. This is why OFDM/OFDMA is employed in DOCSIS 3.1, which allows to use a low-complexity frequency-domain equalizer to reverse the multipath channel effect. In order for the frequency-domain equalizer to work effectively, the multipath channel's parameters must be estimated prior to equalization. Furthermore, the channel estimation is required to be highly accurate. This is because DOCSIS 3.1 employs very high-order modulation schemes, hence a small inaccuracy in channel estimation may lead to a severe demodulation error.

Given the importance of the channel estimation process in DOCSIS 3.1 systems, this chapter proposes an OFDM channel estimation technique that jointly considers the effects of coarse timing error and multipath propagation. Moreover, the proposed technique examines a practical scenario for DOCSIS 3.1 channel that takes into account fractional timing error and non sample-space echo delays. To simplify implementation, the proposed technique does not use the channel state information (e.g. second-order statistic of the channel impulse

[1] A conference version is published as Tung T. Nguyen, Brian Berscheid, Ha H. Nguyen and J. Eric Salt, "Iterative channel estimation for DOCSIS 3.1 uplink channels," *in Proc. IEEE Global Telecommun. Conf.*, Dec. 2016.

[2] A patent application based on this technique has been filed as Brian Berscheid, Tung T. Nguyen, J. Eric Salt, Ha H. Nguyen, "Method of Estimating the Frequency Response of Multipath Channels," US Patent Application 14/976,854 Filed December, 2015.

response or the noise power, which are difficult to obtain in real systems). It is shown that the proposed technique outperforms conventional OFDM channel estimation methods when applied in DOCSIS 3.1 systems.

The main contribution to this manuscript comes from the student (first author), while the three co-supervisors provide equal supervision effort.

A Novel Iterative OFDM Channel Estimation Technique for DOCSIS 3.1 Uplink Channels

Tung T. Nguyen, *Member, IEEE*, Brian Berscheid *Member, IEEE*,
Ha H. Nguyen, *Senior Member, IEEE* and Eric Salt, *Member, IEEE*

Abstract

This paper presents an Orthogonal Frequency Division Multiplexing (OFDM) channel estimation technique that jointly considers the effects of coarse timing error and multipath propagation. Many conventional approaches only consider an optimistic scenario where timing synchronization is perfect and each of the channel delays is an integer number of system samples. In realistic scenarios timing offsets and echo delays are not integer multiples of the systems sampling period. This threatens sub-carrier orthogonality and causes leakage in the discrete Fourier transform (DFT)-based channel estimation method. Such leakage leads to poor estimation and consequently reduces the system's overall performance. This paper proposes a novel iterative channel estimation technique, which considers the practical scenario of fractional timing error and non sample-space echo delays. The proposed method does not require channel state information (e.g. second-order statistic of the channel impulse responses or the noise power). Moreover, timing error can be conveniently obtained with the proposed technique. Simulation shows that, when comparing OFDM channel estimation techniques under Data Over Cable Service Interface Specification (DOCSIS) 3.1 realistic channel conditions, the proposed algorithm significantly outperforms all conventional methods known to the authors.

Index terms

OFDM, DOCSIS, channel estimations, inter-symbol interference, timing error estimation.

5.1 Introduction

The demand for data services has steadily increased putting continuous pressure on data service providers to increase the data throughput of their networks. Cable television (CATV) networks are governed by a set of DOCSIS standards that place hard limits on bandwidth and data rates. The latest version of the DOCSIS standard, DOCSIS 3.1 was released in October 2013. DOCSIS 3.1 increases the bandwidth and data throughput available in CATV networks by up to 10 Gbps downstream and 1 Gbps upstream.

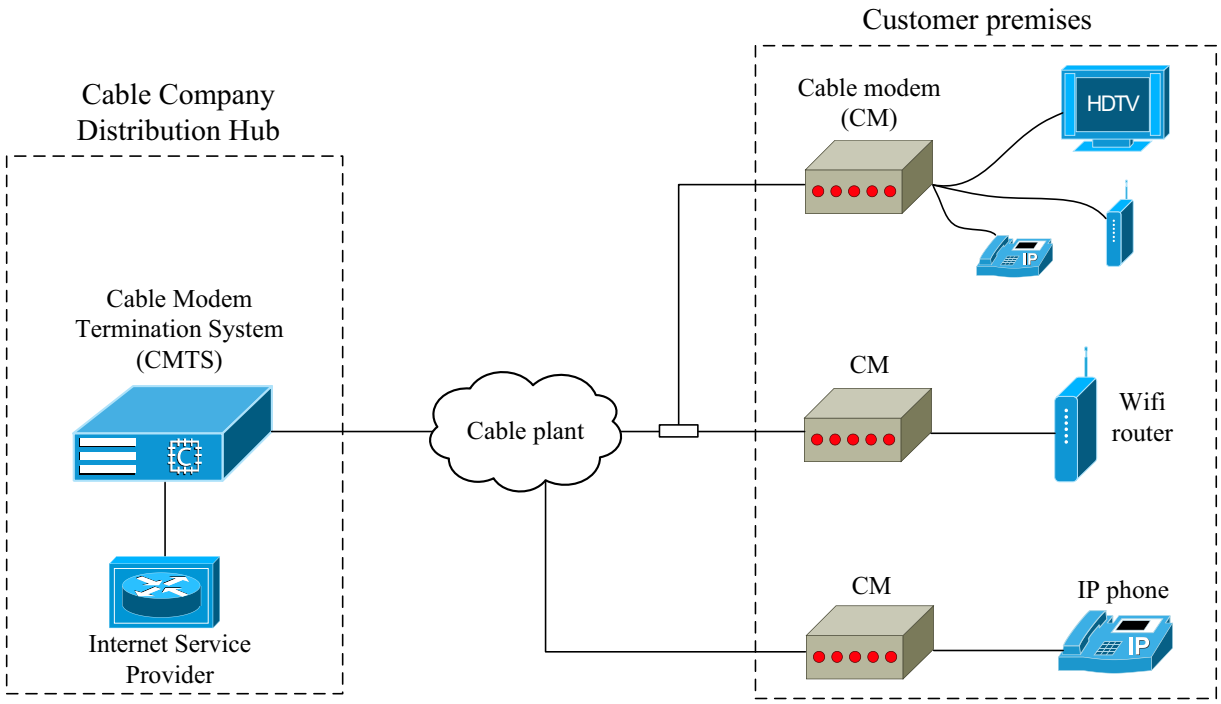

Figure 5.1 DOCSIS broadband cable network.

Fig. 5.1 shows a simplified structure of a cable network. There are two main components in the network: a cable modem (CM), which is located at the customer premises, and a cable modem termination system (CMTS), located at the cable company's headend. The CMTS is responsible for managing a large number of cable modems residing in subscribers' homes. The CMTS allocates channel resources for each CM and schedules times for sending and receiving packets. The CMTS has both Ethernet and Radio Frequency (RF) interfaces, such that the Internet traffic can be routed from the Ethernet interface, through the CMTS and then onto the RF ports that are connected to coaxial cable networks, eventually reaching

the cable modem in the subscriber's home.

DOCSIS 3.1 is markedly different from prior versions of the standard in that OFDM is used in the downstream and Orthogonal Frequency Division Multiple Access (OFDMA) is used in the upstream directions. By effectively modulating signals on narrow-band carriers, OFDM/OFDMA can mitigate inter-symbol interference while simplifying the structure of the channel equalizer.

Cable plants generate a number of channel impairments, some of which differ from typical OFDMA systems discussed in the literature such as 3G, LTE, or WiFi. The greatest difference is in the transmission medium, which is coaxial cable for CATV systems. Coaxial cable is slow time-varying channel, over which the signal from a CM reaches a CMTS via a main path and possibly several echo paths. Aside from using DOCSIS 3.1-compliant modulators/demodulators, cable operators must upgrade their cable infrastructure to satisfy the standard imposed by DOCSIS 3.1. For example, while DOCSIS 3.0 allows the power in a single echo to be 10 dB lower than the main path's power, DOCSIS 3.1 restricts the power in an echo to be at least 16 dB lower than the main path's power. The latest DOCSIS standard opens new opportunities as well as presenting issues and challenges for researchers to make contributions into the newly specified cable systems.

While OFDMA systems have been studied for many years, the DOCSIS 3.1 upstream standard is unique in that it tries to maximize the overall spectral efficiency of the newly upgraded cable system (i.e., to operate as close to the Shannon limit as conditions allow). In particular, the OFDMA upstream multicarrier system contains up to 3800 data sub-carriers occupying a total bandwidth of 96 MHz. Moreover, the DOCSIS 3.1 upstream specifications introduce very high order modulation schemes, with mandatory support up to 1024-QAM and optional support for constellations up to 4096-QAM, which allows the network operators to maximize their network capacity and take advantage of signal quality improvements.

In order to effectively demodulate a spectrally efficient signal, it is necessary to employ coherent demodulation, which involves estimation and tracking of the multipath channel. With a dense constellation such as 4096-QAM, the signal can be easily distorted by a small

impairment, therefore demodulation must be aided with a highly accurate channel estimator. To serve this purpose, DOCSIS 3.1 specifies a pilot-based wide-band probing mode, where the sub-carriers of an OFDMA symbol are dedicated to channel estimation. The method of estimating such a channel from the pilot signal is unspecified, as the standard leaves opportunities for DOCSIS 3.1 device manufacturers to come up with their own design. Since approaches that had been used for typical OFDMA systems are either having inadequate performance, unsuitable for the coaxial cable model or too complex, device manufacturers are eagerly looking for new efficient designs specifically for the DOCSIS 3.1 problem at hand.

There are several channel estimation techniques that have been studied for pilot-based estimation. The simplest one, which is Least Square (LS) estimation [C5.1], does not require any channel state information (CSI). LS estimators work with samples in the frequency domain and are relatively low in complexity. However, they suffer from relatively high mean-square error, which is proportional to the power of additive white Gaussian noise (AWGN).

A better technique, which also performs estimation in the frequency domain, is linear minimum mean-square error (LMMSE) estimation [C5.2]. This technique yields much better performance than the LS estimator, especially under low signal-to-noise ratio (SNR) scenarios. The major drawback of the LMMSE estimator is that it requires knowledge of the channel auto-correlation matrix and the noise variance, which are usually unknown at the receiver. The computational complexity of the LMMSE estimator is also very high as it requires a matrix inversion. Many have attempted to reduce the complexity of the LMMSE estimator [C5.3, C5.4] at the expense of a small sacrifice in estimation accuracy.

Another very good approach uses discrete Fourier transform (DFT) based channel estimation. The DFT-based method firstly employs an LS estimator to obtain the channel's frequency response (CFR). Then the discrete-time channel impulse response (CIR) is obtained by performing an inverse discrete Fourier transform (IDFT) on the CFR. Since the energy of the CIR is typically concentrated in a few taps having short delays, the algorithm's performance can be improved if a few taps whose power is significantly higher than noise are preserved while the rest are forced to zero [C5.5]. This operation is commonly referred to as

denoising. After denoising, the CIR is transformed back to the frequency domain to obtain the estimated CFR. Consequently, the DFT approach helps to remove the noise power from the LS-estimated CFR. In general, DFT-based methods have moderate complexity thanks to Fast Fourier Fransform (FFT) algorithms and perform much better than the LS estimator [C5.6] at low SNRs.

However, with the DFT method, performance degradation can occur due to leakage between samples in the discrete-time CIR. There are two sources of leakage. The first is leakage by multipath components that have non sample-spaced delays. In the case of non sample-spaced delays, the energy from a single multipath component is spread over multiple sample-spaced taps in the discrete time CIR. When the noise-only taps are eliminated, portions of the leakage energy are also removed and thus the estimation will show an error floor. The second type of leakage emerges if not all sub-carriers are used for channel estimation. In particular, in a typical OFDM system, the sub-carriers at both ends of the spectrum are left null to form guard bands. Not using the end sub-carriers degrades the performance of DFT-based techniques as this is equivalent to placing a rectangular window in the frequency domain which translates to convolution with a sinc-like function in the time domain. This causes the energy of the CIR to spread out in time. Denoising cuts off the tails of the sinc-like functions causing ripples around the edge sub-carriers when the denoised CIR is converted back to the frequency domain [C5.7]. This phenomenon is often referred to as an "edge effect" or "border effect" and results in estimation errors not being equally distributed over all sub-carriers. To date studies that effectively address the two leakage issues of the DFT-based techniques have not been found.

The usefulness of the standard channel estimation techniques discussed above is somewhat limited in DOCSIS 3.1 systems, as upstream wideband probing has a subcarrier skipping option. In subcarrier skipping mode, multiple upstream users transmit wideband probing signals on different subcarriers of the same OFDM symbol. Each user transmits on a different set of subcarriers that are spaced K sub-carriers apart, where K is the number of simultaneous users. The use of subcarrier skipping with K simultaneous users allows a K-fold increase in the efficiency of the wideband probing process as compared to a single user

probing scheme. However, it places additional computational burden on the receiver, which must generate an estimate of the entire channel for each user despite receiving pilots on only every Kth subcarrier.

This paper proposes a novel channel estimation technique that can be applied effectively to generic OFDMA systems, but was designed with DOCSIS 3.1 in mind. The technique iteratively removes the DFT leakage energy and detects the major taps in the CIR without any prior knowledge of the CSI. This method not only substantially enhances the channel estimation accuracy, but also can, at the same time, accurately detect the timing error. Furthermore, it is capable of accurately interpolating between received pilot symbols, making it well-suited to channel probing schemes involving DOCSIS 3.1-style subcarrier skipping.

5.2 OFDM Channel Model

Consider the baseband-equivalent OFDMA system shown in Fig. 5.2. The channel bandwidth is divided into N sub-carriers, M of which are used for channel estimation and are assigned BPSK preamble symbols $X[m],\ m = 0, 1, \ldots, M-1$. According to DOCSIS 3.1 specifications [C5.8], there are guard bands at both ends of the allocated spectrum that cannot be used for data transmission. This restricts the location of the pilot sub-carriers, which are usually centered at the middle of the allocated spectrum. Denote the vector of pilot sub-carrier indexes as $\boldsymbol{\mathcal{S}} = [\mathcal{S}(0), \mathcal{S}(1), \ldots, \mathcal{S}(M-1)]$. The vector elements are related by $\mathcal{S}(m) = \mathcal{S}(0) + mK, m = 0, 1, \ldots, M-1$, where $\mathcal{S}(0)$ is the "start" sub-carrier and K is sub-carrier "skipping" factor [C5.8].

The OFDMA transmitter employs an IDFT module of size N for modulation. The standard IDFT/DFT is not used here, but rather the transform pair specified in DOCSIS 3.1, where the sub-carrier indexing is shifted by $-N/2$ sub-carriers. Using the DOCSIS 3.1 IDFT, the transmitted time-domain samples are written as $x_d[n] = \frac{1}{\sqrt{N}} \sum_{m=0}^{M-1} X[m] \exp\left(\frac{j2\pi(\mathcal{S}(m)-N/2)n}{N}\right)$, where $n = 0, 1, \ldots, N-1$ denotes the sample index. To avoid inter-symbol interference (ISI), a cyclic prefix (CP) consisting of N_{CP} samples is prefixed to the OFDMA symbol. After performing parallel to serial (P/S) conversion, the time-domain samples are serially passed through a DAC clocked at sampling rate F_s and filtered with an image rejection filter to

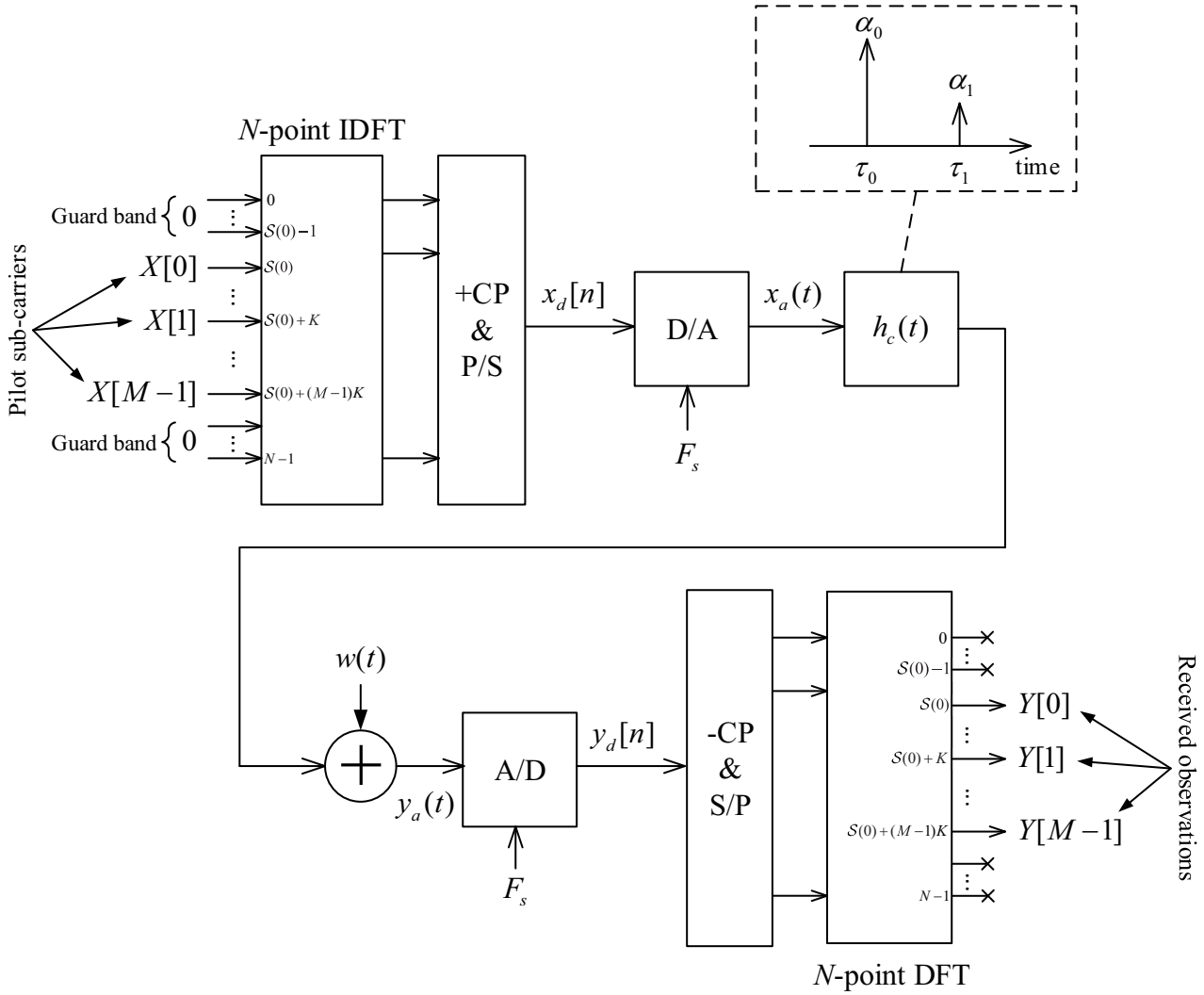

Figure 5.2 Baseband-equivalent OFDM system for channel probing.

generate the continuous-time signal. Assuming ideal digital to analog (D/A) conversion, the continuous-time signal can be expressed as

$$x_a(t) = \frac{1}{\sqrt{N}} \sum_{m=0}^{M-1} X[m] \exp\left(\frac{j2\pi(\mathcal{S}(m) - N/2)(t - T_g)}{NT_s}\right), \quad 0 \le t \le NT_s + T_g, \qquad (5.1)$$

where $T_s = 1/F_s$ is the sampling period and T_g is guard interval in seconds. T_g is the duration of the CP which is $N_{CP}T_s$. It is obvious that after the CP is inserted $x_a(t) = x_a(t+NT_s), \forall\, t \in [0, T_g]$. In general, the validity of (5.1) depends on how well the up-conversion is performed.

A channel in a coaxial cable distribution network consists of many paths created by impedance mismatches among terminals and ports of devices that make up the network. Each path is characterized by a gain factor α_i and an associated delay ϵ_i normalized to sampling period T_s. Without loss of generality, ϵ_0 is taken to be 0 and ϵ_i is the delay of path i^{th} relative to the delay of path 0^{th}. The impulse response of the baseband-equivalent of the multipath channel is given by

$$h_c(t) = \alpha_0 \delta(t) + \sum_{i=1}^{L-1} \alpha_i \delta(t - \epsilon_i T_s), \tag{5.2}$$

where δ is the Dirac delta function. Furthermore, the parameter L is the number of paths in the multipath channel. The channel's delay spread in seconds is $\epsilon_{\max} T_s$, where $\epsilon_{\max} = \max_{i=1,\ldots,L-1} \epsilon_i$ which is the delay of the longest multipath component relative to the first.

The continuous time signal received at the receiver is the convolution of the transmitted signal and the impulse response of the multipath channel. That is

$$\begin{aligned} y_a(t) &= \int_0^\infty h_c(\theta) x_a(t - \tau_0 T_s - \theta) \mathrm{d}\theta + w(t) \\ &= \alpha_0 x_a(t - \tau_0 T_s) + \sum_{i=1}^{L-1} \alpha_i x_a(t - \tau_0 T_s - \epsilon_i T_s) + w(t), \end{aligned} \tag{5.3}$$

where $w(t)$ is a zero-mean AWGN noise process and τ_0 is the timing offset (normalized to sampling period T_s) introduced by error in detecting the start time of the received OFDMA symbol. There are many coarse timing estimation techniques, e.g. [C5.9, C5.10, C5.11, C5.12], that can detect the start time of the received OFDMA frame. With coarse timing, the detection error can be a few samples.

Assume the system is well designed so that the length of the CP is greater than the channels delay spread, i.e., $T_g > \epsilon_{\max} T_s$, as illustrated in Fig. 5.3. To ensure the DFT output is ISI-free, the error in the coarse timing detection must not exceed the slack in the CP. This places the following constraint on coarse timing error:

$$0 \leq \tau_0 \leq N_{CP} - \epsilon_{\max}, \tag{5.4}$$

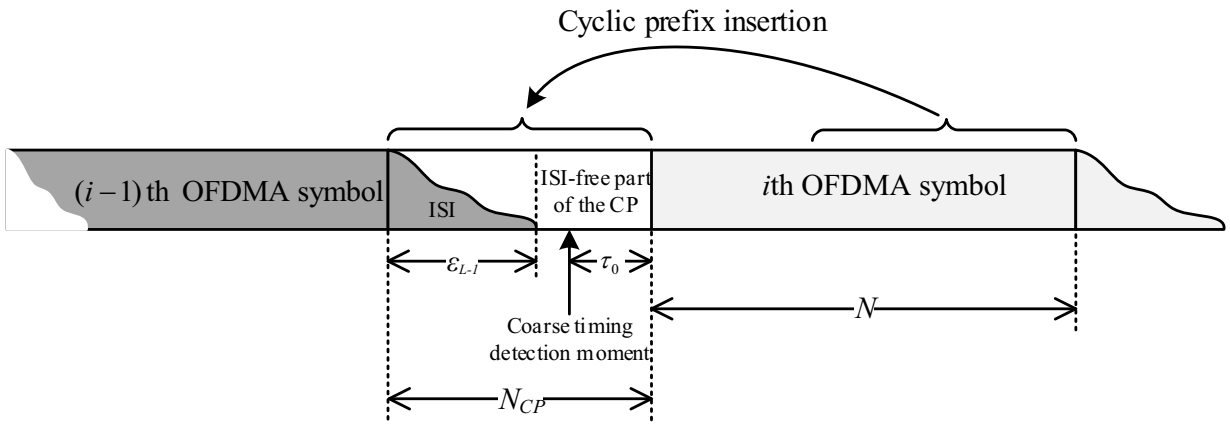

Figure 5.3 ISI-free channel condition.

where τ_0 is the error in coarse timing in samples. By defining $\tau_i = \epsilon_i + \tau_0,\ i = 1, 2, \ldots, L-1$, the timing error can be incorporated into the base-band channel to get the more realistic impulse response given by:

$$h_{\boldsymbol{\tau}}(t) = \sum_{i=0}^{L-1} \alpha_i \delta(t - \tau_i T_s). \tag{5.5}$$

Then (5.3) simplifies to

$$y_a(t) = \sum_{i=0}^{L-1} \alpha_i x_a(t - \tau_i T_s) + w(t), \quad 0 \le t \le NT_s + T_g. \tag{5.6}$$

The continuous time signal is band-limited and digitally sampled at the receiver with the sampling rate F_s. After coarse timing detection is performed, the CP is removed. The discrete-time samples after CP removal are given by

$$y_d[n] = y_a(t)\Big|_{t=nT_s+T_g} = \sum_{i=0}^{L-1} \alpha_i x_a(nT_s + T_g - \tau_i T_s) + w[n], \quad n = 0, 1, \ldots, N-1, \tag{5.7}$$

where $w[n]$ is $w(t)$ sampled at $t = nT_s + T_g$ after it has been band-limited. $w[n]$ is complex white Gaussian noise with zero mean and variance σ_w^2. To recover the data, an N-point DFT

block transforms the time-domain sequence back to the frequency-domain:

$$\begin{aligned} Y[m] &= \frac{1}{\sqrt{N}} \sum_{n=0}^{N-1} y_d[n] \exp\left(\frac{-j2\pi(\mathcal{S}(m) - N/2)n}{N}\right) \\ &= \frac{1}{N} \sum_{n=0}^{N-1} \sum_{i=0}^{L-1} \alpha_i \sum_{k=0}^{M-1} X[k] \exp\left(\frac{j2\pi(\mathcal{S}(k) - N/2)(nT_s - \tau_i T_s)}{NT_s}\right) \times \\ &\quad \exp\left(\frac{-j2\pi(\mathcal{S}(m) - N/2)n}{N}\right) + W[m], \quad m = 0, 1, \ldots, M-1, \end{aligned} \tag{5.8}$$

where

$$W[m] = \sum_{n=0}^{N-1} \frac{w[n]}{\sqrt{N}} \exp\left(\frac{-j2\pi(\mathcal{S}(m) - N/2)n}{N}\right), \tag{5.9}$$

is complex Gaussian noise with zero mean and variance σ_w^2. Then

$$\begin{aligned} Y[m] &= \frac{1}{N} \sum_{k=0}^{M-1} X[k] \sum_{i=0}^{L-1} \alpha_i \sum_{n=0}^{N-1} \exp\left(\frac{j2\pi(\mathcal{S}(k) - \mathcal{S}(m))n}{N}\right) \times \\ &\qquad \exp\left(\frac{-j2\pi(\mathcal{S}(m) - N/2)\tau_i}{N}\right) + W[m] \\ &= X[m] \sum_{i=0}^{L-1} \alpha_i \exp\left(\frac{-j2\pi(\mathcal{S}(m) - N/2)\tau_i}{N}\right) + W[m] \\ &= X[m]H[m] + W[m], \end{aligned} \tag{5.10}$$

where $H[m]$ is the multipath channel's frequency response at sub-carrier $\mathcal{S}(m)$, given as

$$H[m] = \sum_{i=0}^{L-1} \alpha_i \exp\left(\frac{-j2\pi(\mathcal{S}(m) - N/2)\tau_i}{N}\right), \tag{5.11}$$

With the input/output model of (5.10), the signal-to-noise ratio (SNR) of the received signal is defined as

$$\text{SNR} = \frac{\mathbb{E}\{|X[m]H[m]|^2\}}{\mathbb{E}\{|W[m]|^2\}} = \frac{\sum_{i=0}^{L-1} |\alpha_i|^2}{\sigma_w^2}. \tag{5.12}$$

The task of channel estimation is to obtain the frequency response of the *entire* channel,

which is ideally given as

$$F[k] = \sum_{i=0}^{L-1} \alpha_i \exp\left(\frac{-j2\pi(k - N/2)\tau_i}{N}\right), \quad k = 0, 1, \ldots, N-1 \tag{5.13}$$

from known values of $X[m]$ and observed values of $Y[m]$. Since $F[k]$ is a function of the $2L$ unknown parameters $\left\{\alpha_i, \tau_i\right\}_{i=0}^{L-1}$, an estimate of $F[k]$ is obtained from estimates of the $2L$ unknown parameters. Conventional methods estimate M values of $H[m]$ and then interpolate between them to get the entire frequency response, $F[k]$. In this paper we present a novel method to obtain $2L$ values of $\left\{\alpha_i, \tau_i\right\}_{i=0}^{L-1}$. As long as $2L \ll M$, it will be demonstrated in the following section that estimating $\left\{\alpha_i, \tau_i\right\}_{i=0}^{L-1}$ directly provides a better estimate of $F[k]$.

5.3 Conventional Channel Estimation Techniques

This section will discuss several methods that have been used in conventional OFDM/OFDMA systems. The performance measure used for comparison is the mean squared error between the ideal and estimated channel frequency responses.

5.3.1 Least-square (LS) estimation

This is the simplest estimation technique, which can be performed without any knowledge of the channel statistic. In particular, the LS technique estimates the frequency response of the channel at M frequencies from M observations. The M estimates, $\left\{\widehat{H}_{\mathrm{LS}}[m]\right\}_{m=0}^{M-1}$ minimize $\sum_{m=0}^{M-1}\left|Y[m] - \widehat{H}_{\mathrm{LS}}[m]X[m]\right|^2$ [C5.2]. The first step is to estimate the frequency response of the channel at the frequencies of the M pilot tones. The frequency response for pilot tone m, which is sub-carrier $\mathcal{S}(m)$, is calculated by

$$\widehat{H}_{\mathrm{LS}}[m] = \frac{Y[m]}{X[m]} = \frac{H[m]X[m] + W[m]}{X[m]} = H[m] + \widetilde{W}[m], \quad m = 0, 1, \ldots, M-1. \tag{5.14}$$

To be consistent with the literature in the field, the index m in $\widehat{H}_{LS}[m]$ is the pilot tone number, not the more commonly used sub-carrier number. The preamble symbols $X(m)$ are drawn from a BPSK constellation and are taken to be ± 1 without loss of generality. Then

$\widetilde{W}[m] = \frac{W[m]}{X[m]} = \pm W[m]$ are Gaussian distributed random variables with zero mean and variance σ_w^2.

The second step is to apply interpolation on $\widehat{H}_{\text{LS}}[m]$ to obtain the estimated channel transfer function, $\widehat{F}_{LS}[k]$. There are a number of well-known interpolation techniques, including linear interpolation and Spline Cubic interpolation [C5.13]. A detailed discussion of the merits of various interpolation techniques is outside the scope of this paper. Ideally, with zero interpolation error, the MSE performance of the LS estimator can be approximated in closed form as:

$$\text{MSE}_{\text{LS}} = \mathbb{E}\left\{\left|H[m] - \widehat{H}_{\text{LS}}[m]\right|^2\right\} = \mathbb{E}\left\{\left|\widetilde{W}[m]\right|^2\right\} = \sigma_w^2. \tag{5.15}$$

5.3.2 DFT-based estimation

The DFT-based algorithm was designed for channels with an impulse response that has most of its energy concentrated in a small number of taps [C5.14, C5.6, C5.15]. The DFT-based method reduces the noise in the estimate of the impulse response by setting the low energy taps to zero. Therefore, the performance of the DFT-based method depends on the energy distribution in the impulse response. If the energy is concentrated in a few taps then it will outperform the LS estimation.

The method involves a series of steps beginning with an M-point IDFT on $\widehat{H}_{\text{LS}}[m]$ to obtain the approximation of the time-domain channel response of the LS estimated channel[3],

[3]Only under a set of special conditions $g[n]$ becomes the impulse response of the physical channel, i.e. $g[n] = h_c(t)\big|_{t=nT_s}$. The special conditions are $h_c(t) = 0$ for $t > NT_s/K$ and $M = N/K$, i.e. no guard bands.

given as

$$
\begin{aligned}
g[n] &= \frac{1}{M}\sum_{m=0}^{M-1} \widehat{H}_{\mathrm{LS}}[m] \exp\left(\frac{j2\pi mn}{M}\right) \\
&= \underbrace{\frac{1}{M}\sum_{m=0}^{M-1} H[m] \exp\left(\frac{j2\pi mn}{M}\right)}_{d[n]} + \underbrace{\frac{1}{M}\sum_{m=0}^{M-1} \widetilde{W}[m] \exp\left(\frac{j2\pi mn}{M}\right)}_{\eta[n]} \qquad (5.16) \\
&= d[n] + \eta[n], \quad n = 0, 1, \ldots, M-1,
\end{aligned}
$$

where $\eta[n]$ is AWGN noise with zero mean and variance $\sigma_\eta^2 = \frac{\sigma_w^2}{M}$. $d[n]$, which is the signal component of $g[n]$, can be shown to be

$$
\begin{aligned}
d[n] &= \frac{1}{M}\sum_{m=0}^{M-1}\sum_{i=0}^{L-1} \alpha_i \exp\left(\frac{-j2\pi(\mathcal{S}(m) - N/2)\tau_i}{N}\right) \exp\left(\frac{j2\pi mn}{M}\right) \\
&= \frac{1}{M}\sum_{m=0}^{M-1}\sum_{i=0}^{L-1} \alpha_i \exp\left(\frac{-j2\pi(\mathcal{S}(0) + mK - N/2)(M\tau_i/N)}{M}\right) \times \\
&\qquad \exp\left(\frac{j2\pi(\mathcal{S}(0) + mK - N/2)(n/K)}{M}\right) \exp\left(\frac{-j2\pi(\mathcal{S}(0) - N/2)(n/K)}{M}\right) \\
&= \exp\left(\frac{-j2\pi(\mathcal{S}(0) - N/2)n}{MK}\right) \sum_{i=0}^{L-1} \frac{\alpha_i}{M} \sum_{m=0}^{M-1} \exp\left(\frac{j2\pi(\mathcal{S}(0) + mK - N/2)(n/K - M\tau_i/N)}{M}\right) \\
&= \exp\left(\frac{-j2\pi(\mathcal{S}(0) - N/2)n}{MK}\right) \sum_{i=0}^{L-1} \frac{\alpha_i}{M} \exp\left(\frac{j\pi\Delta(n - MK\tau_i/N)}{MK}\right) \frac{\sin\left(\pi(n - MK\tau_i/N)\right)}{\sin\left(\pi(n - MK\tau_i/N)/M\right)},
\end{aligned}
\qquad (5.17)
$$

where $\Delta = 2\mathcal{S}(0) - N + (M-1)K$. It should be noted that if delay τ_i is an integer multiple of $N/(MK)$, the i^{th} channel path energy is concentrated in a single tap located at $n = MK\tau_i/N$, otherwise the energy is distributed among all the taps of $d[n]$.

The second step is to select the significant taps of $g[n]$. A tap is deemed to be significant if its magnitude is much larger than the standard deviation of the noise, i.e. $|g[n]| \gg \sigma_\eta$.

Specifically, the sequence $\widehat{g}[n]$ of significant taps is constructed from $g[n]$ using:

$$\widehat{g}[n] = \begin{cases} g[n], & \text{if } |g[n]| > \Lambda_{\text{th}} \\ 0, & \text{otherwise,} \end{cases} \tag{5.18}$$

where the constant Λ_{th} is a threshold used to select the most significant taps of $g[n]$.

The third step is to estimate the frequency response at all sub-carriers by taking the N-point DFT of $\widehat{g}[n]$. This yields:

$$\begin{aligned} \widehat{F}_{\text{DFT}}[k] &= \sum_{n=0}^{M-1} \widehat{g}[n] \exp\left(\frac{-j2\pi k(nN/MK)}{N}\right), \\ &= \sum_{n=0}^{M-1} \widehat{g}[n] \exp\left(\frac{-j2\pi kn}{MK}\right), \quad k = 0, 1, \ldots, N-1. \end{aligned} \tag{5.19}$$

The MSE of the DFT-based estimator can be conveniently expressed as

$$\begin{aligned} \text{MSE}_{\text{DFT}} &= \mathbb{E}\left\{\frac{1}{N}\sum_{k=0}^{N-1}\left|\widehat{F}_{\text{DFT}}[k] - F[k]\right|^2\right\} = \mathbb{E}\left\{\sum_{n=0}^{M-1}|\widehat{g}[n] - d[n]|^2\right\} \\ &= \mathbb{E}\left\{\sum_{n:|g[n]|>\Lambda_{\text{th}}}\left|g[n] - d[n]\right|^2\right\} + \mathbb{E}\left\{\sum_{n:|g[n]|\leq\Lambda_{\text{th}}}\left|d[n]\right|^2\right\} \\ &= \frac{\sigma_w^2 L_{\text{sig}}}{M} + P_{\text{prune}} \end{aligned} \tag{5.20}$$

where L_{sig} is the number of significant taps and P_{prune} is the power in the $N - L_{\text{sig}}$ taps of $d[n]$ that were pruned in the construction of $\widehat{g}[n]$. Raising the threshold Λ_{th} reduces L_{sig}, thus reducing $\frac{\sigma_w^2 L_{\text{sig}}}{M}$, but increases P_{prune}. Since both contribute to the MSE, there is an optimum value of Λ_{th} that minimizes the MSE [C5.6].

To reduce the complexity of the DFT method, system designers should select parameter M as a power of 2 to make use of the Fast Fourier Transform that can be applied to calculate (5.16), otherwise (5.16) will be computationally demanding.

5.3.3 LMMSE estimator

The LMMSE estimator is a linear estimator that employs the second-order statistics of the channel to minimize the MSE [C5.1, C5.3]. Since it uses information about the channel, the LMMSE estimator performs much better than the LS estimator. This extra information is the auto covariance function of the channel.

The LMMSE estimation of the channel can be done in either the time domain or the frequency domain [C5.3]. In the time-domain, from (5.16) and (5.17), one has

$$\boldsymbol{g} = \boldsymbol{d} + \boldsymbol{\eta}, \tag{5.21}$$

where $\boldsymbol{g}, \boldsymbol{d}$ and $\boldsymbol{\eta}$ are defined as the column vectors:

$$\boldsymbol{g} = \big[g[0], g[1], \ldots, g[M-1]\big]^T, \tag{5.22}$$

$$\boldsymbol{d} = \big[d[0], d[1], \ldots, d[M-1]\big]^T, \tag{5.23}$$

$$\boldsymbol{\eta} = \big[\eta[0], \eta[1], \ldots, \eta[M-1]\big]^T. \tag{5.24}$$

The problem becomes estimating $\boldsymbol{d}$ from $\boldsymbol{g}$. The best linear estimator in the mean-square error sense is given as [C5.2, C5.3, C5.1]

$$\widehat{\boldsymbol{g}} = \frac{\boldsymbol{R}_{dd}}{\boldsymbol{R}_{dd} + \boldsymbol{I}_M \sigma_\eta^2} \boldsymbol{g}, \tag{5.25}$$

where $\boldsymbol{R}_{dd}$ is the auto-covariance matrix of $\boldsymbol{d}$, which is assumed to be known apriori, and $\boldsymbol{I}_M$ is the $M \times M$ identity matrix. From (5.17), the vector $\boldsymbol{d}$ can be expressed as

$$\boldsymbol{d} = \underbrace{\begin{bmatrix} D_{0,0} & D_{0,1} & \cdots & D_{0,L-1} \\ D_{1,0} & D_{1,1} & \cdots & D_{1,L-1} \\ \vdots & \vdots & \vdots & \vdots \\ D_{M-1,0} & D_{M-1,1} & \cdots & D_{M-1,L-1} \end{bmatrix}}_{\boldsymbol{D}} \underbrace{\begin{bmatrix} \alpha_0 \\ \alpha_1 \\ \vdots \\ \alpha_{L-1} \end{bmatrix}}_{\boldsymbol{\alpha}} = \boldsymbol{D}\boldsymbol{\alpha}, \tag{5.26}$$

where $\boldsymbol{D}$ is the $M \times L$ matrix with elements $D_{n,l},\ n = 0, 1, \ldots, M-1,\ l = 0, 1, \ldots, L-1$,

defined as

$$D_{n,l} = \exp\left(\frac{-j2\pi(\mathcal{S}(0) - N/2)n}{MK}\right) \exp\left(\frac{j\pi\Delta(n - MK\tau_l/N)}{MK}\right) \times \frac{\sin\left(\pi(n - MK\tau_l/N)\right)}{M\sin\left(\pi(n - MK\tau_l/N)/M\right)}. \quad (5.27)$$

It is pointed out that matrix $\boldsymbol{D}\boldsymbol{D}^{\mathcal{H}}$, where the superscript $\mathcal{H}$ denote the conjugate transpose operation, is generally known as the leakage matrix [C5.16, C5.17], since it describes the correlation among the discrete channel taps. When the echoes in the channel have delays that are integer multiples of $NT_s/(MK)$, $\boldsymbol{D}\boldsymbol{D}^{\mathcal{H}}$ becomes a size $M \times M$ diagonal matrix.

The delays in the multipath propagation environment in CATV networks change slowly, or not at all, over time. Assuming the delays and magnitudes of the echoes are known, i.e., τ_i and $|\alpha_i|$ are known, the channel auto-covariance matrix can be written as

$$\begin{aligned}\boldsymbol{R}_{dd} &= \mathbb{E}\left\{\boldsymbol{d}\boldsymbol{d}^{\mathcal{H}}\right\} = \mathbb{E}\left\{\boldsymbol{D}\boldsymbol{\alpha}\boldsymbol{\alpha}^{\mathcal{H}}\boldsymbol{D}^{\mathcal{H}}\right\} = \boldsymbol{D}\mathbb{E}\left\{\boldsymbol{\alpha}\boldsymbol{\alpha}^{\mathcal{H}}\right\}\boldsymbol{D}^{\mathcal{H}} \\ &= \boldsymbol{D}\begin{bmatrix} |\alpha_0|^2 & 0 & 0 & 0 \\ 0 & |\alpha_1|^2 & 0 & 0 \\ 0 & 0 & \ddots & 0 \\ 0 & 0 & 0 & |\alpha_{L-1}|^2 \end{bmatrix}\boldsymbol{D}^{\mathcal{H}}\end{aligned} \quad (5.28)$$

The mean squared estimation error can be expressed as [C5.18]

$$\begin{aligned}\mathrm{MSE}_{\mathrm{LMMSE}} &= \mathbb{E}\left\{\|\widehat{\boldsymbol{g}} - \boldsymbol{d}\|^2\right\} = \sigma_\eta^2 \,\mathrm{Trace}\left(\frac{\boldsymbol{R}_{dd}}{\boldsymbol{R}_{dd} + \boldsymbol{I}_M\sigma_\eta^2}\right) \\ &= \frac{\sigma_w^2}{M}\sum_{i=0}^{M-1}\frac{\lambda_i}{\lambda_i + \sigma_w^2/M} = \frac{\sigma_w^2}{M}\sum_{i=0}^{L-1}\frac{|\alpha_i|^2}{|\alpha_i|^2 + \sigma_w^2/M}\end{aligned} \quad (5.29)$$

where $\lambda_i,\ i = 0, 1, \ldots, M-1$ are the eigenvalues of $\boldsymbol{R}_{dd}$.

There are many approaches to finding a good approximation for $\boldsymbol{R}_{dd}$, such as those presented in [C5.14, C5.15, C5.17] and [C5.19]. All require additional observations or some apriori knowledge of the channel. Clearly, the accuracy of the LMMSE channel estimator

depends on quality of the estimate used for $\boldsymbol{R}_{dd}$. The MSE given by (5.29) assumes $\boldsymbol{R}_{dd}$ is known exactly. Since $\boldsymbol{R}_{dd}$ is rarely if ever known exactly, (5.28) serves as an optimistic performance target for channel estimators.

5.4 Iterative Channel Estimation Algorithm

In this section, a novel channel estimation algorithm is developed for channels where the only distortion is due to multipath propagation. This iterative algorithm is developed sequentially in three sub-sections. Sub-section 5.4.1 constructs a basic estimator that illustrates the principle of operation. The algorithm is revised in sub-section 5.4.2 to significantly enhance the accuracy and then generalized in sub-section 5.4.3. Sub-section 5.4.4 then summarizes the final algorithm.

5.4.1 Iterative channel estimation

The iterative algorithm assumes a multipath channel that has a finite number of paths and is designed to estimate the channel parameters, which are time delays τ_i and amplitudes α_i, $i = 0, 1, \ldots, L-1$, of the paths. The estimated parameters, denoted as $\widehat{\tau}_i$ and $\widehat{\alpha}_i$ can be used to obtain the frequency response of the *entire* channel with the following equation:

$$\widehat{F}_{\text{ICE}}[k] = \sum_{i=0}^{L-1} \widehat{\alpha}_i \exp\left(\frac{-j2\pi(k - N/2)\widehat{\tau}_i}{N}\right), \tag{5.30}$$

where $k = 0, 1, \ldots, N-1$. The proposed iterative channel estimation technique starts by performing an inverse Fourier transform on $\frac{Y[m]}{X[m]}$. The transform has a length of NU/K, where U is a parameter which controls the resolution of the resulting time domain vector $q[u]$, given as

$$q[u] = \frac{1}{M} \sum_{m=0}^{M-1} \frac{Y[m]}{X[m]} \exp\left(\frac{j2\pi\left(m + (\mathcal{S}(0) - N/2)/K\right)u}{NU/K}\right). \tag{5.31}$$

Note that U is not necessarily an integer, but rather a number that is chosen to make NU/K an integer. One suggestion is to make NU/K a power of two so that the complexity of (5.31)

can be reduced through the use of Fast Fourier Transform algorithm. Equation (5.31) can be simplified as follows:

$$\begin{aligned} q[u] &= \underbrace{\frac{1}{M}\sum_{m=0}^{M-1} H[m]\exp\left(\frac{j2\pi\big(m+(\mathcal{S}(0)-N/2)/K\big)u}{NU/K}\right)}_{b[u]} + \rho[u] \\ &= b[u]+\rho[u], \quad u=0,1,\ldots,NU/K-1, \end{aligned} \tag{5.32}$$

where $\rho[u]$ is the AWGN noise component given by

$$\rho[u] = \frac{1}{M}\sum_{m=0}^{M-1}\frac{W[m]}{X[m]}\exp\left(\frac{j2\pi\big(m+(\mathcal{S}(0)-N/2)/K\big)u}{NU/K}\right), \tag{5.33}$$

which has zero mean and variance $\sigma_\rho^2 = \frac{\sigma_w^2}{M}$.

Since $M \le N/K$, the complexity of (5.31) is equivalent to an $\frac{NU}{K}$-point IDFT. The signal component of (5.31) can be expressed in a more meaningful form as

$$\begin{aligned} b[u] &= \frac{1}{M}\sum_{m=0}^{M-1}\sum_{i=0}^{L-1}\alpha_i\exp\left(\frac{-j2\pi(\mathcal{S}(m)-N/2)\tau_i}{N}\right)\exp\left(\frac{j2\pi\big(m+(\mathcal{S}(0)-N/2)/K\big)u}{NU/K}\right) \\ &= \sum_{i=0}^{L-1}\alpha_i\frac{1}{M}\sum_{m=0}^{M-1}\exp\left(\frac{-j2\pi(\mathcal{S}(0)+mK-N/2)\tau_i}{N}\right)\exp\left(\frac{j2\pi\big(mK+\mathcal{S}(0)-N/2\big)u/U}{N}\right) \\ &= \sum_{i=0}^{L-1}\alpha_i\frac{1}{M}\exp\left(\frac{j2\pi(\mathcal{S}(0)-N/2)(u/U-\tau_i)}{N}\right)\sum_{m=0}^{M-1}\exp\left(\frac{j2\pi mK(u/U-\tau_i)}{N}\right) \\ &= \sum_{i=0}^{L-1}\alpha_i\frac{1}{M}\exp\left(\frac{j2\pi(\mathcal{S}(0)-N/2)(u/U-\tau_i)}{N}\right)\frac{\exp\left(\frac{j2\pi MK(u/U-\tau_i)}{N}\right)-1}{\exp\left(\frac{j2\pi K(u/U-\tau_i)}{N}\right)-1} \\ &= \sum_{i=0}^{L-1}\alpha_i\underbrace{\exp\left(\frac{j\pi\big(2\mathcal{S}(0)-N+(M-1)K\big)(u/U-\tau_i)}{N}\right)\frac{\sin\big(\pi(u/U-\tau_i)MK/N\big)}{M\sin\big(\pi(u/U-\tau_i)K/N\big)}}_{\Upsilon\left(\frac{u}{U}-\tau_i\right)} \\ &= \sum_{i=0}^{L-1}\alpha_i\Upsilon\left(\frac{u}{U}-\tau_i\right), \quad u=0,1,\ldots,\langle NU/K\rangle-1, \end{aligned} \tag{5.34}$$

where $b[u]$ is represented as a summation of several channel path kernel functions, $\Upsilon(\cdot)$, that

are delayed by τ_i and scaled in amplitude by α_i. Each $\Upsilon(\cdot)$ function represents a path in the channel.

The shape of the $\Upsilon(\cdot)$ function is more clear when it is expressed as

$$\Upsilon(x) = \exp\left(\frac{j\pi\Delta x}{N}\right) \text{psinc}\left(\frac{xK}{N}, M\right), \tag{5.35}$$

where $\Delta = 2\mathcal{S}(0) - N + (M-1)K$ and $\text{psinc}(x, M)$ is the Dirichlet or periodic sinc function, defined as

$$\text{psinc}(x, M) = \begin{cases} \frac{\sin(\pi M x)}{M \sin(\pi x)}, & x \notin \mathbb{Z} \\ (-1)^{x(M-1)}, & x \in \mathbb{Z}. \end{cases} \tag{5.36}$$

The $\Upsilon(x)$ function has zero-crossings at integer multiples of $N/(MK)$, and therefore the width of the main lobe is $2N/(MK)$, which is inversely proportional to KM, as illustrated in Fig. 5.4. This relatively narrow main lobe ensures the magnitude of $\Upsilon(x)$ has a sharp peak at $x = 0$. Furthermore, the peak value of $\Upsilon(x)$ is 1.

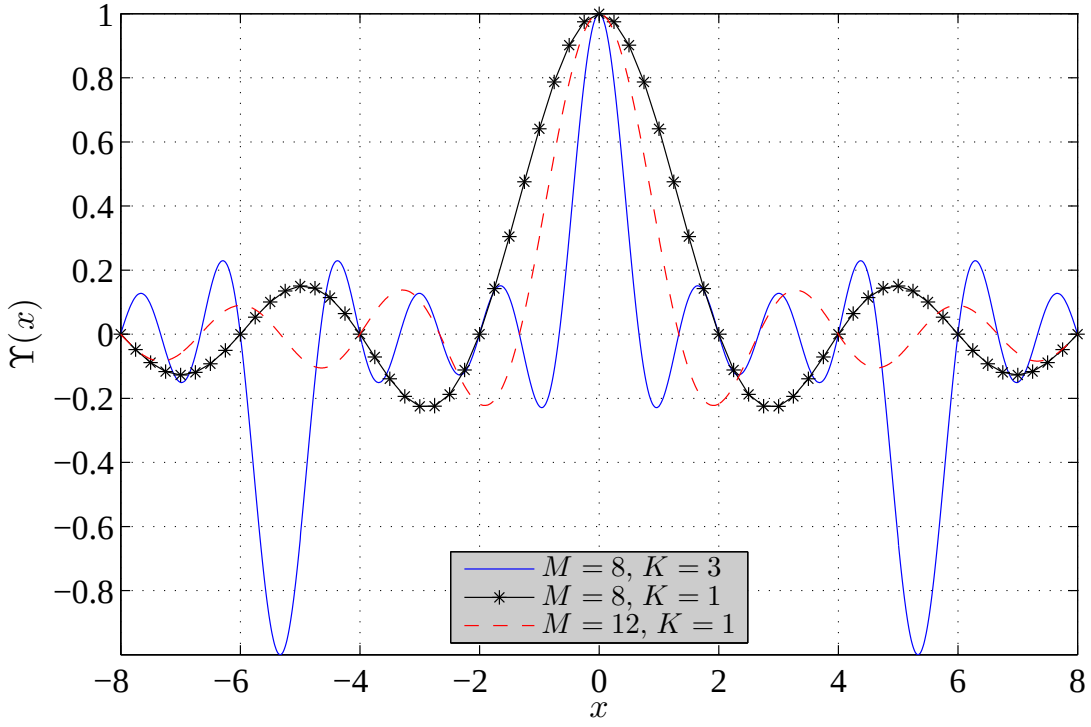

Figure 5.4 Example of Υ function, taken with $N = 16$, $\Delta = 0$ and different values for parameters M and K, indicated on the Figure.

The iterative channel estimation technique centers on peak detection of $q[u]$. Without loss of generality, the path indices are defined based on path strength such that

$$|\alpha_0| \geq |\alpha_1| \geq \ldots \geq |\alpha_{L-1}|. \tag{5.37}$$

Provided U is chosen large enough for

$$\left|\frac{\langle \tau_i U \rangle}{U} - \tau_i\right| < \left|\frac{\langle \tau_j U \rangle}{U} - \tau_i\right|, \quad \forall j \neq i,\ i = 0, 1, 2, \ldots, L-1, \tag{5.38}$$

where $\langle \cdot \rangle$ indicates rounding, then from (5.35), (5.37) and (5.38) it follows that

$$\left|\alpha_0 \Upsilon\left(\frac{\langle \tau_0 U \rangle}{U} - \tau_0\right)\right| > \left|\alpha_i \Upsilon\left(\frac{\langle \tau_0 U \rangle}{U} - \tau_i\right)\right|, \quad \forall i = 1, 2, \ldots, L-1. \tag{5.39}$$

This indicates $\alpha_0 \Upsilon\big(\langle \tau_0 U \rangle / U - \tau_0\big)$ is the dominant magnitude contributor to $b\left[\langle \tau_0 U \rangle\right]$. The estimates of α_i and τ_i can be found iteratively starting with a rough approximation of the parameters of the first path, α_0 and τ_0 as follows:

$$\begin{aligned} u_0^{[1]} &= \underset{u=0,1,\ldots,NU/K-1}{\operatorname{argmax}} \big|q[u]\big|, \\ \widehat{\tau}_0^{[1]} &= u_0^{[1]}/U \text{ and } \widehat{\alpha}_0^{[1]} = q[u_0^{[1]}], \end{aligned} \tag{5.40}$$

where the superscript $^{[1]}$ indicates that the value was found on the first iteration. Rough estimates of the parameters of the second path can then be generated by subtracting the estimated contribution of the first path, $\widehat{\alpha}_0^{[1]} \Upsilon(u/U - \widehat{\tau}_0^{[1]})$, from $q[u]$ to yield:

$$\begin{aligned} u_1^{[1]} &= \underset{u=0,1,\ldots,NU/K-1}{\operatorname{argmax}} \big|q[u] - \widehat{\alpha}_0^{[1]} \Upsilon(u/U - \widehat{\tau}_0^{[1]})\big|, \\ \widehat{\tau}_1^{[1]} &= u_1^{[1]}/U \text{ and } \widehat{\alpha}_1^{[1]} = q[u_1^{[1]}] - \widehat{\alpha}_0^{[1]} \Upsilon(u_1^{[1]}/U - \widehat{\tau}_0^{[1]}). \end{aligned} \tag{5.41}$$

Similarly, rough estimates for $\alpha_i,\ \tau_i,\ i = 2, 3, \ldots, L-1$, are found using

$$\begin{aligned} u_i^{[1]} &= \underset{u=0,1,\ldots,NU/K-1}{\operatorname{argmax}} \Big| q[u] - \sum_{k=0}^{i-1} \widehat{\alpha}_k^{[1]} \Upsilon(u/U - \widehat{\tau}_k^{[1]}) \Big|, \\ \widehat{\tau}_i^{[1]} &= u_i^{[1]}/U \text{ and } \widehat{\alpha}_i^{[1]} = q[u_i^{[1]}] - \sum_{k=0}^{i-1} \widehat{\alpha}_k^{[1]} \Upsilon(u_i^{[1]}/U - \widehat{\tau}_k^{[1]}). \end{aligned} \tag{5.42}$$

After a set of rough estimates are obtained, the estimates for α_0 and τ_0 can be improved by removing the estimated contributions from paths 1 to $L-1$ from $q[u]$. The improved estimates of α_0 and τ_0 in this 2^{nd} iteration are given by

$$\begin{aligned} u_0^{[2]} &= \underset{u=0,1,\ldots,NU/K-1}{\operatorname{argmax}} \left| q[u] - \sum_{k=1}^{L-1} \widehat{\alpha}_k^{[1]} \Upsilon(u/U - \widehat{\tau}_k^{[1]}) \right|, \\ \widehat{\tau}_0^{[2]} &= u_0^{[2]}/U \text{ and } \widehat{\alpha}_0^{[2]} = q[u_0^{[2]}] - \sum_{k=1}^{L-1} \widehat{\alpha}_k^{[1]} \Upsilon(u_0^{[2]}/U - \widehat{\tau}_k^{[1]}). \end{aligned} \tag{5.43}$$

In a similar manner, the better estimates of α_0 and τ_0 can be used to produce better estimates of α_1 and τ_1. The estimates can be continually improved in this iterative fashion. Specifically, the impulse response of path i on iteration ν is approximated by

$$\begin{aligned} q_i^{[\nu]}[u] &\stackrel{\text{def}}{=\!=} q[u] - \sum_{l=0}^{i-1} \widehat{\alpha}_l^{[\nu]} \Upsilon(u/U - \widehat{\tau}_l^{[\nu]}) - \sum_{k=i+1}^{L-1} \widehat{\alpha}_k^{[\nu-1]} \Upsilon(u/U - \widehat{\tau}_k^{[\nu-1]}) \\ &\approx \alpha_i \Upsilon(u/U - \tau_i), \end{aligned} \tag{5.44}$$

and the improved estimates of α_i and τ_i are given by

$$\begin{aligned} u_i^{[\nu]} &= \underset{u=0,1,\ldots,NU/K-1}{\operatorname{argmax}} \left| q_i^{[\nu]}[u] \right|, \\ \widehat{\tau}_i^{[\nu]} &= u_i^{[\nu]}/U \text{ and } \widehat{\alpha}_i^{[\nu]} = q_i^{[\nu]}[u_i^{[\nu]}]. \end{aligned} \tag{5.45}$$

After several iterations the estimates reach, or at least nearly reach, steady state values, which are denoted as $\widehat{\alpha}_i$ and $\widehat{\tau}_i$. These steady state values are used in (5.30) to obtain the estimated frequency response of the channel.

The accuracy of the aforementioned approximation is significantly affected by the error

in $\widehat{\tau}_i$. The proposed approach ideally estimates $\widehat{\tau}_i = \langle \tau_i U \rangle / U$. Thus the estimation error in the worst case could be $0.5/U$, i.e., $|\widehat{\tau}_i - \tau_i| \leq 0.5/U$. Obviously, larger U reduces the error at the cost of increasing the estimator's complexity. Furthermore, the error in $\widehat{\tau}_i$ has the corresponding effect of diminishing the magnitude of $\widehat{\alpha}_i$ by up to $|\Upsilon(0.5/U)|$. For the case of $M = N$, the reduction can be as much as -4 dB, -0.9 dB and -0.2 dB for $U = 1$, $U = 2$ and $U = 4$, respectively.

5.4.2 Further enhancing estimation accuracy

The estimate for τ_i used in section 5.4.1 is rather crude. The accuracy of this estimator, which simply rounds the argument of (5.45) to the sample nearest to the peak, can be improved by interpolating between the two samples nearest the peak, thus eliminating the rounding error, as shown in Fig. 5.5.

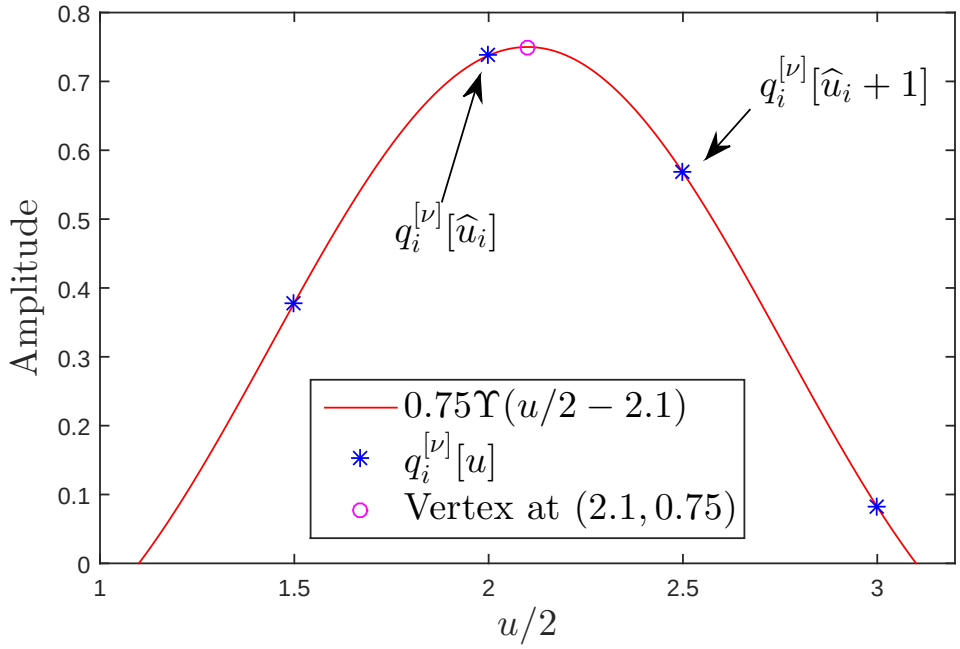

Figure 5.5 Example of interpolation with $U = 2$. Υ function is obtained with $M = N = 32$ and $\Delta = 0$.

There are several ways of interpolating between two samples. The method used here is to find the parameters $\bar{\tau}_i$ and $\bar{\alpha}_i$ that force $\bar{\alpha}_i \Upsilon(\widehat{u}_i/U - \bar{\tau}_i)$ and $\bar{\alpha}_i \Upsilon\big((\widehat{u}_i + 1)/U - \bar{\tau}_i\big)$ to equal the samples on each side of the peak of the argument, where the pair of indices $u = \widehat{u}_i$ and

$u = \widehat{u}_i + 1$ can be found, or at least estimated as

$$\begin{aligned}
\widehat{u}_{i,\max} &= \underset{u=0,1,\ldots,NU/K-1}{\operatorname{argmax}} \left| q_i^{[\nu]}[u] \right|, \\
\widehat{u}_i &= \begin{cases} \widehat{u}_{i,\max}, & \text{if } \left| q_i^{[\nu]}[\widehat{u}_{i,\max}+1] \right| \geq \left| q_i^{[\nu]}[\widehat{u}_{i,\max}-1] \right|, \\ \widehat{u}_{i,\max}-1, & \text{otherwise.} \end{cases}
\end{aligned} \tag{5.46}$$

As shown in Fig. 5.4, the $\Upsilon(\cdot)$ function has multiple extrema. For the interpolation to yield a unique and accurate solution, the two samples used must be on opposite sides of the main lobe peak, i.e. $\widehat{u}_i/U \leq \bar{\tau}_i \leq (\widehat{u}_i+1)/U$. Under this constraint, the solutions for $\bar{\alpha}_i$ and $\bar{\tau}_i$ can be found by simultaneously solving

$$\begin{cases} \bar{\alpha}_i \Upsilon(\widehat{u}_i/U - \bar{\tau}_i) = q_i^{[\nu]}[\widehat{u}_i], \\ \bar{\alpha}_i \Upsilon((\widehat{u}_i+1)/U - \bar{\tau}_i) = q_i^{[\nu]}[\widehat{u}_i+1], \\ \widehat{n}_i/U \leq \bar{\tau}_i \leq (\widehat{n}_i+1)/U. \end{cases} \tag{5.47}$$

The solution for $\bar{\tau}_i$ from (5.47) is given by $\bar{\tau}_i = (\widehat{u}_i + \theta_i)/U$, where θ_i is the root of the following equation:

$$\frac{q_i^{[\nu]}[\widehat{u}_i]}{q_i^{[\nu]}[\widehat{u}_i+1]} = \frac{\Upsilon(-\theta_i/U)}{\Upsilon\big((1-\theta_i)/U\big)} = \exp\left(\frac{-j\pi\Delta}{NU}\right) \frac{\sin\left(\frac{\pi MK\theta_i}{NU}\right) \sin\left(\frac{\pi K(1-\theta_i)}{NU}\right)}{\sin\left(\frac{\pi K\theta_i}{UN}\right) \sin\left(\frac{\pi MK(1-\theta_i)}{UN}\right)}, \tag{5.48}$$

where $\theta_i \in [0,1]$ and Δ is defined in (5.35). Since $\sin(x) > 0 \; \forall x \in (0,\pi)$, equation (5.48) can be simplified to

$$\frac{\left| q_i^{[\nu]}[\widehat{u}_i] \right|}{\left| q_i^{[\nu]}[\widehat{u}_i+1] \right|} = \frac{\sin\left(\frac{\pi MK\theta_i}{NU}\right) \sin\left(\frac{\pi K(1-\theta_i)}{NU}\right)}{\sin\left(\frac{\pi K\theta_i}{UN}\right) \sin\left(\frac{\pi MK(1-\theta_i)}{UN}\right)} = \Gamma(\theta_i). \tag{5.49}$$

Denoting $\kappa = \frac{\left| q_i^{[\nu]}[\widehat{u}_i] \right|}{\left| q_i^{[\nu]}[\widehat{u}_i+1] \right|}$, θ_i can be found as

$$\theta_i = \Gamma^{-1}(\kappa), \quad 0 \leq \theta_i \leq 1. \tag{5.50}$$

Solving (5.50) in real-time is possible, but very costly due to the complexity of $\Gamma^{-1}(\cdot)$. Moreover, the precision of the computation must be very high when θ_i is close to 0 or 1, i.e., when the denominator of (5.49) approaches zero.

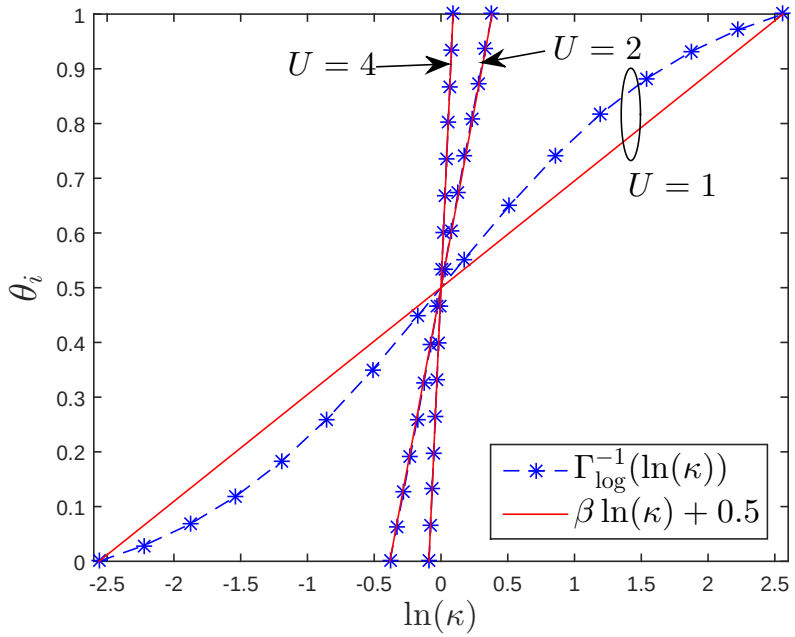

Figure 5.6 θ_i as a function of $\ln(\kappa)$. Other parameters are selected as $M = 1900, K = 1, N = 2048$ and $U = 1, 2, 4$.

Fortunately, (5.50) can be modified to yield a hardware friendly form. Since $\kappa = e^{\ln(\kappa)}$, θ_i can be expressed as the function of $\ln(\kappa)$ defined as $\Gamma^{-1}_{\log}(\ln(\kappa)) = \Gamma^{-1}(e^{\ln(\kappa)}) = \Gamma^{-1}(\kappa)$. The simplicity of the logarithmic form is illustrated in Fig. 5.6, where θ_i is plotted as a function of $\ln(\kappa)$ for 3 values of U. It is apparent from Fig. 5.6 that for $U \geq 2$, $\Gamma^{-1}_{\log}(\cdot)$ is nearly linear and can be approximated by $\Gamma^{-1}_{\log}(\ln(\kappa)) \approx \beta \ln(\kappa) + 0.5$, where β is a coefficient that can be pre-computed from system parameters K, M, N and U as

$$\beta = \frac{-0.5}{\ln\left(\sin(\frac{\pi MK}{NU})/M\right) - \ln\left(\sin(\frac{\pi K}{NU})\right)}. \tag{5.51}$$

θ_i can then be approximated by

$$\theta_i \simeq \beta \ln(\kappa) + 0.5 = \beta\big(\ln(\big|q_i^{[\nu]}[\widehat{u}_i]\big|) - \ln(\big|q_i^{[\nu]}[\widehat{u}_i + 1]\big|)\big) + 0.5, \tag{5.52}$$

for $U \geq 2$. Note that (5.52) does not require a division operation, and is therefore significantly

more hardware friendly than (5.50).

There are two ways to find the echo strength $\bar{\alpha}_i$. The straight forward approach is to substitute θ_i into (5.47), yielding the following expression:

$$\bar{\alpha}_i = \frac{q_i^{[\nu]}[\widehat{u}_i]}{\Upsilon\big(-\theta_i/U\big)}. \tag{5.53}$$

Although (5.53) is computationally simple, it amplifies the noise and ISI present in $q_i^{[\nu]}[\widehat{u}_i]$. In the worst-case scenario, this results in the noise and ISI being increased by a factor of $|\Upsilon(1/U)^{-1}|$. This factor decreases as the resolution factor U increases. For the system parameters shown in Fig. 5.6, the worst case amplification values are 11.12 dB, 1.66 dB and 0.39 dB for $U = 1, 2$ and 4, respectively. Alternatively, $\bar{\alpha}_i$ can be found as:

$$\bar{\alpha}_i = \frac{1}{M}\sum_{m=0}^{M-1} \widehat{H}_{\mathrm{LS}}[m] \exp\left(\frac{j2\pi(\mathcal{S}(m) - N/2)\bar{\tau}_i}{N}\right) - \sum_{k=0,k\neq i}^{L-1} \bar{\alpha}_k \Upsilon\left(\bar{\tau}_i - \bar{\tau}_k\right), \tag{5.54}$$

which is computationally more expensive than (5.53), but it prevents the noise and interference amplification effect. Consequently, for $U \leq 2$, it is advisable to use (5.54) in order to avoid severe performance degradation due to noise amplification. For $U > 2$, the amplification effect is minimal, so the more computationally efficient (5.53) is preferred.

5.4.3 Estimating the number of channel paths

The ICE technique does not require any channel information, except for an initial estimation of the number of channel paths, denoted as $\widehat{L}$, which must be determined before performing the iterative channel estimation. In reality, the parameter L in (5.34) should be replaced by $\widehat{L}$ so that the ICE algorithm will estimate $2\widehat{L}$ channel parameters, $\{\alpha_i, \tau_i\}_{i=0}^{\widehat{L}-1}$, instead of $2L$. Therefore it is reasonable to expect the best performance achieved when $\widehat{L} = L$.

In some cases, such as CATV networks, the plant is maintained to limit the number of dominant echo paths. For example, networks that use DOCSIS 3.0 equipment are restricted to $L \leq 4$ while networks that use DOCSIS 3.1 equipment are restricted to $L \leq 2$. There-

fore it is reasonable to fix parameter $\widehat{L} = 2$ in equipment used in DOCSIS 3.1 upstream transmission.

Although the ICE technique was initially designed for DOCSIS 3.1 systems, it applies to general OFDMA systems, where the parameter L is not so constrained and the initial guesstimation of $\widehat{L}$ affects the channel estimation performance. In particular, with the proposed ICE technique, if the number of paths in the channel is under-detected, i.e. $\widehat{L} < L$, there will be performance degradation as the model is unable to compensate for the least significant channel paths. If the number of path is over-detected, i.e. $\widehat{L} > L$, the ICE technique would interpret noise samples as channel paths. Since the power of noise is much less than the power of an echo, e.g. $|\alpha_{_{L-1}}|^2 \gg \sigma_\eta^2$, performance degradation due to over-detection is generally less than the degradation caused by under-detection. Therefore, it is better to error on the side of over-detection.

Moreover, the performance degradation caused by over-detection can be mitigated as the significant power difference between echoes and noise can be exploited to suppress the over-detected paths. In particular, a threshold can be employed to differentiate the channel paths from the noise. The thresholding process replaces (5.53) and (5.54) with:

$$\bar{\alpha_i} = \begin{cases} 0, & \text{if } \left|q_i^{[\nu]}[\widehat{u}_i]\right| \leq \lambda_T \\ \frac{1}{M}\sum_{m=0}^{M-1} \widehat{H}_{\mathrm{LS}}[m] \exp\left(\frac{j2\pi(\mathcal{S}(m)-N/2)\bar{\tau}_i}{NT_s}\right) & \\ \qquad - \sum_{k=0,k\neq i}^{L-1} \bar{\alpha}_k \Upsilon\left(\bar{\tau}_i - \bar{\tau}_k\right), & \text{if } \left|q_i^{[\nu]}[\widehat{u}_i]\right| > \lambda_T \text{ and } U \leq 2 \\ q_i^{[\nu]}[\widehat{u}_i]/\Upsilon\big(-\theta_i/U\big), & \text{otherwise,} \end{cases} \tag{5.55}$$

where λ_T is the threshold level. With any threshold level decision, there is always some probability of a false alarm where a noise sample is declared as an echo. The threshold can be set to obtain a false alarm probability of P_e, using

$$\lambda_T = \sqrt{\frac{-\sigma_\rho^2}{\ln(P_e)}} = \sqrt{\frac{-\sigma_w^2}{M\ln(P_e)}}. \tag{5.56}$$

Simulation results show that the estimation performance is not particularly sensitive to

threshold level λ_T. A reasonable threshold is obtained by setting the false alarm probability to $P_e = 10^{-3}$.

5.4.4 Summary

The iterative channel detection procedure is summarized below:

1. Perform an $\frac{NU}{K}$-point IDFT on $\widehat{H}_{\text{LS}}[m]$ to obtain a transformation of the channel response, $q[u]$, as given in (5.31).

2. Conservatively guesstimate a value for $\widehat{L}$ based on the assumed characteristics of the channel, making sure $\widehat{L} \geq L$.

3. Initialize the iteration number and channel path parameters, i.e. $\nu = 1$ and $\bar{\alpha}_i^{[0]} = \bar{\tau}_i^{[0]} = 0;\ i = 0, 1, \ldots, \widehat{L} - 1$.

4. Subtract the effect of the estimated channel paths from $q[u]$ using (5.44) with $\bar{\tau}_i$ and $\bar{\alpha}_i$ in place of $\widehat{\tau}_i$ and $\widehat{\alpha}_i$.

5. Estimate $\widehat{u}_i^{[\nu]}$ as in (5.46) then use (5.50) to calculate $\bar{\tau}_i^{[\nu]}$ if $U = 1$. If $U > 1$, use (5.52) instead to simplify the computation.

6. Use (5.55) to obtain $\bar{\alpha}_i^{[\nu]}$.

7. Repeat steps 4) to 6) $\widehat{L}$ times, starting with $i = 0$ and ending with $i = \widehat{L} - 1$ to complete one iteration.

8. Increase ν by 1 and repeat from step 4). Stop the process after a preset number of iterations.

9. Finally, the transfer function of the multipath channel can be computed similarly to (5.30) with channel parameters $\bar{\alpha}_i$ and $\bar{\tau}_i$ obtained from the last iteration.

5.5 Simulation Results

This section investigates the performance of the proposed channel estimation algorithm. At first, the single echo channel model in [C5.8] is considered, which fixes $\widehat{L} = L = 2$. Coarse timing error τ_0 is modeled as a random variable that is uniformly distributed between 0 and 10, i.e. $\tau_0 \sim \mathcal{U}(0, 10)$. The echo delay in seconds, i.e. $\epsilon_1 T_s$, is uniformly distributed between 0 and 0.5 μs. The power of the micro-reflection is -16 dBc relative to the main path, which is the worst case specified in DOCSIS 3.1. The sampling rate of the system is $F_s = 102.4$ MHz. The signal is generated using an $N = 2048$ point IFFT, and has $M = 1900$ pilots indexed by $\mathcal{S}(m) = m + 74,\ m = 0, 1, \ldots, 1899$ (no sub-carrier skipping), which leaves 74 unused carriers as guard bands at both ends of the spectrum.

Fig. 5.7 presents the performance of the proposed iterative channel estimator (ICE) in a DOCSIS 3.1 channel and compares it with the performance of the conventional estimators discussed previously. It can be seen that performance of the simple LS approach (no priori channel information) is the worst among all, followed by the DFT method. Despite having superior performance over the LS method in the low SNR region, the performance of the DFT method is worse than the LS method for SNR greater than 33 dB. It is apparent that 33 dB marks the location where the leakage power in the estimation is greater than noise power and becomes the main source of performance degradation for the DFT method (see Eq. (5.20)).

Performance of the ICE technique is illustrated for three up-sampling factors: $U = 1, U = 2$ and $U = 4$. The ICE method clearly outperforms both the LS and DFT techniques, even with $U = 1$. However, with $U = 1$, the ICE method hits an error floor of $4 \cdot 10^{-5}$ for SNRs above 20 dB that can not be reduced by increasing the number of iterations.

When increasing the up-sampling factor to $U = 2$, it can be seen that the error floor depends on the number of iterations. As can be seen in Fig. 5.7, there is considerable improvement between 2 and 20 iterations. In particular, the MSE level at 20 iterations is 10 times lower than that achieved with 2 iterations. However, only marginal performance gains are obtained by exceeding 20 iterations. Interestingly, a further increase of the up-

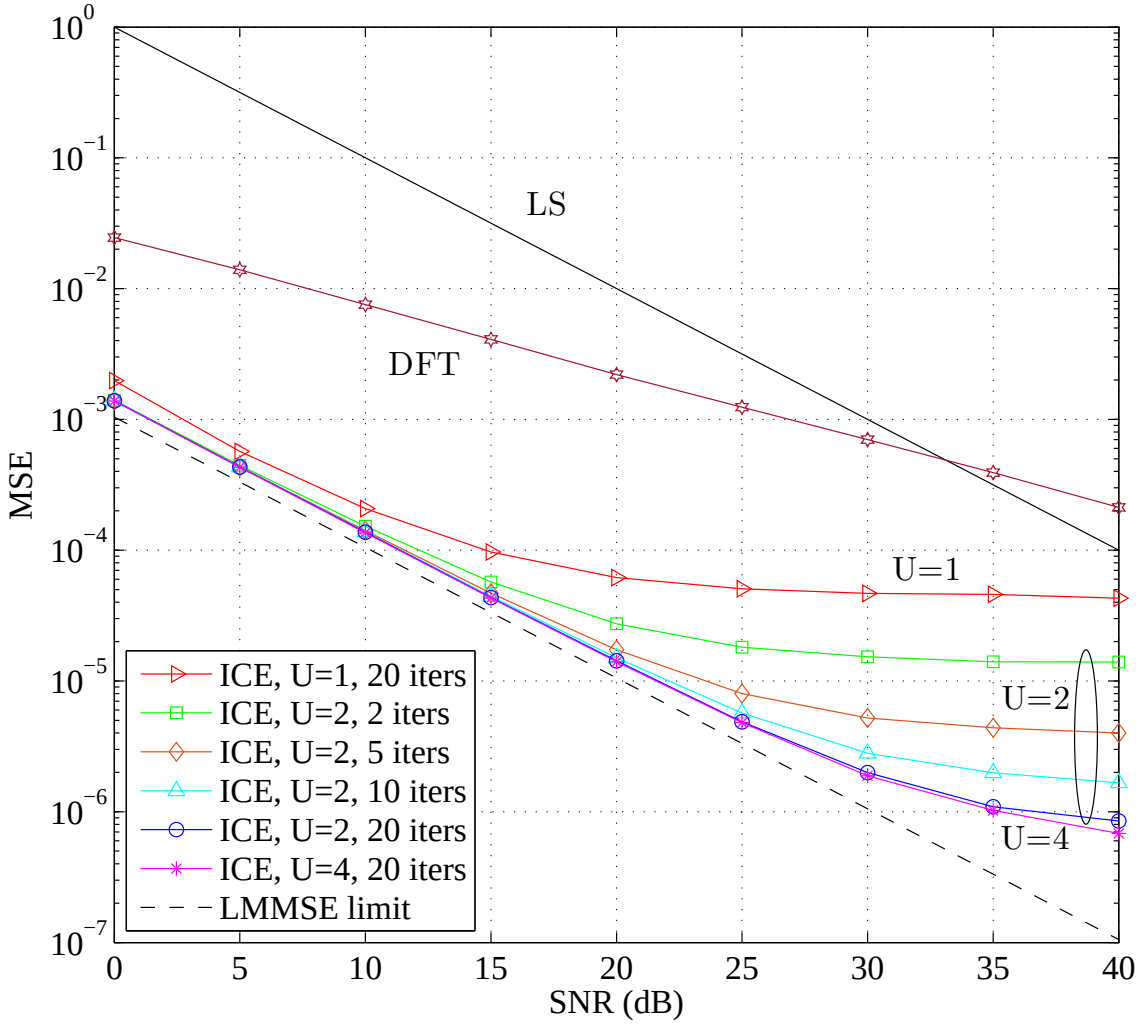

Figure 5.7 Performance of the proposed technique for 1 echo DOCSIS 3.1 channel model.

sampling factor to 4 has little effect on the algorithm performance. Specifically, the MSE level with $U = 4$ and 20 iterations is almost identical to that with $U = 2$ and 20 iterations. The simulation results provide strong evidence that an up-sampling factor of $U = 2$ and 20 iterations should be used.

It can be seen that the proposed algorithm outperforms the conventional methods, especially in the low-SNR region, where the ICE estimator is 30 dB better than the LS. In addition, the performance of the ICE asymptotically approaches that of the LMMSE, but does not need apriori knowledge of the auto-covariance of the channel. Furthermore, the

ICE method requires only a single OFDMA symbol to achieve this level of performance.

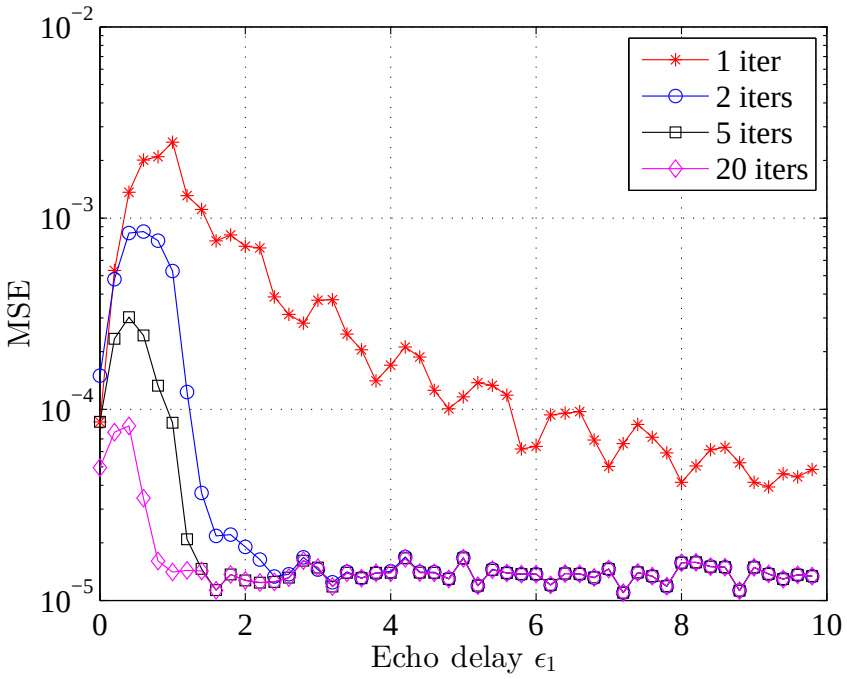

(a)

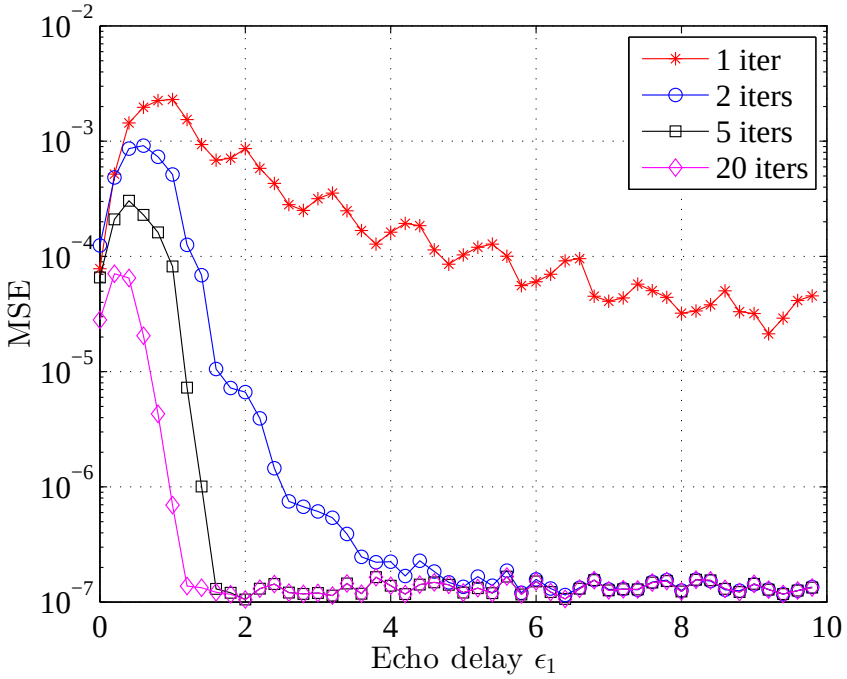

(b)

Figure 5.8 Comparing mean squared error versus echo delay for 2 cases: a) SNR=20 dB and b) SNR = 40dB.

Fig. 5.8 illustrates the MSE of the ICE estimator for different echo delays where $U = 2$ and the SNR is 20 and 40 dB. Simulations were run 10^5 times with different echo delays that are uniformly distributed between 0 and 10 samples. The more realistic fractional delay channel model shows that the leakage becomes significant when $\epsilon_1 \leq 1$. As can be seen from the figure, the estimation error reaches its peak when two paths are separated by about half the sample period. When only one iteration is performed, the estimation error gradually declines as the echo delay increases, as the influence of the main path on the echo and vise versa is lessened when the delay between them increases. Interestingly, when the estimator employs more than 5 iterations, the MSE quickly drops to error floors of 10^{-5} and 10^{-7} for SNR = 20 and 40 dB, respectively, which indicates that the residual leakage is successfully suppressed.

It is notable that when the echo delay is less than a sample period, the estimation error is very high as compared to the error caused by larger echo delay. Specifically, when $\epsilon_1 < 1$, the performance of the ICE technique is limited to around 10^{-4} regardless of SNR level. That observation indicates that the error floor of the ICE method shown in Fig. 5.7 is likely caused by scenarios in which the echo delays are less than 1 sample duration. However, even in such a challenging scenario, the estimation performance is still very reasonable (MSE $\leq 10^{-4}$ after 20 iterations, which is 20dB better than the LS). Note that the algorithm requires a larger number of iterations to accurately detect echoes with less than one sample delays. Therefore, the estimation process can be further simplified by adaptively performing more iterations for echoes with short delays and fewer iterations for echoes with longer delays. Simulations indicate that for any echo delay greater than 6 samples, only 2 iterations are needed to accurately detect the multipath channel's coefficients.

Since τ_0 is the delay of the main path, it is also the timing error. Therefore the proposed technique not only estimates the channel's frequency response, but also detects the timing error. Fig. 5.9 illustrates the variance of timing estimation error normalized to a sample period, i.e., $\mathbb{E}\left\{|\bar{\tau}_0 - \tau_0|^2\right\}$, for various SNR values. The simulation parameters are the same as in Fig. 5.7, where the up-sampling factor U is fixed at 2 and a maximum of 20 iterations were executed for each detection. To avoid the most difficult detection scenario discussed

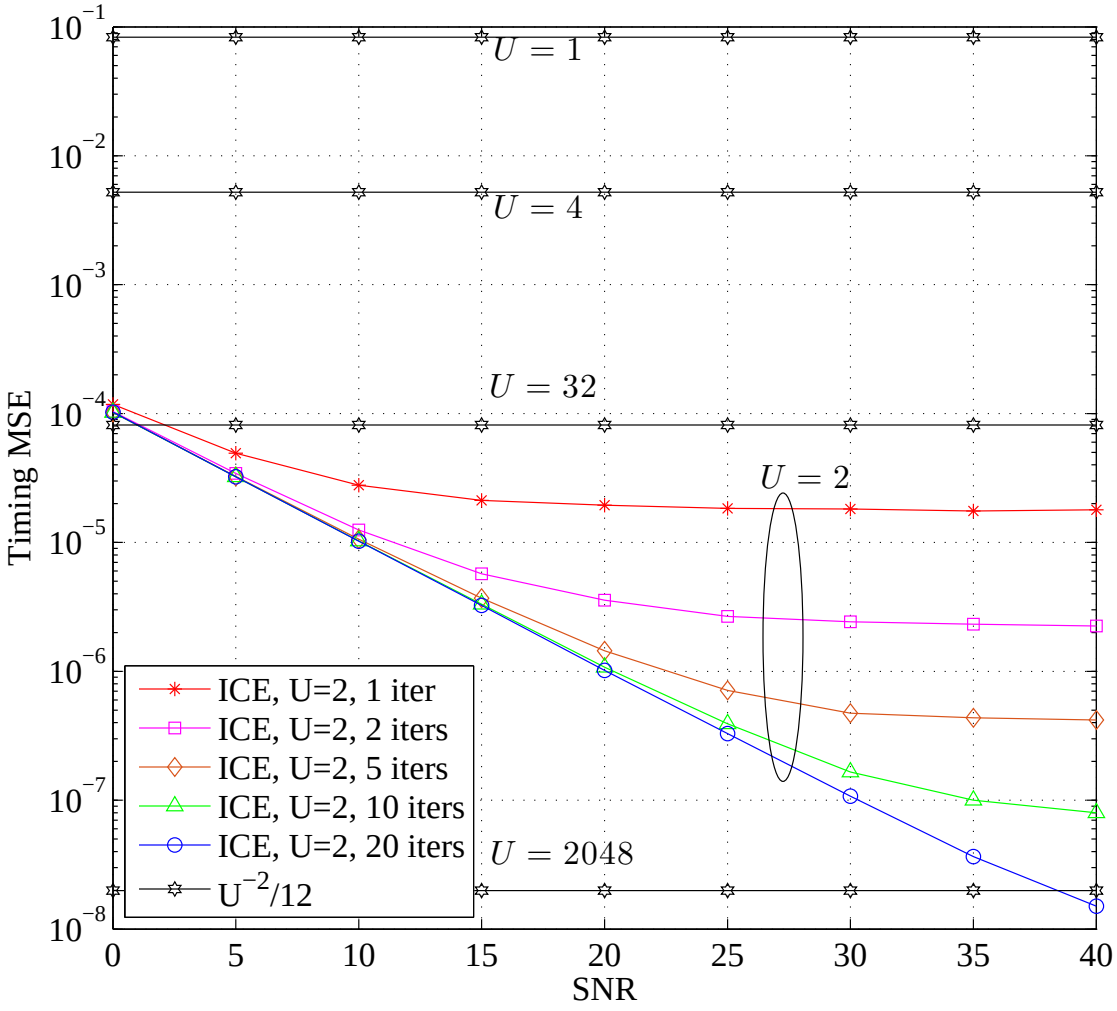

Figure 5.9 MSE of fine timing offset estimation.

previously, ϵ_1 is constrained to be greater or equal to 1. As can be seen in Fig. 5.9, at 20 iterations, the timing MSE decays exponentially with SNR, indicated by the straight line in the figure.

Conventional OFDMA timing detection techniques, such as [C5.9, C5.11, C5.12, C5.10], are all timing-metric based estimation techniques, which limit detection resolution to a sample period. Therefore, timing offset variance of these conventional techniques is inherently greater than 1/12, which is easily outperformed by the proposed algorithm. The initial ICE algorithm of section 5.4.1 has a timing offset that is uniformly distributed between $-0.5/U$ and $0.5/U$. Therefore, the timing variance of the initial ICE algorithm would asymptotically

approach $U^{-2}/12$, which is plot as horizontal lines in Fig. 5.9 for various values of U. As such, the interpolation method introduced in Section 5.4.2 is very important as it provides excellent timing estimates for a small computational cost.

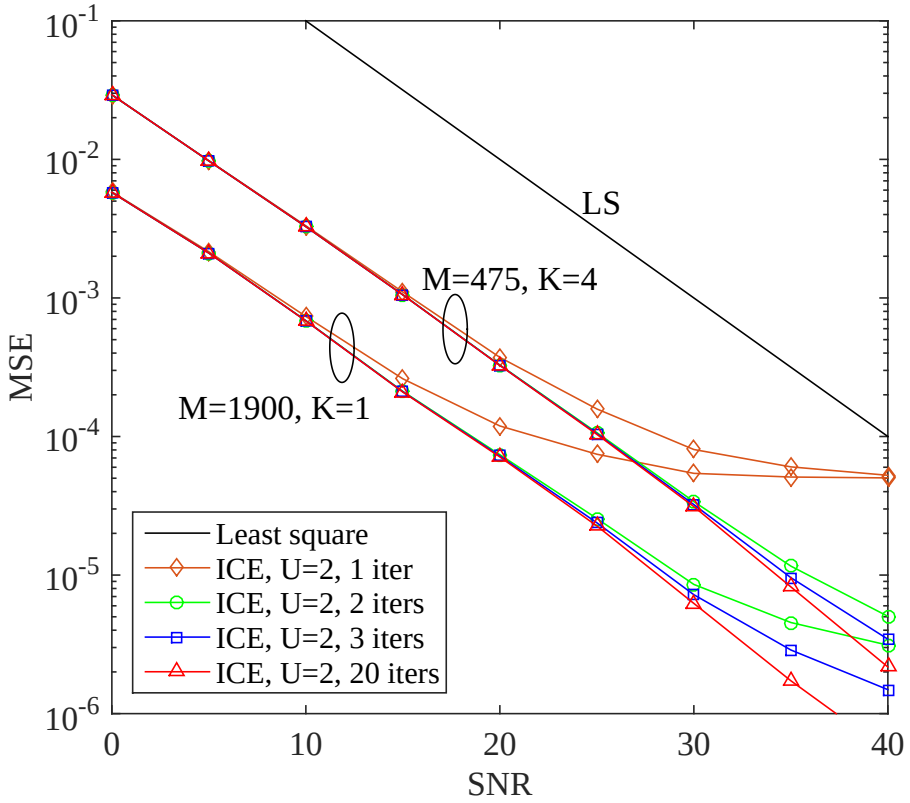

Figure 5.10 Performance of the proposed technique for the case of 6 echoes.

Fig. 5.10 illustrates the performance for a 6 echo scenario (L=7), where the 6 echoes have strengths and delays as specified in Table. 5.1. ϵ_1 is constrained to be greater or equal to 1 and $\widehat{L} = L = 7$. The simulation was run for two different skipping factors: $K = 1$, i.e. no sub-carrier skipping, and $K = 4$ which limits the number of pilot sub-carriers to $M = 1900/4 = 475$. The simulation used $U = 2$ and 20 iterations for each detection. As predicted, when $\epsilon_1 > 1$, performance of the ICE algorithm shows no apparent error floor. Furthermore, significant improvements are seen after the first few iterations, which is consistent with observations made from Fig. 5.8 and Fig. 5.7.

As shown in Fig. 5.10, the performance for $K = 4$ is about 6 dB worse than for $K = 1$. This makes sense since the noise power $\sigma_\rho^2 = \frac{\sigma_w^2}{M}$ is inversely proportional to M, so it increases

Table 5.1 Micro-reflection characteristics for multi-echo scenario

Echo #	Power	Delay in seconds
1^{st}	-16 dBc	$\leq 0.5\ \mu$s ($\sim 51\ T_s$)
2^{nd}	-22 dBc	$\leq 1.0\ \mu$s ($\sim 102\ T_s$)
3^{rd}	-29 dBc	$\leq 1.5\ \mu$s ($\sim 154\ T_s$)
4^{th}	-35 dBc	$\leq 2.0\ \mu$s ($\sim 205\ T_s$)
5^{th}	-42 dBc	$\leq 3.0\ \mu$s ($\sim 307\ T_s$)
6^{th}	-51 dBc	$\leq 4.5\ \mu$s ($\sim 461\ T_s$)

by 6 dB when the number of pilot sub-carriers is reduced from 1900 to 475. Therefore, experimental evidence suggests that the performance of the ICE technique scales well with the number of pilot sub-carriers.

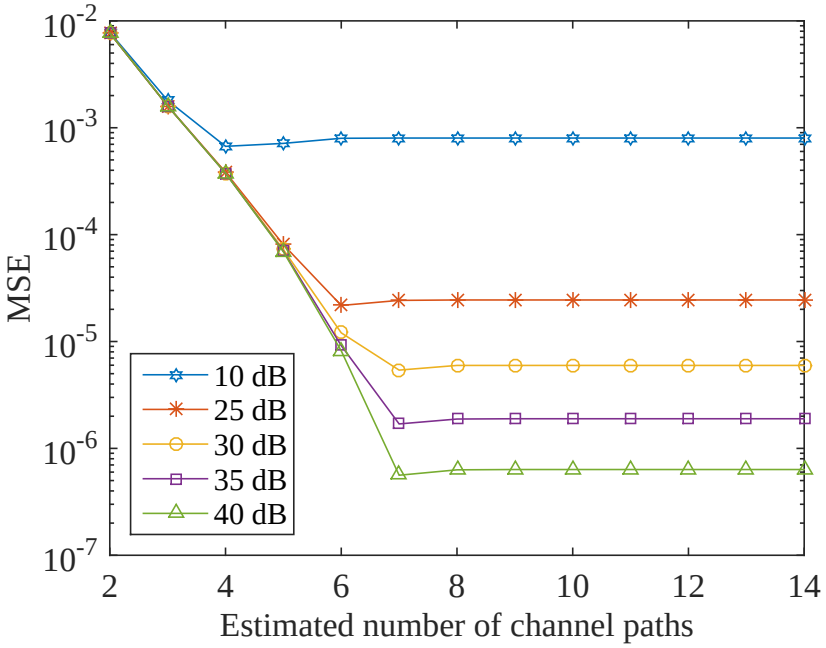

Figure 5.11 MSE performance versus the estimated number of channel paths.

Finally, Fig. 5.11 shows the MSE performance when the estimated number of channel paths, $\widehat{L}$, differs from the true number of paths, L. The simulation parameters are the same as in Fig. 5.10 for the 7 paths channel described in Table 5.1. The skipping factor is $K = 1$ and the SNR is varied from 10 to 40 dB. When SNR = 10 dB, the best performance is achieved when $\widehat{L} = 4$. This is because the power of the 4^{th}, 5^{th} and 6^{th} echoes are close to or less than the noise power, σ_ρ^2, and thus can not be detected properly. A similar trend is

observed when the SNR increases to 25 dB, in which case $\widehat{L} = 6$ gives the best performance since only the last channel tap can not be detected due to noise.

The detection performance behaves differently in the high SNR region, i.e. when SNR $\geq$ 30 dB. In particular, the best performance is observed when $\widehat{L}$ is given the exact number of channel paths, e.g. when $\widehat{L} = 7$. As expected, when $\widehat{L} < 7$, under-detection significantly reduces channel estimation performance. However, only negligible performance degradations are observed with over-detection, e.g. when $\widehat{L} > 7$, due to the threshold that mitigates the possibility of misidentifying noise samples as channel paths.

5.6 Conclusions

The iterative channel estimation (ICE) algorithm proposed in this paper estimates the frequency response of a multipath channel by analyzing a single OFDMA symbol. Its performance in terms of variance of estimation error is markedly better than the conventional LS and DFT-based estimators, especially when the transport delays along the paths are fractional, i.e. the delays are not integer multiples of the system sampling period. The performance of the ICE approaches that of the LMMSE, without needing apriori CSI.

The dominant cost of the ICE algorithm is the computation of a DFT and IDFT that do not depend on the number of paths in the channel. Therefore its cost is virtually independent of L and is comparable to the cost of DFT-based estimators.

In addition to estimating the frequency response of the channel, the ICE algorithm provides, at no cost, estimates of parameters that would otherwise be computed elsewhere in the demodulator. It provides a high precision estimate of the time of arrival of the main path, which is needed to trim the CP. It also provides estimates of echo strengths that can potentially be analyzed to identify the location of degraded or faulty components in the cable network.

Acknowledgments

This work is supported in part by a Natural Science and Engineering Council of Canada (NSERC) Industrial Postgraduate Scholarship (IPS) and Vecima Networks.

References

[C5.1] Y. Shen and E. Martinez, "Channel Estimation in OFDM Systems," *Freescale Semiconductor Application Note*, 2006.

[C5.2] J.-J. van de Beek, O. Edfors, M. Sandell, S. Wilson, and P. Ola Borjesson, "On channel estimation in OFDM systems," in *Proc. IEEE Veh. Technol. Conf.*, vol. 2, pp. 815–819, July 1995.

[C5.3] O. Edfors, M. Sandell, J.-J. van de Beek, S. Wilson, and P. Borjesson, "OFDM channel estimation by singular value decomposition," *IEEE Trans. Commun.*, vol. 46, pp. 931–939, July 1998.

[C5.4] M. Noh, Y. Lee, and H. Park, "Low complexity LMMSE channel estimation for OFDM," *IEE Proc. Commun.*, vol. 153, pp. 645–650, Oct. 2006.

[C5.5] Y. Zhao and A. Huang, "A novel channel estimation method for OFDM mobile communication systems based on pilot signals and transform-domain processing," in *Proc. IEEE Veh. Technol. Conf.*, vol. 3, pp. 2089–2093, May 1997.

[C5.6] Y. Kang, K. Kim, and H. Park, "Efficient DFT-based channel estimation for OFDM systems on multipath channels," *IET Commun.*, vol. 1, pp. 197–202, Apr. 2007.

[C5.7] M. Ozdemir and H. Arslan, "Channel Estimation for Wireless OFDM Systems," *IEEE Commun. Surveys Tutorials*, vol. 9, pp. 18–48, July 2007.

[C5.8] Cable Television Laboratories, Inc., "DOCSIS 3.1 Physical Layer Specification," Oct 2013.

[C5.9] A. Nasir, S. Durrani, and R. Kennedy, "Performance of coarse and fine timing synchronization in OFDM receivers," in *Future Computer and Communication (ICFCC), 2010 2nd International Conference on*, vol. 2, pp. 412–416, May 2010.

[C5.10] M. Morelli, "Timing and Frequency Synchronization for the Uplink of an OFDMA System," *IEEE Trans. Commun.*, vol. 52, pp. 166–166, Mar. 2004.

[C5.11] H. Minn, V. Bhargava, and K. Letaief, "A robust timing and frequency synchronization for OFDM systems," *IEEE Trans. on Wireless Commun.*, vol. 2, pp. 822–839, July 2003.

[C5.12] K. Shi and E. Serpedin, "Coarse frame and carrier synchronization of OFDM systems: a new metric and comparison," *IEEE Trans. on Wireless Commun.*, vol. 3, pp. 1271–1284, July 2004.

[C5.13] A. Khan, V. Jeoti, and M. Zakariya, "Improved pilot-based LS and MMSE channel estimation using DFT for DVB-T OFDM systems," in *IEEE Symp. on Wireless Tech. and Applications*, pp. 120–124, Sept 2013.

[C5.14] H. Minn, D. I. Kim, and V. Bhargava, "A reduced complexity channel estimation for OFDM systems with transmit diversity in mobile wireless channels," *IEEE Trans. Commun.*, vol. 50, pp. 799–807, May 2002.

[C5.15] J. Ma, H. Yu, and S. Liu, "The MMSE Channel Estimation Based on DFT for OFDM System," in *Int. Conf. on Wireless Commun., Networking and Mobile Computing*, pp. 1–4, Sept. 2009.

[C5.16] K. Kwak, S. Lee, J. Kim, and D. Hong, "A New DFT-Based Channel Estimation Approach for OFDM with Virtual Subcarriers by Leakage Estimation," *IEEE Trans. on Wireless Commun.*, vol. 7, pp. 2004–2008, June 2008.

[C5.17] K. J. Kim, H. G. Hwang, K. J. Choi, and K. S. Kim, "Low-Complexity DFT-Based Channel Estimation with Leakage Nulling for OFDM Systems," *IEEE Commun. Letters.*, vol. 18, pp. 415–418, Mar. 2014.

[C5.18] O. Edfors, M. Sandell, J. van de Beek, S. K. Wilson, and P. O. Borjesson, *Analysis of DFT-based channel estimators for OFDM.* Research report, Lulea University of Technology, 1996.

[C5.19] X. Xiong, B. Jiang, X. Gao, and X. You, "DFT-Based Channel Estimator for OFDM Systems with Leakage Estimation," *IEEE Commun. Letters.*, vol. 17, pp. 1592–1595, Aug. 2013.

6. Zero-CP OFDM for DOSCIS-Based CATV Networks

Published as:

Tung T. Nguyen, Ha H. Nguyen, J. Eric Salt and Brian Berscheid, "Zero-CP OFDM for DOSCIS-based CATV networks," To be submitted to *IEEE Transactions on Broadcasting* (after filing a provisional US patent).

As discussed in Chapter 2, an OFDMA link between the CMs and the CMTS has been specified in the latest version of DOCSIS standard and it is very likely that an OFDMA link, perhaps in a modified form, will continue to be employed in subsequent versions of the DOCSIS standard. Despite various advantages, one drawback of OFDMA is the requirement that a cyclic prefix (CP) be inserted at the beginning of each transmitted OFDMA symbol to mitigate inter-symbol interference (ISI). In general, not only the channel but also the transceivers' digital filters determine the length of the CP. Unfortunately, the CP insertion reduces overall transmission throughput by up to 25% for DOCSIS 3.1 upstream transmission.

This chapter first thoroughly investigates all factors that affect the length of the CP. Then performance degradation of an OFDM system with insufficient CP is analyzed. Finally, a novel technique to eliminate the CP is introduced. It is demonstrated that the CP can be completely removed with only a negligible effect on the transmission performance. Moreover, the proposed technique consumes only a small amount of hardware, making it a promising candidate to be included in the next version of DOCSIS standard.

The main contribution to this manuscript comes from the student (first author), while the three co-supervisors provide equal supervision effort.

Zero-CP OFDM for DOSCIS-Based CATV Networks

Tung T. Nguyen, *Member, IEEE*, Ha H. Nguyen, *Senior Member, IEEE*,
Eric Salt, *Member, IEEE*, and Brian Berscheid *Member, IEEE*

Abstract

The current version of DOCSIS, which is DOCSIS 3.1, has recently been released to support very high-rate data transfer over existing cable TV systems. The new standard is markedly different from all previous versions of DOCSIS in that orthogonal frequency-division multiple access (OFDMA) is used together with high-density QAM constellations (up to 4096-QAM) in both the downstream and upstream directions. This is in a sharp contrast with the single-carrier modulation techniques used in prior versions of DOCSIS. Despite many advantages, the major drawback of orthogonal frequency-division multiplexing (OFDM) is the insertion of a cyclic prefix (CP) at the beginning of each transmitted OFDM symbol to mitigate inter-symbol interference (ISI). The CP insertion reduces the overall transmission throughput, by up to 25% for DOCSIS 3.1 downstream transmission. In general, not only the channel but also the transceivers' digital filters determine the length of the CP. In this paper, all the aspects that determine the CP length are thoroughly addressed. Then a novel technique to eliminate the CP is introduced and analyzed. It is demonstrated that the CP can be completely removed with a negligible effect on the transmission performance. Moreover, the proposed technique consumes only a small amount of hardware, making it a promising candidate to be included in the next version of DOCSIS.

Index terms

DOCSIS 3.1, OFDM, OFDMA, cyclic prefix, equalization.

6.1 Introduction

Cable Television Laboratories, Inc. (CableLabs), a not-for-profit research and development organization for multiple network providers, has recently released an update to DOCSIS, referred to as DOCSIS 3.1 [C6.1], which marks a new evolution to the cable industry. DOCSIS 3.1 was developed to provide cable subscribers with service speed up to 10 Gbps downstream and up to 1 Gbps upstream [C6.2]. The new specifications provide both opportunities and challenges for CATV network providers to deploy the new systems.

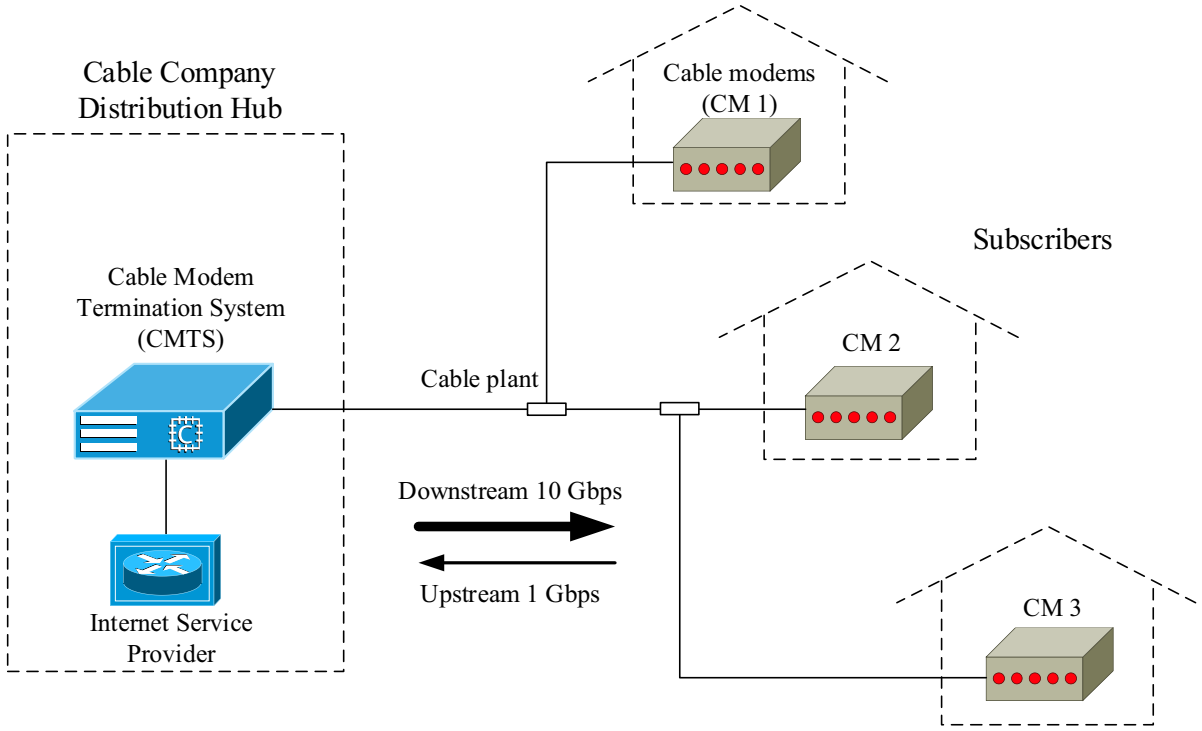

Figure 6.1 DOCSIS 3.1 cable plant.

As seen in Fig. 6.1, there are two main components in the cable network: a cable modem (CM), which is located at the subscriber's home, and a cable modem termination system (CMTS), located at the cable company's head-end. The CMTS is the mastermind of the network, which is responsible for setting up transmission parameters and allocating time-frequency resources for a large number of CMs residing at the subscribers' side. A subscriber is likely to have multiple devices connected to the CM to consume digital contents such as television programs, internet applications and voice over internet protocol.

The most significant area of change provided by DOCSIS 3.1 involves spectrum access at

the physical layer, in which orthogonal frequency division multiplexing (OFDM) is used in the downstream direction and orthogonal frequency division multiple access (OFDMA) is used in the upstream direction. OFDM is the method of choice when designing transmission links for high-speed communication systems. The reason is that OFDM has many advantages, such as low implementation complexity, high robustness to multipath environments and high spectral efficiency. It is not a surprise that OFDM is adopted in many contemporary communication systems, such as WiFi, WiMAX and 4G LTE.

Channel impairments generated by cable plants are significantly different from typical OFDM channels discussed in the literature. The greatest difference is in the transmission medium, which is coaxial for the cable systems. The coaxial channel used to carry DOCSIS signal is a slow time-varying channel, over which the signal from a CM reaches a CMTS via a main path and possibly several echo paths. It should be noted that characteristics of the coaxial channel (i.e. echo gains and delays) change slowly or not at all overtime. Aside from using DOCSIS 3.1-compliant modulators/demodulators, cable operators must upgrade their cable infrastructure to satisfy the standard imposed by DOCSIS 3.1. Those unique characteristics of the latest DOCSIS standard opens new opportunities as well as issues and challenges for researches to make contribution into the newly specified cable systems.

While OFDM systems have been studied for many years, the DOCSIS 3.1 downstream standard is unique in that it tries to maximize the overall spectral efficiency of the system (i.e., to operate as close to the Shannon limit as conditions allow). In particular, the OFDM downstream multicarrier system contains up to 7600 sub-carriers occupying a total bandwidth of 192 MHz. Moreover, the DOCSIS 3.1 downstream specifications introduce very high order modulation schemes, with mandatory support up to 4096-QAM and optionally support up to 16384-QAM, which allows the network operators to maximize their network capacity and take advantage of signal quality improvements.

The major factor that limits performance of an OFDM system is inter-symbol interference (ISI). In general, there are two sources of ISI. The first is caused by multipath propagation, in which a signal from the transmitter reaches the receiver via many different paths, which includes a main path and several echo paths. Since the transmission medium considered in a

DOCSIS system is a coaxial cable distribution network, which consists of many coaxial cable lines and devices such as splitters, taps, and various loads, the echo paths are generated due to impedance mismatch among terminals and ports of devices. As a result, the multipath propagation smears the transmitted waveform, causing ISI between OFDM symbols. The second source of ISI is from digital filters located at the front-end of the transceivers. In particular, the channel linking an OFDM transmitter and a receiver includes more than just echoes. It also includes band limiting reconstruction/anti-aliasing filters, which are required for up-converting signals at the transmitter and down-converting signals at the receiver. These filters introduce delay spreads and cause a smearing effect similar to that due to the multipath propagation.

OFDM systems use block-wise transmission method where each data block represents one OFDM symbol. To mitigate the ISI, a guard time, which is usually in the form of a CP, is inserted between OFDM symbols/blocks. A CP is formed by duplicating the last samples of the block to the beginning. This is done to ensure that the OFDM symbol remains periodic within the receiver's Fourier-transform window. However, since a CP adds an overhead to each data block, it reduces the transmission rate. This can also be considered as a waste of energy by transmitting a part of the symbol that is not used for detection. The amount of overhead depends on the CP duration, which is determined by the sum of the delay spreads of the transceivers' digital filters and multipath channel in the operating environment.

In many practical situations, the total delay spread could be rather large and using a CP of the corresponding length would severely reduce the throughput of the system. For example, in DOCSIS 3.1, the maximum throughput loss in downlink transmission can be up to 25%, since the useful symbol duration is 20 μs while the longest path is expected to have a delay of 5 μs in relation to the main path. Enlarging the data block size, i.e., the Fourier transform size, would mitigate this problem but it would increase the transmission's latency as well the peak-to-average power ratio (PAPR), for which high cost RF amplifiers are required.

The above problems of using CP motivate many investigations into CP shortening techniques. Generally, there are two main approaches to deal with the CP issues. The first ap-

proach employs a time-domain equalizer (TEQ) to artificially shorten the channel response [C6.3, C6.4, C6.5]. A TEQ is basically a finite impulse response (FIR) filter. Designing a good TEQ is often a difficult task as it requires complex operations such as calculation of eigenvalues, matrix inversion, matrix division, etc., which do not lend themselves easily to implementation in hardware. Furthermore, the length of a TEQ in samples is proportional to system rate, which can be high for wide-band signals as those in DOCSIS 3.1 systems. Since most of the computations for TEQ are matrix-based related, complexity of the TEQ grows at least quadruply with the increase of the signal's bandwidth. Therefore, it is highly impractical to employ TEQ for high bandwidth signal.

The second approach involves directly truncating the CP, making OFDM symbols subject to ISI, then using different techniques to minimize the distortion caused by the insufficient CP. In particular, ISI mitigation in OFDM can be done with a precoder employed at the transmitter side [C6.6, C6.7, C6.8] or decision-feedback/turbo equalizer employed at the receiver side [C6.9, C6.10, C6.11], or both can be used at the same time [C6.12]. Complexity is still the main concern for this approach. Since the precoder matrix is large, channel-dependent and requires matrix multiplications to implement, it is not suitable for a system with large number of sub-carriers like DOCSIS 3.1 systems. Although turbo equalizer is an excellent ISI-suppressing technique, its computational complexity is relatively high since the advantage offered by this method derives from the intensive data exchange between the channel decoder and the equalizer.

This paper proposes a novel method to transmit OFDM signals in a multipath channel without using CP for ISI protection. First, detailed analysis on the amount of ISI power when using insufficient CP will be provided. Then it will be shown that using Nyquist filters for the reconstruction/anti-aliasing filters and making them matched would eliminate the ISI caused by band-limiting and there would be no need to use a CP. Lastly, a novel TEQ is introduced to efficiently inverse the multipath channel in the time-domain and significantly suppress ISI caused by the insufficient CP. The proposed TEQ is structured as a sparse recursive filter, which is a very high-order infinite impulse response (IIR) filter that is controlled by only a few coefficients. As an example, it will be shown that, by incorporating the proposed designs, the

DOCSIS 3.1 down-link channel transmission can achieve the maximum bandwidth efficiency regardless of the multipath channel condition.

6.2 OFDM System Model

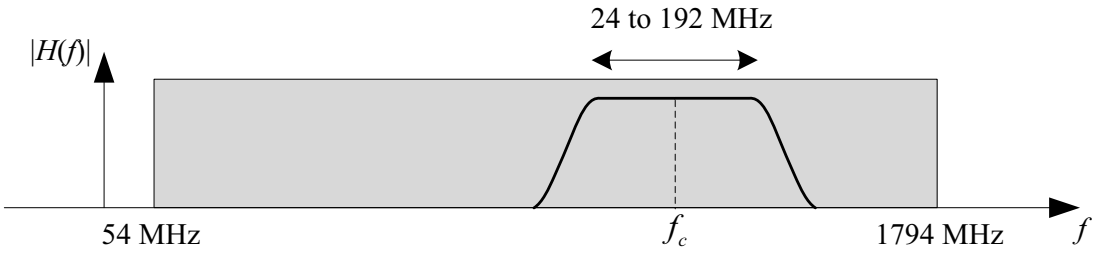

Figure 6.2 DOCSIS 3.1 downstream frequency plan.

The system considered in this paper is structured following specifications of DOCSIS 3.1 [C6.1], which uses OFDM in the downstream channel to support both 25 kHz and 50 kHz sub-carrier spacing options. The normal downstream channel supports channel bandwidths from 54 MHz up to 1002 MHz. However, in order to take the advantage of highly-efficient bandwidth usage enabled by OFDM, the upper downstream edges can be extended, if necessary, to 1218 MHz or even 1794 MHz, as illustrated in Fig. 6.2.

Referring to the OFDM system in Fig. 6.3, the channel bandwidth is divided into N sub-carriers, M of which are used for data transmission. As specified in DOCSIS 3.1 [C6.1], there are guard bands at both ends of the allocated spectrum that cannot be used for data transmission. This restricts the locations of the data sub-carriers, which are usually centered at the middle of the allocated spectrum. For OFDM systems, the two most popular sub-carrier allocation strategies are localized frequency-division multiple access (L-FDMA) and interleaved frequency-division multiple access (I-FDMA). Denote the vector of data sub-carrier indexes as $\boldsymbol{\mathcal{S}} = [\mathcal{S}(0), \mathcal{S}(1), \ldots, \mathcal{S}(M-1)]$, where the elements are related by

$$\mathcal{S}(m) = \mathcal{S}(0) + mN_{\text{skip}}, \quad m = 0, 1, \ldots, M-1. \tag{6.1}$$

Here $S(0)$ is the starting sub-carrier and N_{skip} is an integer number denoting the sub-carrier skipping factor. It can be seen that $N_{\text{skip}} = 1$ corresponds to L-FDMA, whereas $N_{\text{skip}} > 1$

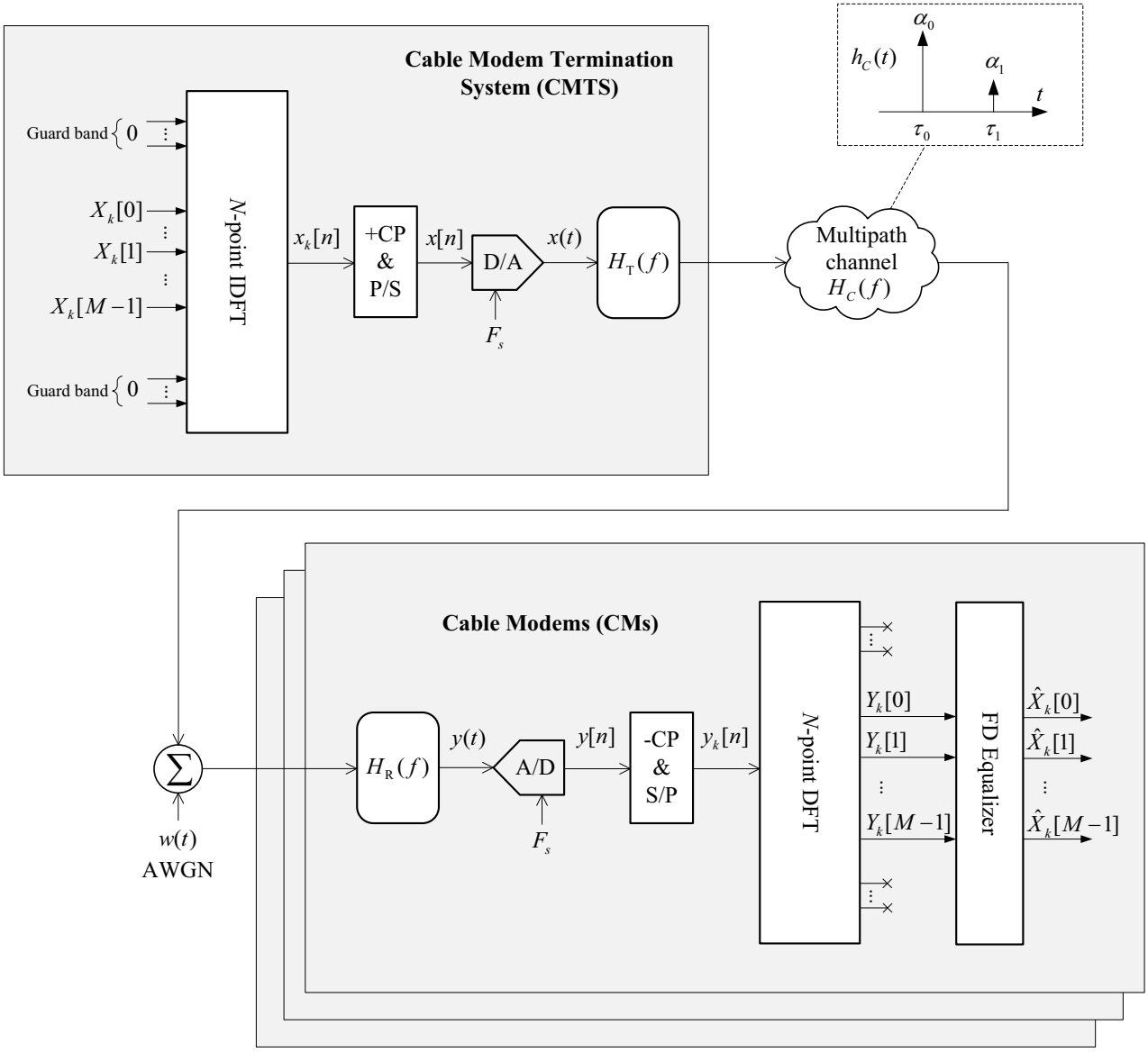

Figure 6.3 Structure of an OFDM system.

generally means I-FDMA.

The OFDM transmitter employs an IDFT module of size N for modulation. The transformed time-domain samples during the k^{th} OFDM symbol interval are written as

$$x_k[n] = \begin{cases} \frac{1}{\sqrt{N}} \sum_{m=0}^{M-1} X_k[m] \exp\left(\frac{j2\pi(\mathcal{S}(m)-N/2)n}{N}\right), & n = 0, 1, \ldots, N-1 \\ 0, & \text{otherwise} \end{cases}, \tag{6.2}$$

where $X_k[m]$ denotes the m^{th} QAM data symbol, which has unit average power, transmitted

during the k^{th} OFDM symbol interval and $n = 0, 1, \ldots, N-1$ denotes the time-domain sample index. It is pointed out that, instead of the standard IDFT/DFT, the Fourier transform pair specified in DOCSIS 3.1 is used in our analysis, where sub-carrier indexing is shifted by $-N/2$ sub-carriers[1]. The sub-carrier index shifting creates equal-size guard bands on both sides of the signal spectrum, which is required to accommodate transition bands of the digital filters that follow (see Fig. 6.4 for the illustration).

The OFDM system in DOCSIS 3.1 uses a CP to avoid inter-symbol interference. In particular, an N_{CP} samples are taken from the end and appended to the beginning of the OFDM symbol. The length of the CP is normally set to accommodate the expected delay spread of the channel. The CP-appended k^{th} OFDM symbol is defined as

$$x_k^{\text{CP}}[n] = \begin{cases} x_k[n - N_{\text{CP}}], & N_{\text{CP}} \leq n \leq N-1 \\ x_k[n + N - N_{\text{CP}}], & 0 \leq n \leq N_{\text{CP}} - 1 \\ 0, & \text{otherwise} \end{cases} . \tag{6.3}$$

Using (6.2), the above expression is mathematically equivalent to

$$x_k^{\text{CP}}[n] = r[n] \frac{1}{\sqrt{N}} \sum_{m=0}^{M-1} X_k[m] \exp\left(\frac{j2\pi(\mathcal{S}(m) - N/2)(n - N_{\text{CP}})}{N} \right), \ \forall n \tag{6.4}$$

where $r[n]$ is a rectangular window function, defined as

$$r[n] = \begin{cases} 1, & \text{if } 0 \leq n \leq N + N_{\text{CP}} - 1 \\ 0, & \text{otherwise} \end{cases} . \tag{6.5}$$

The input $x[n]$ to the D/A block in the transmitter is a concatenation of many OFDM symbols, which can be mathematically written as

$$x[n] = \sum_{k=0}^{\infty} r[n - k(N + N_{\text{CP}})] \ x_k^{\text{CP}}[n - k(N + N_{\text{CP}})], \ \forall n. \tag{6.6}$$

[1]Of course all analysis and results in this paper also apply if the standard IDFT/DFT is used.

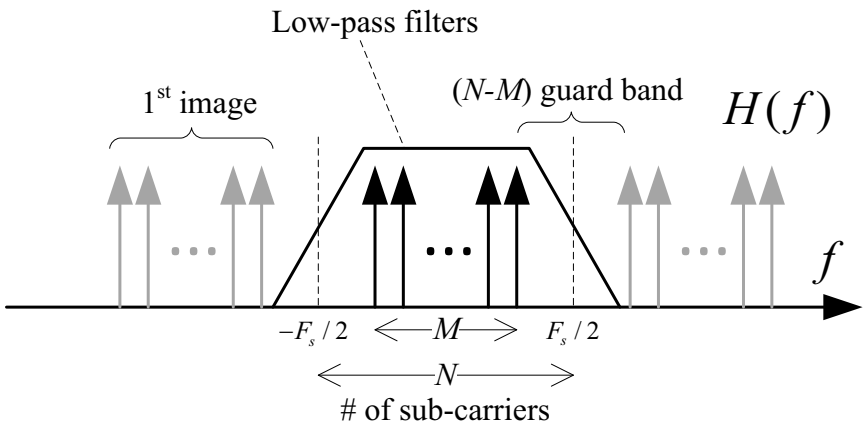

Figure 6.4 Using a low-pass filter to remove spectral images.

The digital signal $x[n]$ is then converted to an analog signal followed by a reconstruction/low-pass filter, $H_{\mathrm{T}}(f)$, to remove spectral images. As illustrated in Fig. 6.4, the width of the guard band on each side of the signal spectrum consists of $(N-M)$ null sub-carriers, which can be used to accommodate the transition band of the low-pass filter.

A channel in a coaxial cable distribution network consists of many paths created by impedance mismatches among terminals and ports of devices that make up the network. Each path is characterized by a gain factor α_i and an associated delay τ_i (seconds). The impulse response and frequency response of the multipath channel are therefore given by

$$h_{\mathrm{C}}(t) = \sum_{i=0}^{N_p-1} \alpha_i \delta(t-\tau_i) \quad \overset{\mathcal{F}}{\longleftrightarrow} \quad H_{\mathrm{C}}(f) = \sum_{i=0}^{N_p-1} \alpha_i \exp(-j2\pi f \tau_i) \tag{6.7}$$

where δ is the Dirac delta function. Furthermore, the parameter N_p is the number of paths in the multipath channel. Note that the spectrum considered in Fig. 6.4 is at base-band, i.e., no up/down frequency translation is considered. Thus, for the equivalent base-band channel modeled in (6.7), the gain factors $\{\alpha_i\}$ are complex values. Also note that τ_0 is not necessarily the time-of-arrival of the main path but rather indicates the timing detection error at the receiver, which typically takes a value between $-T_s/2$ and $T_s/2$, where T_s is the sampling period of the analog-to-digital converter in the receiver.

At the receiver, the received signal is passed through a low-pass filter $H_{\mathrm{R}}(f)$ to reject adjacent channel's spectrum, remove out-of-band noise power and prevent aliasing. Since the

analog-to-digital conversion is performed at system rate F_s, the width of transition bands of $H_{\mathrm{R}}(f)$ must be less than or equal to $\frac{N-M}{2}F_s$ (Hz) in order to prevent aliasing. Let $p_{\mathrm{T}}(t)$ and $p_{\mathrm{R}}(t)$ be the impulse responses corresponding to $H_{\mathrm{T}}(f)$ and $H_{\mathrm{R}}(f)$, respectively. Because of the low-pass filters, the equivalent analog channel between the transmitter and the receiver is band-limited and can be written as

$$g(t) = p_{\mathrm{T}}(t) * h_{\mathrm{C}}(t) * p_{\mathrm{R}}(t), \tag{6.8}$$

where $*$ denotes convolution. It follows that the analog signal received at the receiver can be written as

$$y(t) = x(t) * g(t) + w(t) * p_{\mathrm{R}}(t), \tag{6.9}$$

where $w(t)$ is zero-mean additive white Gaussian noise (AWGN). The signal $y(t)$ is then digitally sampled at the receiver with the sampling rate F_s to obtain digital signal $y[n] = y(t)|_{t=nT_s}$.

Assume that the filtering processes are perfect so that there is no alias caused by the digital-to-analog (D/A) and analog-to-digital (A/D) conversions. In that case, the analog band-limited channel is equivalent to a digital channel, whose impulse response is obtained by sampling the analog channel's impulse response at sampling duration $T_s = 1/F_s$, given as $g[n] = g(t)|_{t=nT_s}$. Under the equivalent digital channel $g[n]$, the signal $y[n]$ can be alternatively expressed as

$$y[n] = x[n] * g[n] + w[n] = \sum_{l=0}^{N_g-1} g[l]x[n-l] + w[n], \tag{6.10}$$

where N_g is the length of $g[n]$ in samples and the noise sample $w[n]$ is obtained by band limiting and sampling $w(t)$, i.e., $w[n] = \big(w(t) * p_{\mathrm{R}}(t)\big)\big|_{t=nT_s}$. Note that N_{CP} and N_g are generally not equal. In order to archive zero-ISI, the length of CP must be made long enough to satisfy $N_{\mathrm{CP}} \geq N_g - 1$ [C6.13]. Since $H_{\mathrm{R}}(f)$ has a flat frequency response at pass-band, $w[n]$ can be considered as complex white Gaussian noise with zero mean and variance σ_w^2.

There are two sources of ISI in the system. The first comes from the multipath channel, which makes the received signal consisting of the direct path signal overlaid with echoes of smaller amplitudes. The second comes from the filters employed between the transmitter and the receiver. In particular, the low-pass filter causes a smearing effect [C6.13]. The narrower the filter's transition band, the longer the impulse response gets, which results in severer smearing effect. As a consequence, the CP must be long enough to cover both the channel's delay spread and the lengths of the filters' impulse responses. The following sub-sections analyze the effects of ISI on signal detection under the cases of sufficient and insufficient cyclic prefixes.

6.2.1 Sufficient cyclic prefix

If sufficient CP is employed, i.e., $N_{\mathrm{CP}} \geq N_g - 1$, the received signal corresponding to the k^{th} OFDM symbol after removing CP can be written as

$$\begin{aligned} y_k[n] &= \sum_{l=0}^{N_g-1} g[l]x[n-k(N+N_{\mathrm{CP}})+N_{\mathrm{CP}}-l]+w[n] \\ &= \sum_{l=0}^{N_g-1} g[l]x_k^{\mathrm{CP}}[n+N_{\mathrm{CP}}-l]+w[n],\ n=0,1,\ldots,N-1. \end{aligned} \tag{6.11}$$

To recover the data, an N-point DFT block transforms the time-domain samples back to the frequency-domain values:

$$\begin{aligned} Y_k[m] &= \frac{1}{\sqrt{N}}\sum_{n=0}^{N-1} y_k[n]\exp\left(\frac{-j2\pi(\mathcal{S}(m)-N/2)n}{N}\right) \\ &= \frac{1}{N}\sum_{n=0}^{N-1}\sum_{l=0}^{N_g-1} g[l]\frac{1}{\sqrt{N}}\sum_{m=0}^{M-1} X_k[m]\exp\left(\frac{j2\pi(\mathcal{S}(m)-N/2)(n-l)}{N}\right)\times \\ &\qquad \exp\left(\frac{-j2\pi(\mathcal{S}(m)-N/2)n}{N}\right)+W[m],\ m=0,1,\ldots,M-1, \end{aligned} \tag{6.12}$$

where

$$W[m] = \sum_{n=0}^{N-1}\frac{w[n]}{\sqrt{N}}\exp\left(\frac{-j2\pi(\mathcal{S}(m)-N/2)n}{N}\right), \tag{6.13}$$

is complex Gaussian noise sample with zero mean and variance σ_w^2. Then

$$\begin{aligned} Y_k[m] &= \frac{1}{N}\sum_{d=0}^{M-1} X_k[d] \sum_{l=0}^{N_g-1} g[l] \sum_{n=0}^{N-1} \exp\left(\frac{j2\pi(\mathcal{S}(d)-\mathcal{S}(m))n}{N}\right) \times \\ &\qquad \exp\left(\frac{-j2\pi(\mathcal{S}(m)-N/2)l}{N}\right) + W[m] \\ &= X_k[m] \underbrace{\sum_{l=0}^{N_g-1} g[l] \exp\left(\frac{-j2\pi(\mathcal{S}(m)-N/2)l}{N}\right)}_{G[m]} + W[m] \\ &= X_k[m]G[m] + W[m], \end{aligned} \tag{6.14}$$

where $G[m]$ is the digital-equivalent channel's frequency response at sub-carrier $\mathcal{S}(m)$. Since the QAM symbol $X_k[m]$ has unit average power, the signal-to-noise ratio (SNR) can therefore be expressed as

$$\text{SNR} = \frac{\mathbb{E}\left\{\left|X_k[m]G[m]\right|^2\right\}}{\left|W[m]\right|^2} = \frac{\mathbb{E}\left\{\left|G[m]\right|^2\right\}}{\sigma_w^2} = \frac{\sum_{l=0}^{N_g-1}\left|g[l]\right|^2}{\sigma_w^2} \tag{6.15}$$

The above analysis clearly shows that there is no ISI effect in the received signal. The CM can simply employ a frequency domain (FD) equalizer to reverse the multipath channel effect. In particular, the symbol detection can be performed based on the minimum mean-square error (MMSE) criterion, i.e., using an MMSE equalizer in the frequency domain. That is

$$\widehat{X}_k[m] = \frac{Y_k[m]G^*[m]}{G[m]G^*[m] + \sigma_w^2}. \tag{6.16}$$

6.2.2 Insufficient cyclic prefix

For the case of insufficient CP, i.e., $N_{\text{CP}} < N_g - 1$, the number of received samples getting affected by ISI is $N_{\text{ISI}} = N_g - 1 - N_{\text{CP}}$. In this case, the signal after removing CP can be

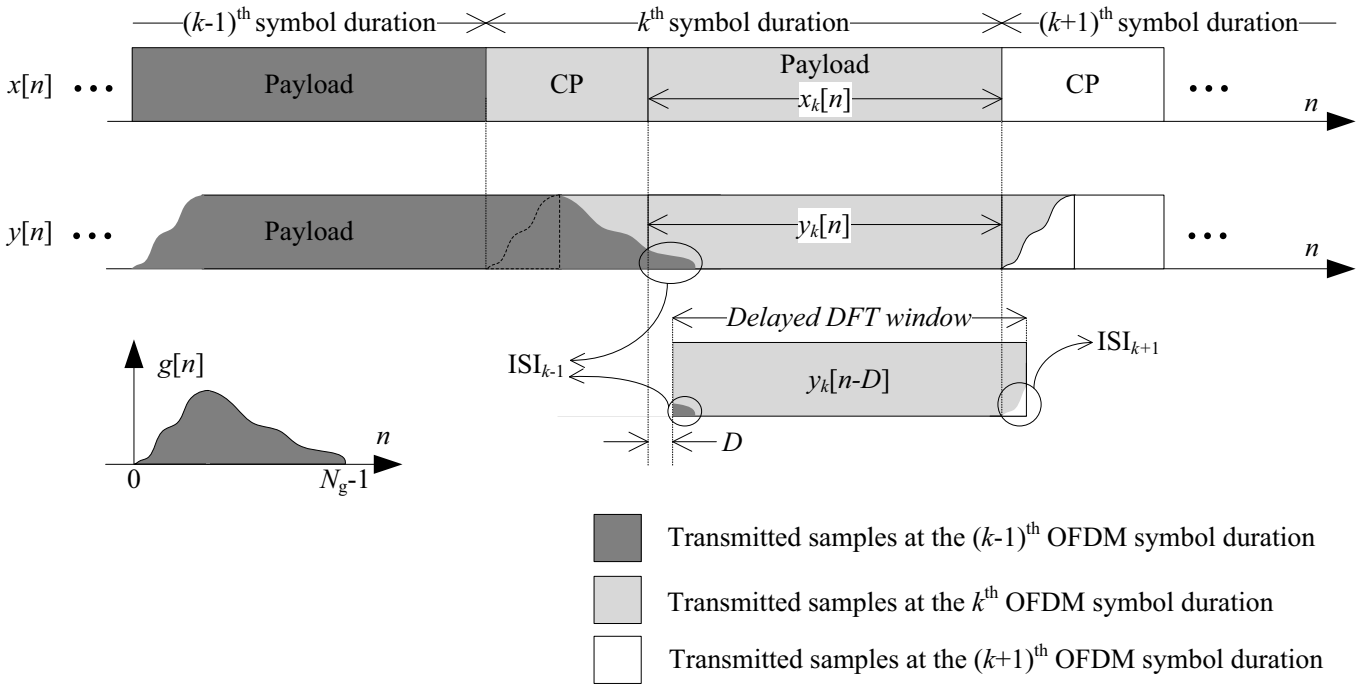

Figure 6.5 Inter-symbol interference caused by insufficient CP.

written as

$$
\begin{aligned}
y_k[n] &= \sum_{l=0}^{N_g-1} g[l]x[n-k(N+N_{\mathrm{CP}})+N_{\mathrm{CP}}-l]+w[n] \\
&= \sum_{l=0}^{N_g-1} g[l]x_k[n-l] + \sum_{n=0}^{N_{\mathrm{ISI}}-1} \underbrace{\sum_{\eta=0}^{N_{\mathrm{ISI}}-n} g[N_{\mathrm{CP}}+\eta]\big(x_{k-1}[n+N-\eta]-x_k^{\mathrm{CP}}[n-\eta]\big)}_{\mathrm{ISI}_{k-1}[n]} + w[n] \\
&= \sum_{l=0}^{N_g-1} g[l]x_k[n-l] + \sum_{n=0}^{N_{\mathrm{ISI}}-1} \mathrm{ISI}_{k-1}[n] + w[n],\ n=0,1,\ldots,N-1,
\end{aligned}
\tag{6.17}
$$

where $\mathrm{ISI}_{k-1}[n],\ n=0,1,\ldots,N_{\mathrm{ISI}-1}$ denotes the ISI caused by the decay tail from the $(k-1)^{\mathrm{th}}$ OFDM symbol which smears through the CP and into the first N_{ISI} samples of the k^{th} OFDM symbol. In the above equation, the portion $x_{k-1}[n+N-\eta]$ denotes a sample at the tail of the $(k-1)^{\mathrm{th}}$ OFDM symbol that causes interference to $y_k[n]$ and the portion $x_k^{\mathrm{CP}}[n-\eta]$ denotes a missing/should be CP sample used to prevent ISI. Since the frequency-domain QAM symbols $X_k[m]$ have unit average power and the fact that there is only M active sub-carriers out of N in the system, the time-domain samples $x_k[n]$ obtained after the

IDFT transformation in (6.2) should have an average power of M/N. Thus the average ISI power that affects the k^{th} OFDM symbol can be calculated as

$$\begin{aligned} P_{\text{ISI}} &= \mathbb{E}\left\{ \sum_{n=0}^{N_{\text{ISI}}-1} \left|\text{ISI}_{k-1}[n]\right|^2 \right\} \\ &= \left(\mathbb{E}\left\{|x_{k-1}[n]|^2\right\} + \mathbb{E}\left\{|x_k^{\text{CP}}[n]|^2\right\} \right) \sum_{\eta=0}^{N_{\text{ISI}}-1} \left|g[N_{\text{CP}}+n]\right|^2 (n+1) \\ &= \frac{2M}{N} \sum_{n=0}^{N_{\text{ISI}}-1} \left|g[N_{\text{CP}}+n]\right|^2 (n+1). \end{aligned} \tag{6.18}$$

The above expression shows that the ISI power clearly depends on the N_{ISI} tail values of $g[n]$ and that the ISI is caused solely by the previous OFDM symbol.

It should be noted that the low-pass filtering causes ramp-up and ramp-down effects on $g[n]$, so that the few first and the few last values of $g[n]$ are quite small in amplitude as compared to the values around the center of $g[n]$ (see Fig. 6.5). Therefore the ISI power can be reduced by delaying the DFT window by D samples. By doing so, there will be $N_{\text{ISI}} - D$ samples less contributing to ISI from the previous OFDM symbol, but there will be ISI contributed from samples of the next OFDM symbol. In particular, (6.17) can be re-written as

$$\begin{aligned} y_k^D[n] &= \sum_{l=0}^{N_g-1} g[l]x[n-D-k(N+N_{\text{CP}})+N_{\text{CP}}-l] + w[n] \\ &= \sum_{l=0}^{N_g-1} g[l]x_k[n-D-l] + w[n] \\ &\quad + \sum_{n=D}^{N_{\text{ISI}}-1} \underbrace{\sum_{\eta=0}^{N_{\text{ISI}}-n} g[N_{\text{CP}}+D+\eta]\big(x_{k-1}[n+N-D-\eta] - x_k^{\text{CP}}[n-D-\eta]\big)}_{\text{ISI}_{k-1}[n]} \\ &\quad + \sum_{n=N}^{N+D-1} \underbrace{\sum_{\eta=0}^{n-N} g[\eta]\big(x_{k+1}^{\text{CP}}[n-N-\eta] - x_k[n-\eta]\big)}_{\text{ISI}_{k+1}[n]}. \end{aligned} \tag{6.19}$$

In this case, the total ISI power can be shown to be

$$P_{\text{ISI}}^{(D)} = \frac{2M}{N}\left(\sum_{n=0}^{D-1}\left|g[n]\right|^2(D-n) + \sum_{n=1}^{N_{\text{ISI}}-D}\left|g[N_{\text{CP}}+D+n]\right|^2 n\right). \tag{6.20}$$

It is clear that, depending on the specific impulse response of $g[n]$, there is an optimum value for D that minimizes the interference power $P_{\text{ISI}}^{(D)}$.

The ISI in the time-domain is considered as noise that spreads out to all frequency-domain symbols, thanks to the DFT operation. The frequency-domain symbols can be recovered as

$$\begin{aligned} Y_k^{(D)}[m] &= \frac{1}{\sqrt{N}}\sum_{n=0}^{N-1} y_k^D[n]\exp\left(\frac{-j2\pi(\mathcal{S}(m)-N/2)n}{N}\right) \\ &= X_k[m]G^{(D)}[m] + W^{(D)}[m] + I[m], \end{aligned} \tag{6.21}$$

where

$$G^{(D)}[m] = G[m]\exp\left(\frac{-j2\pi(\mathcal{S}(m)-N/2)D}{N}\right), \tag{6.22}$$

and

$$W^{(D)}[m] = W[m]\exp\left(\frac{-j2\pi(\mathcal{S}(m)-N/2)D}{N}\right). \tag{6.23}$$

The term $I[m]$ is noise caused by ISI, which can be approximated as an AWGN sample with variance $\sigma_{\text{ISI}}^2 = P_{\text{ISI}}^{(D)}/N$.

The main focus of the paper is to design an OFDM system with severely insufficient CP, i.e., very short or no CP at all. An ultimate goal for the design is to make the total ISI power significantly less than the noise power so that shortening the CP would result in a negligible SNR loss, i.e. $\sigma_{\text{ISI}}^2 \ll \sigma_w^2$. To this end, the two aforementioned main sources of ISI, which come from low-pass filtering and multipath channel propagation, will be addressed in Sections 6.3 and 6.4, respectively.

6.3 Suppressing ISI Caused by the Filtering Effect

The block diagram in Figure 6.6 illustrates a practical implementation of the digital low-pass filters used in the D/A and A/D converters of an OFDM system. Since it is

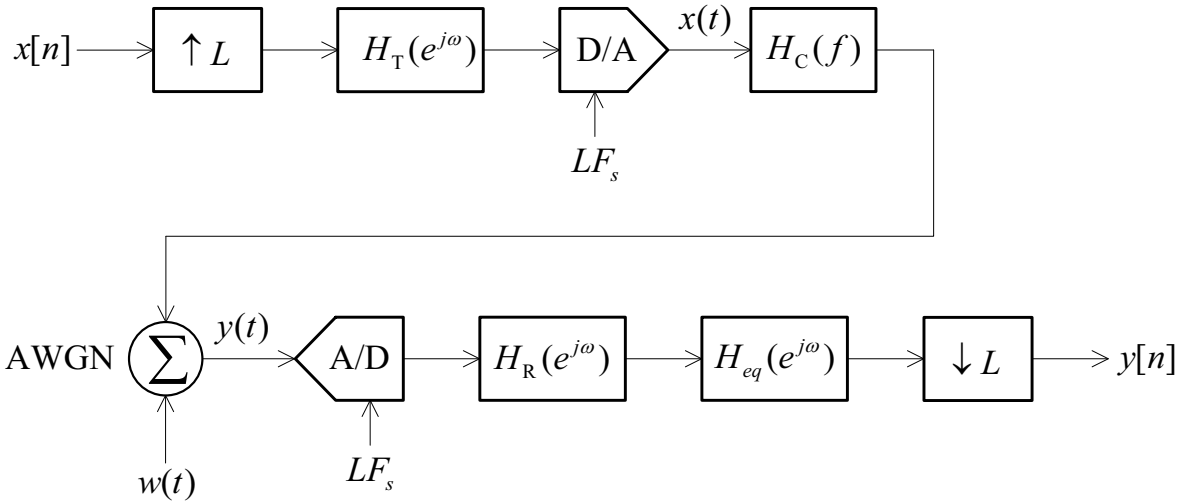

Figure 6.6 Digital low-pass filters used in the D/A and A/D converters of an OFDM system (the IDFT and DFT blocks are omitted).

difficult and expensive to design analog filters with sharp transition band, a low-pass digital filter in the transmitter, $H_{\mathrm{T}}(e^{j\omega})$, is included to increase the sampling rate. With this implementation, the guard-bands, which consist of $(N-M)$ vacant frequency sub-carriers, can be kept low without stressing the design requirements of the analog reconstruction filter[C6.13]. Similarly, there is a digital decimation filter, $H_{\mathrm{R}}(e^{j\omega})$, at the receiver side, that has a similar spectral mask with that of $H_{\mathrm{T}}(e^{j\omega})$. The digital filters and the D/A conversion run at rate LF_s where L is the up-sampling factor. For a system designed with analog up/down converters (frequency translators), $L = 2$ is generally recommended in order to achieve highest complexity reduction [C6.13]. Larger L might be required for a system that employs digital frequency translators or having multiple channels per radio frequency (RF) port.

The multipath channel can be considered as an equivalent digital filter $H_{\mathrm{C}}(e^{j\omega})$, which runs at rate LF_s so that

$$H_{\mathrm{C}}(e^{j\omega}) = H_{\mathrm{C}}(f)\Big|_{f=\frac{\omega LF_s}{2\pi}}. \tag{6.24}$$

To focus on the ISI caused by filtering effect, assume that the receiver employs a time-domain equalizer, $H_{\mathrm{eq}}(e^{j\omega})$, which is capable of inverting the multipath channel effect, i.e.,

$$H_{\mathrm{T}}(e^{j\omega})H_{\mathrm{C}}(e^{j\omega})H_{\mathrm{eq}}(e^{j\omega})H_{\mathrm{R}}(e^{j\omega}) = H_{\mathrm{T}}(e^{j\omega})H_{\mathrm{R}}(e^{j\omega}). \tag{6.25}$$

Provided that (6.25) holds, one can design $H_{\mathrm{T}}(e^{j\omega})$ and $H_{\mathrm{R}}(e^{j\omega})$ as Nyquist pulse shaping and matched filters, respectively, so that they can work together to mitigate the ISI after down-sampling to the symbol rate. A popular choice for the pair of pulse shaping and matched filter is the square-root raised cosine (SRRC) filter, whose frequency response is:

$$H_{\mathrm{SRRC}}(e^{j\omega}) = \begin{cases} 1, & \text{for } |\omega| \leq \frac{\pi(1-\beta)}{L} \\ \sqrt{\frac{1}{2}\left[1+\cos\left(\frac{\pi}{2\beta}\left(\frac{|\omega|L}{\pi}-1+\beta\right)\right)\right]}, & \text{for } \frac{\pi(1-\beta)}{L} < |\omega| \leq \frac{\pi(1+\beta)}{L} \\ 0, & \text{otherwise,} \end{cases} \tag{6.26}$$

where ω, β, L are frequency in radians/sample, the filter's roll-off factor and the ratio of sampling rate to symbol rate, respectively. To make sure the edge sub-carriers on both sides of the spectrum are not distorted by the filtering effect, the roll-off factor, i.e., the amount of exceed bandwidth, must satisfy

$$\beta \leq \frac{N-M}{N}. \tag{6.27}$$

If $H_{\mathrm{T}}(e^{j\omega}) = H_{\mathrm{R}}(e^{j\omega}) = H_{\mathrm{SRRC}}(e^{j\omega})$ and perfect equalization is assumed, it follows that the impulse response of the equivalent digital channel becomes $g[n] = \delta(n)$, and therefore $y[n] = x[n] + w[n]$ and there is no ISI when converting the signal $y[n]$ back to the frequency domain for OFDM demodulation.

However, to produce a causal filter with spectral mask specified in (6.26), the filter's impulse response must be delayed and truncated. There are many techniques to design an SRRC filter [C6.14]. The simplest method is taking the inverse Fourier transform of (6.26), truncate and delay the result. In particular, an order-Ω FIR filter that approximates the

SRRC filter can be obtained as

$$h^{\Omega}_{\mathrm{SRRC}}[n] = \begin{cases} \frac{1}{L}\left(1-\beta+\frac{4\beta}{\pi}\right), & \text{for } n = \frac{\Omega}{2} \\ \frac{\beta}{\sqrt{2}L}\left[\left(1+\frac{2}{\pi}\right)\sin\left(\frac{\pi}{4\beta}\right)+\left(1-\frac{2}{\pi}\cos\left(\frac{\pi}{4\beta}\right)\right)\right], & \text{for } n = \frac{\Omega}{2} \pm \frac{L}{4\beta} \\ \dfrac{\sin\left(\frac{\pi(1-\beta)(n-\varphi)}{L}\right)+\frac{4\beta(n-\varphi)}{L}\cos\left(\frac{\pi(1+\beta)(n-\varphi)}{L}\right)}{\pi(n-\varphi)\left[1-\left(\frac{4\beta(n-\varphi)}{L}\right)^2\right]}, & \text{for } \begin{array}{l} 0 \le n \le \Omega, \\ n \neq \frac{\Omega}{2}, n \neq \frac{\Omega}{2} \pm \frac{L}{4\beta} \end{array} \\ 0, & \text{otherwise.} \end{cases} \tag{6.28}$$

where $\varphi = \Omega/2$ is a delay in samples of the truncated FIR filter.

The truncation causes ripples in the passband of the signal spectrum as well as ISI, since the two filters' impulse responses no longer convolve into a Nyquist pulse. In particular, the impulse response $g[n]$ shows a main tap which has a dominant magnitude and the rest are ISI taps. To minimize the ISI power, especially when no CP is employed, it is obvious that one should exclude the main tap from the ISI equation (6.20), which means taking D as the location of the main tap in $g[n]$, i.e.,

$$D = \underset{n=0,1,\ldots,N_g-1}{\operatorname{argmax}} \left\{|g[n]|\right\}. \tag{6.29}$$

Then the total ISI power in one OFDM symbol in the case of zero-CP is

$$P_{\mathrm{ISI-ZCP}} = \frac{2M}{N}\left(\sum_{n=0}^{D-1}\left|g[n]\right|^2(D-n) + \sum_{n=1}^{N_g-D-1}\left|g[D+n]\right|^2 n\right), \tag{6.30}$$

which is spread out to all N sub-carriers after performing DFT. Thus each sub-carrier suffers from an interference power of $P_{\mathrm{ISI-ZCP}}/N$, which is considered as noise power. Since the average signal power at each sub-carrier is 1, the signal-to-interference ratio can be computed as

$$\mathrm{SIR} = \frac{\mathbb{E}\left\{X_k[m]G^{(D)}[m]\right\}}{P_{\mathrm{ISI-ZCP}}/N} = \frac{N^2}{2M}\frac{\sum_{n=0}^{N_g-1}\left|g[n]\right|^2}{\sum_{n=0}^{D-1}\left|g[n]\right|^2(D-n)+\sum_{n=1}^{N_g-D-1}\left|g[D+n]\right|^2 n}. \tag{6.31}$$

For example, with $L = 2$, $N = 4096$, $M = 3800$ and the pulse shaping and matched filters taken from the truncated FIR design as in (6.28), the SIR are 48 dB, 56 dB and 61 dB with $\Omega = 20$, 40 and 48, respectively. In general the filters should be designed so that the SIR is significantly higher (e.g., ≈ 20 dB more) than the best expected SNR in the system. In this way, the effect caused by zeroing the CP is negligible.

6.4 Recursive Time-Domain Equalizer

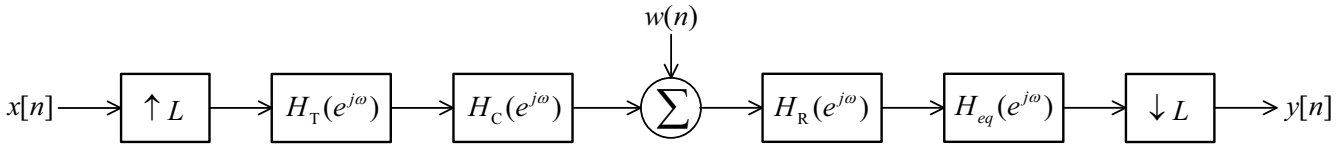

Figure 6.7 System in Fig. 6.6 with the digital equivalent channel.

Although there are many TEQ techniques proposed in the literature, they are only suitable for small-bandwidth systems. This is because the complexity of the TEQ grows linearly (e.g., LMS approach) or quadruply (e.g., RLS approach) with the system's symbol rate [C6.15]. For example, DOCSIS 3.0 employs a 24-tap adaptive equalizer for a single-carrier QAM system with symbol rate 5.357 MHz, which occupies a 6 MHz bandwidth (with a roll-off factor 0.12). The length of the TEQ equalizer should be large enough in order to equalize the longest expected delay spread of the system. If the same TEQ design is employed for the DOCSIS 3.1 channel with a symbol rate of 204.8 MHz, it would require a 918-tap TEQ to equalize such a wide-band channel. Therefore the frequency-domain equalizer (FEQ) has been a popular option when it comes to equalize large bandwidth signals, even when it suffers from the throughput loss due to CP insertion.

In contrast, this section proposes a novel design for a TEQ, whose complexity is very low and does not depend on the signal's bandwidth. Since the signal is band-limited by the pulse shaping and matched filters, the multipath channel can be represented by the following frequency response

$$H_{\mathrm{C}}(e^{j\omega}) = \sum_{i=0}^{N_p-1} \alpha_i \exp(-j\omega\tau_i), \quad \text{for } \frac{-(1+\beta)\pi}{L} \le \omega \le \frac{(1+\beta)\pi}{L}. \tag{6.32}$$

An ideal TEQ should have a frequency response expressed as

$$H_{\text{eq}}(e^{j\omega}) = \frac{1}{H_{\text{C}}(e^{j\omega})} = \frac{1}{\sum_{i=0}^{N_p-1} \alpha_i \exp(-j\omega\tau_i)}, \quad \text{for } \frac{-(1+\beta)\pi}{L} \leq \omega \leq \frac{(1+\beta)\pi}{L}. \tag{6.33}$$

It should be noted that $H_{\text{eq}}(e^{j\omega})$ is not a causal filter for $\tau_0 > 0$. As such, to design a practical filter that approximates $H_{\text{eq}}(e^{j\omega})$, the equalizer can be split into a negative delay portion and a recursive equalizer portion as follows:

$$\begin{aligned} H_{\text{eq}}(e^{j\omega}) &= \frac{\exp(j\omega\tau_0)}{\alpha_0} \times \frac{1}{1 + \sum_{i=1}^{N_p-1} \frac{\alpha_i}{\alpha_0} \exp\big(-j\omega(\tau_i - \tau_0)\big)} \\ &= \underbrace{\frac{\exp(j\omega\tau_0)}{\alpha_0}}_{H_d(e^{j\omega})} \times \underbrace{\frac{1}{1 + \sum_{i=1}^{N_p-1} \kappa_i \exp\big(-j\omega\mu_i\big)}}_{H_m(e^{j\omega})} \\ &= H_d(e^{j\omega}) H_m(e^{j\omega}). \end{aligned} \tag{6.34}$$

In the above expression, $H_d(e^{j\omega})$ is the negative delay portion to compensate for the timing error between the transmitter and the receiver, and $H_m(e^{j\omega})$ is the recursive equalizer.

First, consider the negative delay portion $H_d(e^{j\omega})$, which is created by fractional sample timing error τ_0 and a scale factor of α_0^{-1}. In order for the SRRC scheme described in section 6.3 to have a small amount of ISI, the fractional sample timing must be recovered correctly in the receiver. This is markedly different from normal OFDM systems where information about fractional sample timing is not important as long as starting of the DFT processing window is recovered at the correct time. A practical method for estimating the timing error can be found in [C6.16].

It can be seen that for $\tau_0 > 0$, $H_d(e^{j\omega})$ is the frequency response of a digital filter with a negative delay, which is not causal. However $H_d(e^{j\omega})$ can be delayed to become a causal filter. In particular, the delay part of the equalizer can be modified to be causal and have the following frequency response:

$$\overline{H}_d(e^{j\omega}) = \frac{\exp\left(-j\omega\gamma_0\right)}{\alpha_0}, \tag{6.35}$$

where the positive delay value γ_0 is a complement of the negative delay such that $\gamma_0 = d_0 T_s - \tau_0$ (seconds), where d_0 is an integer delay in samples that satisfy $d_0 > \tau_0/T_s$. With the modified delay, it can be seen that

$$H_{\mathrm{C}}(e^{j\omega})\overline{H}_d(e^{j\omega})H_m(e^{j\omega}) = \exp\left(-j\omega d_0 T_s\right), \ \frac{-(1+\beta)\pi}{L} \leq \omega \leq \frac{(1+\beta)\pi}{L}, \tag{6.36}$$

which means the TEQ introduces d_0 samples delay to the down-converted signal, i.e., $y[n] = x[n-d_0]$. The modified delay part of the equalizer is causal if $d_0 > \tau_0/T_s$.

In the special case, where γ_0 is an integer multiple of T_s/L, the digital filter can be easily obtained as $\overline{H}_d(z) = \alpha_0^{-1} z^{-\frac{\gamma_0}{(T_s/L)}}$, i.e., a scaled pure delay. However, the chance for that to happen is slim to non-existing. Instead, $L\gamma_0/T_s$ is generally a fractional delay and $\overline{H}_d(z)$ must be designed accordingly.

Many design techniques have been proposed for digital FIR and IIR filters to approximate a fractional delay's transfer function (e.g., [C6.17, C6.18] and the references therein). One of the most cost-effective and well known design is the Thiran allpass filter/interpolator [C6.19]. In particular, a fractional delay $\epsilon \in [0, 1]$ can be approximated by employing a Thiran interpolator as

$$z^{-\epsilon} \approx z^{\Theta-1} F_\Theta(z;\epsilon), \tag{6.37}$$

where $F_\Theta(z;\epsilon)$ is the transfer function of an order-Θ allpass filter, given as

$$F_\Theta(z;\epsilon) = \frac{a_\Theta + a_{\Theta-1}z^{-1} + \cdots + a_1 z^{-(\Theta-1)} + z^{-\Theta}}{1 + a_1 z^{-1} + \cdots + a_{\Theta-1}z^{-(\Theta-1)} + a_\Theta z^{-\Theta}}. \tag{6.38}$$

There is a closed form solution to design the allpass filter's coefficients to have maximally flat phase delay equal to $\epsilon + \Theta - 1$ at DC. The formula is [C6.19]

$$a_k = (-1)^k \binom{\Theta}{k} \prod_{d=0}^{\Theta} \frac{\epsilon - 1 + d}{\epsilon - 1 + k + d}, \quad k = 1, 2, \ldots, \Theta, \tag{6.39}$$

where

$$\binom{\Theta}{k} = \frac{\Theta!}{k!(\Theta - k)!}. \tag{6.40}$$

With the allpass delay filter, the Thiran interpolator as in (6.37) has no magnitude distortion. The phase delay is approximately ϵ, as there is no phase error at DC and more phase distortion towards higher frequency. As examples, Figure 6.8 shows the fractional phase delay ϵ versus frequency for 1st and 4th-order Thiran allpass interpolators.

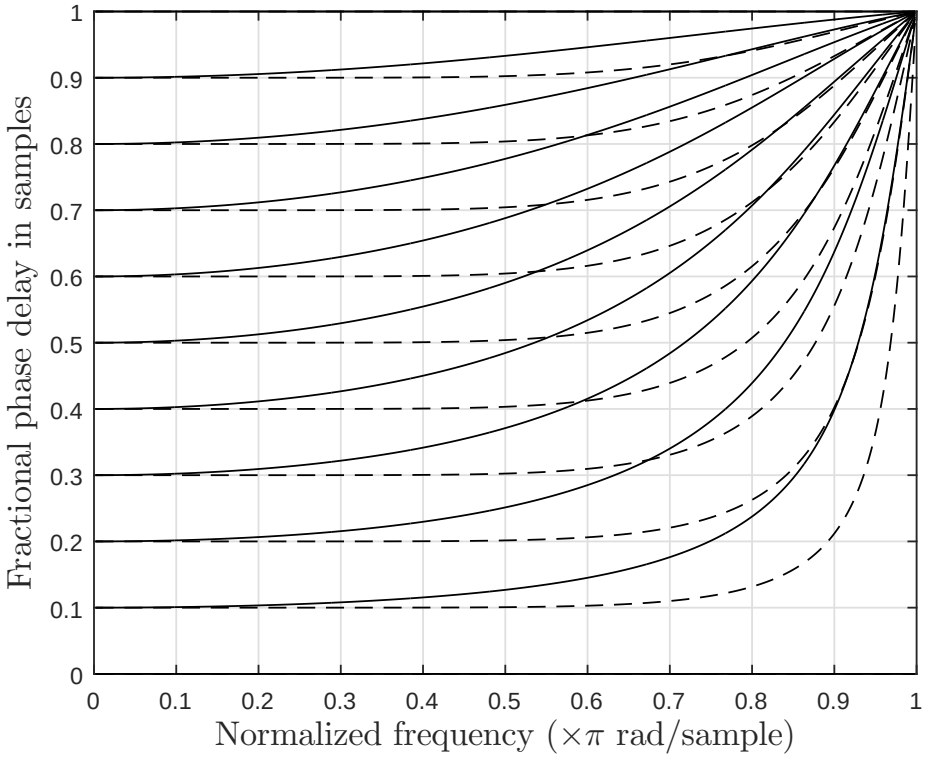

Figure 6.8 Fractional phase delay of the 1st-order (solid lines) and 4th-order (dashed lines) Thiran interpolators for various delays.

It can be seen from the figure that the delay is almost constant for $\omega < \pi/8$ for the 1st-order filter. The flatness can go upto $\pi/2$ for the 4th-order filter, which indicates that the 4th-order filter should perform closely to a pure delay for signals with over-sampling factor of $L = 2$.

From (6.37) and the fact that signal spectrum has a raised cosine shape, the approxima-

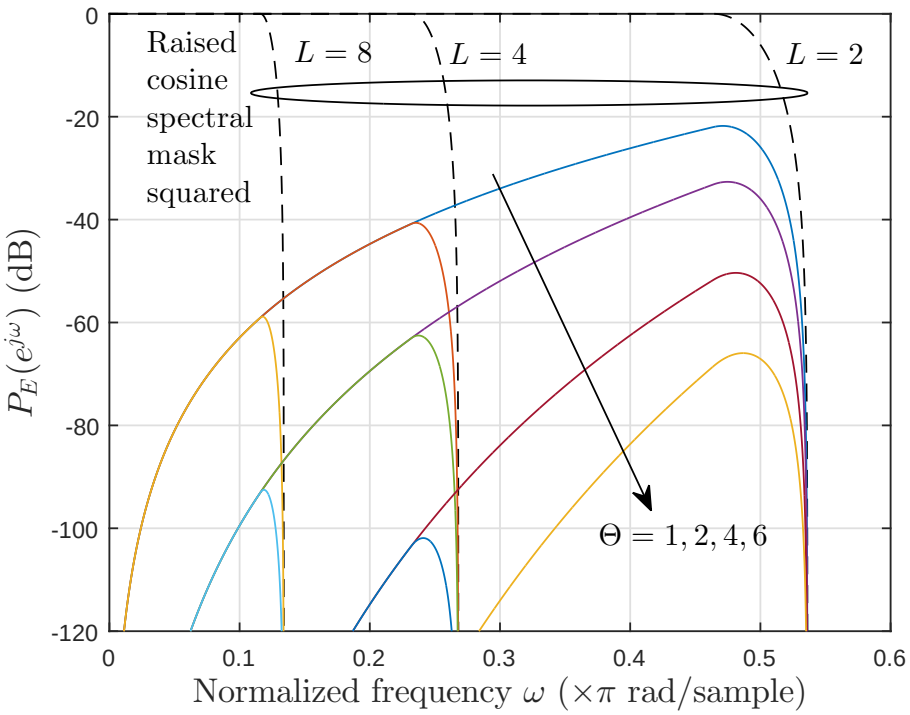

Figure 6.9 Average power of fractional delay approximation error versus normalized frequency.

tion error with fractional delay ϵ at frequency ω can be expressed as

$$\begin{aligned} E_\epsilon(e^{j\omega}) &= \left(e^{-j\omega\epsilon} - z^{\Theta-1}F_\Theta(e^{j\omega},\epsilon)\right) H_{\mathrm{T}}(e^{j\omega})H_{\mathrm{R}}(e^{j\omega}) \\ &\approx \left(e^{-j\omega\epsilon} - z^{\Theta-1}F_\Theta(e^{j\omega},\epsilon)\right) H^2_{\mathrm{SRRC}}(e^{j\omega}). \end{aligned} \tag{6.41}$$

Thus the average power of the approximation error at frequency ω can be expressed as

$$P_E(e^{j\omega}) = \mathbb{E}\left\{|E_\epsilon(e^{j\omega})|^2\right\}, \tag{6.42}$$

which is plotted with solid lines in Fig. 6.9 for various orders of the Thiran interpolator. The squared spectral mask of the raised cosine filters (i.e., $H^4_{\mathrm{SRRC}}(e^{j\omega})$) are also shown as dashed lines in the figure with various up-sampling factors, $L = 2$, 4 and 8. It can be seen that the approximation error becomes larger towards the edge of the signal's spectrum. However, one can keep the worst case error below a certain level by selecting appropriate combinations of parameters L and Θ. For example, one can keep the approximation error

below -60 dB by choosing up-sampling factor $L = 2$ and Thiran interpolator order $\Theta = 6$, or other combinations such as $L = 4$ and $\Theta = 2$, or $L = 8$ and $\Theta = 1$.

The Thiran interpolator can be concatenated with a pure delay element to yield an interpolator with a larger delay. In particular, the delay in samples $(L\gamma_0/T_s)$ can be expressed as a sum of the integer delay part $\eta_0 = \lfloor L\gamma_0/T_s \rfloor$ and the fractional delay part $\epsilon_0 = (L\gamma_0/T_s) - \eta_0$. Thus the delay portion of the equalizer can be built to approximate (6.35) as

$$\widehat{H}_d(z) = \frac{z^{-\eta_0} z^{\Theta_0 - 1} F_{\Theta_0}(z; \epsilon_0)}{\alpha_0} = \frac{z^{-(\eta_0 - \Theta_0 + 1)} F_{\Theta_0}(z; \epsilon_0)}{\alpha_0}. \tag{6.43}$$

It is obvious that $\widehat{H}_d(z)$ is a causal filter if $\eta_0 \geq \Theta - 1$. This means that in designing the interpolator, one can choose a small filter order to accommodate a short delay, or increase the delay to make interpolation with a higher order all-pass filter possible.

Next, attention is turned to the recursive equalizer portion. Similarly, (6.34) can be approximated using Thiran interpolators as

$$\widehat{H}_m(z) = \frac{1}{1 + \sum_{i=1}^{N_p - 1} \kappa_i z^{-(\eta_i - \Theta_i + 1)} F_{\Theta_i}(z; \epsilon_i)}, \tag{6.44}$$

where η_i and ϵ_i are the integer and fractional parts of $(L\mu_i/T_s)$, $i = 1, 2, \ldots, N_p - 1$, so that $\widehat{H}_m(e^{j\omega}) = \widehat{H}_m(z)|_{z=e^{j\omega}} \approx H_m(e^{j\omega})$, $\forall\ \omega \in [-(1+\beta)\pi/L,\ (1+\beta)\pi/L]$. Note that the recursive equalizer design allows using Thiran interpolators with different orders, i.e., $\{\Theta_i\}_{i=1}^{N_p - 1}$, for different echo delays.

The recursive equalizer has to be a causal and stable IIR filter. In order to make the filter causal, the term $z^{-(\eta_i - \Theta_i + 1)}$ must be causal, i.e., $\eta_i - \Theta_i + 1 \geq 0$. Therefore causality is maintained by taking the order of the all-pass filter as

$$\Theta_i = \min\left(\eta_i + 1, \Theta_{\max}\right) \tag{6.45}$$

where $\Theta_{\max}$ is the maximum order allowed for any all-pass interpolator in the equalizer. The worst case scenario is when $\eta_i = 0$, which happens when there is an echo that is less than a sampling period away from the main path, i.e., $\tau_i - \tau_0 < T_s/L$. In this case, one needs

to increase the up-sampling factor L or employ the first order all-pass filter, i.e., $\Theta_i = 1$, to make the equalizer causal. It should be noted that, the worst case scenario is very unlikely to happen with extremely small T_s, i.e., with a large-bandwidth system.

Finally, examine the stability problem. Let $F_\kappa(z)$ denote the negative of the summation term in (6.44). That is

$$F_\kappa(z) = -\sum_{i=1}^{N_p-1} \kappa_i z^{-(\eta_i-\Theta_i+1)} F_{\Theta_i}(z;\epsilon_i). \tag{6.46}$$

Assuming $|F_\kappa(z)| < 1$, so that $\lim_{k\to\infty}(F_\kappa^k(z)) = 0$. Then $\widehat{H}_m(z)$ can be expanded as a convergent geometric series as

$$\widehat{H}_m(z) = \frac{1}{1-F_\kappa(z)} = \frac{1-F_\kappa^\infty(z)}{1-F_\kappa(z)} = 1 + \sum_{k=1}^{\infty} F_\kappa^k(z), \tag{6.47}$$

which is equivalent to a causal FIR filter with a decaying impulse response. Therefore the recursive equalizer is stable under the following condition:

$$\left|\sum_{i=1}^{N_p-1} \kappa_i e^{-j\omega(\eta_i-\Theta_i+1)} F_{\Theta_i}(e^{j\omega};\epsilon_i)\right| < 1, \quad \frac{-(1+\beta)\pi}{L} \le \omega \le \frac{(1+\beta)\pi}{L}. \tag{6.48}$$

Since the magnitude response of an all-pass filter is unity at all frequencies, the condition (6.48) is guaranteed if the following condition is met:

$$\left|\sum_{i=1}^{N_p-1} \kappa_i\right| < 1, \text{ or equivalently } \left|\sum_{i=1}^{N_p-1} \alpha_i\right| < |\alpha_0|. \tag{6.49}$$

Figure 6.10 shows a circuit diagram of the proposed TEQ. The delay part $\widehat{H}_d(z)$ is implemented with $\Theta_{\max}$ real multiples for the allpass filter and one complex multiply for scaling, whereas the recursive equalizer part $\widehat{H}_m(z)$ requires $\Theta_{max}(N_p-1)$ real and (N_p-1) complex multiplies. It is pointed out that, although the recursive filter order is $\eta_{N_p-1} + 1$, which could be quite big and proportional to the up-sampling factor and the system's bandwidth, the complexity of the recursive equalizer is still low since most of the coefficients

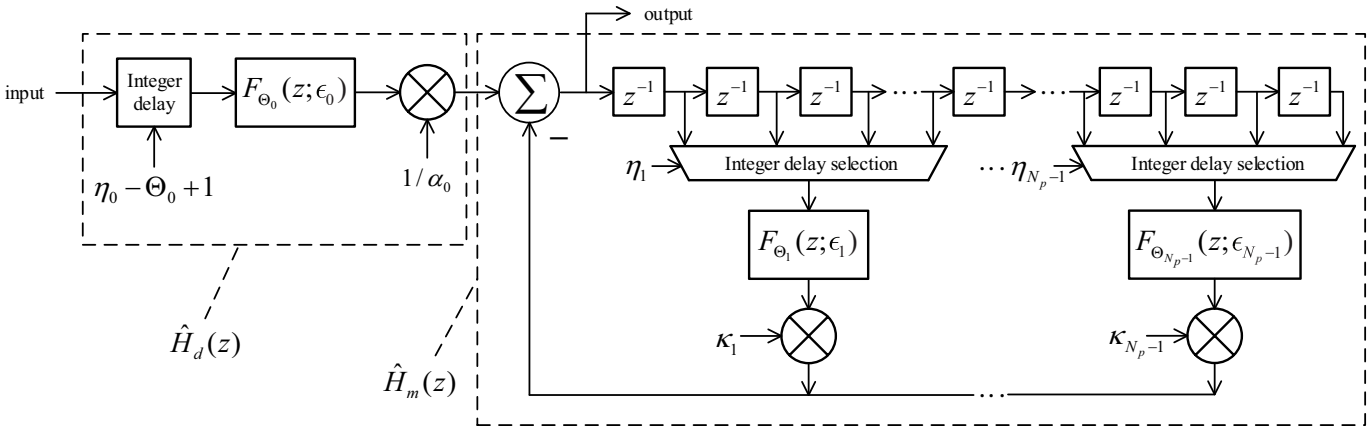

Figure 6.10 Hardware implementation of the TEQ.

are zeros, i.e., it is a sparse IIR filter. Overall, the TEQ's coefficients are determined by $2N_p$ parameters $\{\tau_i,\ \alpha_i\}_{i=0}^{N_p-1}$ and the implementation requires N_p complex multiplies and $N_p\Theta_{\max}$ real multiplies.

6.5 Simulation Results

This section investigates the performance of the proposed zero-CP OFDM design. The simulation results are provided for DOCSIS 3.1 downstream channels, which can have up to 7 echoes with the characteristics listed in the Table 6.1. The downstream sampling rate is $F_s = 204.8$ MHz.

Table 6.1 Micro-reflection characteristics for multi-echo scenario.

Echo #	Power	Relative delay versus the main path in seconds (μ_i)
1^{st}	-20 dBc	$\leq 0.5\ \mu$s ($\sim 102\ T_s$)
2^{nd}	-25 dBc	$\leq 1.0\ \mu$s ($\sim 205\ T_s$)
3^{rd}	-30 dBc	$\leq 1.5\ \mu$s ($\sim 307\ T_s$)
4^{th}	-35 dBc	$\leq 2.0\ \mu$s ($\sim 410\ T_s$)
5^{th}	-40 dBc	$\leq 3.0\ \mu$s ($\sim 614\ T_s$)
6^{th}	-45 dBc	$\leq 4.5\ \mu$s ($\sim 922\ T_s$)
7^{th}	-50 dBc	$\leq 5.0\ \mu$s ($\sim 1024\ T_s$)

To test the performance of the system under the extreme scenario, all the simulations are carried out with channels having all 7 echoes simultaneously present. The delay of the main path τ_0 is modeled as a random variable that is uniformly distributed between 0 and T_s, whereas the relative delay between an echo and the main path is modeled as

a random variable that is uniformly distributed within its range, i.e., $\mu_1 \sim \mathcal{U}(0,\ 0.5\mu\text{s})$, $\mu_2 \sim \mathcal{U}(0.5\mu\text{s},\ 1\mu\text{s})$, ..., and so on. The signal is generated with 4096-point IDFT, and has $M = 3800$ active sub-carriers indexed by $\mathcal{S}(m) = m+148,\ m = 0, 1, \ldots, 3799$ (no sub-carrier skipping), which leaves 148 unused carriers as guard bands at both ends of the spectrum. The modulation type for each active sub-carrier is 4096-QAM, which is the highest modulation order that DOCSIS 3.1 transceivers must support.

Table 6.2 Design options for OFDM systems without CP.

Design	L	$\Theta_{\max}$	$P_E^{\max}$ (dB)	Ω	SIR (dB)	$\text{MSE}^{\max}$ (dB)	MSE^{avg} (dB)	Complexity	
								Real multiply	Complex multiply
A	2	6	-65.9	20	48.3	-44.9	-50.4	48	8
B	2	6	-65.9	32	52.4	-47.6	-55.3	48	8
C	2	6	-65.9	48	61.5	-55.9	-63.4	48	8
D	4	2	-62.5	96	60.2	-54.9	-62.3	16	8
E	8	1	-58.9	208	63.2	-55.8	-62.8	8	8

The simulation examines 5 different designs, labeled as designs A, B, C, D and E, whose design parameters are listed in Table 6.2. The column $P_E^{\max}$ denotes the maximum Thiran approximation error, i.e., $P_E^{\max} = \max\{P_E(e^{j\omega});\ \forall\omega \in [-\pi, \pi]\}$, which occurs at sub-carriers located near the band-edge, as seen in Fig. 6.9. The equalization performance of each system is measured, with the absence of AWGN noise, in terms of the mean square error of the demodulated frequency-domain QAM-symbol at each sub-carrier, which is expressed as

$$\text{MSE}[m] = \mathbb{E}\left\{\left|X_k[m] - \widehat{X}_k[m]\right|^2\right\}. \tag{6.50}$$

The maximum and averaged values of the mean squared error in dB are also given in Table 6.2 (denoted with column names $\text{MSE}^{\max}$ and MSE^{avg}, respectively). The last two columns of the table provide the complexity of the proposed time-domain equalizer in terms of the numbers of real multiplies and complex multiplies required to implement the equalizer.

The first 3 designs, i.e., A, B and C, are selected to examine the impact of the pulse shaping and matched filtering on the system performance. The equalizer performance of the three designs is selected to be the same with $P_E^{\max} = -65.9$ dB. The only difference among

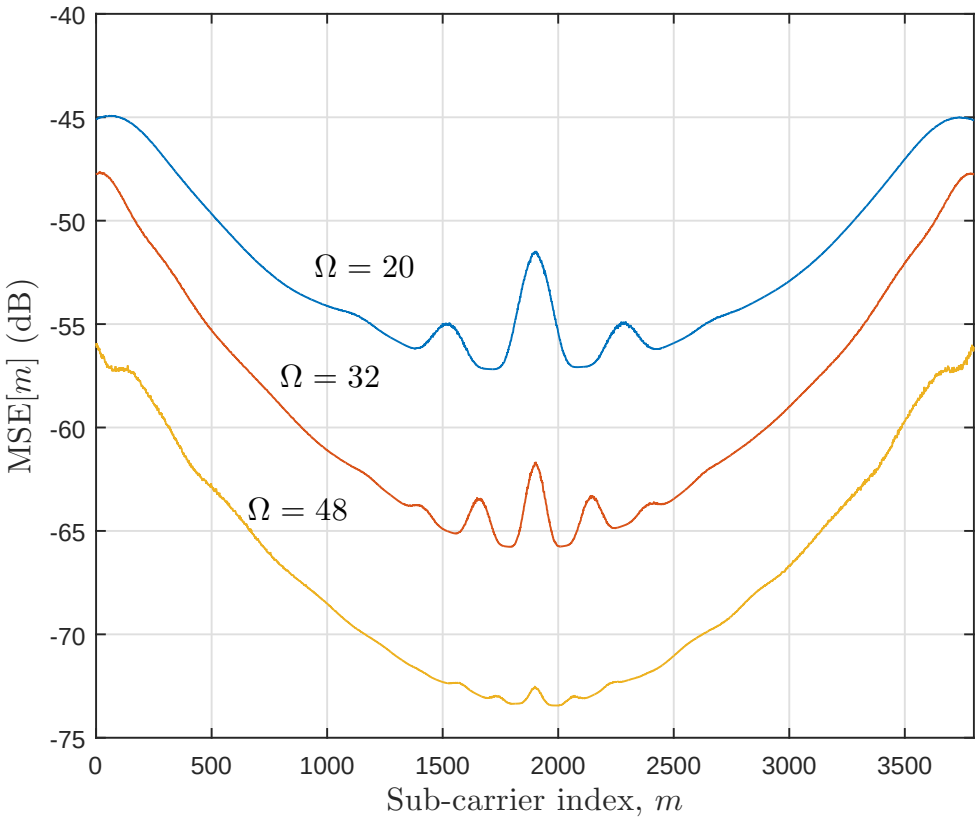

Figure 6.11 MSE of demodulated OFDM symbols for designs A, B and C.

the 3 designs is the order of the pulse shaping and matched filters, which is 20, 32 and 48, corresponding to SIR of 48.3 dB, 52.4 dB and 61.5 dB for designs A, B and C, respectively. The mean squared error at each sub-carrier is plotted in Fig. 6.11 for the three designs. It can be seen that, due to the characteristic of the all-pass approximation, there is a larger error towards the band-edges and less error at sub-carriers located around the middle of the band. For low-order filters, i.e., $\Omega = 20$ and 32, there are ripples at the middle of the band, shaped up according to the stop-band ripples of the filters, which is an indication of a poor anti-aliasing performance. Therefore the difference between the maximum and the minimum of the MSE increases with a higher order filter. Furthermore, it can be seen that the average MSE scales well with the interference power, i.e., $\text{MSE}^{\text{avg}} \approx -\text{SIR} - 2$ dB.

It is obvious that L and $\Theta_{\max}$ determine $P_E^{\max}$ and Ω determines SIR. Both $P_E^{\max}$ and SIR are good indications of the system's MSE performance. The last 3 designs, namely C, D and

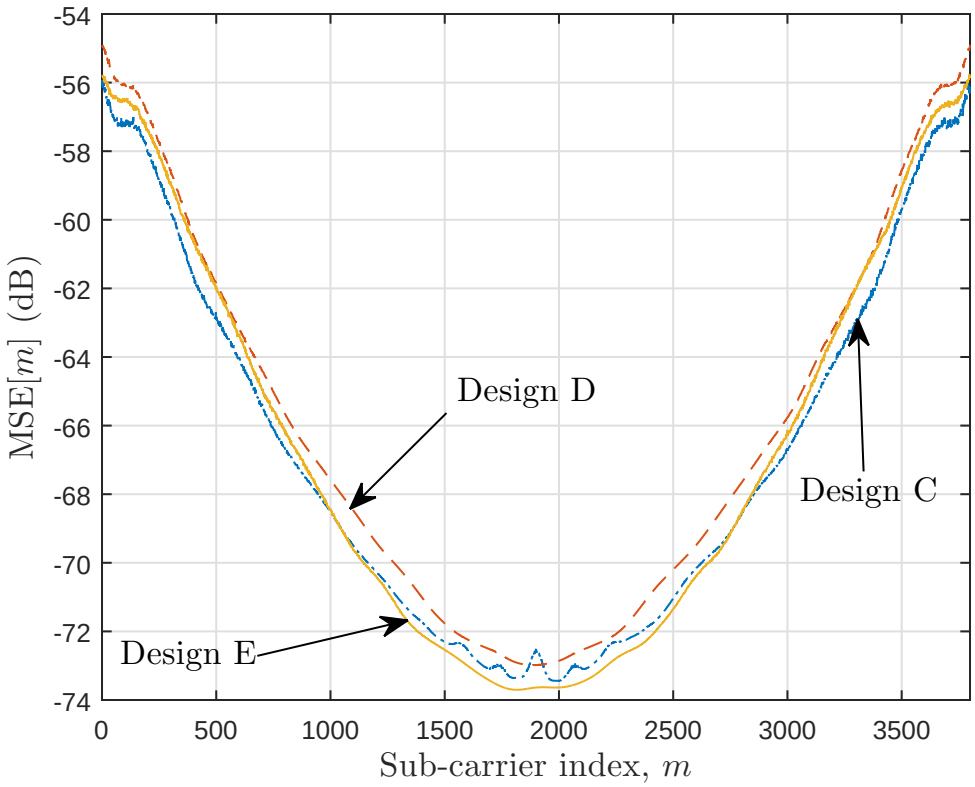

Figure 6.12 MSE of demodulated OFDM symbols for designs C, D and E.

E, are set up so that their $P_E^{\max}$ and SIR are about the same. In particular, the 3 designs have different up-sampling factors and the filter lengths are selected to be shortest possible to give SIR $\geq$ 60dB [2]. Also the maximum all-pass order $\Theta_{\max}$ is selected in these three designs so that $P_E^{\max} \approx -60$ dB. As expected, the MSE performance of the 3 designs, shown in Fig. 6.12, are about the same across all sub-carriers, with the maximum difference among them is less than 1 dB. The complexity of the pulse shaping and matched filters increases linearly with the up-sampling factor, which requires 49, 97 and 209 multiplies for $L = 2$, 4 and 6, respectively. It should be noted that, the higher up-sampling factor would greatly facilitate the design of analog filters in the system. Higher L also simplifies the design of the time-domain recursive equalizer, especially when $L \geq 8$, since the equalizer only requires N_p real and N_p complex multiplies.

[2]The maximum throughput of a DOCSIS 3.1 system is likely to be achievable with SNR $\geq$ 43 dB. Therefore a good rule-of-thumb is that any imperfection introduced to the system should be limited to be less than or equal to -60 dB, in order to be considered as negligible.

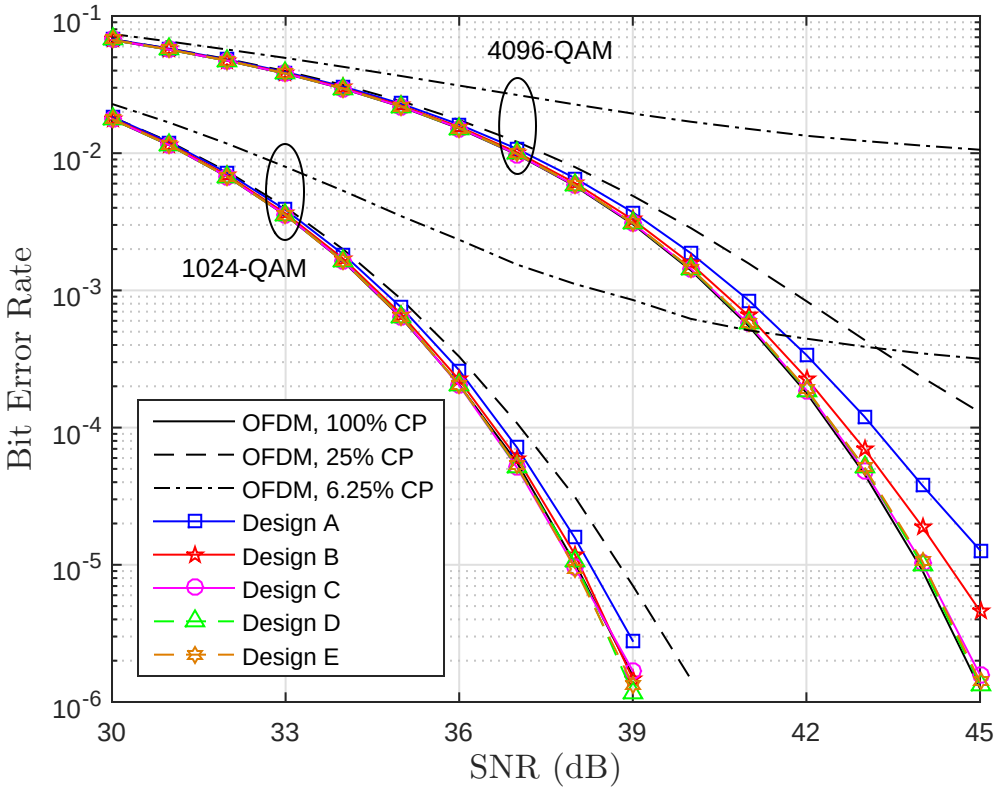

Figure 6.13 Bit error rate of the 5 designs and the conventional OFDM.

Next, the raw bit error rate performance (i.e., without channel coding) of the 5 designs are compared against the conventional OFDM system in Fig. 6.13. The conventional OFDM system under comparison employs the MMSE frequency-domain equalizer with sufficient cyclic prefix (100% CP) and non-sufficient cyclic prefix (25% and 6.25%). Two modulation types considered are 4096-QAM and 1024-QAM, whose performances are about 6 dB away from each other. It can be seen that the performance of the conventional OFDM system degrades significantly when the CP is insufficient. The 5 designs of the proposed system works very well without any CP. In particular, for 4096-QAM modulation, the performance curves of designs C, D and E completely overlap with that of the OFDM system using 100% CP. For 1024-QAM, the performance curves of designs B, C, D and E completely overlap with that of the OFDM system using sufficient CP. Overall, depending on how much the base-band signal is up-sampled, designs C, D and E appear to be excellent solutions to transmit OFDM signals without CP.

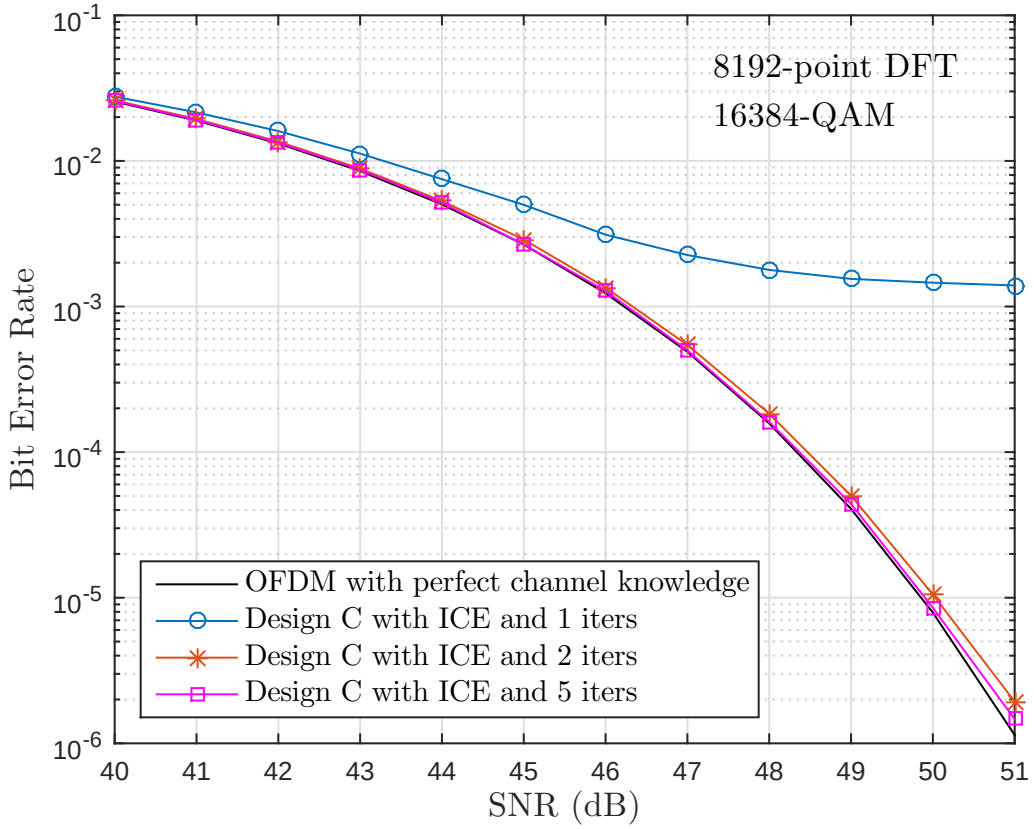

Figure 6.14 Bit error rate of the design C with estimated channel versus conventional OFDM with perfect channel knowledge.

Lastly, a realistic system is constructed to examine the performance of the Zero-CP OFDM scheme with estimated channel parameters. Design C from Table. 6.2 is selected and the system is constructed with 8192-point DFT/IDFT that allows upto 7600 active sub-carriers. Also the modulation type at each sub-carrier is increased to 16384-QAM. The system is set up to reach the highest throughput that DOCSIS 3.1 can optionally achieve. Moreover, rather than taking the perfect channel parameters as the above simulations, an iterative channel estimator (ICE) [C6.16] is employed to obtain the channel parameters. The ICE technique is selected since it is a practical implementation for DOCSIS 3.1 system and more importantly, the technique can estimate exact channel path gains and delays, which is required for the TEQ, rather than just frequency response as almost all other methods in the literature did. To keep the complexity of the channel estimator low and speed up the simulation, the channel estimation is performed with resolution factor of 2 and sub-carrier

skipping factor of 8 [C6.16]. As shown in Fig. 6.14, 1 iteration channel estimation is clearly not sufficient as the BER of the Zero-CP system reaches an apparent error floor around 0.001. However, with just one more iteration performed, the BER reduces significantly and even on par with the performance of conventional OFDM system with perfect channel knowledge which indicates the performance limitation of OFDM signaling. Since the performance of the Zero-CP OFDM system with 2-iteration ICE is already very close to the limit, performing more iterations only shows marginal performance gain, as seen in Fig. 6.14.

6.6 Conclusions

In this paper, a design to transmit and receive OFDM signals over a multipath channel without the use of CP is proposed. The design employs Nyquist filters as interpolation/anti-aliasing filters to eliminate the ISI caused by band-limiting the signal. A novel TEQ design, which uses Thiran interpolator to approximate fractional delay elements, is proposed to synchronize the receiver to the transmitter and inverse the multipath channel effect. It is shown that performance of the proposed design compares favorably to the performance of a conventional OFDM system that employs the MMSE frequency-domain equalizer but requires sufficient CP. Implementation of the proposed zero-CP OFDM system is simple since finding the TEQ's coefficients is straight forward and the hardware requirement for the TEQ can be as little as one real and one complex multiply per channel path (i.e., design E presented before). The proposed design is initially conducted with DOCSIS 3.1 systems in mind, therefore so far the design only works for minimum phase and slow-fading channels. Further research can be done to make the design work for a more general channel.

Acknowledgments

This work is supported in part by a Natural Science and Engineering Council of Canada (NSERC) Industrial Postgraduate Scholarship (IPS) and Vecima Networks.

References

[C6.1] Cable Television Laboratories, Inc., "DOCSIS 3.1 Physical Layer Specification," Oct 2013.

[C6.2] B. Hamzeh, M. Toy, Y. Fu, and J. Martin, "DOCSIS 3.1: scaling broadband cable to Gigabit speeds," *IEEE Commun. Mag.*, vol. 53, pp. 108–113, Mar. 2015.

[C6.3] G. Arslan, B. Evans, and S. Kiaei, "Equalization for discrete multitone transceivers to maximize bit rate," *IEEE Trans. Signal Process.*, vol. 49, pp. 3123–3135, Dec. 2001.

[C6.4] S. Celebi, "Interblock interference (IBI) minimizing time-domain equalizer (TEQ) for OFDM," *IEEE Signal Process. Letters*, vol. 10, pp. 232–234, Aug. 2003.

[C6.5] A. Tkacenko and P. Vaidyanathan, "A low-complexity eigenfilter design method for channel shortening equalizers for DMT systems," *IEEE Trans. Commun.*, vol. 51, pp. 1069–1072, July 2003.

[C6.6] Y. Jin and X.-G. Xia, "A Robust Precoder Design Based on Channel Statistics for MIMO-OFDM Systems with Insufficient Cyclic Prefix," *IEEE Trans. Commun.*, vol. 62, pp. 1249–1257, Apr. 2014.

[C6.7] Y. Jin and X.-G. Xia, "An Interference Nulling Based Channel Independent Precoding for MIMO-OFDM Systems with Insufficient Cyclic Prefix," *IEEE Trans. Commun.*, vol. 61, pp. 131–143, Jan. 2013.

[C6.8] M. Malkin, C.-S. Hwang, and J. Cioffi, "Transmitter Precoding for Insufficient-Cyclic-Prefix Distortion in Multicarrier Systems," in *Proc. IEEE Veh. Technol. Conf.*, pp. 1142–1146, May 2008.

[C6.9] A. Farsiabi and M. Sabbaghian, "Iterative interference reduction in single carrier block transmission without cyclic prefix," in *Int. Symp. on Telecommun.*, pp. 226–231, Nov. 2012.

[C6.10] M. Nisar, W. Utschick, H. Nottensteiner, and T. Hindelang, "On Channel Estimation and Equalization of OFDM Systems with Insufficient Cyclic Prefix," in *Proc. IEEE Veh. Technol. Conf.*, pp. 1445–1449, Apr. 2007.

[C6.11] S. Kunaruttanapruk and S. Jitapunkul, "The novel decision feedback equalizer for OFDM system with insufficient cyclic prefix," in *Proc. IEEE on Commun. Networks and Services Research*, pp. 19–24, May 2004.

[C6.12] I. Freire, C. Lu, P.-E. Eriksson, and A. Klautau, "Low complexity precoder and equalizer for DMT systems with insufficient cyclic prefix," in *Proc. IEEE Global Telecommun. Conf.*, pp. 3243–3248, Dec. 2014.

[C6.13] M. Faulkner, "The effect of filtering on the performance of OFDM systems," *IEEE Trans. Veh. Technol.*, vol. 49, pp. 1877–1884, Sept. 2000.

[C6.14] T. Nguyen, J. Salt, H. Nguyen, and B. Berscheid, "Optimizing Pulse Shaping Filter for DOCSIS Systems," *IEEE Trans. on Broadcasting*, vol. PP, no. 99, pp. 1–12, 2016.

[C6.15] B. Farhang-Boroujeny, *Adaptive Filters: Theory and Applications*. Wiley, 2013.

[C6.16] T. Nguyen, J. Salt, H. Nguyen, and B. Berscheid, "A Novel Iterative OFDM Channel Estimation Technique for DOCSIS 3.1 Uplink Channels," *Unpublished manuscript.*, 2016.

[C6.17] A. Charef and T. Bensouici, "Digital fractional delay implementation based on fractional order system," *IET Signal Process.*, vol. 5, pp. 547–556, Sept. 2011.

[C6.18] H. K. Kwan and A. Jiang, "FIR, Allpass, and IIR Variable Fractional Delay Digital Filter Design," *IEEE Trans. Circuits and Systems.*, vol. 56, pp. 2064–2074, Sept. 2009.

[C6.19] J.-P. Thiran, "Recursive digital filters with maximally flat group delay," *IEEE Trans. Circuit Theory.*, vol. 18, pp. 659–664, Nov. 1971.

7. Summary and Suggestions for Further Studies

7.1 Summary

This thesis proposed several techniques to improve the efficiency of data transmission in cable networks. The thesis concentrated on three areas of cable networks: (i) efficient implementations of backward-compatibility functions from the old DOCSIS standards (i.e., prior to version 3.1) that employ SC-QAM, (ii) addressing and providing solutions for technically-challenging issues in the current DOCSIS 3.1 standard that employs OFDM/OFDMA and, (iii) introducing prospective features that can be implemented in the future standard.

The first contribution to the first area was a hybrid parameterization of the filter transfer function for the pulse shaping in combination with the Gauss-Newton optimization approach. The resulting IIR pulse shaping filters satisfied the DOCSIS 3.0's out-of-band emission requirements, yielded sufficiently low ISI and had better efficiency than linear-phase FIR filters, windowed or otherwise.

A contribution to the second area was an introduction of a new fractional timing estimation algorithm. The proposed approach performed an interpolation between two sampled points in the vicinity of the peak. The algorithm is highly practical since the interpolation is approximately linear in log-domain. The technique outperformed the well-known three-sample parabolic interpolation technique in applications where the channel has either no echoes or weak echoes or echoes with long delays. Moreover, the log-domain peak detection technique was used to significantly enhance the performance of the OFDMA channel estimation algorithm proposed in Chapter 5.

The second contribution to the second area was a novel technique to estimate the multi-

path channel for DOCSIS 3.1 cable networks. Unlike most of the channel estimation methods for OFDMA systems which estimate the channel in the frequency-domain, the proposed technique iteratively searches for parameters of the channel paths in the time domain. Furthermore, the technique was able to estimate/interpolate the entire channel's frequency response for each user despite receiving pilots on only every K^{th} sub-carrier. The proposed technique not only substantially enhanced the channel estimation accuracy, but also can, at no cost, accurately identify the delay of each echo in the system, which is valuable information for proactive maintenance of the network.

The third contribution to the second area was a novel scheme that allows OFDM transmission without the use of a cyclic prefix (CP). First, performance degradation of an OFDM system with a CP with insufficient length was analyzed. Then major alterations to the current DOCSIS 3.1 OFDM/OFDMA structure were proposed. The alterations involved using a pair of Nyquist filters at the transmitter and receiver, and an efficient time-domain equalizer (TEQ) at the receiver to reduce ISI down to a negligible level without any CP.

Finally, Chapter 5 and Chapter 6 contribute to a realistic cable system that is able to transmit OFDM symbols without a CP under the DOCSIS 3.1 multipath channel condition. The BER performance of that system is almost the same as the theoretical performance of a system that has a CP of sufficient length and perfect knowledge of the channel.

7.2 Suggestions for Further Studies

The novel techniques proposed in this thesis made significant improvements to data transmission in the cable networks. While conducting the research works, several issues arose that would be interesting for further studies. These issues are elaborated below.

- In Chapter 5, a novel channel estimation technique was proposed. It was shown that the algorithm requires a reasonably larger number of iterations to accurately detect short echo delays, while only a few iterations are needed to accurately detect longer echo delays. Therefore, further improvement can be realized by adaptively adjusting the number of iterations based on an initial estimation of the echo delays. In doing

so, the complexity of the algorithm might be reduced without sacrificing the channel estimation performance.

- The algorithm introduced in Chapter 5 was designed with DOCSIS 3.1 systems in mind and shown to work well with coaxial cable channels. The analysis was performed with echoes having pure delays. However, if the echoes are not pure-delays, but rather frequency-selective, i.e., due to non-linearity characteristic of the coaxial cables for wide-band signals, the channel estimation accuracy is expected to degrade. Therefore, more research effort is needed to address this issue.

- As mentioned in Chapter 6, the proposed design of zero-CP OFDM systems only works for minimum phase and slow-fading channels. Therefore, in order to make the design useful for different types of channels, e.g., wireless channels, further studies should be carried out.

- The contribution in Chapter 6 on zero-CP OFDM systems focused mainly on the TEQ design, while the most popular filter design, namely rectangular-windowed FIR design, was applied to obtain the pair of pulse shaping and matched filters. However, different filter design techniques, such as those presented in Chapter 3, can be used to obtain more efficient filters. As such, further analysis should be carried out to find the most effective filter design for particular applications of zero-CP OFDM systems.

Title:	Optimizing Pulse Shaping Filter for DOCSIS Systems
Author:	Tung T. Nguyen; Joseph Eric Salt; Ha H. Nguyen; Brian Berscheid
Publication:	Broadcasting, IEEE Transactions on
Publisher:	IEEE
Date:	June 2016

Thesis / Dissertation Reuse

The IEEE does not require individuals working on a thesis to obtain a formal reuse license, however, you may print out this statement to be used as a permission grant:

Requirements to be followed when using any portion (e.g., figure, graph, table, or textual material) of an IEEE copyrighted paper in a thesis:

1) In the case of textual material (e.g., using short quotes or referring to the work within these papers) users must give full credit to the original source (author, paper, publication) followed by the IEEE copyright line © 2011 IEEE.
2) In the case of illustrations or tabular material, we require that the copyright line © [Year of original publication] IEEE appear prominently with each reprinted figure and/or table.
3) If a substantial portion of the original paper is to be used, and if you are not the senior author, also obtain the senior author's approval.

Requirements to be followed when using an entire IEEE copyrighted paper in a thesis:

1) The following IEEE copyright/ credit notice should be placed prominently in the references: © [year of original publication] IEEE. Reprinted, with permission, from [author names, paper title, IEEE publication title, and month/year of publication]
2) Only the accepted version of an IEEE copyrighted paper can be used when posting the paper or your thesis on-line.
3) In placing the thesis on the author's university website, please display the following message in a prominent place on the website: In reference to IEEE copyrighted material which is used with permission in this thesis, the IEEE does not endorse any of [university/educational entity's name goes here]'s products or services. Internal or personal use of this material is permitted. If interested in reprinting/republishing IEEE copyrighted material for advertising or promotional purposes or for creating new collective works for resale or redistribution, please go to http://www.ieee.org/publications_standards/publications/rights/rights_link.html to learn how to obtain a License from RightsLink.

If applicable, University Microfilms and/or ProQuest Library, or the Archives of Canada may supply single copies of the dissertation.